Contributions to the chemistry of heteroleptic coordination compounds based on 3d metal ions with special properties for applications in medicine

Adelina-Antonia S. Andelescu

IOD: ACADEMIA ROMANA
ICA: INSTITUTUL DE CHIMIE „CORIOLAN DRĂGULESCU"

Bd. Mihai Viteazu, nr. 24, RO-300223, Timişoara, România
tel: 0256-491818; fax: 0256-491824

UNIVERSITÉ DE STRASBOURG
ÉCOLE DOCTORALE
ED182

INSTITUT DE PHYSIQUE ET CHIMIE DES MATERIAUX DE STRASBOURG

Département des Matériaux Organiques

- CNRS UMR 7504 -

A doctoral thesis submitted
by
Adelina-Antonia S. ANDELESCU

Contribuții la chimia compușilor coordinativi heteroleptici ai unor ioni 3d cu proprietăți speciale pentru aplicații în medicină

Contributions to the chemistry of heteroleptic coordination compounds based on 3d metal ions with special properties for applications in medicine

Thesis directors:

Dr. Otilia Costișor	"Coriolan Dragulescu" Institute of Chemistry - ICT, Timișoara, Romania.
Dr. Bertrand Donnio	Institut de Physique et Chimie des Materiaux de Strasbourg - IPCMS, UMR 7504, Strasbourg, France.

Members of the committee:

1. **Dr. Franck CAMEREL**	Institut des Sciences Chimiques de Rennes, UMR 6226, Rennes, France. (Rapporteur)
2. **Dr. Francisc PETER**	University "Politehnica"Timisoara- Faculty of Industrial Chemistry and Enviromental Engineering, Timișoara, Romania. (Rapporteur)
3. **Dr. Ramona TUDOSE**	"Coriolan Dragulescu" Institute of Chemistry - ICT, Timișoara, Romania.
4. **Dr. Dana VLASCICI**	West University of Timisoara - Faculty of Chemistry, Biology, Geography, Timișoara, Romania.

Table of contents

Abbreviation list

2,2’-biquinoline – *bq*;

2,2’-bipyridine – *bpy*;

2,2-di-phenyl-1-picryl hydrazyl – DPPH;

4-dimethylaminopyridine – DMAP;

1,10-phenanthroline – *phen*;

Absorbance – A;

Acetonitrile – CH_3CN;

Analytical calculated - Anal. Calcd.;

Atomic absorption spectroscopy – AAS;

Circa – *ca.*;

Concentration – C (mol/L);

Chloroform – $CHCl_3$;

Dichloromethane – CH_2Cl_2;

Dicyclohexylurea – DCU;

Dimethylsulfoxide – DMSO;

Differential scanning calorimetry – DSC;

Ethanol – EtOH;

Et alia (lat. „and others”) – *et al.*;

Exempli gratia – *e.g.*;

Entalphy - ΔH ($kJ \cdot mol^{-1}$);

Id est (lat. „that is”) – *i.e*;

Intraligand charge-transfer – ILCT;

Fourier-Transform Infrared Spectroscopy – FT-IR;

Liquid crystal – LC;

Lamello-columnar – L_{col};

Mass – m (%);

Metallomesogen – MM;

Metal to ligand charge transfer – MLCT;

Methanol – MeOH;

Molar conductivity – Λ_M ($\Omega^{-1}mol^{-1}cm^2$);

N,N’-dicyclohexylcarbodiimide – DCC;

Nanoparticle – NP ;

Nuclear Magnetic Resonance spectroscopy – NMR;

Powder X-ray diffraction – PXRD;

Phosphate buffered saline solution – PBS;

Quantum yield - Φ (%);

Scanning Electron Microscopy – SEM;

Smectic – Sm;

Synchronous differential thermal analysis – SDTA;

Small- and wide- angle X-ray scattering – SWAXS;

Temperature – *T* (ºC);

Thermogravimetric analysis – TGA;

Time – t (min);

THF – tetrahydrofuran;

Transmittance – T (%);

Transmision Electron Microscopy – TEM;

Transition metal complex – TMC;

Trimethylsilyl bromide – TMSBr;

Ultraviolet visible spectroscopy - UV-Vis ;

Versus – *vs.;*

Wavelenght – λ (nm);

Wavenumber – $1/\lambda$ (cm^{-1});

Quantum yield - Φ (%);

Scanning Electron Microscopy – SEM;

Synchronous differential thermal analysis – SDTA;

Small- and wide- angle X-ray scattering – SWAXS;

Temperature – *T* (ºC);

Thermogravimetric analysis – TGA;

Time – t (min);

THF – tetrahydrofuran;

Transmittance – T (%);

Transmision Electron Microscopy – TEM;

Trimethylsilyl bromide – TMSBr;

Ultraviolet visible spectroscopy - UV-VIS

Versus – *vs.;*

Wavelenght – λ (nm);

Wavenumber – $1/\lambda$ (cm^{-1});

List of figures

List of schemes

List of tables

Résumé

Le concept de chimie médicinale inorganique a reçu une attention accrue avec la découverte des propriétés bactériostatiques et anticancéreuses des complexes polypyridyles de ruthénium par le groupe de Dwyer dans les années 1950-1960, et la découverte des propriétés anticancéreuses du *cis*-platine en 1969 par Rosenberg. Malgré son excellente activité contre le cancer, les patients traités avec le *cis*-platine présentent souvent de graves effets secondaires et peuvent développer une résistance aux médicaments, ce qui limite l'efficacité de ces derniers. Pour surmonter ces limitations, d'intenses recherches ont été consacrées à la synthèse de nouveaux médicaments selon essentiellement deux voies orthogonales : i) la conception de composés de platine classiques et non classiques, ou ii) la mise au point de nouvelles thérapies anti-tumorales contenant des métaux autres que le platine, basées sur le Zn(II), le Ru(II), l'Ag(I), l'Au(I), le Cu(I), etc.

La présente thèse porte sur la synthèse de complexes de métaux de transition (CMT) contenant des centres métalliques biocompatibles d'une part et des nanoparticules d'or (Au NP) fonctionnalisées avec des CMT dendritiques d'autre part, comme alternatives au *cis*-platine et à ses analogues. La conception des nouveaux CMT est également axée sur l'induction de propriétés spécifiques telles que la luminescence et/ou le mésomorphisme afin d'obtenir des matériaux fonctionnels avancés pouvant être utilisés comme des nanoplateformes multitâches. En effet, les composés biocompatibles luminescents sont pertinents pour les techniques d'investigation en imagerie, tandis que les films de métallomésogènes sont connus comme détecteurs d'espèces biologiques. Certaines études ont également révélé que l'ion métallique, en plus de jouer un rôle important dans l'efficacité des médicaments basés sur les CMT, peut également être considéré comme un bon transporteur de ligands biologiquement actifs. Par conséquent, le choix approprié des différents constituants moléculaires permet de combiner un ensemble de propriétés photophysiques et photochimiques habituellement inaccessibles au sein d'un seul système moléculaire, ce qui donne des matériaux intelligents avec de multiples centres thérapeutiques et de diagnostic ainsi que des capteurs potentiels pour les tissus biologiques, le tout au sein d'une plateforme unique.

En raison de leur forte capacité à former des complexes stables avec divers métaux, les hétérocycles azotés aromatiques constituent l'une des classes de ligands les plus étudiées en

chimie de coordination. Les oligopyridines (2,2'-bipyridine - *bpy*, 1,10-phénanthroline - *phen*, 2,2'-biquinoléine - *bq*, 2,2':6'2"-terpyridine - *tpy*) présentent un intérêt en médecine car : i) ils sont capables de former des composés de coordination stables avec divers ions métalliques par liaison dπ→pπ*, ii) leur structure plane les rend aptes à intercaler l'ADN, iii) la chélation d'un ion métallique d^6, d^8 ou d^{10} peut donner lieu à des CMT luminescents adaptés comme agents de bio-imagerie ou comme photosensibilisateurs pour la thérapie photodynamique (TPD), etc. En particulier, la quinoléine fait l'objet de recherches approfondies pour le développement de molécules bioactives, ayant des activités antibactériennes, antidépressives, antivirales, anticancéreuses et anti-inflammatoires.

Dans cette thèse, nous avons développé de nouveaux complexes de Cu(I) et Zn(II) avec des ligands hétérocycliques aromatiques azotés (N-donneurs), des métallomésogènes, des métallodendrimères et des NP dendronisées. Dans le premier chapitre, une introduction générale sur les CMT et les hybrides Au@TMC, avec un accent sur leurs applications potentielles dans les systèmes biologiques. Le deuxième chapitre concerne la synthèse de nouveaux complexes de coordination basés sur des centres métalliques biocompatibles tels que le Zn(II) et Cu(I) avec des ligands chélatants biologiquement actifs (N^N de type oligopyridines et/ou O^O de type flavonoïdes). L'optimisation des propriétés photophysiques des complexes a été réalisée par ingénierie moléculaire via la modification des différentes parties moléculaires : ligands, centres métalliques, contrions. Dans le troisième chapitre, les résultats prometteurs obtenus dans le deuxième chapitre et la plus grande stabilité des complexes de Zn(II) par rapport aux complexes de Cu(I), nous ont incités à développer de nouveaux cristaux liquides luminescents de Zn(II) avec des ligands terpyridine (*tpy*).

Afin d'obtenir une bonne efficacité thérapeutique et de minimiser les effets secondaires dans le traitement du cancer, des efforts croissants ont été faits pour combiner les fonctions thérapeutiques, d'imagerie et de ciblage dans une seule plate-forme théranostique. Ainsi, les travaux présentés dans le chapitre quatre visent à développer de nouveaux CMT et des nanosystèmes originaux en tant que matériaux avancés d'imagerie et de détection constitués de CMT fixés à des nanoparticules d'or (Au NP) fonctionnalisées par des coquilles dendritiques. Par conséquent, à partir des nouveaux CMT synthétisés, le complexe le plus performant sera positionné par ingénierie moléculaire judicieuse dans le champ plasmonique des Au NPs en utilisant des dendromésogènes comme connecteurs pour ajuster la séparation entre les deux espèces. L'utilisation de branches dendritiques pour ordonner et positionner le chromophore du complexe métallique autour des NP métalliques générera des réseaux "souples" ordonnés auto-assemblés où un effet antenne pourra être obtenu.

Les chapitres cinq et six contiennent respectivement les procédures expérimentales et les conclusions.

. Tous les nouveaux ligands et complexes métalliques ont été entièrement caractérisés par méthodes analytiques et spectroscopiques standard (analyse élémentaire, RMN, spectroscopie d'absorption atomique (AAS), FT-IR et UV-Vis), tandis que leur luminescence a été mise en évidence par spectroscopie de fluorescence. La stabilité thermique et le comportement ont été étudiés par analyse thermogravimétrique (ATG). Le cas échéant, leur comportement mésomorphe a été étudié par microscopie en lumière polarisée (POM), calorimétrie (DSC) et diffusion des rayons X (SAXS).

Complexes de Zn(II) et Cu(I) avec des ligands bidentés N^N

Malgré une recherche active et de grandes avancées dans le domaine, la synthèse de nouveaux CMT luminescents ayant des propriétés biologiques reste un véritable défi. Dans cette optique, l'ensemble des dérivés d'oligopyridines, du type 2,2'-bipyridine (*bpy*, ligand **L1**), 1,10-phénanthroline (*phen*, ligand **L2**), 2,2'-biquinoline (*bq*, ligand **L4** - **L6**) et la quercétine-$2H_2O$ (ligand O^O, **L3**), représentés dans la **Figure S-1**, ont été utilisés pour la synthèse de complexes de Zn(II) et de Cu(I).

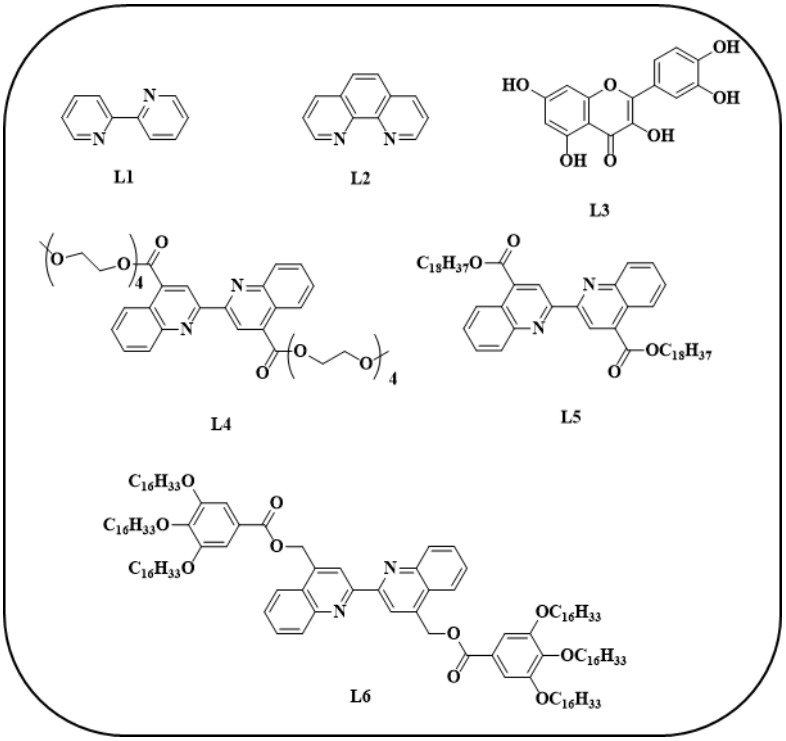

Figure S-1. Structures moléculaires des ligands bidentés utilisés pour la synthèse des complexes de Zn(II) et Cu(I).

Les structures planes des ligands donneurs (*bpy*, *phen* et *bq*) en font de bons intercalateurs d'ADN, tandis que la quercétine est un ligand luminescent O^O bioactif, connu pour être un puissant antioxydant, utilisé principalement pour réduire le stress oxydant. De plus, elle est un bon neutralisateur de radicaux libres et un chélateur de métaux. En outre, des études ont montré que la chélation renforce les propriétés de la quercétine (par exemple, activité antioxydante, protection de l'ADN, activité antitumorale et anticancérigène).

La quinoléine fait également l'objet de recherches approfondies pour le développement de molécules bioactives, ayant des activités antibactériennes, antidépressives, antivirales, anticancéreuses et anti-inflammatoires. Le greffage de fragments hydrophiles sur le ligand *bq* (**L4**) a été pris en considération pour la synthèse de complexes Zn(II) afin d'augmenter sa solubilité dans l'eau. En outre, le ligand *phen* et les dérivés *bq* **L5** et **L6**, contenant de longues chaînes alkyles, ont été synthétisés pour induire des propriétés mésomorphes dans les complexes de Cu(I).

Complexes de Zn(II) avec des ligands de donneurs N^N

Zn(II) est un ion bio-métallique dont la chimie polyvalente permet de synthétiser facilement des complexes avec des ligands luminescents et biologiquement actifs, afin d'obtenir des métallodrogues efficaces et en même temps de stabiliser les états excités produisant de bons émetteurs. Le zinc a une variété de fonctions biochimiques et physiologiques (catalytiques, structurales et régulatoires) dans les processus biologiques, ce qui le rend prometteur dans la chimie bio-inorganique médicale. En raison de leur faible toxicité et de leurs faibles effets secondaires, les complexes de Zn(II) sont donc étudiés comme liants de l'ADN, photosensibilisateurs de tumeurs, médicaments antibactériens et antimicrobiens, et pour des applications biomédicales telles que le traitement du cancer ou du diabète. Combiné à des ligands N-chélatants, l'interaction des ions métalliques Zn(II) avec des ligands donneurs O^O bioactifs et/ou biodisponibles augmente l'activité biologique de ces ligands. Des complexes hétéroleptiques de Zn(II) contenant des dérivés *phen* ou *bpy* et la quercétine **L3** comme co-ligand ont été synthétisés comme décrit dans la **Figure S-2**.

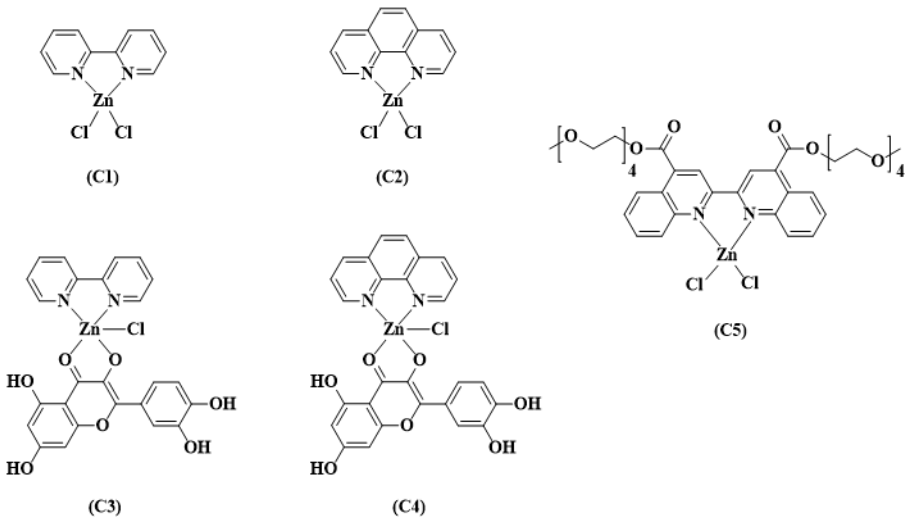

Figure S-2. Structures moléculaires des complexes de Zn(II) et rendements (**C1**: 94%; **C2**: 95; **C3**: 84%; **C4**: 94%, **C5**: 95%).

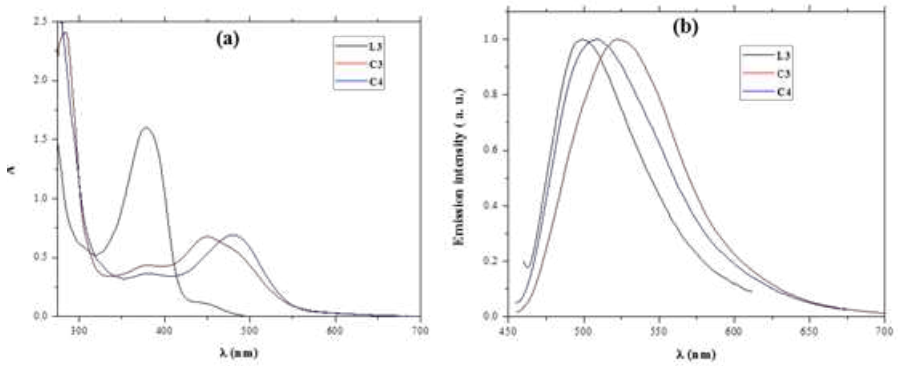

Figure S-3. Spectres (a) d'absorption et (b) d'emission des complexes **C3** et **C4** en solutions dégazées de DMSO (100 μM).

Comme attendu, les complexes sont luminescents en solution (**Figure S-3 b**) avec un maximum d'émission décalé vers le rouge par rapport à celui de la quercétine seule (496 nm) à 522 nm pour **C3** et 508 nm pour **C4**.

L'activité antioxydante de la quercétine joue un rôle important dans la prévention et le traitement de l'ostéoporose, du cancer, des tumeurs, des maladies cardiovasculaires, etc. Les effets d'oxydation et de coordination de la quercétine en présence d'un co-ligand N^N (*bpy* ou *phen*) et de l'ion Zn(II) ont été étudiés en présence du radical 2,2-diphényl-1-picrylhydrazyl (DPPH$^{\bullet}$). D'après les résultats, les complexes **C3** et **C4** ont montré une activité antioxydante comparable à celle du ligand **L3** libre. La bonne activité antioxydante et les propriétés de luminescence démontrées dans le DMSO par les complexes de Zn(II) leur permettent de faire l'objet d'autres études dans le domaine biomédical.

Le greffage de substituants hydrophiles sur le ligand peut être une stratégie pertinente pour induire la solubilité dans l'eau et/ou dans les solvants polaires des complexes de coordination résultants. Par conséquent, le ligand biquinoléine (*bq*) a été décoré avec des chaînes tétraéthylèneoxy hydrophiles, **L4**, puis complexé à $ZnCl_2$, générant le nouveau complexe **C5** présenté dans la **Figure S-2**. Le complexe est soluble dans les solvants polaires (CH_3CN, DMF, EtOH et MeOH), à peine soluble dans l'eau et insoluble dans les solvants non polaires. Cependant, l'ajout d'eau aux solutions polaires ne provoque pas la précipitation du complexe même à forte teneur en eau (95% en volume) et aucun changement d'absorption n'a été détecté. Bien que le complexe n'émette pas dans ces solvants purs, on a observé, lors de l'ajout d'eau, une émission similaire à celle du ligand **L4** avec de petits décalages vers le bleu dans CH_3CN et EtOH et vers le rouge dans MeOH (**Figure S-4 c**). Après dissolution du complexe, un changement de la géométrie peut être induit par les solvants coordinants donnant des espèces penta- ou hexacoordonnées responsables du solvatochromisme.

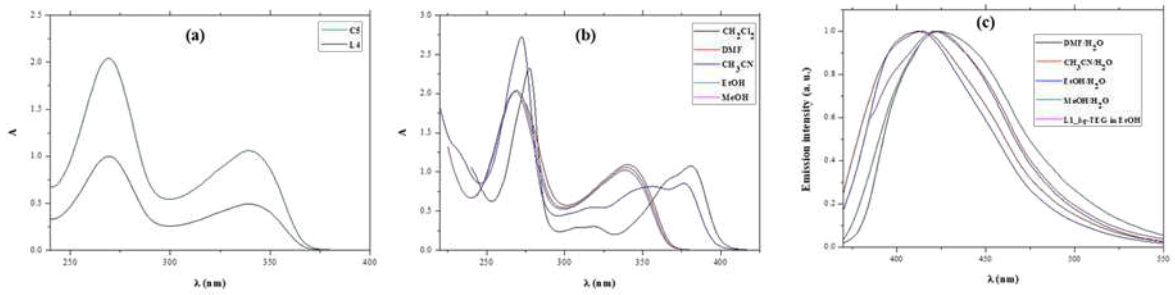

Figure S-4. Spectres d'absorption de: (a) **C5** et **L4** dans EtOH; de (b) **C5** dans CH_2Cl_2, DMF, CH_3CN, EtOH et MeOH; (c) Spectres d'emission du complexe **C5** dans des mélanges solvants/eau.

Complexes de Cu(I) avec des ligands de donneurs N^N

Le cuivre est un biométal peu coûteux, facilement disponible, qui trouve des applications dans plusieurs domaines, de l'électro-optique à la catalyse et à la biomédecine. Les complexes de Cu(I) sont de plus en plus considérés, tant du point de vue photochimique que photophysique, comme des alternatives aux complexes de métaux nobles. Cependant, les complexes de coordination du Cu(I) contenant des ligands donneurs bis-chélates de type N^N

sont fortement soumis à l'oxydation. Leur stabilité peut être améliorée par l'utilisation de substituants volumineux en position adjacente à l'atome d'azote et par la nature du contre-ion.

Nous avons d'abord étudié l'influence des contrions sur la stabilité des complexes Cu(I) à base du ligand phen (**L2**) non substitué avec divers contrions : Y^- = ClO_4^-, I^-, SCN^- et BF_4^-. Les contrions qui ont montré les meilleures capacités à stabiliser la tétracoordination ont ensuite été utilisés pour obtenir des métallomésogènes stables de Cu(I) basés sur des ligands promésomorphes bq fonctionnalisés (**L5** et **L6**). Les structures de tous les complexes de cuivre sont présentées dans la **Figure S-5**.

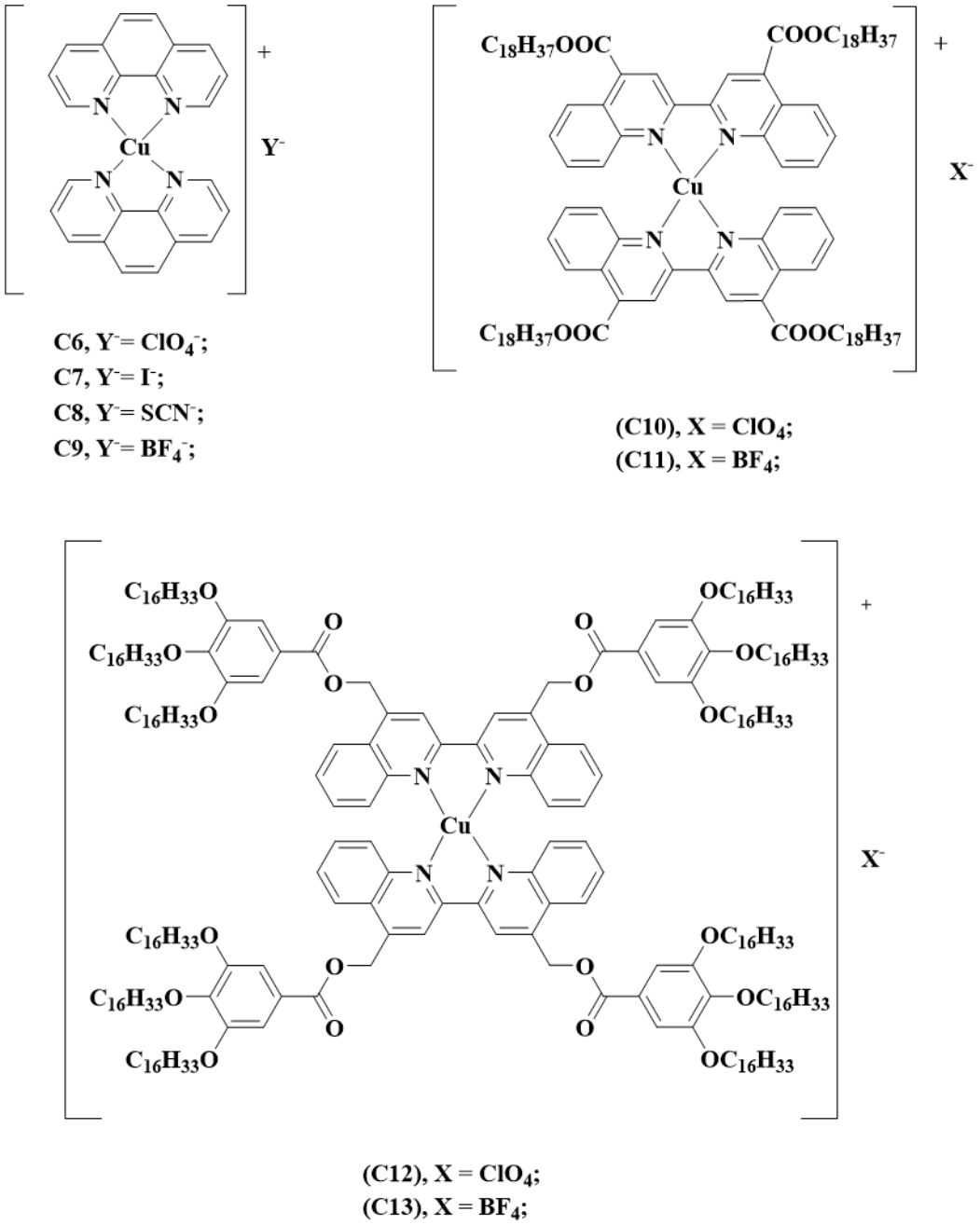

Figure S-5. Structures moléculaires de complexes de Cu(I).

Des études spectroscopiques combinées (IR, UV, RMN), il apparaît que les contrions ayant un pouvoir de coordination plus élevé, I- et SCN-, favorisent le processus fluxionnel de la géométrie plus déformée du "Cu(II)", tandis que les anions non-coordinants, ClO_4^- et BF_4^-, contribuent à la stabilisation de la géométrie du Cu(I). L'analyse thermique des complexes **C7 - C9** réalisée dans l'air, a montré que les complexes étaient stables jusqu'à 250°C, sans qu'aucun processus thermique ne soit détecté jusqu'à décomposition dans le cas de **C7** et **C9**.

Les spectres électroniques de **C6 - C9** sont presque tous identiques et ne présentent pas d'effet solvatochrome. Le contrion n'influence pas non plus les propriétés d'absorption, les spectres des complexes étant entièrement superposables, ce qui suggère une structure similaire en solution avec une symétrie D_{2d}. En solution concentrée et à l'état solide, la nature des contrions affecte l'environnement tétraédrique de l'ion Cu(I): un aplatissement de la symétrie des complexes ($D_{2d} \rightarrow D_2$) est mis en évidence à la fois par l'analyse RMN ^1H en solution concentrée et par la spectroscopie d'absorption UV-Vis à l'état solide, et cet effet est plus important pour les sels I^- et SCN^- que pour les sels ClO_4^- et BF_4^-.

Les contrions qui ont montré les meilleures capacités à stabiliser la tétracoordination, ClO_4^- et BF_4^-, ont ensuite été utilisés pour obtenir des métallomésogènes du Cu(I) stables (**C10 - C13**) avec les ligands promesomorphes *bq* fonctionnalisés (**L5** et **L6**). La coordination avec Cu(I) modifie les bandes d'absorption des deux ligands de manière similaire, quel que soit le contrion. Cependant, aucune émission n'a été détectée pour aucun des quatre complexes Cu(I) examinés dans l'air ou en solutions dégazées de CH_2Cl_2. Les complexes tétracaténaires **C10 - C11** présentent des mésophases lamello-colonnaires, L_{col}, tandis que les complexes **C12 - C13** s'auto-assemblent en phases hexagonales colonnaires bidimensionnelles, Col_{hex}, qui, en refroidissant, gèlent à l'état vitreux (**Figure S-6**). Tous les complexes émettent faiblement dans le rouge, avec des rendements quantiques d'émission variant selon le type d'état d'agrégation.

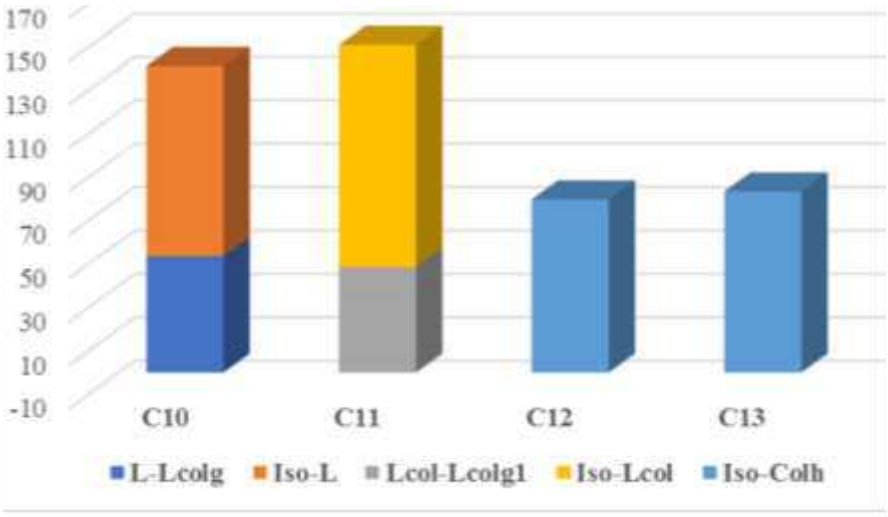

Figure S-6. Diagramme de phases des complexes **C10** – **C13**.

Complexes de Zn(II) avec des ligands tpy

La plus grande stabilité des complexes de Zn(II) par rapport à celle des complexes de Cu(I) nous permet de concevoir des métallomésogènes luminescents de Zn(II). Dans cette étude présentée dans le chapitre trois, un ensemble de ligands dérivés de la terpyridine, *tpy*, a été choisi pour plusieurs raisons : si elle est connue pour être une source utile dans la synthèse de complexes du Zn(II) luminescents, *tpy* est également connue pour s'intercaler dans l'ADN, et l'altération de la structure *tpy* génère des dérivés ayant un impact majeur sur le pouvoir anticancéreux. Par conséquent, la fonctionnalisation de la *tpy* avec différents groupes a été réalisée (**Schéma S-1**). Les dérivés *tpy* **L9** et **L10** ont été fonctionnalisés avec des groupes qui permettent une déclinaison plus poussée, potentiellement utilisable pour lier les complexes sur des dendrimères et/ou des nanoparticules métalliques et/ou d'oxyde fonctionnalisées ou sur des structures de silice mésoporeuse à des fins théranostiques (chapitre quatre). Pour abaisser les températures de fusion des métallomésogènes finaux, le ligand **L11** fonctionnalisé avec une unité gallate a été synthétisé. Le ligand **L7**, disponible dans le commerce, a été utilisé comme composé modèle.

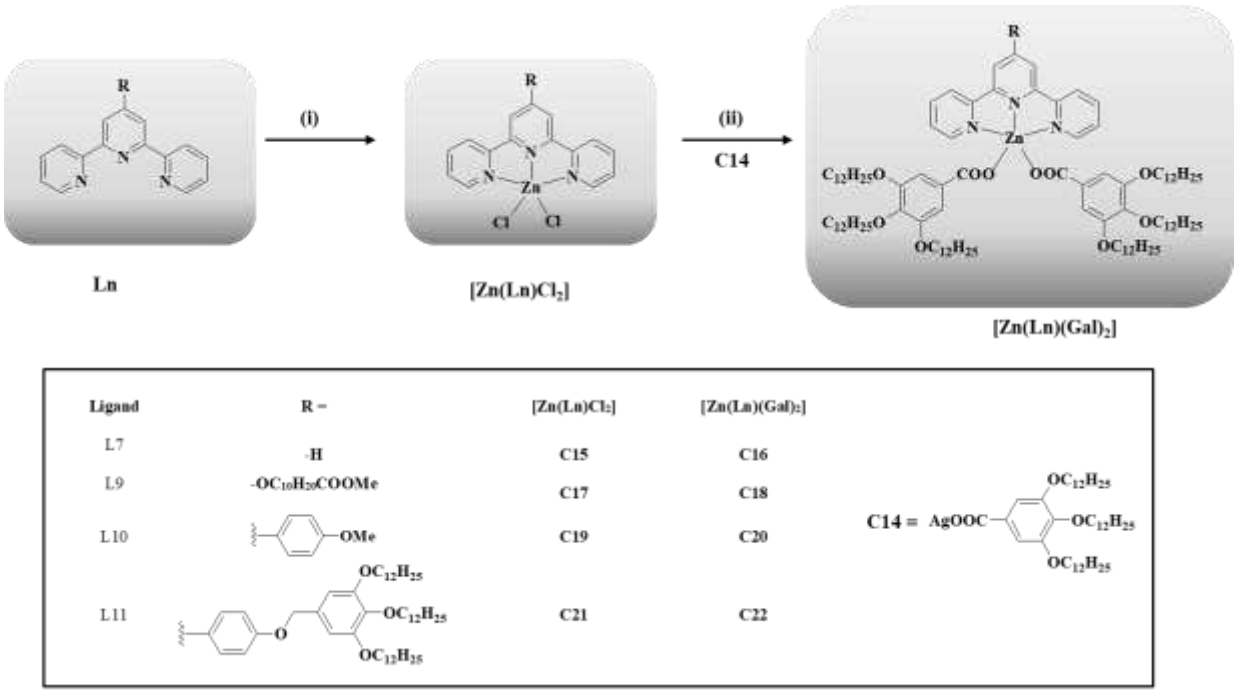

Scheme S-1. Voie de synthèse des complexes de *tpy* de Zn(II).

Les complexes dichlorure de Zn(II) ont été préparés par une synthèse polyvalente et simple qui permet une ingénierie moléculaire facile, par le déplacement des co-ligands chlorés par le sel d'argent(I) du 3,4,5-triméthyldodécyloxybenzoate (**C14**), comme présenté dans le **Schéma S-1**. Cette stratégie nous a permis de produire divers complexes de Zn(II) en évitant les nombreuses étapes nécessaires pour fonctionnaliser précisément les ligands à base de *tpy*. La substitution des ligands auxiliaires du chlorure par l'unité gallate a conduit à de nouveaux complexes pentacoordonnés neutres **C16**, **C18**, **C20** et **C22** de formule générale $[Zn(Ln)(Gal)_2]$ avec des propriétés mésomorphes.

Les propriétés d'absorption et d'émission des complexes **C15 - C22** ont été étudiées dans DMSO, CH_2Cl_2 et $CHCl_3$. Tous les échantillons apparaissent incolores dans les solutions diluées et absorbent dans la région UV du spectre électromagnétique. Les complexes ne suivent pas la loi de Lambert-Beer: l'absorption molaire ($\varepsilon(\lambda)$) d'une solution diluée (10^{-6} M) est supérieure à celle d'une solution concentrée (10^{-5} M) pour tous les échantillons. Les spectres d'absorption des complexes enregistrés en solution montrent une série de bandes dans la partie UV du spectre électromagnétique, toutes issues des transitions LC du *tpy*. Ces transitions se chevauchent avec celles localisées sur le ligand benzoate, donnant lieu à une large bande en dessous de 300 nm. Tous les complexes étudiés se sont révélés fluorescents. En particulier, une bande d'émission asymétrique à 365 nm (avec un épaulement vibratoire à 386 nm) a été mise

en évidence pour **C17**, et à 379 nm (et une longue queue s'étendant vers le domaine spectral vert) pour **C18** (**Figure S-7 a**).

Dans les états condensés originels, tous les complexes étudiés sont également fluorescents. Par exemple, en comparant les propriétés de luminescence du complexe **C17** en solution avec celles mesurées à l'état condensé (**Figure S-7 c**), le maximum d'émission est resté pratiquement inchangé (365 contre 360 nm, respectivement), tandis que le rendement quantique a doublé, passant de 6,4 % à 15,8 %, et la durée de vie a augmenté de 1,2 ns à 78,5 ns. Ce comportement est attribuable à la réduction des voies de désexcitation non radiative qui se produisent dans la phase solide, où les modes vibratoires de la molécule unique sont quelque peu réduits.

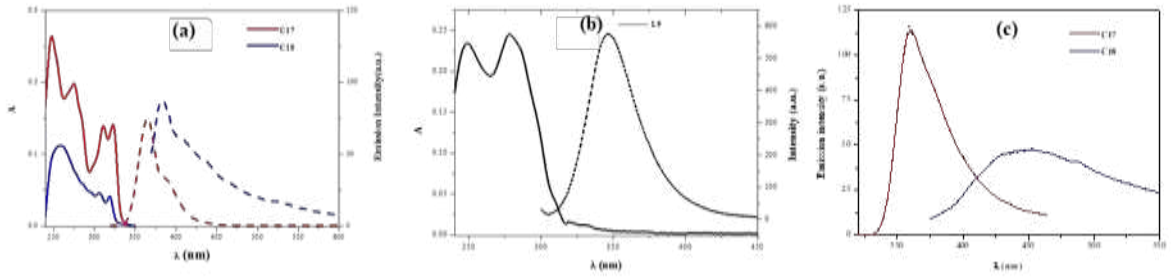

Figure S-7. Spectres d'absorption (ligne continue) et d'émission (ligne pointillée) des complexes **C17** et **C18** (a) et du ligand **L9** (b) dans CH_2Cl_2 à la température ambiante; (c) spectre d'émission des complexes **C17** et **C18** à l'état solide.

L'analyse thermogravimétrique (ATG) a révélé que les complexes **C16**, **C18**, **C20** et **C22** étaient stables jusqu'à la fusion dans l'état isotrope. Tous les complexes de gallate sont mésomorphes. Avec l'augmentation du nombre de chaînes latérales, la nature et la stabilité thermique des mésophases évoluent d'une SmA dans le cas d'un complexe avec **L7** (**C16**), à une mésophase Col_{hex} (**C18**, **C22**) dans le cas des complexes avec **L9** et **L11**, via une mésophase M_{hex} hexagonale intermédiaire de type 3D pour **L10** (**C20**), respectivement. C'est un bon exemple de la grande sensibilité du système et de sa capacité à adapter sa périphérie aliphatique pour s'auto-organiser de la manière la plus optimale.

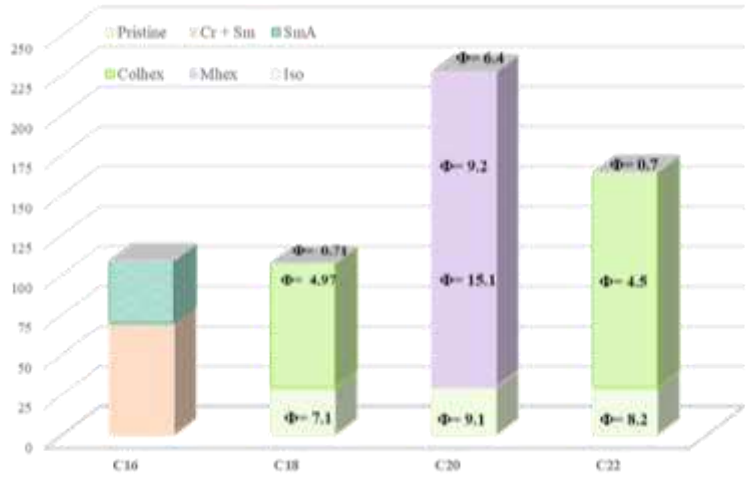

Figure S-8. Diagramme de phases et rendements quantiques d'émission des complexes **C16, C18, C20** et **C22**.

De plus, les propriétés luminescentes des complexes mésomorphes de Zn(II) ont été mesurées à l'état solide en fonction de la température. À l'état originel, tous les complexes sont fluorescents. Comme prévu, les rendements quantiques d'émission ont diminué avec l'augmentation de la température dans tous les cas. Un comportement intéressant a été observé pour le complexe avec **L10**, auquel cas, en chauffant l'échantillon de la température ambiante à 80°C (lors de la transition vers une phase 3D), le rendement quantique est passé de 9,1 % à 15,2 %. Un chauffage supplémentaire a entraîné une diminution du rendement. La **Figure S-8** présente le diagramme de phase des métallomésogènes de Zn(II), et la valeur des rendements quantiques d'émission dans les différents états.

Ces résultats encourageants nous ont motivés à synthétiser des complexes de Pt(II) correspondants en utilisant les ligands **L7** - **L11.**

Systèmes dendritiques et nanoparticulaires

La conception des métallodendrimères portant des dérivés *tpy*, permet d'étendre le domaine de la chimie de coordination, du niveau *moléculaire* au niveau *supramoléculaire*. Dans la recherche de nouveaux matériaux fonctionnels, les métallodendrimères supramoléculaires jouent un rôle de plus en plus important. En outre, une voie possible pour délivrer des composés de coordination appropriés (un médicament ou un composé pour l'imagerie) à une cible spécifique dans les systèmes biologiques consiste à fixer ce composé sur un support, qui peut être observé de l'extérieur. Un tel support a été reconnu comme étant les nanoparticules d'or (Au NPs). Les complexes de métaux nobles comme l'or, l'argent, le platine, le rhodium, l'iridium, le palladium, etc. ont fait l'objet de recherches intensives, qui ont conduit à la synthèse

de médicaments anticancéreux, antirhumatismaux, antipaludéens et antimicrobiens. L'état colloïdal est une autre forme dans laquelle les métaux nobles sont utilisés à des fins thérapeutiques. Parmi eux, les nanoparticules d'Au et d'Ag (NP) sont les plus recherchées.

Par rapport aux petites molécules ou aux matériaux massifs, les structures à l'échelle nanométrique expriment diverses propriétés physiques, chimiques, optiques et électromagnétiques, qui dépendent fortement de leurs caractéristiques physiques et sont influencées par leur taille et leur forme. Les NPs possèdent une réactivité intrinsèque particulière en raison de leur surface accrue, de sorte qu'un choix approprié de matériaux pour la fabrication de produits thérapeutiques à base de nanoparticules doit être effectué. Les NP des métaux nobles se différencient des autres nanoplateformes (par exemple, les semi-conducteurs quantiques, les NP magnétiques et les NP polymères), par leur résonance plasmonique de surface (RPS) unique, qui améliore toutes les propriétés radiatives et d'irradiation des NPs. Parmi les autres propriétés importantes des Au NPs, on peut citer la biocompatibilité et la capacité à atténuer la fluorescence.

Les Au NPs recouvertes de diverses coquilles organiques, inorganiques ou hybrides combinent des fonctions thérapeutiques, d'imagerie et de ciblage au sein d'un seul système de délivrance de médicaments. Leurs propriétés physiques et chimiques explicites en font des supports importants pour diverses applications allant de la thérapeutique, la détection et le diagnostic, le biomarquage, la délivrance de médicaments, la détection chimique et biologique, l'imagerie.

L'assemblage des NPs en structures nanométriques définies permet d'accéder à des nanocomposites par des stratégies d'assemblage non covalentes telles que les interactions van der Waals/stériques, les liaisons hydrogène, les appariements d'ions et la chimie d'inclusion hôte-invité. De plus, en formant des systèmes métal-ligand, on peut s'attendre à de la diversité structurale des processus d'auto-assemblages, et des propriétés redox et photochimiques des constructions qui en résultent. Pour assurer la solubilisation et la stabilisation, les Au NPs sont fonctionnalisées par des agents de recouvrement qui se lient fortement à leur surface, tels que des thiols, des oxoanions, des amines ou des thiocyanates. À cet égard, nous avons conçu et synthétisé des nanostructures hybrides contenant des Au NPs et des CMTs liés par des structures dendritiques afin de produire des matériaux avancés à des fins théranostiques. Les hybrides CMTs/Au NPs possèdent une composition noyau-coquille avec un noyau Au NP et une coquille de ligands stabilisateurs de surface (**Figure S-9**). Les propriétés des matériaux seront contrôlées par la croissance de la génération, afin de tirer profit des phénomènes de SPR du noyau des Au NPs.

L'assemblage des parties susmentionnées permettrait de créer des nanoplateformes multifonctionnelles potentielles à des fins théranostiques. En utilisant les quatre unités de base de la **Figure S-9**, plusieurs stratégies de synthèse peuvent être envisagées pour la synthèse des matériaux avancés visés, telles que : i) la construction de la structure dendritique autour des Au NPs, "coiffées" d'oleylamine ou ii) la synthèse des branches dendritiques suivie de leur fixation sur les Au NPs. Dans la présente thèse, la deuxième stratégie a été suivie, ce qui a nécessité plusieurs étapes de synthèse, réalisées en modules parallèles : i) synthèse des Au NPs, ii) synthèse des unités de chélation des donneurs d'azote, iii) synthèse des branches dendritiques, iv) chélation métallique des branches dendritiques contenant des ligands donneurs N^N, v) échange de ligands entre les Au NPs et les branches métallodendritiques.

Pour les ligands N^N, plusieurs dérivés *bpy* et *tpy* ont été pris en compte, comme le montre la **Figure S-9**. Deux types de branches dendritiques ont également été pris en compte dans la conception des assemblages, basés respectivement sur l'acide 3-hydroxy-2-(hydroxyméthyl)-2-méthylpropanoïque (**G_A**) ou sur le 3,5-dihydroxy méthyl benzoate (**G_B** et **G_C**) comme synthons de départ, comme le montre la **Figure S-9**.

Les branches dendritiques de type **G_A** ont été fonctionnalisées avec le dérivé *tpy* **L13** et avec l'unité d'ancrage **Anc_1** (**G_A0_L13**, **G_A1_L13**). Pour la synthèse des branches dendritiques de type **G_B**, le ligand **L14** a été utilisé, tandis que pour celles de type **G_C**, le ligand **I4** a été considéré. Dans le cas des branches dendritiques dérivées du 3,5-dihydroxy méthyl benzoate (**G_B** et **G_C**), l'acide thioctique disponible dans le commerce (**Anc_2**) a été utilisé (**G_B0_L14**, **G_B1_L14**, **G_C0_I4** et **G_C1_I4**). Les premiers résultats ont été obtenus en utilisant le ligand **I4** et la branche **G_C** pour assurer la croissance dendritique (**Schéma S-2**). Cela nous a permis de synthétiser la génération du **G_C0_I4** en une seule étape, alors que la synthèse du **G_C1_I4** nécessite quatre étapes, comme décrit dans le **Schéma S-2**.

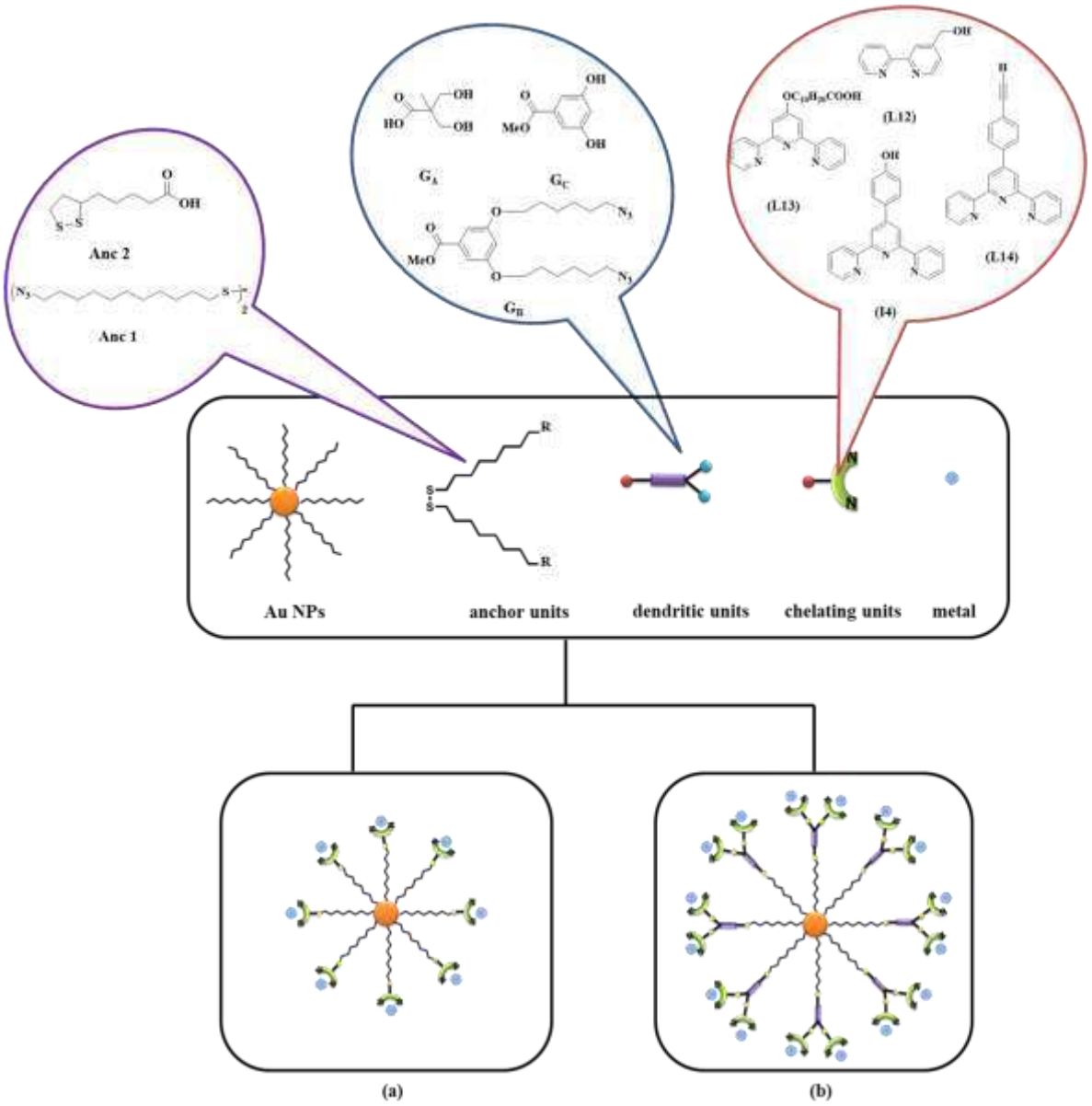

Figure S-9. Représentation schématique du concept de dendronisation des NPs avec des ligands donneurs de type N- terminaux: unités de base (en haut) utilisées pour obtenir les structures visées (en bas).

Le premier hybride **Au@G$_C$0_I4_Zn** a été obtenu par échange de ligands entre **Au@OA** et le complexe **G$_C$0_I4_Zn(II)**. En raison de la faible dispersion de l'hybride dans les solvants organiques classiques, aucun spectre RMN n'a pu être enregistré. La présence du complexe **G$_C$0_I4_Zn** a néanmoins été confirmée par analyse EDX. En comparant les spectres de **Au@OA** avec celui de **Au@GC0_I4_Zn**, la réussite de l'échange de ligands a pu être confirmée par la disparition des bandes d'absorption caractéristiques ν_{as}(N-H) correspondant à l'oleylamine. De plus, un autre signe de la formation du composé ciblé a été donné par le déplacement des bandes caractéristiques $\nu_{C=C}$ et $\nu_{C=N}$ vers des fréquences plus élevées par rapport à **G$_C$0_L14_Zn**. La caractérisation de l'auto-organisation des hybrides ainsi que la

synthèse d'autres branches dendritiques et d'hybrides, et l'étude des propriétés optiques sont prévues ou en cours.

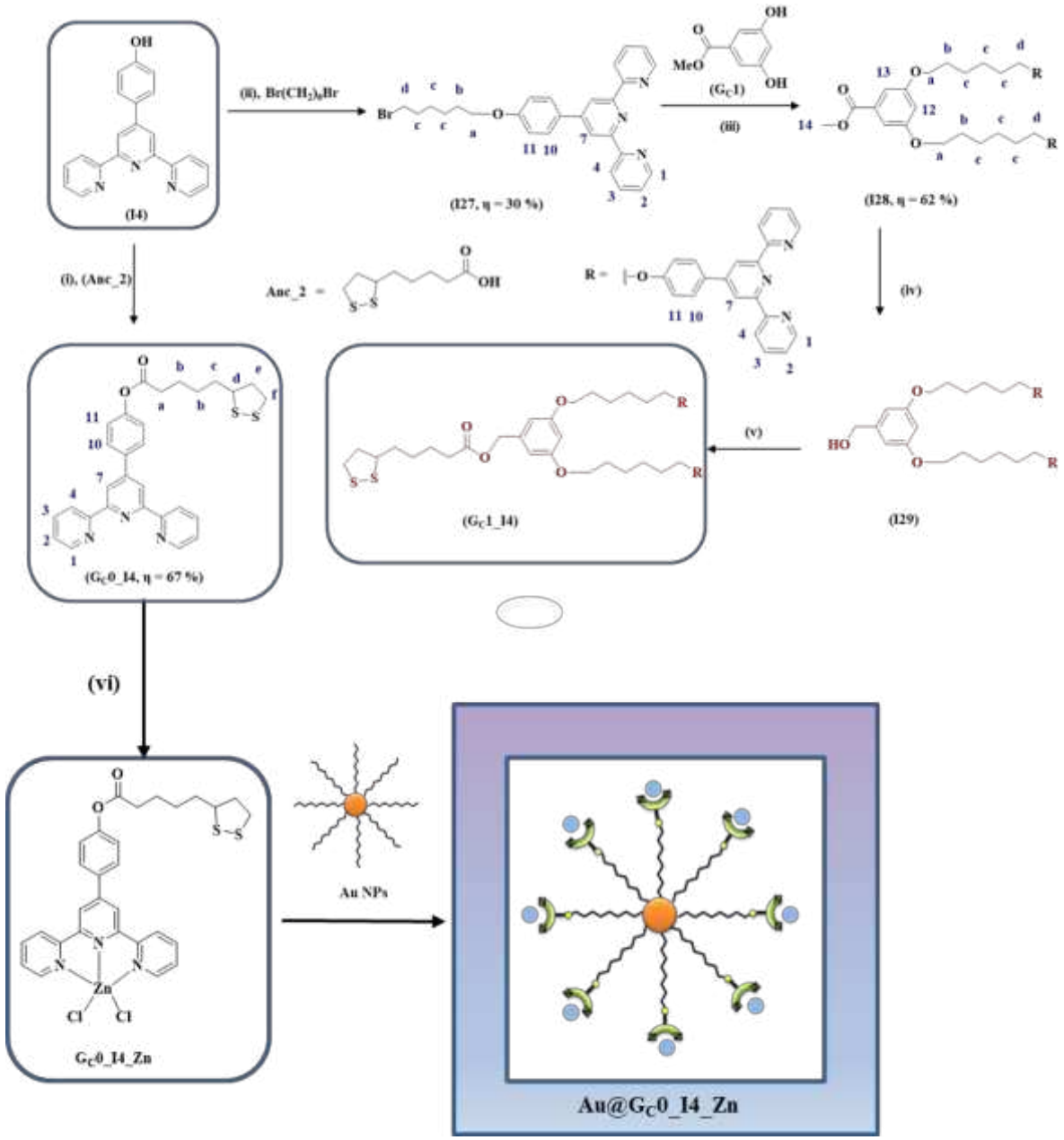

Schéma S-2. Voie synthétique des **GC0_I4** et **GC1_I4** (marquage des atomes en bleu).

Conclusions

La contribution originale présente les résultats concernant la synthèse et la caractérisation des CMT à base de ligands oligopyridines (*phen*, *bpy*, *bq* et *tpy*) ayant Zn(II) et Cu(I) comme centres métalliques, et les résultats suivants :

- La synthèse et la caractérisation structurale de nouveaux complexes de coordination de Zn(II) de formule générale (N^N)ZnQCl ayant des propriétés luminescentes et une activité antioxydante.
- La synthèse et la caractérisation de nouveaux complexes de coordination Cu(I) stables de formule $[(phen)_2Cu(I)]^+Y^-$, où $Y^- = ClO_4^-$, I^-, SCN^- et BF_4^-, et leurs études de stabilité en solution et en phase condensée.
- Synthèse et caractérisation de complexes de coordination mésomorphes du Cu(I) luminescents.
- Synthèse et caractérisation de nouveaux complexes mésomorphes du Zn(II) luminescents de formule générale $[Zn(Ln)(Gal)_2]$, où Ln est un dérivé *tpy* et Gal un gallate lipophile.
- La synthèse de Au NPs fonctionnalisé avec des coquilles dendritiques qui contiennent un dérivé *tpy* coordonné aux centres métalliques de Zn(II). Pour le moment, un seul système hybride a été obtenu, à savoir **Au@G_C0_I4_Zn**, à titre d'exemple préliminaire représentatif. D'autres structures dendritiques ont été prévues, mais pas encore réalisées au cours de ces travaux.

Chapter 1. Introduction

Nowadays, new coordination/organometallic transition metal complexes (TMCs) are designed as alternatives to *cis*-platin and its analogues, which are currently in routine clinical use by offering unique properties such as higher cytotoxicity and lower side effects in cancer therapy. To achieve good therapeutic efficacy and to minimize side effects in cancer treatment, increasing efforts have been made to combine therapeutic, imaging and targeting functions together in a single theranostic platform. Two of the current and most important strategies that are followed in order to obtain theranostic compounds are the synthesis of: i) coordination complexes based on biocompatible metal centres and ii) gold nanoparticles functionalized with coordination complexes.

The design of the new coordination compounds is also focused on the induction of specific properties like luminescence and/or liquid crystallinity in order to obtain advanced functional and multifunctional materials. Luminescence biocompatible compounds are relevant for imagistic investigation techniques whereas, metallomesogens are known as sensors for biological species. A proper choice of the molecular constituents allows combining a variety of photophysical and photochemical properties almost inaccessible for a simple molecular system, yielding coordination complexes to be used as opportune theranostic (diagnosis and therapeutic) agents or as potential sensors for biological tisues.

The first strategy has been considered in this thesis: the synthesis of Zn(II) and Cu(I) complexes with biologically active chelating ligands like N^N oligopyridines and/or O^O flavonoids. By molecular engineering, the optimization of these properties of the complexes will be carried out following the modification of different molecular parts: ligands, metallic centres, counterions.

In order to increase the efficiency and reduce the side effects, some strategies to deliver active compound at a specific target have been developed. With this aim, one of the new obtained coordination compounds is attached to gold nanoparticles (Au NPs) functionalised with dendritic shells. The original nanosystems thus obtained can therefore act as imaging and sensing advanced materials. The new synthesized coordination compounds will be positioned by a judicious molecular engineering in the plasmonic field of Au NPs using dendrons as connectors. The use of dendritic branches to order and position the metal-complex chromophore around the metal NPs will generate self-assembled ordered ‘soft’ arrays where antenna effect may be obtained. Therefore, three fundamental classes of compounds/materials and their specific properties will be merged: i) TMCs with luminescence and/or mesogenic properties; ii) dendrimers (conformational flexibility, nano-scale dimensions, periodic 3D branched

architectures, hyperfunctionalisation and multivalency) and iii) Au NPs as localized surface plasmon resonance (SPR).

1.1. Transition metal complexes and metallomesogens in biological systems

Because of "*the size, charge distribution, stereochemistry, redox potential and other physical properties of the metal chelates*" which "*can be varied during chemical synthesis*", Dwyer visualized coordination metal complexes as "*ideal pharmacological tools with which to investigate many functional systems in the living cell".*[1]

The concept of inorganic medicinal chemistry has received increased consideration[2] with the discovery of the bacteriostatic and anticancer properties of Ru(III) polypyridyl complexes by the group of Dwyer in the 1950-1960s,[3,4,5] and the discovery of the anticancer properties of *cis*-platin, (**Figure 1-1**), in 1969 by B. Rosenberg.[6,7]

The anticancer properties of *cis*-platin were discovered accidentally while Rosenberg and group were investigating if the growth process of *Escherichia coli* might be influenced by an electric field, using platinum electrodes in the growth chamber. The researchers noticed that during the electrolysis process, a soluble platinum complex was generated, which caused cell division arrest, whilst cell growth continued, the bacteria growing in very long filaments. After chemical analysis, they identified two active complexes of the diaminodichloroplatinum(II), namely the *cis* and *trans* isomers (**Figure 1-1**). The authors concluded that the square planar Pt(II) complex *cis*-isomer was responsible for the inhibition of the cell division, whereas the *trans*-isomer was less effective.[8] Later, Rosenberg and co-workers,[6] tested *cis*-platin for antitumor activity, against sarcoma and leukaemia in mice, and noticed that it could cause tumour inhibition too. In 1978, *cis*-platin was approved for use as an anticancer drug for clinical treatment of genito-urinary tumours.

(1), *cis*-platin **(2), *trans*-platin**

Figure 1-1. Schematic representation of diaminodichloroplatinum(II) *cis* and *trans* isomers.

After the clinical approval of *cis*-platin, research was conducted to determine the mechanism of its anticancer activity, and the following principal steps in its action mechanism were identified: a) aquation/activation, b) cellular uptake, c) DNA platination, and d) cellular processing of Pt–DNA damages, inducing cell survival or apoptosis.[9]

Also, a list of requirements, respectively the Structure Activity Relationships (SARs) rules, governing the molecular structure required for a platinum complex to possess antitumor activity, was postulated: i) a square-planar geometry, ii) neutrality of charge, iii) two *cis*-amine ligands, which can be replaced by a chelating diamine, and iv) two *cis*-anionic ligands, which do not link the metal too strongly, or activity would be diminished, but are not too labile either, or compounds will exhibit high toxicity.[9]

Despite its excellent success against cancer, patients treated with *cis*-platin can present severe side effects and may develop drug resistance, thus limiting the effectiveness of the drug.[10]

Therefore, with the hope to overcome these limitations, intense research has been achieved to synthesize new drugs following two pathways: i) designing classical and non-classical platinum compounds[10] or ii) developing new non-platinum metal-containing antitumor therapeutics, based on Zn(II), Ru(II), Ag(I), Au(I), Cu(I) etc. [11,12,13,14,15]

Following the SARs rules, analogues of *cis*-platin have received international approval: carboplatin and oxaliplatin (**Figure 1-2**).[10] The first *cis*-platin analogue used clinically approved was carboplatin,[16] where the two chlorides were displaced by a bidentate dicarboxylate. Although it exhibited lower reactivity and slower DNA binding kinetics, carboplatin has been approved to be used as a chemotherapeutic drug for ovarian, lung, head and neck tumours. Later, oxaliplatin was developed which had higher potency against tumours compared to *cis*-platin or carboplatin.[17]

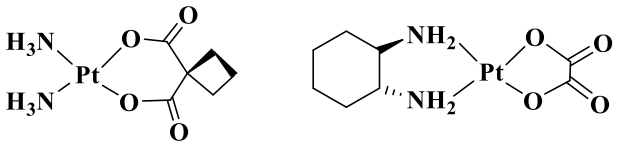

(3), carboplatin **(4), oxaliplatin**

Figure 1-2. Schematic representation of classical platinum metallodrugs.

Although the first direction in the design of *cis*-platin analogues retains its relevance,[18] the hypothesis that altering the molecular structure will have as consequence an altered action mechanism and, therefore, a diverse anticancer activity, platinum compounds deviating in structure from SARs rules have been investigated, among which Pt(IV) complexes (prodrugs that release active Pt(II) species),[19,20,21] monofunctional compounds (pyriplatin), cationic square planar complexes, intercalator-linked species (oligopyridine complexes),[9] etc.

J. R. Aldrich-Wright and co-workers reported a cationic metallointercalator with square planar geometry,[22] of type $[Pt(I_L)(A_L)]^{2+}$, where A_L (ancillary ligand): 1S,2S-diaminocyclohexane, *DACH* and I_L (intercalating ligand): 5,6-dimethyl- *phen* (complex **5**, **Figure 1-3**) which was found to exhibit a higher cytotoxicity than *cis*-platin.[23]

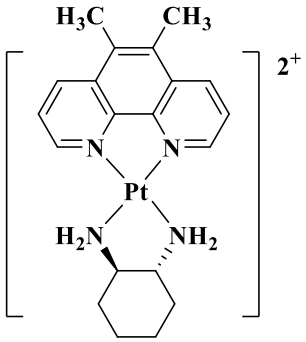

(5)

Figure 1-3. Schematic representation of [(5,6-dimethyl-1,10-*phen*)(1S,2S-DACH)Pt(II)]Cl_2.

Besides square planar geometry, also tetrahedral, pyramidal, trigonal bipyramidal, and octahedral geometries can be envisaged,[24] therefore different types of binding with DNA are expected: i) covalent binding: *cis*-platin,[25] carboplatin,[26] $[Ti(bzac)_2(OEt)_2]$,[27] where bzac = 1-phenylbutane-1,3-dionate, ii) intercalation: platinum complexes of type: $[Pt(I_L)(A_L)]^{2+}$ [23,,28] bis-(*phen*)copper(II) complexes,[29,30] iii) bimodal – covalent binding and intercalation, such as $[Pt(tpy)Cl]^+$,[31] iv) groove binding: cobalt(III) complexes such as $[Co(en)_2(bpy)]^{3+}$, $[Co(en)_2(phen)]^{3+}$, where en = ethylenediamine,[32,33,34] etc.

Lahiri *et al.*,[35] reported the anaerobic DNA photocleavage activity and photocytotoxicity of copper(II) complexes **6** (**a – c**) with distorted square pyramidal geometry, having the formula $[Cu(L_1)(N\hat{}N)]$, whereas L_1 = thiolate salicylidene-2-aminothiophenol and oligopyridine as ancillary ligands N^N: *phen*, dipyrido[3,2-d:2′,3′-f]quinoxaline, *dpq*, and dipyrido[3,2-a:2′,3′-c]phenazine, *dppz,* (**Figure 1-4**). From viscosity data, thermal melting, and with molecular docking calculations, the authors suggested that these complexes bind to DNA through groove and/or partial intercalation.

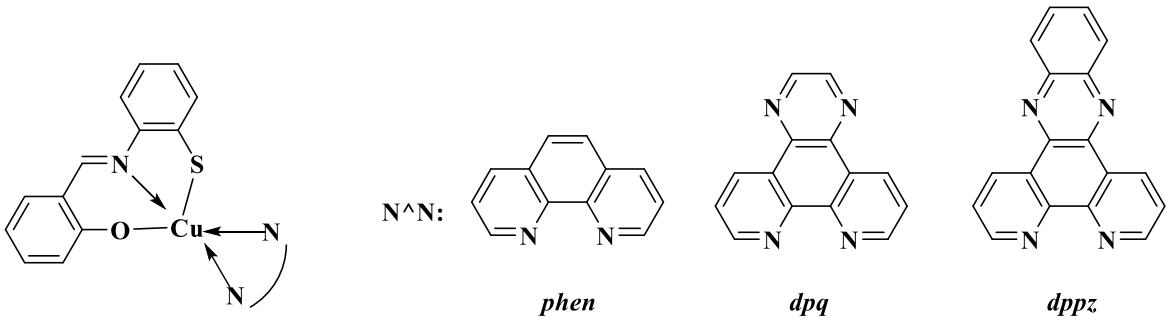

(6a): N^N = *phen*;
(6b): N^N = *dpq*;
(6c): N^N = *dppz*;

Figure 1-4. Schematic representation of **6** (**a**−**c**) complexes and the oligopyridine co-ligands (N^N).

Therefore, efforts are made lately in search of coordination complexes with increased cytotoxic activity based on ionic species with higher coordination number metal centres. Due to their capability to form coordination compounds with a wide range of metals, N-donor heterocycles are highly researched ligands in coordination chemistry. Oligopyridines (**Figure 1-5**: 2,2'-bipyridine - *bpy*, 1,10-phenanthroline - *phen*, 2,2'-biquinoline- *bq*, 2,2':6'2"-terpyridine - *tpy*), as part of this class, are of interest in medicine because: i) they are able to form stable complexes with various *d*-block metal ions by dπ→pπ* bonding,[36] ii) their planar structure makes them suitable to intercalate DNA,[37] iii) the chelation of a metal may result in luminescent TMC suitable as bioimaging agents or as photosensitizers for photodynamic therapy (PDT), etc.[38]

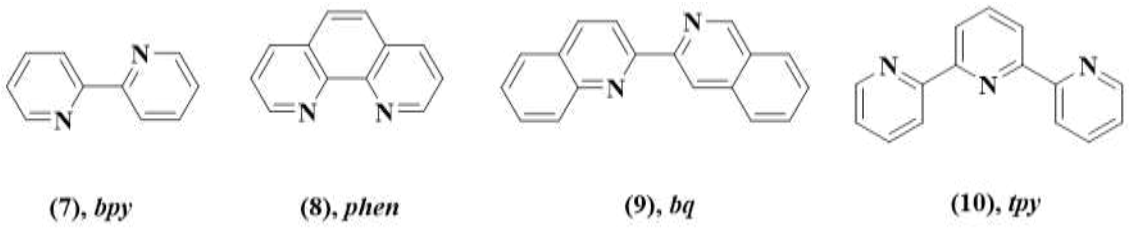

Figure 1-5. The most common oligopyridine ligands and the abbreviations used.

Some studies have also revealed that the metal, besides playing an important role in the efficiency of the TMC based drugs, can be also seen as a carrier of biologically active ligands.[39] Therefore, by a judicious choice of the metal ion and of the coordinating ligands, new smart materials with multiple therapeutic and diagnostic centres in a single platform can be developed, leading thus to theranostic agents.[40]

The photophysical properties of luminescent TMCs are of interest for the potential and real-market application in bio-sensing and bio-imaging. For example, Alzeer *et al.*[41] reported a zinc-containing guanidinium modified phthalocyanine, tetrakis(diisopropylguanidinio)Zn(II) phthalocyanine (Zn-digp), which exhibited a strong "light-switch" effect in the presence of nucleic acids, with a 200-fold luminescence enhancement.

Unlike organic luminophores, many types of excited states can be formed in the case TMCs having d^6, d^8 and d^{10} electronic structures, which are dependent on the metal centres and ligand structures.[42]

The most common excited states are: i) metal-to-ligand charge-transfer (MLCT), ii) intraligand charge-transfer (ILCT), iii) ligand-to-metal charge-transfer (LMCT), iv) ligand-to-ligand charge-transfer (LLCT) states, v) metal-metal-to-ligand charge-transfer (MMLCT), and vi) ligand-to-metal-metal charge-transfer (LMMCT).[43]

MLCT states involve the electronic transitions from a metal-based *d* orbital to a ligand-based delocalized π* antibonding orbital and are usually observed in TMCs with d^6 and d^8 configurations. These states are common to coordination compounds of low-valent metal atoms with electron accepting ligands like *bpy*, *phen* and related polypyridyls etc.[44] Ranjan *et al.*[45] reported pyrazolato diimine rhenium(I) carbonyl complexes $[Re(CO)_3(N\hat{}N)(btpz)]$ (N^N: *bpy* or *phen*, and btpz: 3,5-bis(trifluoromethyl) pyrazolate) whose photoluminescent emission in solution and solid-state, originated from MLCT transitions, which were overlapped by IL transitions.

IL ππ* excited states involve electronic transitions principally localized on the ligand between π orbitals,[46] as in the case of $[Zn(btz)_2]$ (bzt = 2-(2-hydroxyphenyl)benzothiazolate).[47]

Complexes containing high oxidation state metal atoms may emit from LMCT states. For example, Yam *et al.*[48,49] reported the long lived emission of Cu(I) complex $[Cu_4(\mu\text{-dppm})_4(\mu_4\text{-S})]^{2+}$ and the selenide analogue $[Cu_4(\mu\text{-dppm})_4(\mu_4\text{-Se})]^{2+}$ (where dppm: bis(diphenylphosphino)methane), which were assigned to an excited state with substantial LMCT character.

LLCT bands can be identified in the absorption spectra of TMC which contain X^- (halides), RS^- (thiolates), R^- (carbanions) as donor ligands and as acceptor ligands nitrogen heterocycles such as: polypyridyls (*bpy*, *phen*), porphyrins.[50]

MMLCT excited states may occur when two TMCs units are in close proximity, to allow metal-metal contacts, and so low energy photoluminescence that is shifted from MLCT or IL may be observed. A lower-energy absorption band, assigned as MMLCT transition, was observed and enhanced, in the case of a dimorphic complex, [Pt(tpy)(C≡C–C≡CH)]OTf (Tf -

triflate) by varying the acetonitrile-diethyl ether ratios.[51]

The valuable electronic properties make polypyridine TMCs suitable for applications which are not only restricted to the development of anticancer drugs, being also researched for their biological and cellular applications (bioimaging reagents, biomolecular probes, phototherapeutic agents, etc).[52,53,54,55,56]

Over the last decades, since their first discovery, *metallomesogens* (MMs), metal-containing liquid-crystals (LCs), have received growing attention. MMs combine the properties of LCs, such as self-organization and self-healing ability, with the properties imparted by the metal component, such as magnetic, electrical, and optical properties.[57] The coordinating ligands do not necessarily need to present liquid crystalline properties since the presence of the metal may induce mesomorphic properties upon coordination due to additional intermolecular interactions, *e.g.* metallophilic (between metal centres), interactions between ligands or between metal and ligand that can greatly change the self-assembling abilities. MMs form the same type of mesophases as the purely organic LCs (nematic, columnar and smectic) and they can be neutral or ionic charged.[58,59]

The nature of the metal ion that is coordinated to form metallomesogens, has an obviously large impact to the phase behaviour and the photophysical properties of the final material. Different geometries like square planar, square pyramidal, trigonal bipyramidal, or octahedral geometries, and therefore more intricate organisation of the supramolecular liquid crystalline phases may be expected with respect to the organic counterparts.[60,61]

Surprisingly, despite of being rather attractive building blocks for the design and fabrication of supramolecular structures,[62] only few metallomesogens made with *bpy*, *tpy*, *phen* and other oligopyridine-based ligands have been reported so far.[63,64] For example, Pucci *et al.* investigated the influence of metals from group 10 of the periodic table, Pd(II), Pt(II) and Ni(II), (**Figure 1-6**) on the LC and luminescent properties of the complexes formed with *bpy* ligands having aliphatic tails of different lengths (n = 8, 16, 22). The square-planar Pd(II) thermotropic liquid crystals bearing a *bpy* derivative, compounds **11** –**13**, presented only a crystalline polymorphism whereas the compound with the longest alkyl chain compound **13** exhibit an enantiotropic lamellar mesophase.[65] When changing the metal with Pt(II), all complexes **14** – **16** were mesomorphic, exhibiting the same enantiotropic lamellar mesophase observed for complex **13**. The authors reported that by increasing the lipophilic part the clearing temperatures decreased. In case of Ni(II) complexes **18** –**19** the high transition temperatures prevented a

complete identification by polarized optical microscopy (POM) and powder X-ray diffraction (PXRD).[66] Moreover, in case of complexes **12** and **15** a solid-state luminescence at room temperature was also observed. In this simple example, the mesomorphic behaviour of these complexes with the same aliphatic tail is clearly affected by the nature of the metal centre.[66]

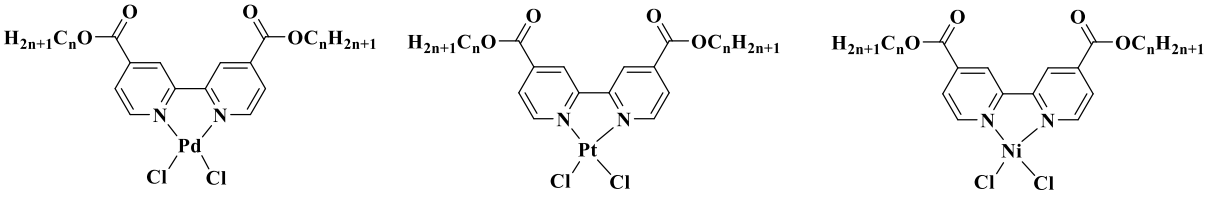

(11), n = 8;
(12), n = 16;
(13), n = 22;

(14), n = 8;
(15), n = 16;
(16), n = 22;

(17), n = 8;
(18), n = 16;
(19), n = 22;

Figure 1-6. Schematic representation of *bpy* Pd(II), Pt(II) and Ni(II) complexes.

Another important factor in inducing mesogenic properties is the environmental geometry around the metal centre and its influence on the overall molecular shape.[67] When the metal was changed to Ag(I), in the reaction with *bpy* only cationic bis-chelated complexes **20** and **21** with a distorted tetrahedral geometry, were obtained (**Figure 1-7**). Both complexes presented enantiotropic LC properties with columnar ordering, despite the length of the terminal alkyl chains.[68]

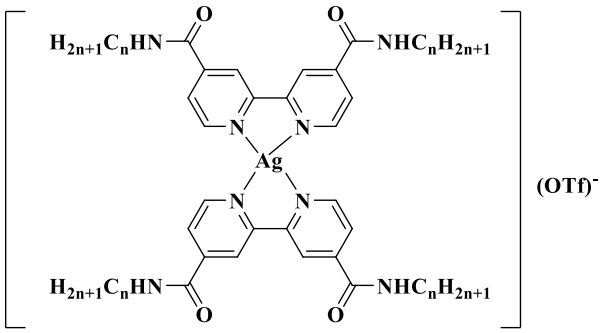

(20), n = 10;
(21), n = 18;

Figure 1-7. Schematic representation of *bpy* Ag(I) complexes.

The nature of the ligand is obviously another essential and determining parameter. For example, when changing the chelating *bpy* ligand with monodentate alkoxystilbazole, Ag(I) two-coordinated, linear complexes were obtained. D. W. Bruce[69] rationalized the role of the

anion nature, the alkoxy chain length, and type of the substituents on inducing liquid crystalline properties and the mesophases formed on alkoxystilbazole Ag(I) complexes (**Figure 1-8**).

For example, in case of complexes **22** (**a – c**), the variation of Ag(I) salts from BF_4^- (a), triflate - OTF^- (b), to dodecylsulfate – DOS (c), led to a decrease in the transition temperatures and of the type of mesophases formed. Smectic A and C (SmA and SmC) phases were detected for all complexes. Moreover, complex **22 b** presented an additional nematic phase (N), which was attributed to strong, isotropic, Coulombic forces. When replacing the anion with a bulkier one (DOS, complex **22 c**), a cubic phase (Cub) was identified.[69]

When fluorinated stilbazole ligands were used, the Ag(I) complexes with DOS anion behaved differently. The fluorination in the 3rd position, led to the promotion of the SmA phase and the destabilization of the N phase (complex **24 c**), and the destabilization of the Cub phase, while 2-fluoro substitution behaved oppositely: the cubic phase was retained and the N phase was promoted (complex **23 c**).[69]

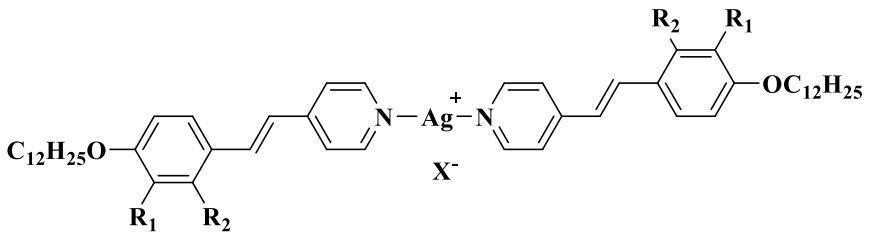

(22 a - c), $R_1 = R_2 = H$; **(23 a - c), $R_1 = F$, $R_2 = H$;** **(24 a - c), $R_1 = F$, $R_2 = H$;**

a: BF_4^-;
b: $CF_3SO_3^-$;
c: $^-O_3SOC_{12}H_{25}$; **c: $^-O_3SOC_{12}H_{25}$;** **c: $^-O_3SOC_{12}H_{25}$;**

Figure 1-8. Schematic representation of Ag(I) complexes with alkoxystilbazole.

Therefore, by a proper choice of the metal centre and the nature of the ligand, luminescent MMs may be obtained which can be used as multifunctional materials with great potential in bio-medical field. Indeed, luminescent MMs were reported as potential bio-imaging agents,[70,71,72] or as photosensitizers for photodynamic therapy (PDT) or cancer therapy.[73]

Oligopyridine complexes based on platinum group metals (Ru(II), Os(II), Pd(II), Pt(II), Rh(III) and Ir(III)), are highly researched due to their long-lived excited states, photochemical and electrochemical stability, and intense luminescent properties. However, are toxic and their abundance in the Earth crust is low.[74] In this context, a particular interest has been devoted

to the synthesis of luminescent first row TMCs, like Cu(I) and Zn(II),[75] less toxic, very abundant and cheaper alternatives to noble metals.

1.1.1 Cu(I) oligopyridine complexes

Copper belongs to group 11 of the periodic table, along with silver and gold having various oxidation states ranging from 0 to +4. The most usually encountered oxidation states are +2 (cupric) and +1 (cuprous). Cu(I) ions having a d^{10} configuration prefer two-coordinated linear, three-coordinated trigonal planar, and four-coordinate tetrahedral geometries.[76]

Due to its abundancy in the Earth crust,[74] Cu(I) complexes are more and more considered, from both photochemical and photophysical viewpoints, as alternatives of noble metal complexes.[76] Cu(I) complexes are known to present MLCT transitions and also LC transition[77] which are schematically represented in **Figure 1-9**.

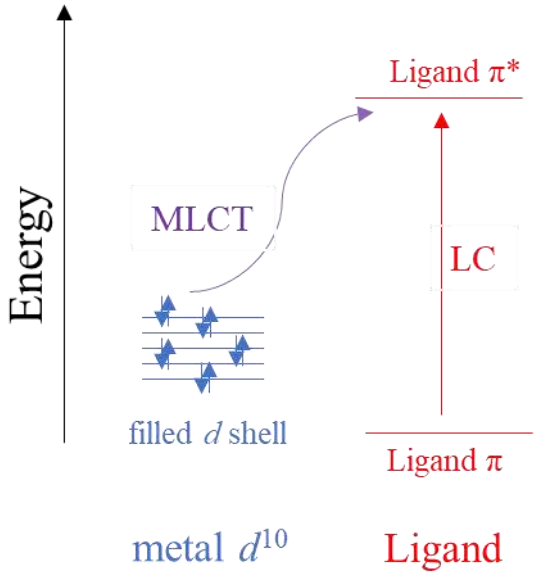

Figure 1-9. Electronic transitions in Cu(I) complexes with d^{10} configuration.[76]

Distortions from these ideal geometries are expected, especially in the case of the complexes with chelating ligands. Diamine Cu(I) complexes prefer a tetrahedral environment, however, in solution are easily attacked by nucleophiles and are rapidly oxidized to Cu(II) compounds which are stabilized by higher number coordination geometries. Therefore, the stability of these low-oxidation state copper complexes is highly connected to the geometrical environment around the metal centre.[76]

Although it is expected from Cu(I) coordination complexes to be good emitters, there are several factors that contribute severly to the quenching of their luminescence. For exemple in case of tetrahedral Cu(I) homoleptic complex, [Cu(*phen*)$_2$]BF$_4$, the formation of the MLCT state leads to a change in the oxidation of the Cu atom from (+1) with d^{10} electronic configuration to (+2) having a d^9 electronic configuration. This temporary Cu(II) specie has a tendency to form a square planar geometry, via a pseudo-Jahn-Teller distortion, which is lower in energy, as compared to the pseudo tetrahedral MLCT state. This leads to a quenching of the excited state by a nonradiative decay pathway, leading to weak or non-luminescent materials.[78]

Flattening distortions of the tetrahedral geometry facilitate the nucleophilic attack by solvent (or other molecules present in the environment) of the copper metal centre also in the excited state,[79] leading to quenching of the excited state by exciplex formation (i.e: in the excited state a different complex forms). This can be explained by the Lewis concept of acids and bases: the Cu(II) is a borderline Lewis acid, being readily attacked by Lewis bases, such as solvent molecules (MeOH, DMF, CH$_3$CN, etc).[78] For example, the geometry of [Cu(*dmp*)$_2$]PF$_6$ complex (dmp – 2,9-dimethyl-*phen*) in the presence of toluene and CH$_3$CN solvents, is changed and leads to the formation of pentacoordinated Cu(II) specie. The dynamics of this complex were determined through pump probe X-ray and laser spectroscopies and DFT calculations.[80]

Thus, in order to block the access of the fifth coordination position, the steric hindrance around the metal centre was enhanced by functionalising the ligand with bulky voluminous groups.

An important class in the field of luminescent Cu(I) complexes is represented by Cu(I)-diiminephosphine complexes, which started with the pioneering work of McMillin *et al.*[81] They were first to report the long-lived emission of [Cu(PPh$_3$)$_2$(*phen*)]BF$_4$ arising from IL and CT transitions. Since this first report of this luminescent Cu(I) complex, increasing effort have been made to stabilize of Cu(I) either by replacing the monophosphines with diphosphines which, due to their chelating effect, can suppress the dissociation of phosphine ligands in solution and improve the stability of Cu(I) complexes.[82,83]

Alkan-Zambada and Hu[84] synthesized heteroleptic complexes of type [Cu(N^N)(P^P)][PF$_6$], where N^N: *bpy* and P^P: bisphosphine ligand, (**Figure 1-10**). The complexes exhibited longer excited state lifetimes and higher Cu(I)/Cu(II) potentials compared to [Cu(dap)$_2$]Cl (dap =2,9-bis(para-anisyl)-*phen*), the most widely used Cu catalyst. Complex **25** was proven to be an efficient photoredox catalyst for chlorotrifluoromethylation of terminal alkenes, especially styrenes.

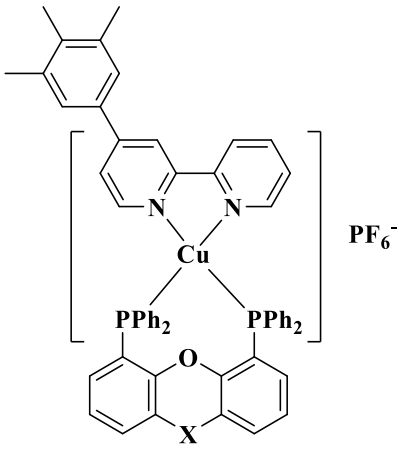

(25), X = $C(CH_3)_2$;
(26), X = CH_2;

Figure 1-10. Structure of the [Cu(N^N)(P^P)]PF_6 complexes.

Cu(I) complexes in medicine

At proper physiological concentrations, copper is a non-toxic element. Therefore, the suitable choice of the ligand will lead to complexes which do not affect the healthy cells, but accumulate copper in high concentrations in tumou cells, leading to an improved cytotoxic efficacy.[85]

Due to the poor stability of Cu(I) complexes in aqueous medium, only few studies are reported on their antitumor activity.[86] Following some examples of Cu(I) complexes with oligopyridines with biological activity are given, schematically representated in **Figure 1-11**.

The homoleptic complex $[Cu(phen)_2]^+$, **27**, was reported to bind to double-stranded DNA by partial intercalation,[87,88] and to oxidatively degrade DNA and RNA by attacking the sugar groups.[89] Moreover, Veal and Rill[90] reported that the interaction with DNA enhanced the charge-transfer absorption intensity which occurred around 525 nm. Later, Basak and Nagaraja, showed that complex **27** could be used as a tool to study the *in vivo* DNA-protein interaction in biological systems.[91]

In the case of the hydrophobic complex **29**, Sigman et al.[92] have reported an intercalative binding, which occurred with significantly reduced rate and with less sequence specificity than complex **27**.

Compared to the above mentionned complexes, complex **28**, having a methyl group in the 2,9-position, did not bind DNA by intercalation,[90] but it was found to be cytotoxic, killing at low concentration L1210 cells and P388 murine lymphoma, according to their reported *in*

vitro and, respectively *in vivo* studies.[93] Moreover, further studies have revealed that it also inhibited the integrase of human immunodeficiency virus (HIV).[94]

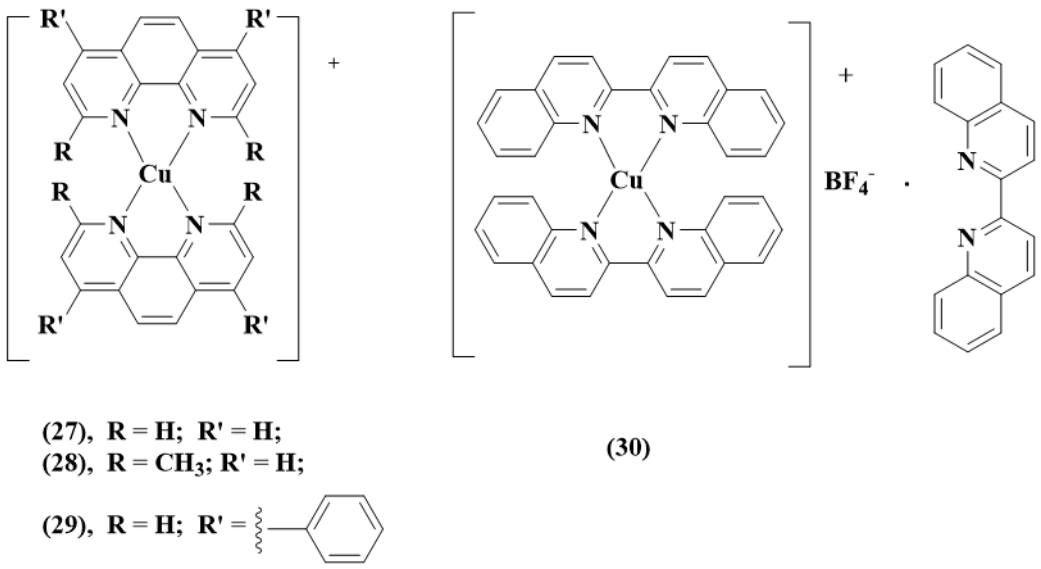

Figure 1-11. Oligopyridine Cu(I) complexes with relevance in the bio-medical field.

Complex **30**, $[Cu(bq)_2]BF_4 \cdot bq$, was reported to have a high activity against *Candida albicans*, and a moderate activity against bacteria. The authors also noted that complex **30** presented higher antimicrobial activity against bacteria and fungi than that observed for its Cu(II) analogue, $[Cu(bq)_2]Cl_2$.[95]

Although there are few reports on homoleptic Cu(I) complexes, it is worth mentioning that heteroleptic Cu(I) with phosphines and *bpy*, *phen* or *bq* were reported for their *in vitro* antibacterial,[96] antifungal[97] and anticancer[98,99,100,101] activities.

Also, due to their higher stability, Cu(II) complexes with oligopyridines have been reported for their anticancer,[102,103,104] antiviral,[105] and antibacterial[106,107] activities.

For example, Kashanian *et al.*[108] studied the DNA binding behavior of complexes **31** and **32** (**Figure 1-12**) using UV–Vis and circular dichroism spectroscopies, and viscometric methods. The results suggested a mixed binding, partially intercalative and partially hydrogen binding, of Cu(II) complexes with calf thymus DNA. Moreover, the complexes were showed to induce cleavage in pUC18 plasmid DNA and excellent antitumor activity against K562 myeloid leukemia cells.

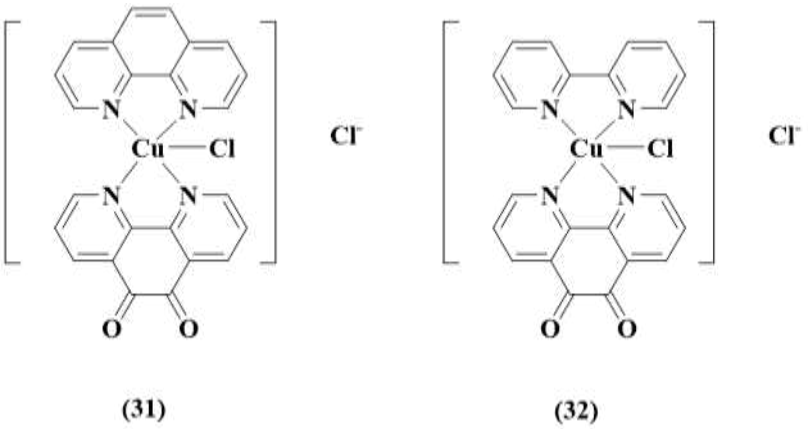

Figure 1-12. Schematic structure of Cu(II) complexes **31** and **32**.

Devereux *et al.*[109] reported the carboxylate complexes with a four-coordinate copper ion **33**, distorted tetragonal motif and **34**, with a square planar geometry (**Figure 1-13**). The complexes exhibited superoxide dismutase (SOD) mimetic activity and displayed potent in vitro cytotoxicity against human hepatic (Hep-G), renal (A-498) and lung (A-549) cancer cell lines.

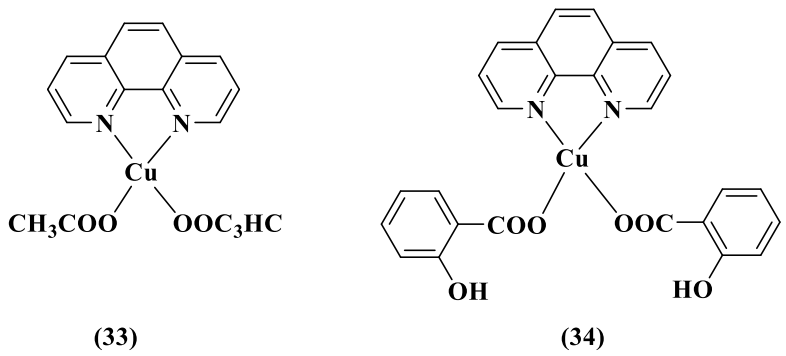

Figure 1-13. Schematic representation of *phen* Cu(II) with acetate (**33**) and salycilate (**34**) co-ligands.

Luminescent Cu(I) complexes

Xu *et al.*[77] reported the ground-state electronic properties of three monocationic Cu–*bpy* complexes, **35**–**37** with N_2, H_2O and Cl as co-ligands, with different interaction strength (**Figure 1-14**) in the UV-vis range. They investigated these complexes by photodissociation spectroscopy and computational analysis. All three complexes showed similar π-π* and *bpy* ring deformation vibrational bands. Measurements conducted at low temperatures evidenced for the width of the vibrational features, the excited-state lifetime as limiting factor. In the case of complex **37** (**Figure 1-14**), a lower lying bright LLCT state around 2.75 eV was assigned.

The authors concluded that the nature of the co-ligand did not have an effect in changing the position of the bright π-π * state, but it drastically changed the excited-state dynamics.

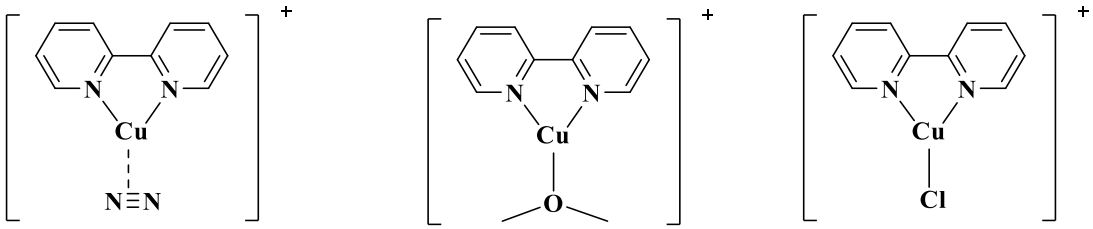

(35) **(36)** **(37)**

Figure 1-14. Copper complexes with *bpy* and N_2, H_2O and Cl as ancillary ligands.

Another class of luminescent Cu(I) complexes is represented by homoleptic Cu(I) complexes bis-chelated with oligopyridine ligands. The luminescent properties of these complexes are dependent on the chemical nature, size, and position of substituents on ligands.[78]

Figure **1-15** presents the structures of some relevant homoleptic Cu(I) complexes with luminescent properties.

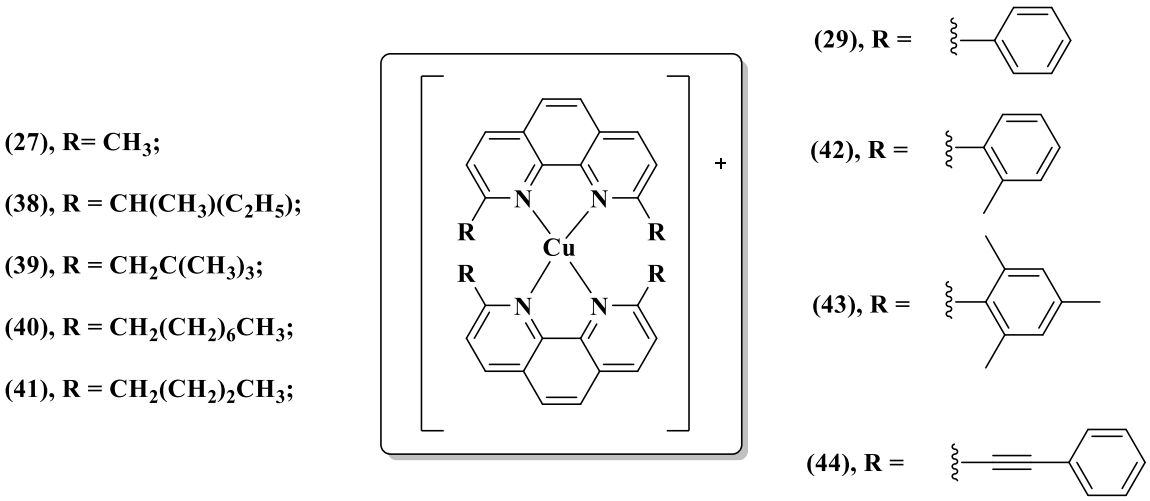

Figure 1-15. Cu(I) complexes with *phen* having different substituents in 2,9-position.

Blaskie and McMillin[110] reported the luminescent properties of complex **27** in CH_2Cl_2, which occurred due to MLCT transitions, but when using nuclephilic solvents such as MeOH the emission was quenched. When replacing the methyl groups with a phenyl one, resulting in

complex **29** with a distorted tetrahedral geometry, the emission was preserved also in MeOH, due to the sterical effects given by the bulkier size of the substituent.[111]

The electronic effects that contribute to the excited-state lifetimes of Cu(I) bis-*phen* complexes, have also been inspected.

Eggleston *et al*. reported Cu(I) bis-*phen* complexes **27, 38-41**, with alkyl substituents, and PF_6^- as counterion, and found that complex **39** exhibited the longest excited-state lifetime in CH_2Cl_2. Bulky substituents and also the spatial distribution of the atoms involved inhibited the quenching of the excited state.[112]

A detailed research on examining complexes **29**, **42-44** has revealed that two types of distorsion that occur in the MLCT excited states may lead to the quenching of luminescence: i) substituents that are too large prevent the formation of the bis-*phen* complexes, suggesting that an optimum size for these substituents should be found and ii) a reduction in ligand π-electron delocalization. The authors concluded that the phenyl substituent found in complex **29** reduced both of the above-mentioned distortion.[113]

By taking advantage of the photophysical properties of Cu(I) complexes, various applications have been reported such as: photoredox catalyst, photovoltaic and dye-sensitized solar cells. Following some examples are given, which are represented in **Figure 1-16**.

Sakaki *et al.*[114] reported the synthesis of complex **45**, with a large MLCT absorption band around 450 nm, which was successfully applied in solar cell with TiO_2, whereas complex **46** was reported as a visible-light-driven photoredox catalyst in carbon–carbon bond reactions.[115]

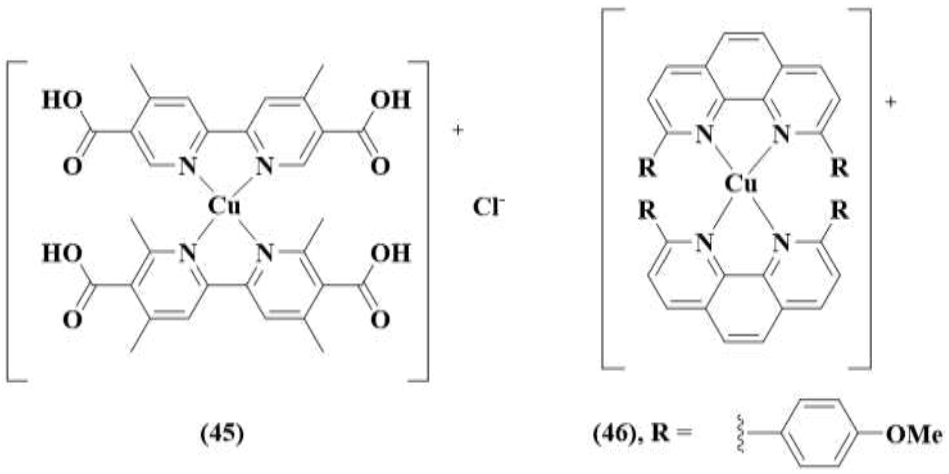

Figure 1-16. Schematic representation of Cu(I) complexes applied as solar cells or as photoredox catalysts.

Ashbrook and Elliott[116] prepared bis-*phen* complexes of Cu(I) based dyes $[Cu(dmp)_2]^+$ for study in DSSCs paired with $[CoL_3]^{2+/3+}$ mediators (where L = *bpy* or *phen*). The Cu(I) based dye had a covalently attached electron donor, whose purpose was to rapidly reduce the Cu(II) generated by photoinjection. The authors compared the behaviour of this dye with analogues that lack the donor moiety. The presence of the donor was found to significantly alter the dye's behaviour in favourable ways. While these dyes were reported to be stable under operating cell conditions, when oxidized to Cu(II) the metal centre appeared to interact with the mediator solution and solvent, which are Lewis bases.

Cu(I) metallomesogens

There are only few reports on Cu(I) complexes-based MMs, although Cu(I) can form complexes with low coordination number, which is a requierement for liquid crystalline (LC) phase stabilization. Cu(I) complexes with LC properties which have been reported so far contain classes of ligands such as alkylthiolates, isocyanides, oligopyridines, azamacrocycles, forming either mono- or binuclear two- or tetracoordinate complexes.[117] However, the poor stability towards oxidation may constitute the main reason of the difficulty of obtaining liquid crystalline Cu(I) complexes. Following, some representative examples are given, which are schematically represented in **Figure 1-17**.

Ziessel and co-workers[118] reported the first liquid crystalline metallohelicate, complex **47**, obtained by the self-association of a polycatenar *bpy* derivative in the presence of $[Cu(CH_3CN)_4]BF_4$. The optical textures observed upon cooling of the isotropic melt revealed the existence of a viscous columnar phase. Later, they reported also the first thermotropic Cu(I) *tpy* based metallomesogen, complex **48**, with a lamellar morphology.[119] Organogelation and thermotropic mesomorphic behavior could be observed in parallel for complexes **49** and **50** having an asymetric *phen* derivative as ligand. These complexes were reported to self-organize into a columnar LC phase.[120]

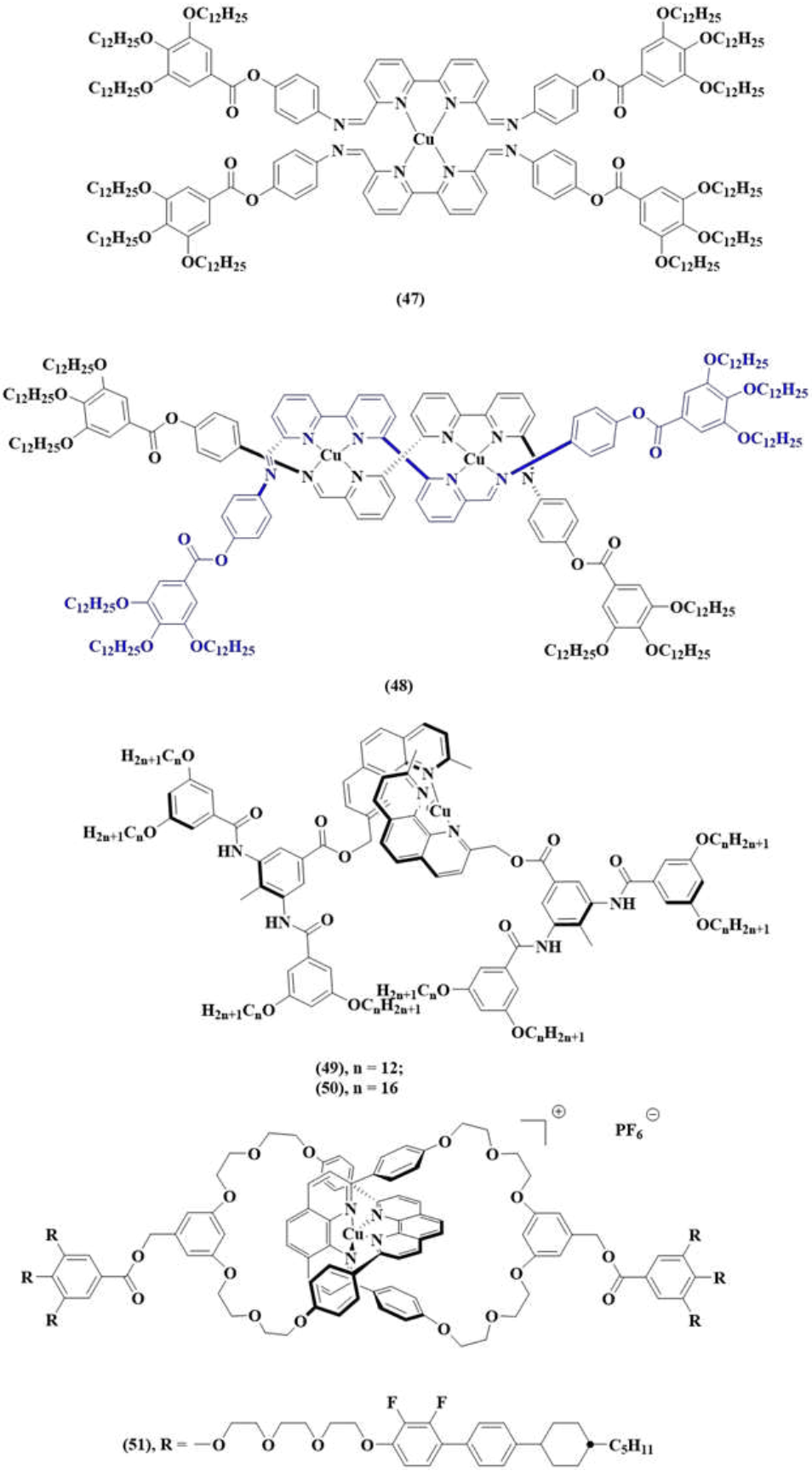

Figure 1-17. Schematic representation of Cu(I)-based metallohelicates.

Baranoff *et al.*[121] have successfully synthesized a LC free [2]catenane and reacted it with $[Cu(CH_3CN)_4]PF_6$, yielding Cu(I) mettalomesogen, complex **51.** Both the ligand and the complex presented which formed organized structures in their bulkstates over a wide range of temperatures. The authors reported that the mesogenic core induced a smectic A organization, with alternating layers of free [2]catenane or the Cu(I) complex and of the mesogenic moieties.

1.1.2 Zn(II) oligopyridine complexes

Zinc belongs to group 12, and its most common oxidation state is +2, with a filled *d*-shell.[122] Due to its closed d-shell electronic configuration, Zn(II) imparts the following properties: i) the ligand-field stabilization energy is not dependent of the geometry, ii) possesses a borderline Lewis acid character, iii) redox inertness, iv) diamagnetism and v) no d–d transitions.[123] Zn(II) complexes do not have a stereochemistry preference, with 4, 5, and 6 being the most common coordination numbers, leading to (distorted) tetrahedral, trigonal-bipyramidal, and octahedral geometries.[124,125]

Because of the complete d-shell, Zn(II) complexes do not present low lying energy charge transfer or metal-centred transitions and only present LC transitions or LLCT transitions (**Figure 1-18**).

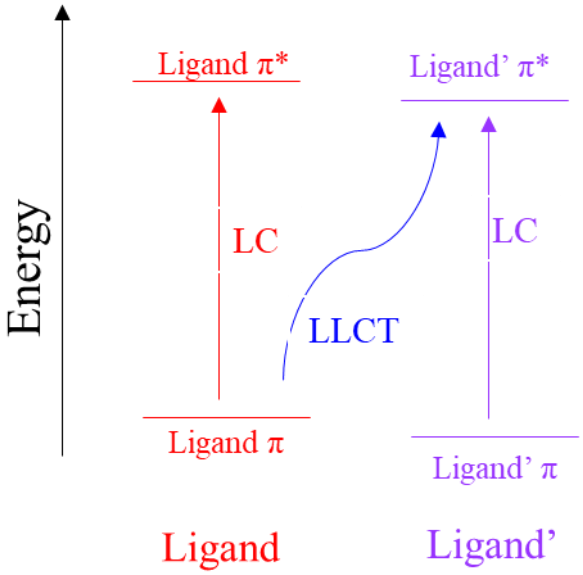

Figure 1-18. Electronic transitions in Zn(II) complexes with d^{10} configuration.[123]

For example, with *tpy*, depending on the nature of the type of Zn(II) salt, X^- and on the ligand to metal ratio (L:M), Zn(II) can form mono- (with a penta-coordination geometry) or bis-*tpy* complexes (with an octahedral geometry) (**Figure 1-19**).[126]

Bi and Pang studied the Zn(II) binding characteristics of complexes **52** (**a** – **b**), R = CH_3, NMe_2, $NPhen_2$, X = Cl^-, by spectroscopy at room and low temperature and concluded that: i) when Zn(II) concentration was low, *tpy* ligands readily reacted with $ZnCl_2$, forming Zn(II) complex **52** a with L:M = 2:1, with a decrease in luminescence, and ii) when increasing the Zn(II) concentration the reaction of complex **52 b** was favoured, with L:M= 1:1, accompanied by an increase in luminescence.[127]

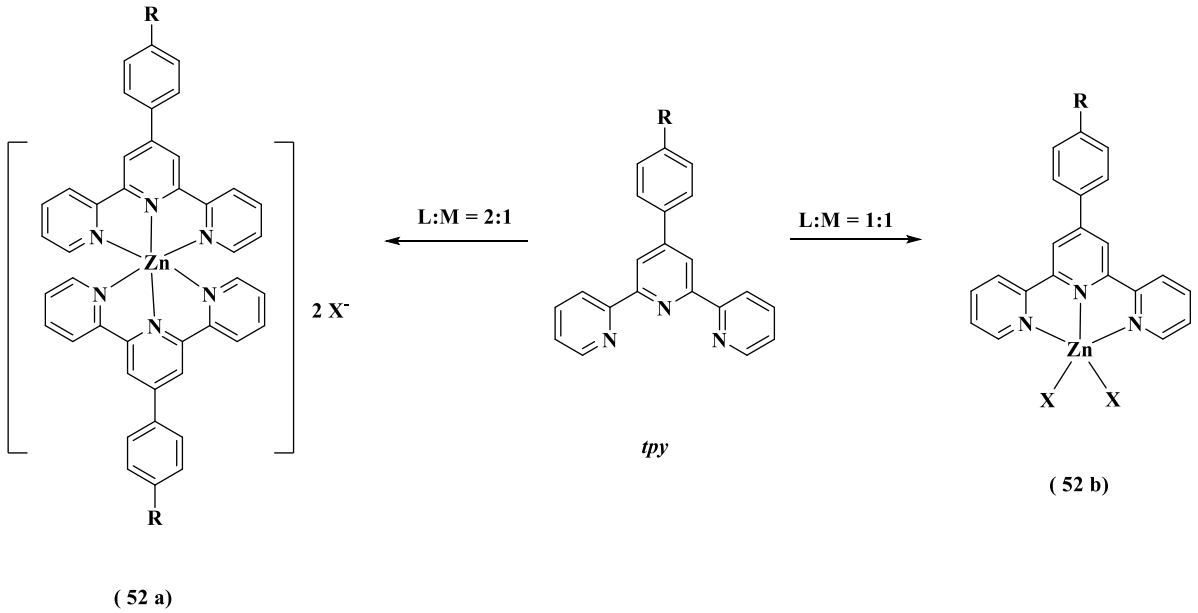

Figure 1-19. Reaction pathway towards mono- and bis-*tpy* Zn(II) complexes.

By using a Zn(II) salt with strongly coordinating anions, Li *et al.*[128] reported the formation of a penta-coordinated neutral mono-*tpy* specie complex **52 b** (R = CH_3 and X = Cl^-) with an irregular square based pyramid. When using a non-coordinating anion, Zare *et al.*[129] reported the formation of the bis-*tpy* specie, complex **52 a** (R = Br and X = $CF_3SO_3^-$) with an octahedral coordination geometry.

Zinc has a variety of bio-chemical and physiological functions (catalytic, structural and regulatory) in the biological processes,[130] therefore making it a promising metal centre ion in medicinal bio-inorganic chemistry.[131,132] Due to their low toxicity and low side effects, Zn(II) complexes are studied as DNA binders, tumour photosensitizers, antibacterial and antimicrobial drugs, and for bio-medical applications such as cancer or diabetes treatment.[133,134]

Zn(II) complexes in medicine

In general, N-chelating ligands are the key structural features in biologically active Zn(II) complexes.[135] Moreover, the interaction of Zn(II) metal ions with bioactive and/or bioavailable O^O-donor ligands increases the biological activity of the ligands.[136,137]

Figure 1-20 represents some of the Zn(II) complexes with N^N donor ligands and O^O bioactive ligands reported so far.

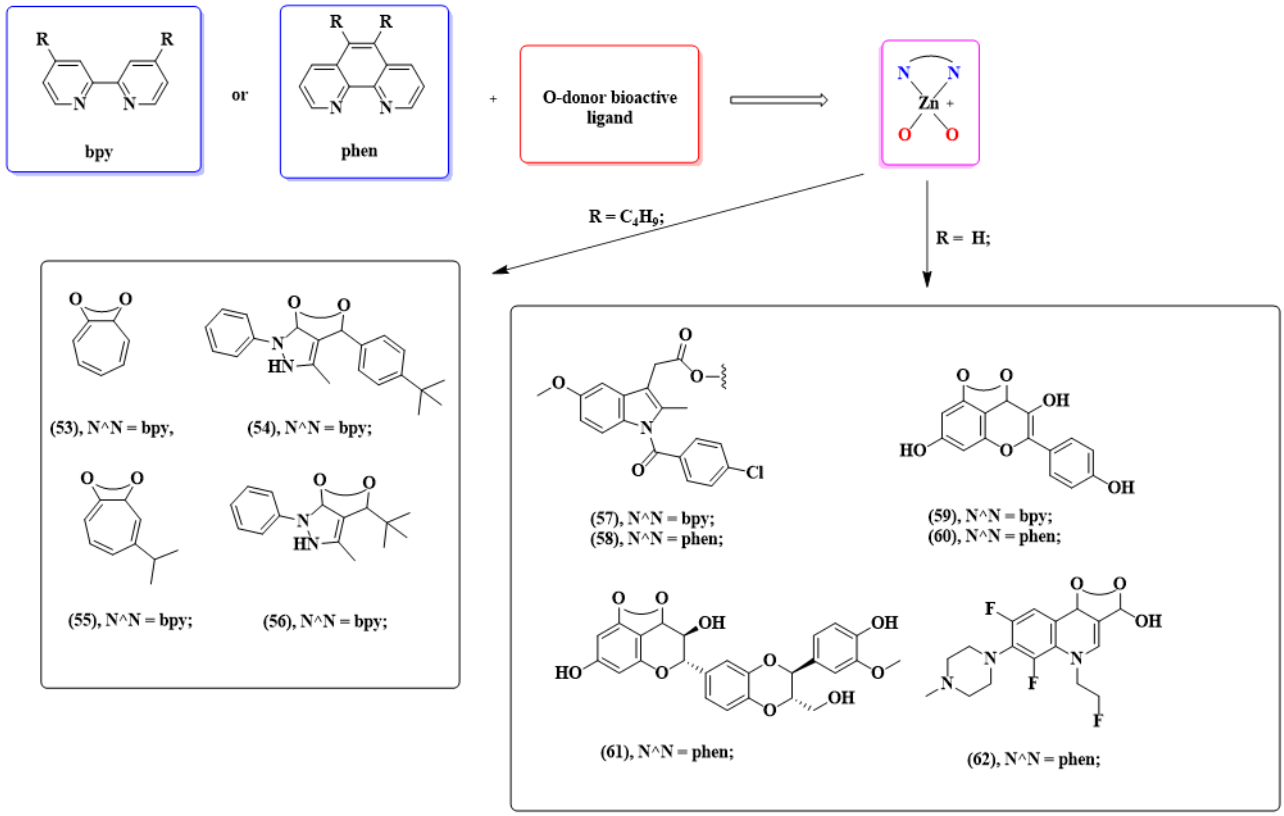

Figure 1-20. Schematic representation of bis-chelated heteroleptic Zn(II) complexes (top) and some representative examples from literature (bottom).

Phen Zn(II) complex, **62**, containing the quinolone antibacterial drug fleroxacin as co-ligand was investigated for the binding to CT-DNA; the complex combined with the groove region of DNA mainly through hydrophobic force. The results of the research indicated that complex **62** would cause low damage to mammalian cell DNA and, due to its stability and low genetic toxicity, could be used as a metallodrug.[138]

Oligopyridine Zn(II) complexes **57** and **58**, with indomethacin as co-ligand, were reported to have activity against breast cancer stem cell, which are thought to be partly

responsible for cancer relapse and metastasis, and a single dose of the Zn(II) complexes could theoretically be administered to eliminate whole tumour populations.[139]

O^O donor ligands of natural extraction, e.g. tropolonoids and flavonoids, are commonly reported for their pharmacological and therapeutic activities of the free flavonoids such as antioxidant, anti-inflammatory, antitumor or antidepressant.[140] While their homoleptic complexes with Zn(II) as metal ion, have been intensively studied for their DNA binding abilities and antioxidant properties,[141,142,143,144,145] as DNA probes and/or diagnostic agents,[146] as anti-diabetic drugs,[147148] anti-tumour drugs,[149,150] very few reports regarding the pharmaceutical and bio-medical applications of heteroleptic complexes with N^N intercalating agents were made.

Pucci *et al.*[151] evaluated the *in vitro* antiproliferative activity of the five-coordinated complexes **53** – **56**, with a chlorine in the apical position, towards DU145, LNCaP and PC-3 cell lines, which were shown to have a good selectivity towards the tested cancer cell lines, having IC_{50} values comparable with those of *cis*-platin.

The binding and cleavage abilities with DNA of complexes **59** and **60**, with kaempferol as bioactive ligand, were studied by means of fluorescence spectroscopy, viscosity measurements, and gel electrophoresis. The experimental results indicated that the complexes bind to CT-DNA through intercalation.[152]

Complex **61**, with silibinin, was tested for its potential biological activities and it was found to possess significant anti-bacterial activity against Gram-negative (*E. coli*) and Gram-positive (*S. aureus*) stains. Moreover, due to the increased metabolic activity of cells and a favourable condition of cell growth, this complex could be a promising biomolecule for osteoblast differentiation and, therefore, could be used in orthopaedic applications.[153]

Besides the Zn(II) complexes with N^N chelating ligands, terpyridine is another highly research ligand and a useful source towards the synthesis of Zn(II) complexes. The ligand is known to intercalate into DNA,[154] and the alteration of *tpy* structure generates derivatives with major impact on the anticancer potency.[155,156] Due to the peculiar resulting properties, such as luminescence,[127,157,158,159,160,161] these complexes are of interest in materials science[160,162,163,164,165] and medical applications.[166,167,168,169,170,171]

The chemical structures of some Zn(II) complexes with relevance as therapeutic agents are presented in **Figure 1-21**.

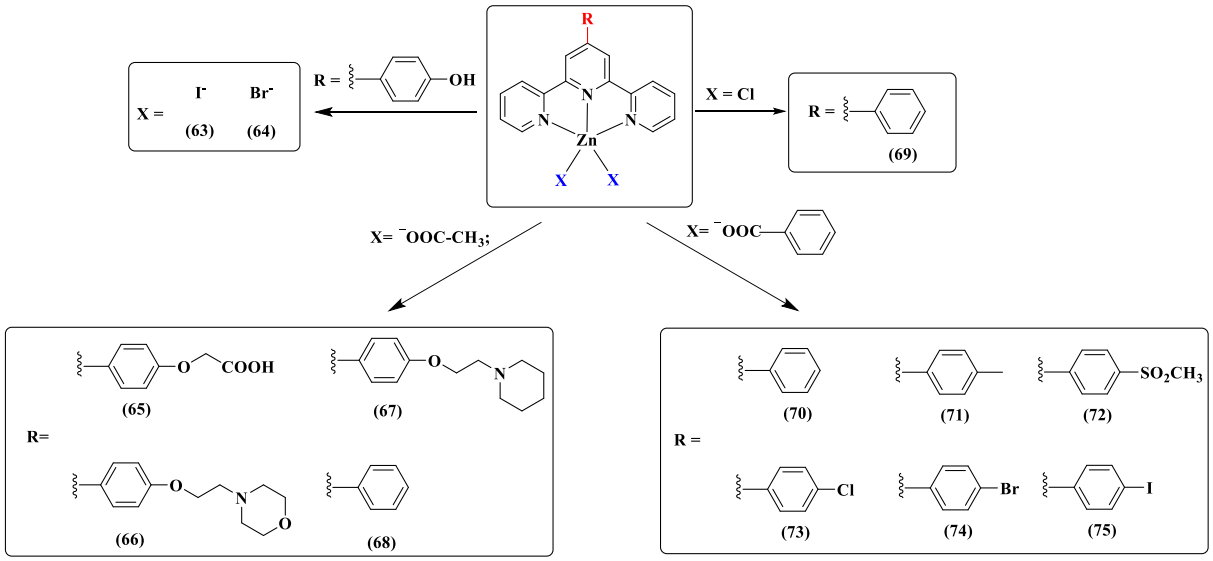

Figure 1-21. Schematic representation of *tpy* Zn(II) complexes with relevance in the bio-medical field.

Complexes **63** and **64** were reported as potential candidates for chemotherapeutic agents, having higher antiproliferative activity against A549, HCT-8, and MCF-7 compared to *cis*-platin.[172] Complexes **65** and **66** were reported to have high *in vitro* cytotoxicity and selectivity against HL-60, BGC-823, Bel-7402 and KB cell lines, and the authors related this cytotoxicity of these complexes to the terminal group of the ligands.[155] Chu *et al.*[173] evaluated the *in vitro* cytotoxicity of complex **67** against HL-60, BGC-823, KB, Bel-7402, A549, Hela, K562 and MCF-7 cell lines by MTT method. It was found that this complex exhibited better cytotoxicity than *cis*-platin and bonded DNA via intercalation mode. Complexes **68** and **69** were reported to exhibit *in vitro* tumour-inhibiting activities, which are higher than that of *cis*-platin, against HL-60, Bel-7402, BGC-823, and KB human tumour cell lines.[174]

The anticancer potencies of complexes **70** – **75** were evaluated against A549, Eca-109, and MCF-7 human cancer cell lines. Moreover, the DNA binding properties were also studied. The authors reported that all complexes zinc complexes presented good inhibitory effects on cancer cells, better than that of the commonly used clinical drug cisplatin. Regarding the DNA binding studies it was found that the complexes binded to DNA, mainly through intercalation.[175]

On this background, developing new Zn(II) complexes based on oligopyridines and the evaluation of their pharmacological properties and their screening as antitumor agents remains a matter of high interest.[174]

Luminescent Zn(II) complexes in medicine

Because it is known that many Zn(II) complexes exhibit intense fluorescence, even at room temperature, a plethora of research papers have reported their photophysical properties,[176,177,178,179,180] and their (potential) application as DNA photocleavage agents[181] and as molecular probes in bio-imaging,[182,183,184,185,186,187] which target cytoplasm, nuclear membrane, nucleic acids and other intracellular organelles. Furthermore, Zn-complexes were tested for the labelling of adenosine triphosphate (ATP), adenosine diphosphate (ADP) and pyrophosphate (PPi).[188]

The combination of the intercalating abilities of oligopyridines[189,190] with bioactive O^O-donor ligands, could lead to new complexes with intrinsic biological properties and potential diagnostic abilities.[134] Moreover, the fluorescent properties of these complexes will combine the therapeutic properties with the ability of investigating the mechanism of action through optical methods into a single molecule, without the use of additional external agents, yielding thus theranostic agents.[191]

Figure 1-22 summarizes some examples of luminescent Zn(II) heteroleptic complexes with N^N donor ligands with relevance in the bio-medical field.

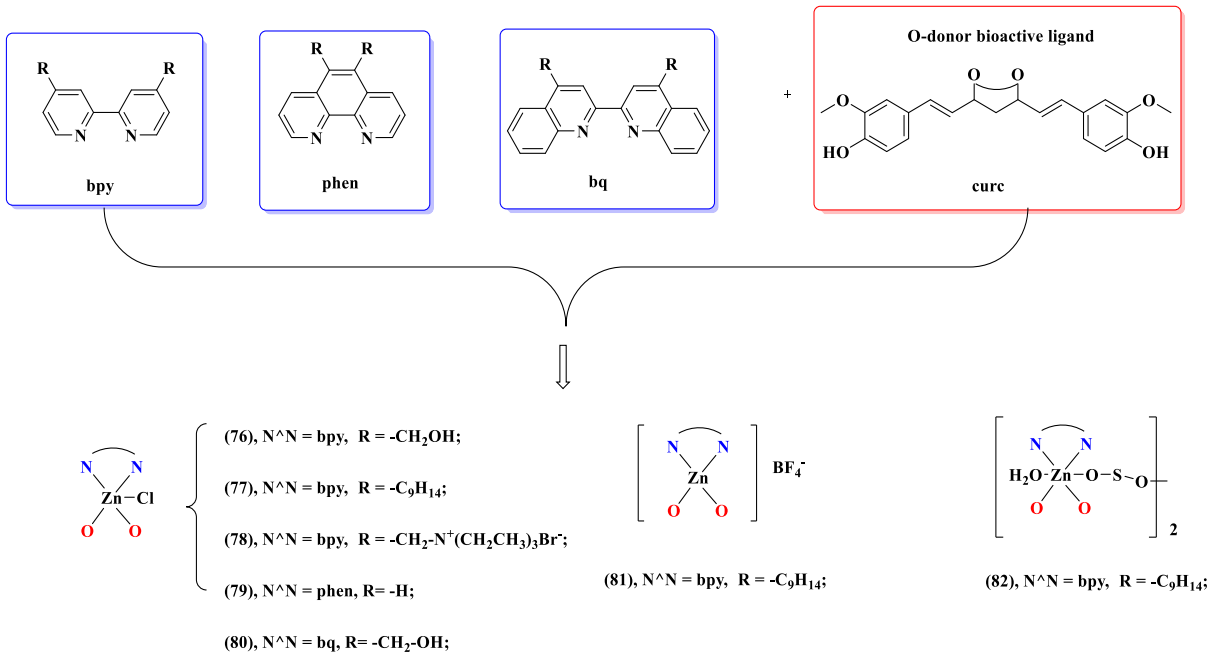

Figure 1-22. Schematic representation of luminescent Zn(II) heteroleptic complexes with relevance in the bio-medical field.

Pucci *et al.*[191] evaluated the *in vitro* anticancer properties towards a panel of human cell prostate cancer cells, DU145, LNCaP and PC3 of curcumin (curc) -based Zn(II) complexes **76** and **77**, and promising results regarding selective anticancer properties were reported. Due to the intrinsic fluorescence of the complex **77**, the authors were able to determine the interaction with DNA through an optical method, and the results suggested a partial inter-base intercalation. Complex **77** was further characterized from a photophysical point of view, showing a green emission and a positive solvato-chromism which permitted the authors to study its interaction with Human Serum Albumin (HSA). The complex was found to be a useful tool to expand the knowledge in the area of protein–ligand binding and confirmed the important role of the fluorescence spectroscopy in biomedical research.[192]

Later, the same group reported Zn(II) heteroleptic complexes **78** – **82**, also having *curc* as O^O ancillary ligand. The complexes were stable both in aqueous medium and in physiological conditions. The authors evaluated the biological activity by investigating the viability of human neuroblastoma cell line SH-SY5Y. It was found that all complexes exhibited significant cytotoxic activity and the cell response was due to an apoptotic mechanism. Moreover, the intrinsic fluorescence of these compounds allowed deep investigation of their interaction with DNA suggesting a partial inter-base intercalation**.**[133]

Therefore, by taking advantage of the fluorescent nature of the compounds and the biological activities, highly active theragnostic agents could be obtained.[133]

Additionally, *tpy* based Zn(II) complexes have been explored for their photophysical properties,[193] as optical materials, with application as chemosensors[194] and in fluorescence imaging.[195] Some examples are summarized in **Figure 1-23**.

Complex **83**, derivatized with a coumarin moiety was reported as a fluorescent chemosensor for ATP and PPi and ADP, which are biologically important phosphates.[196] Complexes **84** – **86** were reported for their low cytotoxicity and their *in vivo* cellular imaging using HepG2 cells as models. The authors showed that upon the addition of the Zn(II) complexes the cells displayed intense luminescence which may facilitate future biological membrane system research.[197] Complexes **87** – **94** were reported to have a higher *in vitro* antiproliferative activity on tumour cells compared with *cis*-platin, with complexes **87** and **88** having a fluorine substituted terpyridine presenting the highest antitumor activity. Fluorescence spectroscopic measurements revealed that the complexes presented a high affinity binding to CT-DNA.[198]

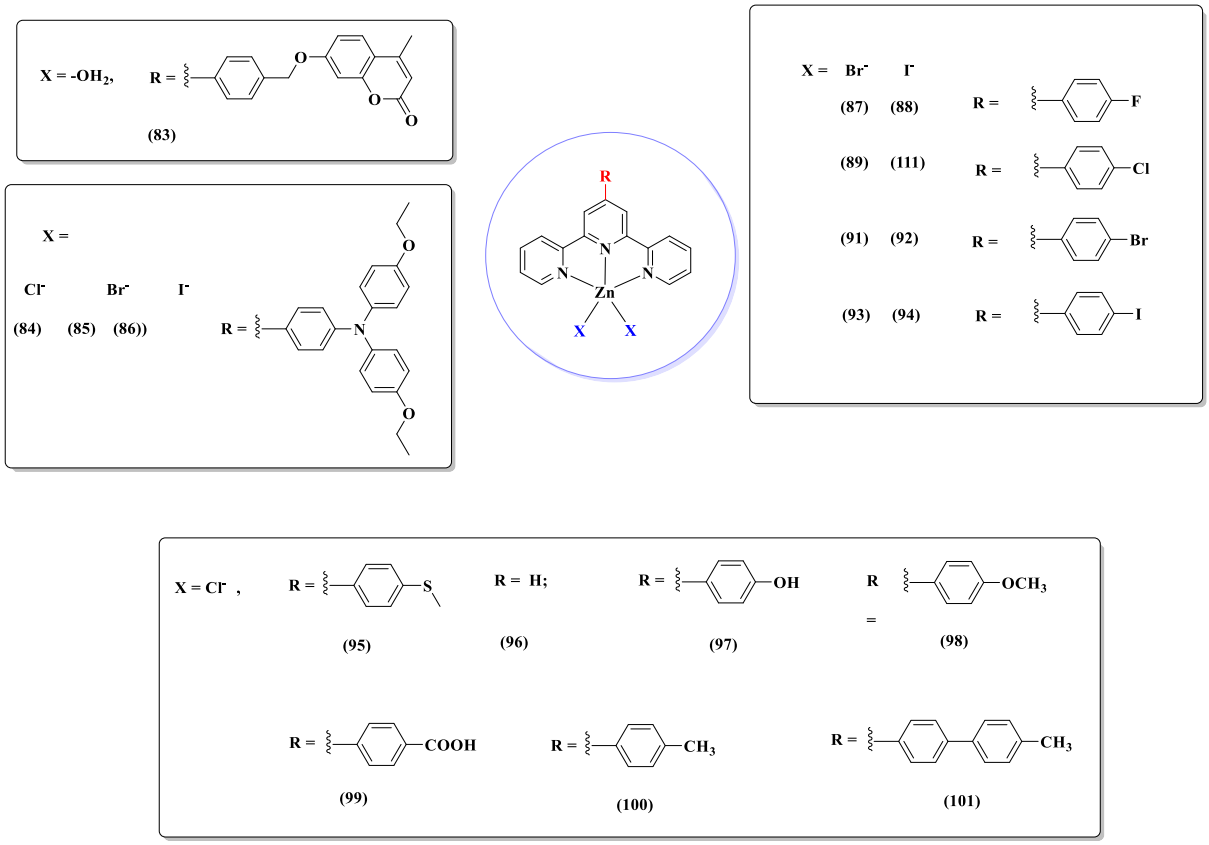

Figure 1-23. Schematic representation of luminescent Zn(II) *tpy* complexes with relevance in the bio-medical field.

Complex **95** was successfully applied as a turn–off fluorescent probe for its application in bioimaging. The carried-out cytotoxicity experiments showed that the complex possessed low cytotoxicity towards HeLa cells. To verify if complex **95** can detect exogenous HClO in HeLa cells, firstly the complex was incubated with HeLa cells, exhibiting a green luminescence. When incubated with NaClO, no fluorescence was observed.[199] The series of complexes **95** – **101** were studied for their photoluminescent properties and the antiproliferative activities against A549, Bel-7402, MCF-7, and Eca-109 cancer cell lines. The authors reported that all complexes presented strong emission. The *in vitro* cytotoxicity assay showed that the compounds possessed good anticancer activity against the tested carcinoma cell lines. The results of electronic absorption, fluorescence titration, and circular dichroism spectroscopy showed that the ten compounds have strong affinity to bind DNA.[128]

Zn(II) complexes of bis-*tpy* were also reported as chemosensors for the recognition of PPi under alkaline conditions,[194] ATP,[200] and also as potential bio-imaging agents.[193,201,202,203,204] Therefore, the growth of Zn(II) sensors encourages the fast development of fluorescent zinc coordination complexes suitable for cellular imaging.[188]

Zn(II) metallomesogens

MMs based on Zn(II) ions are of interest, due to the fact that Zn(II) has a strong tendency to adopt tetrahedral or higher coordination number geometries, which is an important factor for enhancing the luminescence properties,[205] but detrimental for inducement of low temperature mesomorphism.[57] Zn(II) complexes combining the order, mobility with changes in molecular organization when an external stimuli is applied could lead to the development of new soft materials for innovative applications.[61]

Some examples of thermotropic Zn(II) mesogens with N^N donors are depicted in **Figure 1-24**.

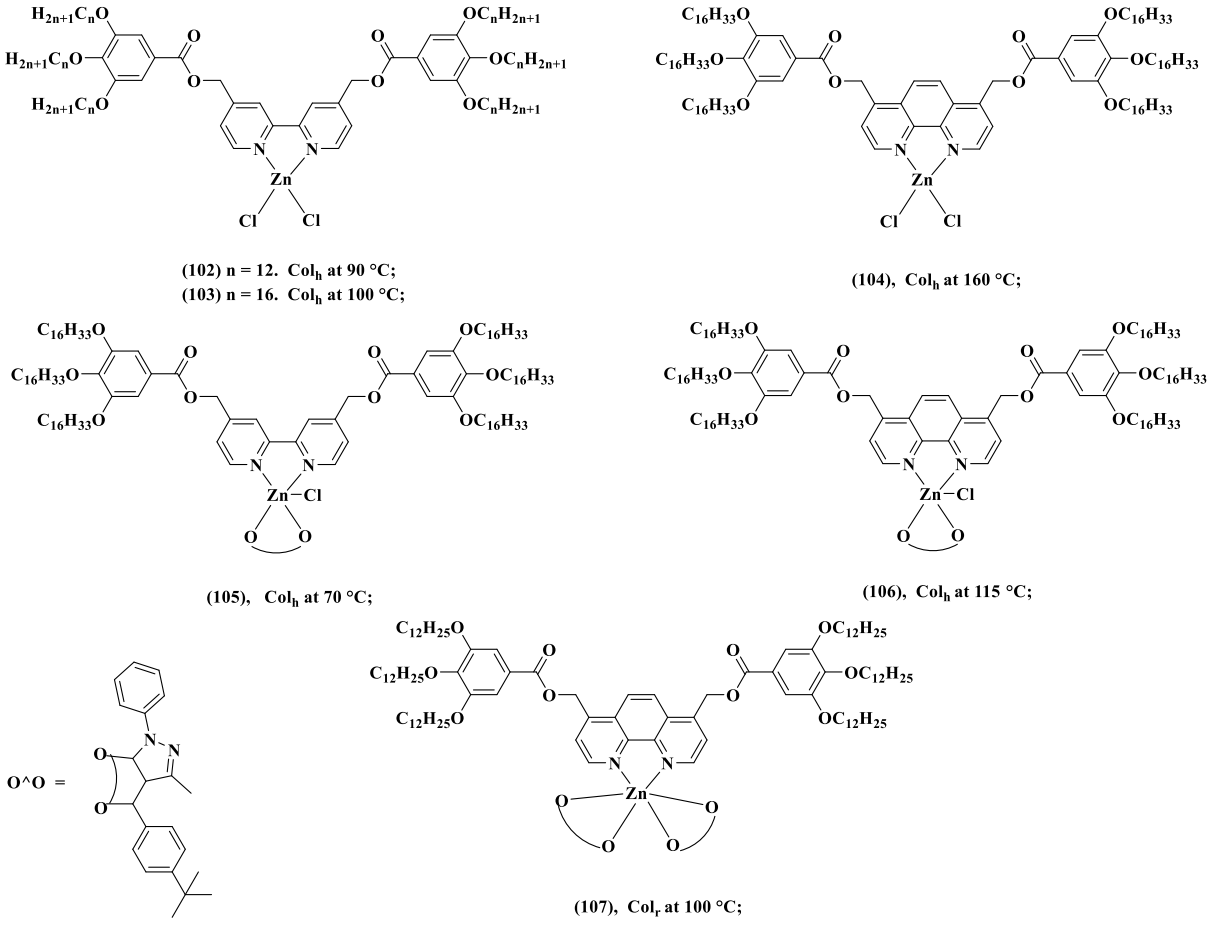

Figure 1-24. Schematic representation of Zn(II) mesogens with *bpy* and *phen* derivatives.

Barberio *et al.*[206] were the first to report mesomorphism in tetrahedral coordinated zinc complexes containing hexacatenar *bpy* derivatives (n = C_{12}, complex **102** and n = C_{16}, complex **103**). The self-assembly into columnar phases was assigned to the ability of the hemi-disc

shaped Zn(II) molecules to form face-to-face disc shaped dimers, through complementary-shape approach.

Pucci *et al.*[207] have reported Zn(II) complexes containing the hexacatenar *bpy* and *phen* ligands. As a function of the nature of co-ligands, the geometries varied from tetracoordination in the case of complex **104**, pentacoordination for complexes **105** and **106**, and hexacoordination for complex **107**. The peripheral polycatenar tails grafted on the oligopyridine ligands promoted columnar mesomorphism, even at very low temperatures. The authors studied the complexes photophysical properties by varying temperature, in different condensed states. The results indicated that the complexes emit in the green region of the visible spectra at room temperature, their emission being retained in the mesophase and in the isotropic state, with a reversible red-shift related to a temperature increase.

Kumar *et al.*[208] reported Zn(II) mesogens **108** – **114,** containing a hexacatenar *tpy*, with a fused cyclopentene ring attached to each lateral pyridyl unit, **108 - 112**, and without cyclopentene rings, **113** and **114** (Figure 1-25). The authors carried out absorption and emission studies in solvents of varying polarity. The complexes were found to be luminescent in solution, in the solid state and in the mesophase. Significant changes in the emission wavelength were observed as a function of temperature, both in the solid and LC state, which could be attributed to different levels of organisation in the materials. Complexes with the fused ring presented solvatochromism, which was not observed in the case of complexes without the cyclopentene ring.

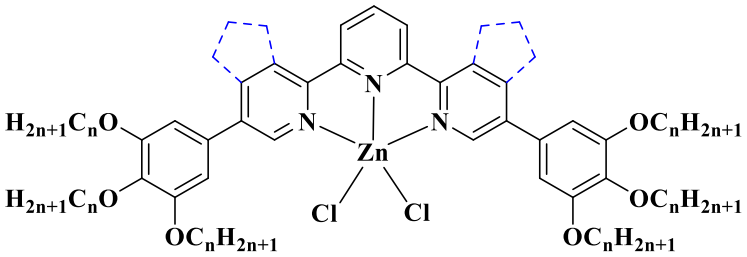

(108), n = 8. Col_h at 190 °C;
(109), n = 10. Col_h at 194 °C;
(110), n = 12. Col_h at 191 °C;
(111), n = 14. Col_h at 221 °C;
(112), n = 16, Col_h at 160 °C;

(113), n = 12. Col_h at 286 °C;
(114), n = 16. Col_h at 254 °C;

Figure 1-25. Schematic representation of Zn(II) mesogens with *tpy* derivatives.

Despite excellent luminescence efficiencies, TMCs have some major drawbacks, like insufficient solubility, targeting and local delivery. A strategy to overcome these drawbacks is to attach the TMCs onto nanoparticles (NPs) leading to *self-assembled complex hybrid systems.*[192]

1.2. Gold nanoparticles

Noble metals complexes like gold, silver, platinum, rhodium, iridium, palladium, etc. have been the subject of intensive investigations, which led to the synthesis of anticancer, antirheumatic, antimalarial, and antimicrobial drugs. The colloidal state is another form in which noble metals are used as therapeutics.[209] Among them, Au and Ag nanoparticles (NPs) are the most researched.[210]

The use of gold for medicinal purposes dates back to ancient times[211] and has found different medicinal applications throughout the centuries,[212] but its use decreased due to the discovery of associated severe side effects. However, recently, nanomaterials with Au-containing drugs showed several excellent therapeutic benefits and low toxicities.[213]

Compared to small molecules or bulk materials, nanoscale structures express various physical and chemical properties. NPs possess particular intrinsic reactivity as a result of increased surface area, so an appropriate choice of materials for the manufacture of nanoparticle-based therapeutics would be made.[214]

The chemical, optical, and electromagnetic properties of gold nanoparticles (Au NPs) are highly dependent on their physical characteristics and are influenced by their size and shape. As result, many simple synthetic routes were developed to control these characteristics.[215] These methods imply either “top-down” (physical manipulation) and “bottom-up” (chemical transformation) approaches.[216]

Synthesis

The first Au NPs were synthesized as nanospheres. Later, various other forms were obtained, such as nanoclusters, nanorods, nanoshells, nanostars, and nanocages.[217,218,219,220,221,222]

The most employed methods used to obtain Au NPs are the Turkevich[223] (for aqueous synthesis) and Brust−Schiffrin[224] (for organic-based synthesis) methods, which consist in the

chemical reduction of gold salt to metallic gold in the presence of a capping ligand.[225] Other synthetic routes include physical approaches such as microwaves and UV irradiation to nucleate the Au NPs[225] or biological routes, which imply the use of plant extracts or microorganism for the formation of the nanostructures.[226]

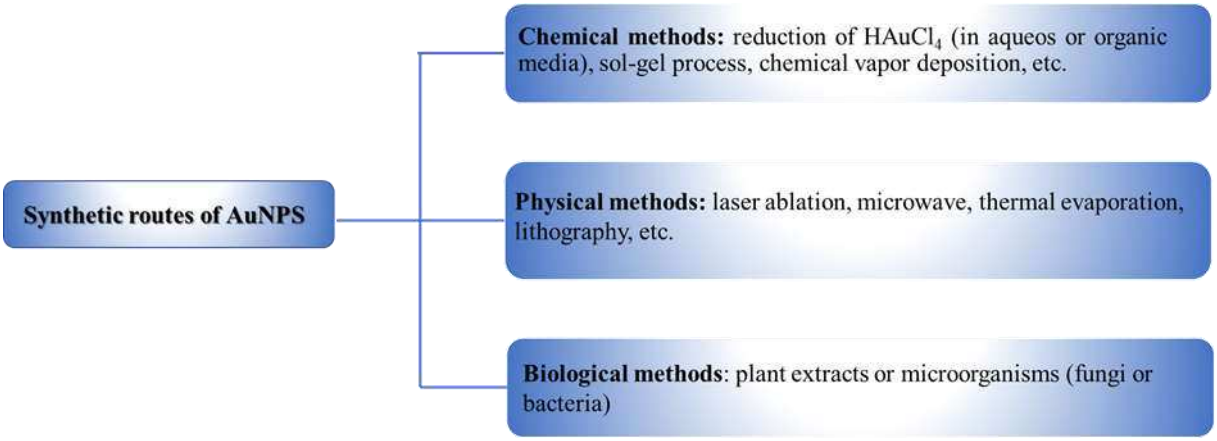

Figure 1-26. Different synthesis routes of Au NPs.

Properties

Noble metal NPs differentiate from other nanoplatforms (e.g. semiconductor quantum dots, magnetic NPs and polymeric NPs), through their single surface plasmon resonance (SPR), which enhances all the radiative and irradiative properties of the NPs.[218] Other important properties of Au NPs include biocompatibility[227], and the ability to quench fluorescence.[228]

The SPR absorption gives the brilliant colours of Au NPs, and its due to the fact that gold is a conductive material and its free electrons can move freely within the material,[229] giving rise to optical properties which are not found for the bulk solid metals. The exposure of Au NPs to light, gives rise to the collective oscillation of the free electrons of the metal, entailing an accumulation of a negative real and small positive imaginary dielectric charges[230] as schematized in **Figure 1-27**. Because the electromagnetic wave is sinusoidal, it results in the oscillation of the metal particles electrons, and when it reaches a maximum at a specific frequency (SPR) it results in a strong absorption of the incident light,[231] which can be measured using a UV-Vis spectrometer. SPR is strongly dependent on the particle metal, size, shape, environment and interparticle distance.[232] The brilliant colour of Au NPs is explained by the fact that the absorption occurs in the visible range of the electromagnetic spectrum.

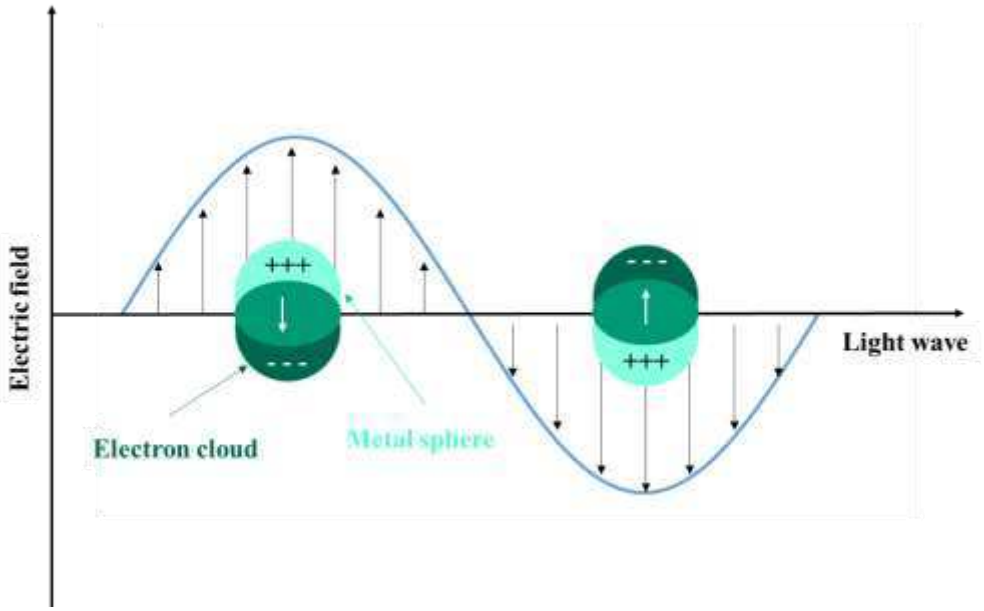

Figure 1-27. Illustration of SPR phenomena of Au NPs.

The ability of the AuNPs to quench the fluorescence is realized through the deactivation pathway based on the good overlap between the emission spectrum of excited fluorophores and the surface plasmon band of the AuNPs.[233]

AuNPs coated with various organic,[234,235,236] inorganic[237] or hybrid[238,239,240]shells combine therapeutic, imaging and targeting functions within one single drug delivery system. Their explicit physical and chemical properties make them important scaffolds for various applications ranging from therapeutics, detection and diagnostics, biolabeling, drug delivery, chemical and biological sensing, imaging as depicted in **Figure 1-28**. [241,242]

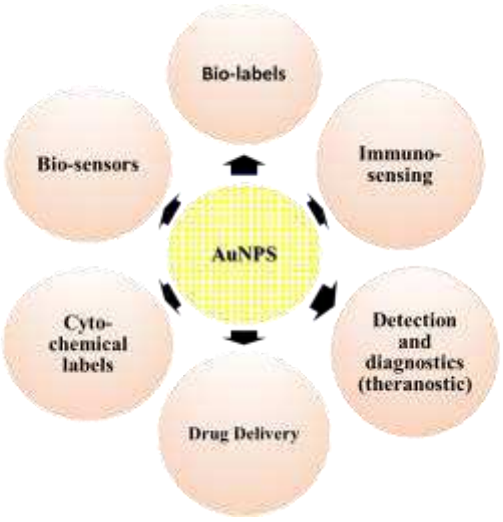

Figure 1-28. Medical applications of Au NPs.

1.3. Au NPs assemblies with tpy derivatives

The assembly of NPs into defined nanoscale structures provides access to nanocomposites through noncovalent assembly strategies, van der Waals/packing interactions, hydrogen bonding, ion pairing, and host-guest inclusion chemistry.[243] Moreover, by forming metal-ligand systems the structural diversity of self-assembly processes, redox and photochemical properties to the resulting constructs may be expected.

To ensure the solubilization and stabilization, Au NPs are functionalized with capping agents that strongly bind to their surfaces such as thiols, oxoanions, amines or thiocyanates.[244] Also, oligopyridines, in particular *tpy* derivatives, have been employed as unconventional capping agents.[245]

Montalti *et al.*[244] tested the stability of Au NPs decorated with *tpy* ligands functionalized with thiol after ligand-exchange on their surface (**Scheme 1-1**). The authors concluded that a low concentration of *tpy* derivative does not affect the Au NPs stability, however aggregation occurs at a certain critical concentration value. The binding of the *tpy* fragment to the Au NPs surface was followed by UV-Vis and fluorescence spectroscopies. The authors noticed that the fluorescence of the *tpy* was quenched when bound to the gold surface. They also demonstrated that complexation of Zn(II) of the *tpy* ligands on the surface of gold colloids was possible and it contributed to the stabilization of the nanoparticles in solutions. Moreover, the luminescence was quenched after complexation of Zn(II).

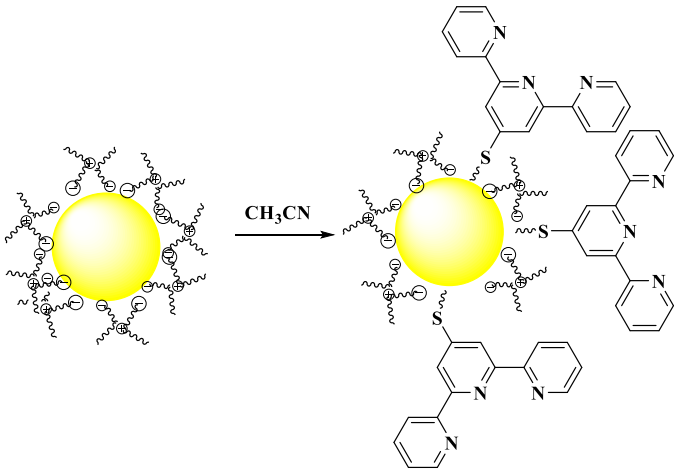

Scheme 1-1 Synthesis pathway Au NPs capped with tpy derivative. Adapted from **244**

Norsten *et al.*[243] synthesized Au NPs bearing *tpy* ligands (**Figure 1-29**) and studied their metal-mediated self-assembly by using different metal ions: Fe(II), Ag(I), Zn(II) and Cu(I). The variation of the distance of the *tpy* to the metal core was realized by altering the length of the aliphatic tail of the *tpy* ligand. Coordination to Fe(II) was followed by UV-vis spectroscopy by the formation and subsequent increase of the distinctive Fe(*tpy*)$_2$ MLCT absorption band (450-600 nm). The authors reported that no visible aggregation was observed at low concentrations necessary to study the association by UV-vis spectroscopy. When using concentrated solutions of the metal salt, the authors obtained extended aggregates of **115** – **117** of Fe(II), Ag(I), Zn(II) and Cu(I).

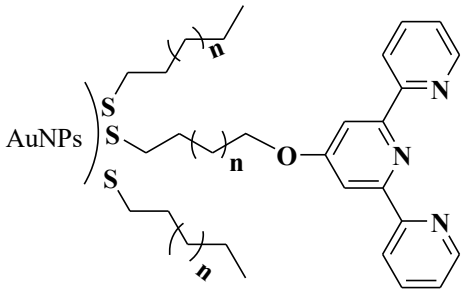

(115), n = 1;
(116), n = 3;
(117), n = 6;

Figure 1-29. Schematic representation Au NPs assemblies **115 – 117.** Adapted from ref. **243**

One of the researched domains regarding Au NPs assemblies with oligopyridines is the construction of photoresponsive materials. Most of these assemblies are based on Fe(II) metal ions.[246,247]

Alvaro *et al.*[248] obtained Au NPs functionalized with a Fe(II) *tpy* complex (**Figure 1-30**) and studied the photophysical properties of this assembly. The authors concluded that this assembly was able to generate microsecond charge separated states in conventional organic solvents that even become much longer lived in ionic liquids. The authors suggested that these systems could be used for the construction of photoresponsive materials. The authors also demonstrated the ability of the Fe(II) complex functionalized Au NPs to act as integrated photocatalyst for H_2 photogeneration from the splitting of water.

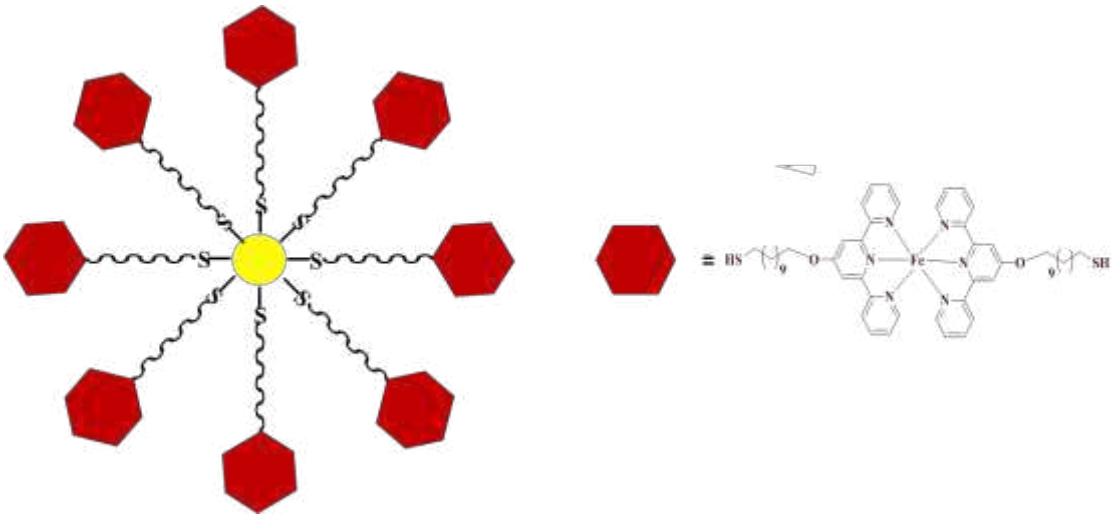

Figure 1-30. Schematic representation of Au NPs Fe(II) *tpy* assembly. Adapted from ref. **248.**

Au NPs assemblies have attracted interest in the medical field because they are inert, biocompatible, and easily prepared and functionalized. Because NPs can reach solid tumors via the enhanced permeability and retention (EPR) effect, their specificity for tumor tissues could significantly be improved. The release kinetics of drug molecules from NPs can be controlled by internal and external stimuli. NP-based delivery possesses many advantages, such as enhanced drug accumulation and sustained drug release in tumor tissues. Hence, the conjugation of common platinum complexes with NPs in order to obtain smart materials has prompted interest for biomedical applications.[249]

Au NPs coated with poly(ethylene glycol) (PEG) conjugated with *cis*-platin and oxaliplatin have been synthesized and presented results comparable or significantly higher cytotoxicity comparted to nontargeted *cis*-platin or oxaliplatin. Also, carboplatin[250] conjugated onto Au NPs containing cetuximab, an FDA approved antibody, has been tested for the treatment of different types cancers, such as colorectal, lung, pancreatic, and ovarian cancers. The results showed that this nanoconjugate presented an enhanced therapeutic efficacy toward both lung and ovarian cancer cell lines compared with its nontargeted counterpart.

A special interest has been granted towards obtaining Au NPs conjugated with different metal complexes, which are less toxic and less expensive, such as Zn(II).

The group of Nyokong[251] have reported the coordination of Zn(II) phthalocyanine to Au NPs nanoparticles. The authors noticed an improvement in the photophysicochemical behaviour and antimicrobial activity against *B. subtilis* of Zn(II) complex in the presence of Au NPs. Also Au NPs (nanospheres and nanorods) conjugated with a Zn(II) phtalocyanine derivative

were reported for their potential application as as photosensitizers in photodynamic therapy (PDT) by Dube *et al.*[252]

Recently, oligopyridines conjugated Au NPs have been reported as potential agents for bioimaging application. Sun *et al.*[253] synthesized Au NPs functionalized with a Zn(II) *tpy* complex which could be used to target mitochondria under two-photon laser confocal microscopy. Moreover, due to laser induced coagulation, fragmentation and dissolution of metal nanoparticles, the authors concluded that this assembly could penetrate into living cells and stained with mitochondria, and could be used in optical device and bio-imaging.

Therefore, based on their unique properties and multiple surface functionalities, conjugated Au NPs can be successfully employed as biomaterials for the investigation of biological systems. In diagnostics, the binding event between the analytes and the Au NPs can alter the physicochemical properties of Au NPs such as SPR, conductivity, and redox behavior, leading to detectable signals. Au NPs also serve as practical platforms for therapeutic agents, with their high surface area allowing a dense presentation of multifunctional moieties (e.g., drugs and targeting agents).[233]

1.4. Dendrimers

Dendrimers are regularly and hierarchically branched synthetic macromolecules exhibiting a tree-like nanometer sized architecture, first derived by the “cascade molecule” approach. They are known to possess low polydispersity (ideally monodisperse), nearly spherical topology, internal void regions for hostguest chemistry, and unique tailorable surface characteristics.[254, 255] The term dendrimer refers to its characteristic appearance and it derives from the Greek words dendron (tree) and meros (part). They were first synthesized by Fritz Vögtle in 1978, but it was not until 1990s that they began to be appreciated for their true application potentials.[256]

Synthesis

Dendrimers are constructed in cyclic stages using repetitive synthetic strategies, following either a divergent or a convergent mode.[257]

The divergent synthetic approach is characterized by the fact that branching units are attached to the core molecule, thus multiplying the number of peripheral groups at each new step, creating a highly branched structure as the growth is pursued. Using the divergent

approach, it is possible to prepare up to ten generations of dendrimers.[258] As mentioned above, in 1978 Vogtle and co-workers[259] reported the first ''cascade-like'' synthesis of branched acyclic, branched polyamines, synthesized by the divergent approach. A schematical representation of the divergent method is given in **Figure 1-31**.[260]

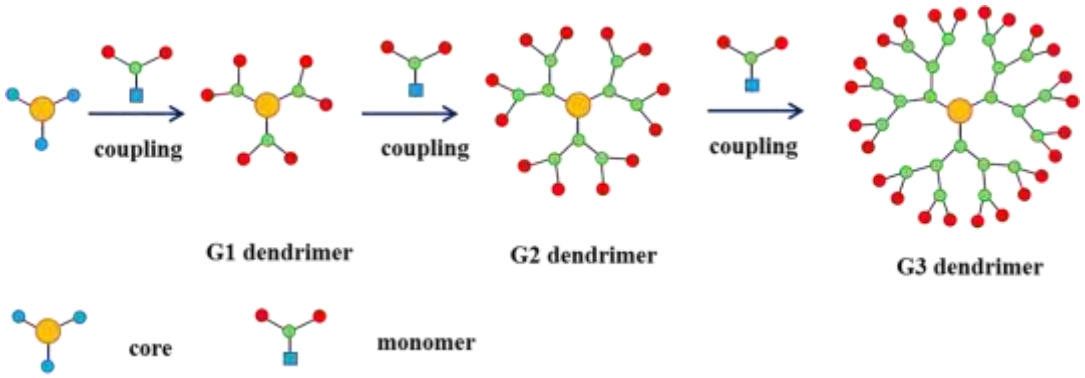

Figure 1-31. Schematic representation of the synthesis of dendrimers by the divergent method. Adapted from ref. **260**.

The convergent method, first reported by Hawker and Frechet,[261] is an alternative route to constructing dendrimers. This method implies that the skeleton is built up from the end groups to the inside ones, then finally reacting them with the core molecule yielding the desired dendrimer. Using this method they prepared monodisperse poly(aryl ether) dendrimers, based on 3,5-dihydroxybenzyl alcohol as the monomer unit. A schematical representation of the divergent method is given in **Figure 1-32**.[260]

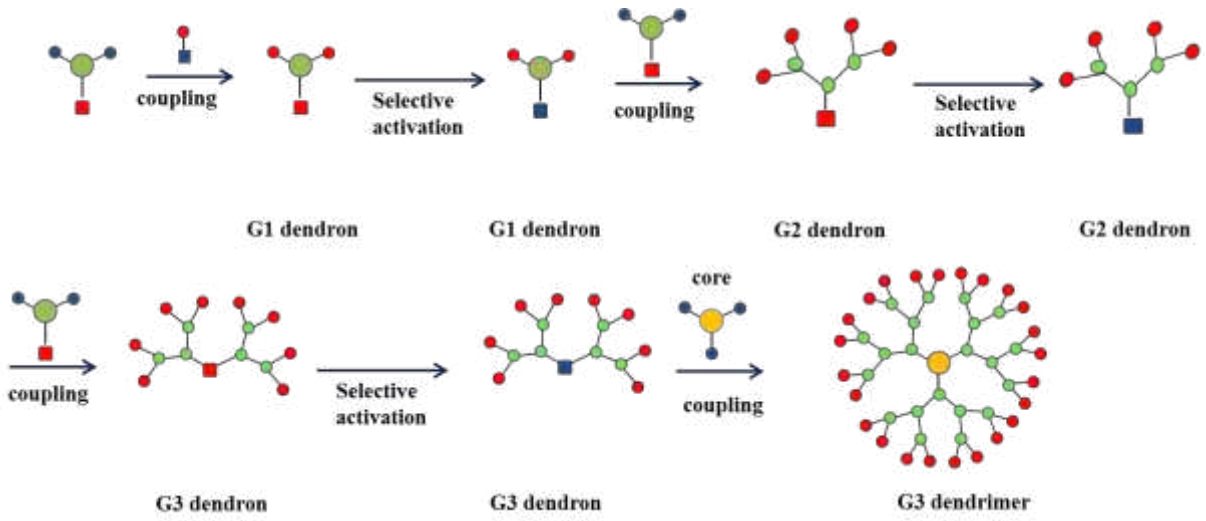

Figure 1-32. Schematic representation of the synthesis of dendrimers by the convergent method. Adapted from ref. **260.**

Overall, the convergent approach is preferred since it allows greater control over the process, with a reduced consumption of the reagents, yielding dendrimers with higher purity and without structural defects.

By linking together dendrons with different molecular composition and/or generation, different morphologies and/ or special physical and chemical properties may be induced in the final dendrimer.[260] The largest group of this class are constructed from two dendrons whose terminal functionalities have different nature, known as ‘‘Janus dendrimers”.

Many different and very performing synthetic methods have since been developed, rendering the field very accessible for potentially applicative purposes, like medical or technological. The accelerated methods for the synthesis of dendrimers (e.g: double-stage convergent method, hypermonomer method, double-exponential method, orthogonal coupling method, the click chemistry concept, multicomponent reaction, etc.)[260] represent further optimization of the combination of convergent–divergent methods and facilitate a high degree of structure control of multifunctional dendritic peripheries. The application of versatile click methodology is seen as a green-alternative in the synthesis of dendrimers and their conjugates. The multicomponent reaction methodology is a great synthethic pathway, which accelerates the synthesis of dendrimers and allows a well-controll of topology and composition.[260]

Functionalization and properties

The special chemical and physical properties possessed by dendrimers, and the possibility to be functionalized in predetermined sites of their structures (centre, nodes, branches, periphery, cavities), have directed researcher’s attention to use dendrimers in biomedical applications, such as targeted drug carrier systems, photodynamic and photothermal therapies and imaging.[254]

The introduction of chelating units in the dendritic framework, allows the incorporation of a wide variety of metallic fragments, leading to the formation of metallodendrimers. In this way, the properties of dendrimers (conformational flexibility, nano-scale dimensions, architectural diversity, etc) are augmented with the specific properties of metal complexes (absorption of visible light, luminescence, redox, magnetic, radioactive, etc.), which can be controlled through generation growth, compartmentalization and topology of the dendrimeric structure.[262]

From a structural point of view, metal-containing dendrimers can be synthesized in many different ways, leading to a wide range of possible structures. Indeed, the metallic

residues can be integrated into various parts of the dendritic architecture (i.e. at the nodal core, the branching points, as hosts in the cavities, at the periphery, or at all or some of the singularities), and according to different modes increasing furthermore their molecular complexity (**Figure 1-33**) etc.[262]

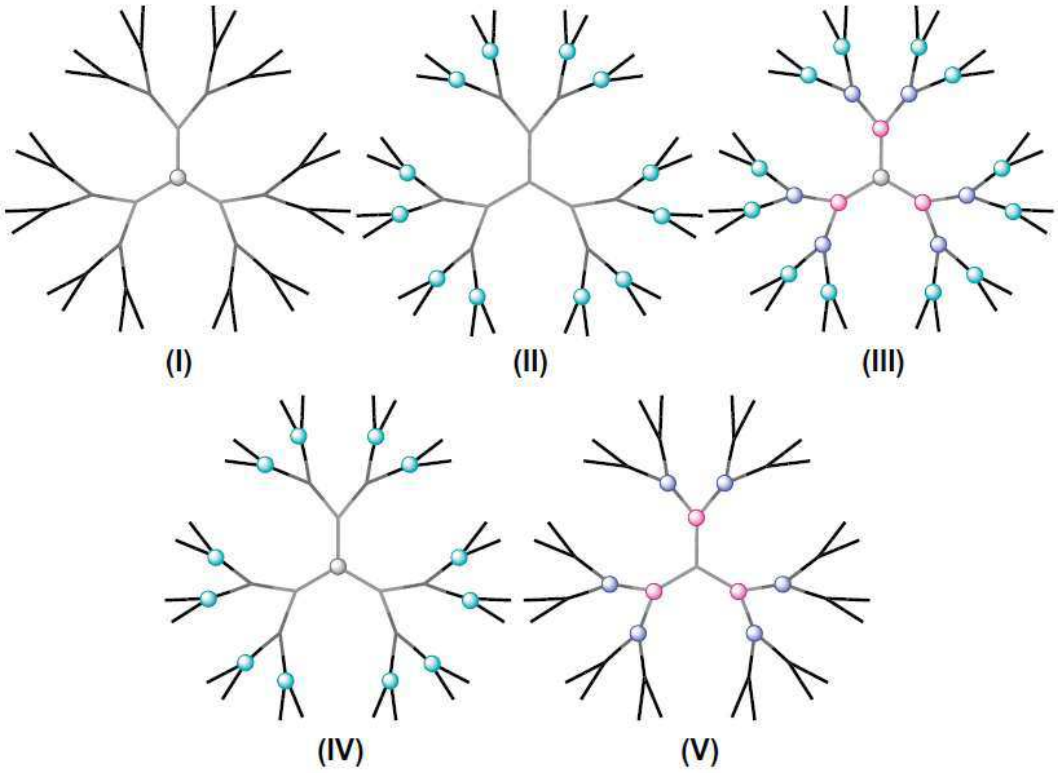

Figure 1-33. Schematic representations and classification of selected symmetrical structures of metallodendrimers, with emphasis of the different metallic ion fragments locations within the dendritic frame: at the center (I), at the periphery (II), at all junctions (III), or at specific generations (IV and V). From ref. **262**.

Terpyridine based metallodendrimers

For this purpose, oligopyridines (*bpy*, *tpy*, *phen*, etc.) represent some particularly attractive ligands to generate building blocks for the preparation of supramolecular structures, since they can easily form well-defined chelate complexes with a wide variety of metals. Among the most researched systems are those which contain Ru(II) as metal residue. Following some representative examples of *tpy* metallodendrimers are listed.

The first dendrimer was assembled via bis-*tpy*-Ru(II), $[Ru(tpy)_2]^{2+}$, connectivity when Newkome *et al.*[263] used 4′-chloro-*tpy* in the construction process, to form appropriate dendrons with crucially located terpyridine moieties (**Figure 1-34**).

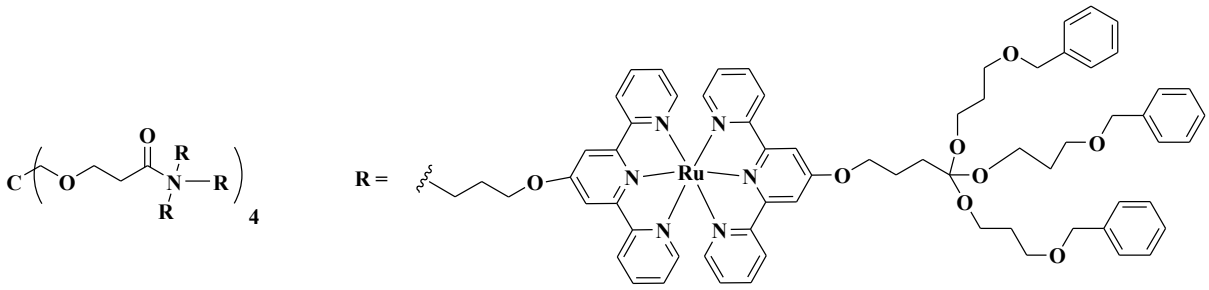

(118)

Figure 1-34. A metallodendritic superstructure obtained via the metal-centered assembly process. Adapted from ref. **263**.

Marvaud and Astruc[264] reported aromatic stars containing hexa-*tpy* branches with or without the central ferrocene group and coordinated to Ru(II) polypyridine moities to construct hexa-*tpy* complexes (**Figure 1-35**), as redox-active metallodendrimers for molecular recognition and electronics and polyelectronic redox catalysis.

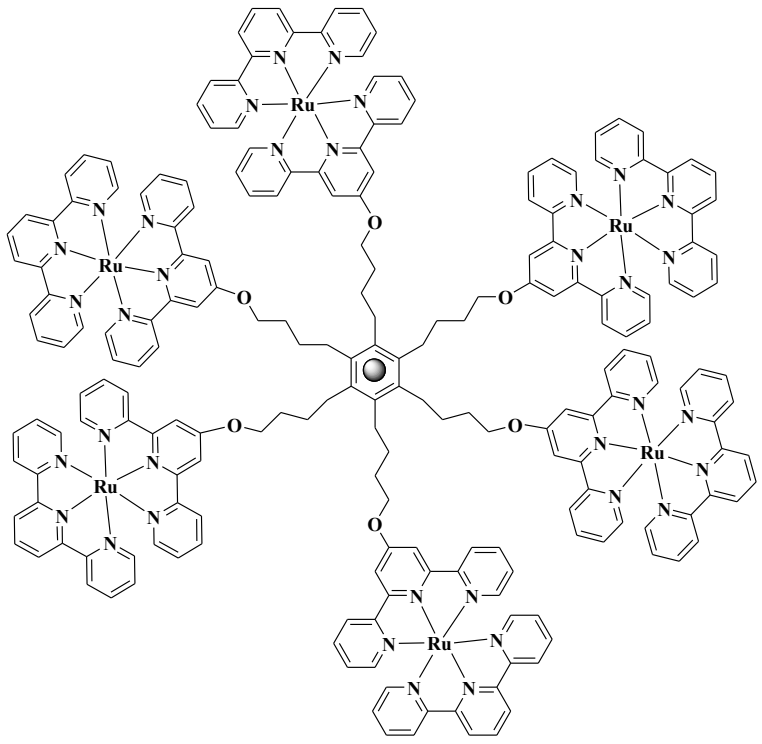

(119)

Figure 1-35. Aromatic stars containing hexa-*tpy* branches coordinated to Ru(II) groups with a ferrocene group as a central unit. Adapted from ref. **264**.

Several homo- and heteroleptic dendrimers based on benzyl ether fragments with a $[Ru(tpy)_2]^{2+}$ connectivity were reported by Chow *et al.*[265] (**Figure 1-36**).

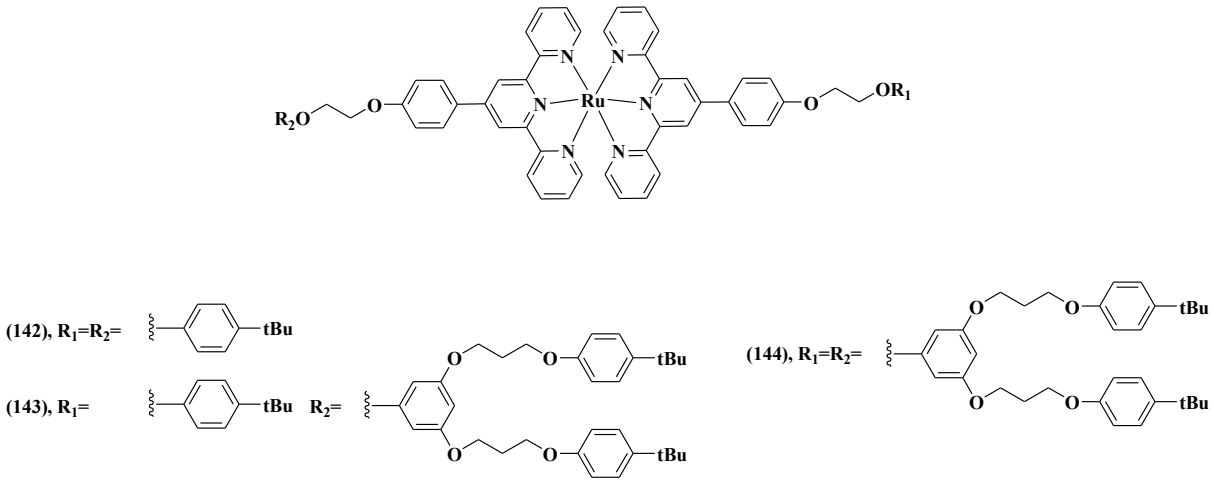

Figure 1-36. Structures of homo- and heteroleptic benzyl ether Ru(II) *tpy* dendrimers. Adapted from ref. **265.**

The design of metallodendrimers bearing *tpy* derivatives, permits the extension of the coordination chemistry area, from the molecular to the supramolecular level. In the quest for new functional materials, supramolecular metallodendrimers have played an ever-increasing role.[266]

On this background, the design and synthesis of hybrid nanostructures containing Au NPs and TMCs linked by dendritic structures will result in the obtaining advanced materials for theranostic purposes. The properties of the materials will be controlled by generation growth, aiming to take advantage of the SPR phenomena of the Au NP core.

In the quest for new functional materials, supramolecular metallodendrimers, micelles, and resins have played an ever-increasing role. In particular, metal-containing dendrimers are of interest because of their potential use as catalysts or molecular carriers for catalysts and light-harvesting arrays.[267]

Original contributions

Chapter 2. Zn(II) and Cu(I) complexes with bidentate N^N

The objective of the thesis was the synthesis and characterization of luminescent transition metal complexes (TMCs) where the metal centre acts as a carrier of biological active ligands, which may be good alternatives to *cis*-platin by offering unique properties such as higher cytotoxicity, antitumor activities and lower side effects in cancer therapy.

Despite active research and great advances in this domain, the synthesis of new luminescent TMCs with biological properties remains a very challenging approach. With this in mind the following oligopyridines: 2,2'-bipyridine (*bpy,* ligand **L1**), 1,10-phenanthroline (*phen,* ligand **L2**), 2,2'-biquinoline (*bq,* ligand **L4 – L6**) derivatives and quercetin·$2H_2O$ (ligand **L3**), schematically represented in **Figure 2-1**, were used in the synthesis of Zn(II) and Cu(I) complexes.

The planar structures of the N-donor ligands (*bpy, phen* and *bq*) makes them good DNA intercalators,[37,277] whereas *quercetin* is an O^O-bioactive luminescent ligand, which is known to be a potent antioxidant, primarily used to reduce oxidative stress. Also, it is a good free radical scavenger and a metal chelator.[278] Moreover, studies have shown that through chelation, the properties of quercetin (*e.g.* antioxidant activity, DNA protection, antitumor and anticarcinogenic activity) are enhanced.[279,280,281] Therefore, the synthesis of Zn(II) complexes with the biologically active chelating ligands *phen* or *bpy* and antioxidant properties of the O^O-donor like quercetin are of current interest.

The quinoline ring is highly researched in the development of bioactive molecules, with antibacterial, antidepressant, antiviral, anticancer, and anti-inflammatory activities.[282] The insufficient solubility in water of the final complexes can affect the bioavailability of the drugs.[283] Therefore, the *bq* ligand with hydrophilic moieties (ligand **L4**) was further taken into consideration for the synthesis of Zn(II) complexes. Furthermore, *bq* derivatives **L5** and **L6**, containing long alkyl chains were taken into consideration in the synthesis of Cu(I) complexes.

Upon coordination to metals, luminescent TMCs may be obtained, which will make them potential candidates as bioimaging agents or as photosensitizers for photodynamic therapy (PDT), etc.[38,284] Moreover, by combining the therapeutic and luminescence properties, may lead to dual-functional materials, which may be applied as theranostic (therapeutic and diagnostic) agents. With the continuous advancement of modern healthcare, the theranostic agents are seen as future tools in the development of precise and personalized medicine.[285]

Ligands **L1**, **L2**, **L3** presented in **Figure 2-1** were commercially available, whereas the synthesis of *bq* derivatives **L4**, **L5** and **L6** is described henceforward.

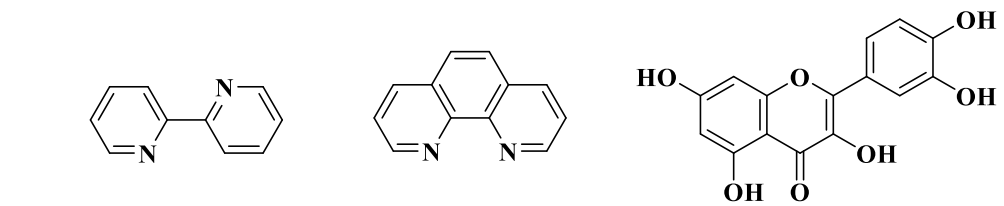

2-(pyridin-2-yl)pyridine

L1

1,10-phenanthroline

L2

quercetin

L3

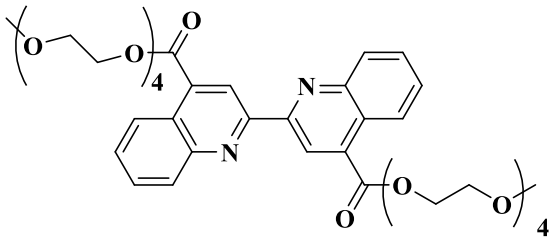

2-(2-(2-(2-methoxyethoxy)ethoxy)ethoxy)ethyl 2-(4-((2-(2-(2-(2-methoxyethoxy)ethoxy)ethoxy)ethoxy)carbonyl)quinolin-2-yl)quinoline-4-carboxylate

L4

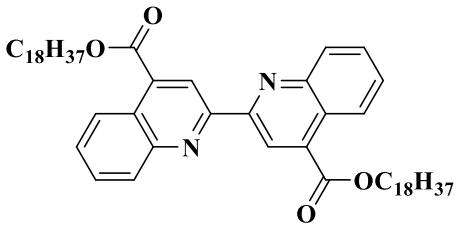

octadecyl 2-(4-((octadecyloxy)carbonyl)quinolin-2-yl)quinoline-4-carboxylate

L5

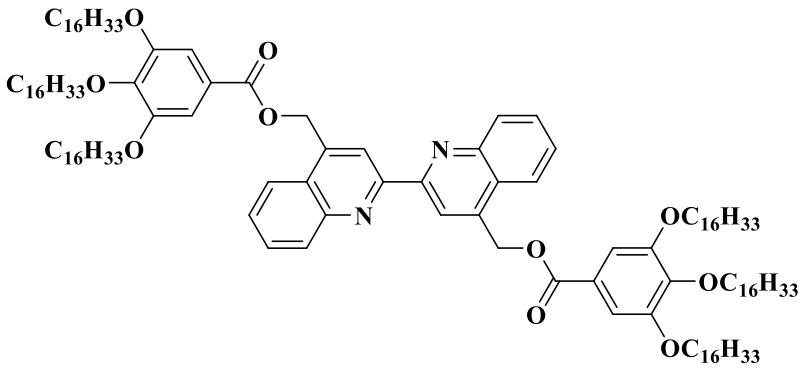

4,4'-bis[3,4,5-tri(hexadecyloxy)benzoyloxymethyl)]-2,2'-biquinoline

L6

Figure 2-1. Schematic representation of oligopyridines derivatives and quercetin used as ligands in this chapter.

2.1 Synthesis and characterization of the ligands L4 – L6

The three *bq* derivatives (**L4**, **L5** and **L6**) were synthesized as shown in **Scheme 2-1** and **Scheme 2-2**. Ligands **L5** and **L6** were prepared according to reported literature.[286,287] Following the same synthetic strategy,[286] **L4** was obtained as a new compound and was reported here.[288] In particular, for the synthesis of *bq* derivatives **L4** and **L5**, **I1** was reacted with the

corresponding alcohol: tetraethyleneglycol monomethyl ether for **L4**, and n-octadecanol for **L5**, as shown in **Scheme 2-1**. Ligand **L6** was synthesized as described in **Scheme 2-2**, using the Steglich esterification method, which involves the reaction between 4,4'-bis(hydroxymethyl)-2,2'-biquinoline and **I2**, using N,N'-dicyclohexylcarbodiimide (DCC) as coupling reagent and 4-dimethylaminopyridine (DMAP) as a catalyst.

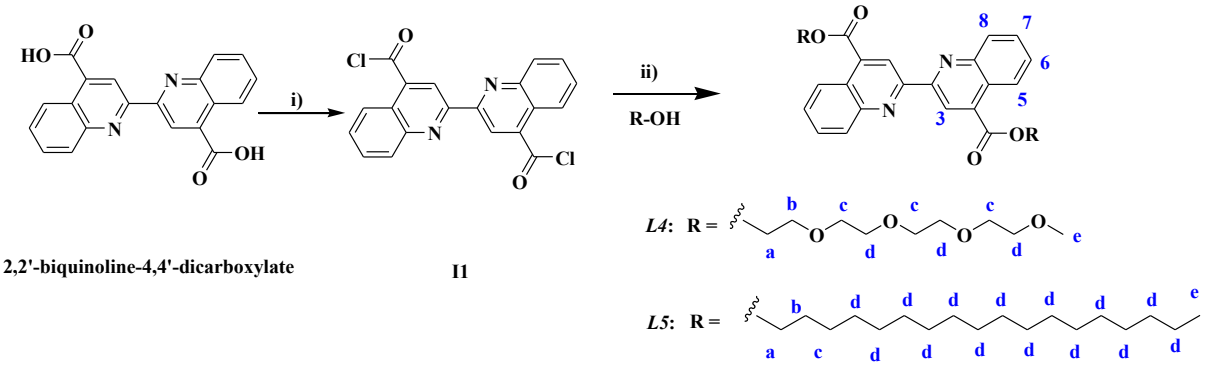

2,2'-biquinoline-4,4'-dicarboxylate **I1**

Scheme 2-1. Reaction pathway of ligand **L4** and **L5** and their atom labelling (blue). Reagents and conditions: i) $SOCl_2$, ΔT, overnight; ii) toluene, ΔT, 24h.

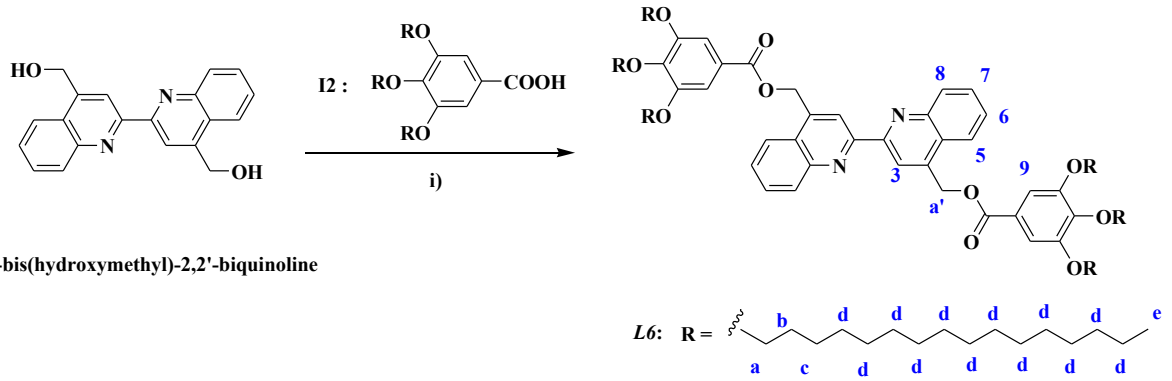

4,4'-bis(hydroxymethyl)-2,2'-biquinoline

Scheme 2-2. Reaction pathway of ligand **L6** and atom labelling (blue). Reagents and conditions: i) DCC, DMAP, THF, Ar, 4 days.

L4 ligand was purified by column chromatography, whereas **L5** and **L6** were isolated by recrystallisation from $CHCl_3$/MeOH. The ligands were isolated as waxy white solids. The nature of **L4** ligand was confirmed by elemental analysis and the chemical structures were proved by FT-IR and ^{1}H-NMR spectroscopies. Ligands **L5** and **L6** were also characterized by FT-IR and ^{1}H-NMR spectroscopies.

FT-IR spectroscopy

FT-IR spectroscopy was used to gain information regarding the functional groups present in the molecules of the ligands, which give rise to characteristic bands both in terms of intensity and position (frequency). The FT-IR of the *bq* ligands presents the characteristic absorption bands of $\nu_{C=N}$ and $\nu_{C=C}$ modes between 1605 – 1435 cm^{-1}.[289] The presence of the aliphatic chains is evidenced by the absorption bands for $\nu_{as,(CH_3)}$ around 2920 and around 2850 cm^{-1} for $\nu_{as(CH_2)}$.[290] Also the absorption bands characteristic for the carboxylate unit can be evidenced at *ca.* 1720 cm^{-1} for $\nu_{C=O}$, and around 1150, 1050 for $\nu_{as(C-O-C)}$ and $\nu_{s(C-O-C)}$, respectively.[291] The FT-IR assignments of the characteristic bands are summarized in **Table 2-1**.

Table 2-1. Assignment of the characteristic absorption bands of ligands **L4**, **L5** and **L6** (wavenumber values in cm^{-1})

Compound	Assignment of the characteristic absorption bands (wavenumber values in cm^{-1})					
	$\nu_{as,(CH_3)}$	$\nu_{as,(-CH_2-)}$	$\nu_{as,(COO^-)}$	$\upsilon_{C=C}$, $\upsilon_{C=N}$	$\nu_{as,(C-O-C)}$	$\nu_{s,(C-O-C)}$
L4	2922	2876	1719	1588 - 1459	1153	1040
L5	2921	2849	1719	1586 - 1472	1152	
L6	2920	2844	1713	1604 - 1435	1151	1053

^{1}H-NMR measurements

In order to determine the purity and to obtain information regarding the molecular structure of ligands **L4**, **L5** and **L6**, ^{1}H-NMR spectra were recorded. The chemical shifts of the *bq* ligands are summarized in **Table 2-2**. The labelling of the atoms of the structures can be seen in **Scheme 2-1**. Based on the obtained results, and on literature data reported for similar compounds,[286,292] the chemical shifts indicate that the esterification reactions took place and we obtained the desired compounds.

Table 2-2. Chemical shifts (in δ/ppm) of ligands **L4**, **L5** and **L6**, recorded in $CDCl_3$.

	Chemical shifts (in δ/ppm)		
	L4	**L5**	**L6**
H^3	9.33	9.31	9.24
H^5	8.79	8.79	8.60
H^6	7.70	7.70	7.75
H^7	7.83	7.82	7.89
H^8	8.32	8.32	8.19
H^9			7.40
$H^{a'}$			6.02
H^a	4.69	4.53	4.03
H^b	3.98	1.85	1.79
H^{c-d}	3.85 - 3.45*	1.72 – 1.1	1.65 – 1.16*
H^e	3.34	0.87	0.90
* overlapped peaks			

Absorption and emission spectroscopy of bq ligands

Absorption and emission spectra of **L4** are shown in **Figure 2-2**. The *absorption spectrum* of **L4** recorded at room temperature in ethanol solution consists in two bands centred at 279 nm ($\varepsilon = 31500\ M^{-1}\cdot cm^{-1}$) and 340 nm ($\varepsilon = 15550\ M^{-1}\cdot cm^{-1}$) respectively, originating from π–π* transitions on the aromatic rings of the 2,2'-biquinoline.[286] The ligand presents an emission centred at 422 nm in the violet region, derived from the deactivation of intraligand charge-transfer (ILCT) excited state.[286]

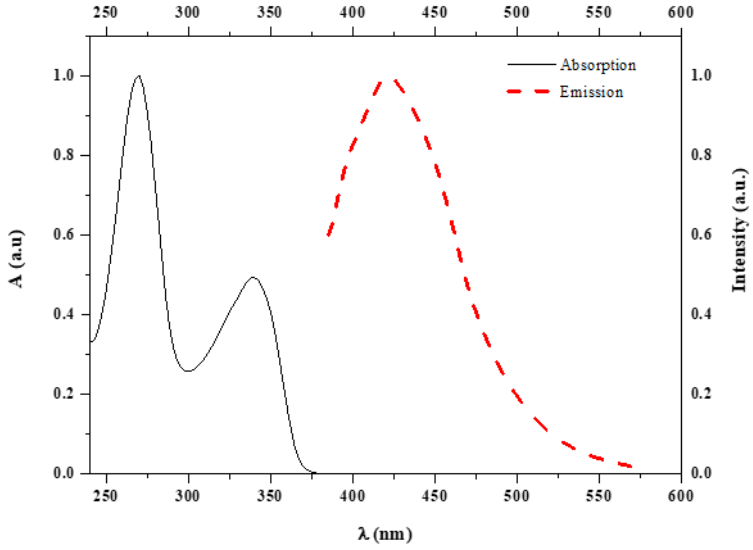

Figure 2-2. Absorption and emission spectra of **L4** in EtOH solution.

The absorption and emission properties of both ligands **L5** and **L6** were published earlier.[286] However, for a clearer view, they are presented herein. The spectra were recorded in dichloromethane solutions and are presented in **Figure 2-3**. The **L5** absorption spectrum shows two principal bands, both originated from π–π* transitions on 2,2'-biquinoline aromatic rings: an intense band at 270 nm, deriving from an excitation on the pyridyl ring, and a band at 340 nm (with a series of vibronic components), due to an ILCT from the pyridyl to the phenyl ring of the quinoline unit.[286] The **L6** absorption spectrum shows bands, which were assigned to the same transitions as those described for **L5**, but slightly blue-shifted. A new band is observed at 300 nm and is assigned to π–π* transitions localized on the trihexadecyloxybenzoyl substituent. In both ligands, beyond 360 nm a very weak band is detected, due to n-π* excitation on carbonyl group. The ligands emit in the spectral blue range as seen in **Figure 2-4**, showing a band centred at 385 nm (**L5**) and at 403 nm (**L6**), deriving from deactivation of the ILCT excited state.

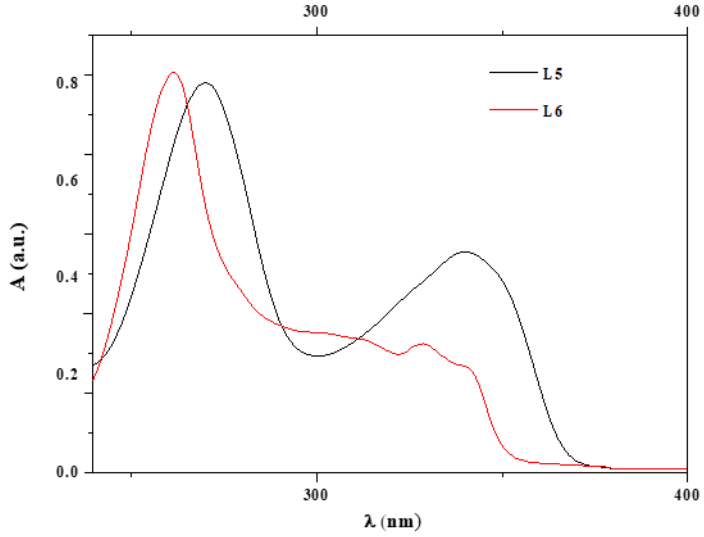

Figure 2-3. Absorption spectra of **L5** and **L6** in CH_2Cl_2 solution.

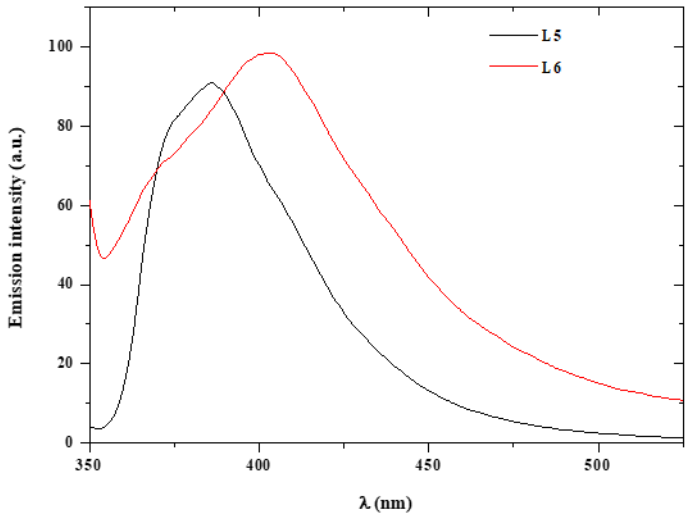

Figure 2-4. Emission spectra of **L5** and **L6** in CH_2Cl_2 solution.

2.2 Synthesis and characterization of Zn(II) complexes

Zn(II) is a bio-metallic ion whose versatile chemistry allows to easily synthesize complexes with luminescent and biologically active ligands, in order to obtain efficient metallodrugs and at the same time to stabilize the excited states yielding good emitters. For a compound to be used in biological systems it should have a certain solubility in water or water-DMSO mixtures, commonly used as drug vehicles to carry an active biological agent to the site of its action.[293] For this purpose two types of Zn(II) complexes were obtained: complexes with *bpy* or *phen* with *quercetin* as co-ligand and the second type with a *bq* derivative ligand (**L4**), containing tetraethylene glycol monomethyl ether as soluble moieties.

2.2.1 Zn(II) complexes with bpy or phen ligands and quercetin as co-ligand

The new **C3** and **C4** Zn(II) heteroleptic complexes containing *bpy* or *phen* and *quercetin* were synthesized as shown in **Scheme 2-3** and were reported in reference **288**.

Due to the high sensitivity of Zn(II) complexes with *quercetin* **L3** towards oxygen, the synthesis and certain characterization methods were performed under inert atmosphere. The experimental conductivity values measured on 10^{-3} mol/L degassed solutions in DMSO at room temperature, falling in the range for non-electrolytes. The proposed structure is pentacoordinated, with a monodentate chlorine ligand filling the fifth position.

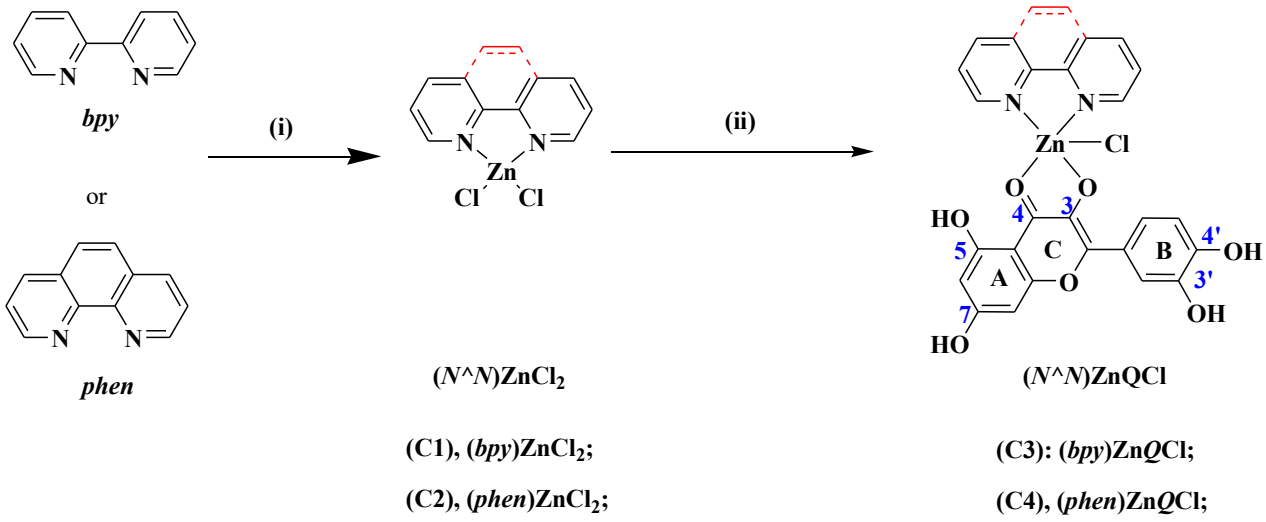

Scheme 2-3. Reaction pathway of C**1** – **C4** complexes. Reagents and conditions: (i) H_2O/EtOH, r.t., 4h; (ii) NEt_3, Ar, H_2O/EtOH, r.t., 10 min.

The synthesis of the complexes **C3** and **C4** presented in experimemental chapter occurs in two steps as depicted in **Scheme 2-3**. In the first step, precursor metal complexes **C1** and **C2** with *bpy* or *phen* ligands, with the general formula (*N*^*N*)$ZnCl_2$, were synthesized as previously reported.[289] The second step was carried out under argon atmosphere and it implied a ligand exchange reaction between the chlorine ligands and ligand **L3**, yielding **C3** and **C4** complexes in high yields (84-94%). The solid powders can be stored under argon atmosphere, without change in their composition for several weeks. Due to their low solubility (DMSO and DMF $<10^{-3}$ mol/L), not as expected, a reliable ^{1}H-NMR analysis could not be performed. Furthermore, suitable monocrystals could not be obtained for X-ray diffraction studies. In oxygen-saturated solution the **C3** and **C4** heteroleptic complexes rapidly undergo oxidation and/or decomposition. However, in degassed DMSO solution the complexes are stable for a few hours. The high sensitivity to oxygen is one of the most important properties of flavonols, strongly related to their antioxidant activity due to a direct trapping of reactive oxygen species mechanism.[294]

FT-IR spectroscopy

The FT-IR spectra of complexes shows the characteristic absorption bands of both the N^N ligands ν_{NC}, δ_{NCH} and Γ_{NCCH}[295,296] and quercetin, $\nu_{C=O,\ COH,\ COC}$.[297,298] **Figure 2-5** and **Figure 2-6** present the FT-IR spectra of **C3** and **C4** complexes, respectively, plotted against their precursors: quercetin, **C1** or **C2**. The shift of the stretching mode of $\nu_{C=O}$ with 20 cm^{-1},

suggests that the chelation of the quercetin occurs through the carbonyl oxygen and the 3-OH close hydroxyl group, more acidic than 5-OH.[298,299] The characteristic bands of the *N^N* ligands are shifted with respect to the (*N^N*)$ZnCl_2$ precursors, showing a different coordination environment. Moreover, for both heteroleptic complexes the broad absorption band between 3600 – 3000 cm^{-1} attributed to ν_{O-H} stretching mode attributed to ν_{O-H} suggest also the existence of water molecules for both heteroleptic complexes. The values of main characteristic bands are summarized in **Table 2-3**.

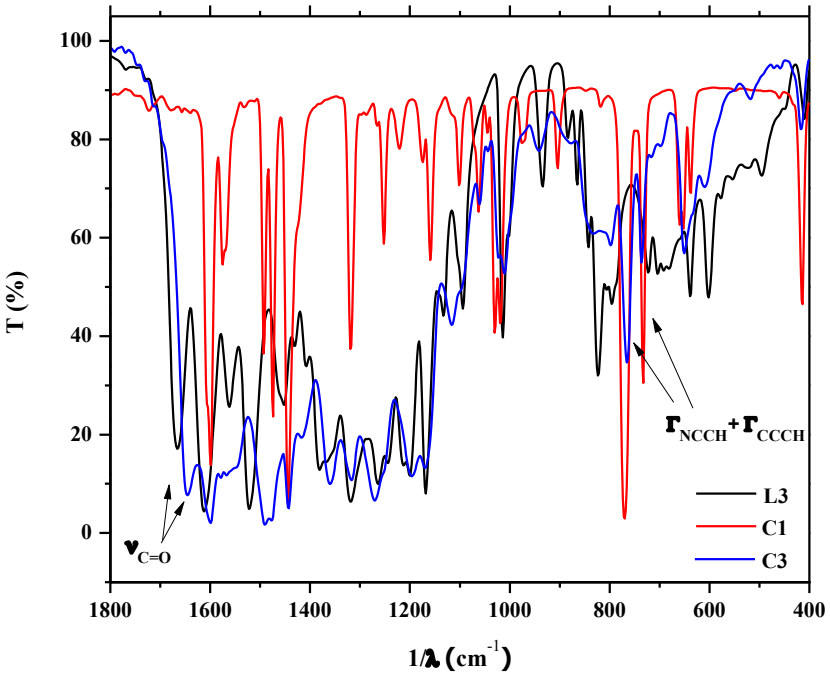

Figure 2-5. FT-IR spectra of complex **C3,** plotted against its precursors quercetin and **C1**.

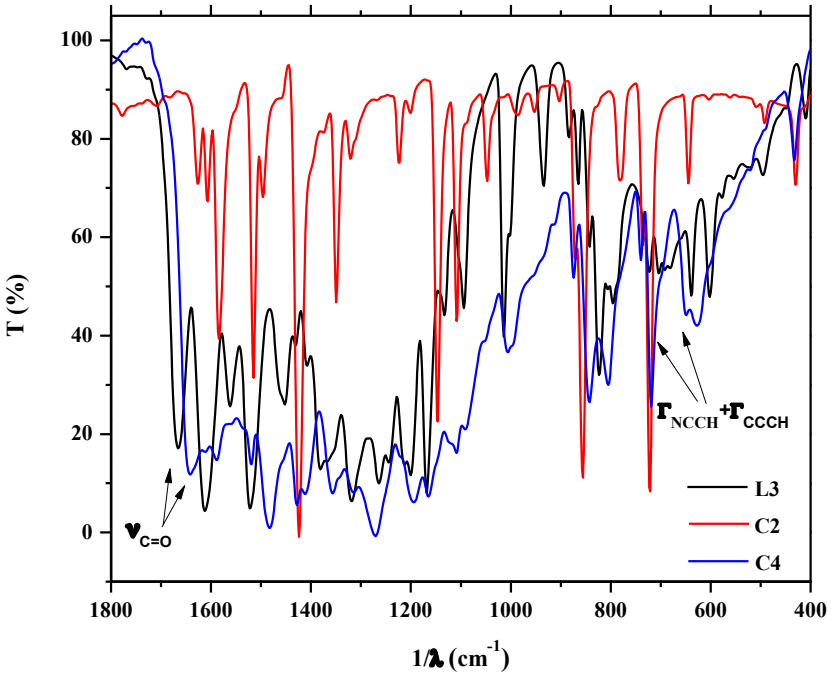

Figure 2-6. FT-IR spectra of complex **C4,** plotted against its precursors quercetin and **C2**.

Table 2-3. Assignment of the characteristic absorption bands of **C3** and **C4** (wavenumber values in cm^{-1}).

Assignment of the characteristic absorption bands (wavenumber values in cm^{-1})					
Compound	ν_{O-H}	$\nu_{C=O}$	$\upsilon_{C=C}$, $\upsilon_{C=N}$	ν_{COC}	$\Gamma_{NCCH}+\Gamma_{CCCH}$
C3	3433, 3076	1643	1600 - 1567	1269	764, 735
C4	3415, 3063	1645	1594 - 1518	1269	845, 726

Thermal analysis

In order to study the stability of the complexes thermal analysis was performed and compared with that of quercetin. The thermal stability of Zn(II) heteroleptic complexes, **C3** and **C4**, in solid state was tested in air-flow and the corresponding TGA and DTA curves are showed in **Figure 2-7**, plotted against quercetin. For both complexes, firstly, a dehydration process was observed between 30 and 150°C corresponding to the loss of 3 water molecules (**Table 2-4**). Afterwards, several decomposition-oxidation steps for the Zn(II) complexes accompanied by moderate exothermic effects occur between 220 – 500°C. The thermal stability of complexes drastically decreases with respect to free quercetin, the decomposition-oxidation processes starting at lower temperatures with about 110 – 115°C, explained by the catalytic oxidation on metal centres and the weakening of some ligand bonds by complexation. The experimental

mass of the residue corresponds to theoretical ZnO, calculated from the proposed stoichiometry (**Table 2-4**).

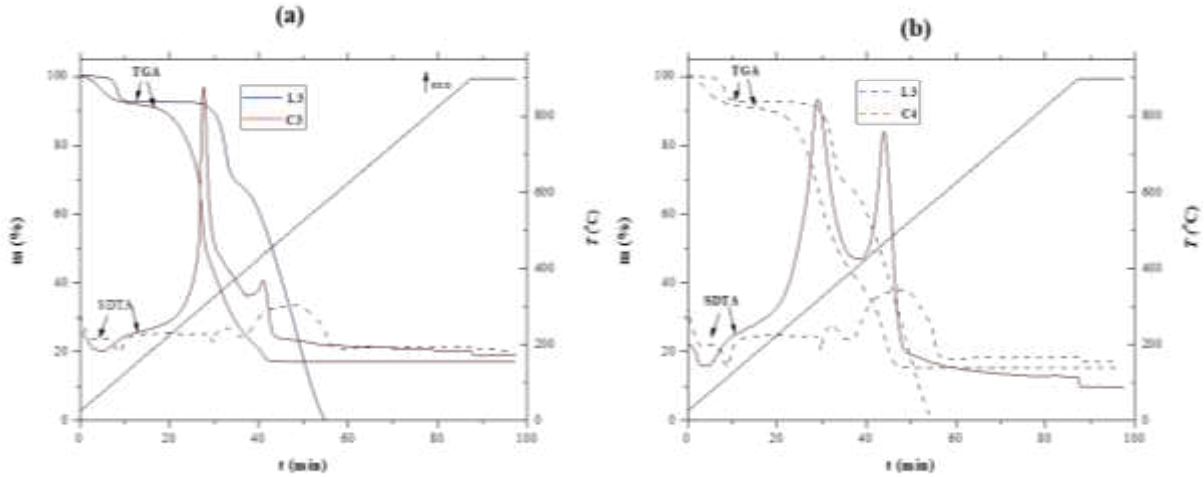

Figure 2-7. TGA and SDTA traces for: (a) complex **C3** and (b) complex **C4** plotted against the quercetin ligand.

Table 2-4. Thermogravimetric analysis results of **C3** and **C4**.

Compound	**Thermal process (onset peak/ °C)**	**Weight loss (%)**		**ZnO residue (%)**	
		Calc.	Found	Calc.	Found
C3	Weight loss: 3·H_2O (63.9)	8.37	8.82	13.65	13.29
C4	Weight loss: 3·H2O (70.3)	8.49	8.90	12.35	12.79

Absorption and emission spectroscopy

Electronic absorption spectroscopy gives information about the structure of the complexes, suggesting the type of metal oxygen bond formed between quercetin and Zn(II) metal centre, while along with emission studies, is used to investigate the type of interaction of the complexes with DNA. Therefore, the *absorption and emission spectra* of quercetin and both **C3** and **C4** complexes were recorded in DMSO deoxygenated solutions. The spectra are presented in **Figure 2-8** and the *absorption and emission* maxima are summarized in **Table 2-5**.

The *absorption spectra* of the complexes consist of the main absorption bands related to the π-π* transitions of the quercetin and the corresponding *N^N* ligands.[300] The large bathochromic shift corresponding to the band of the aromatic fragment of **L3** involved in coordination (cinnamoyl fragment) from 378 nm to 451 nm for complex **C3** and 480 nm for complex **C4** respectively, as shown in **Figure 2-8 (a)**, with the formation of the metal-oxygen bond in ring C (see **Scheme 2-3**) and the involvement of the 3-OH group in the chelation.

Therefore, based on literature data,[301] the large bathochromic shifts from the absorption spectra of complexes **C3** and **C4** revealed the chelation site of L3 ligand and it involved the carbonyl unit and the vicinal 3-OH group.

Quercetin emits in the visible region showing a structureless band centred at 496 nm in deaerated DMSO solution, while after coordination to the metal centre the emission maxima is red-shifted with respect to quercetin free ligand to 522 nm for complex **C3** and 508 nm for complex **C4** respectively as seen in **Figure 2-8 (b)**.

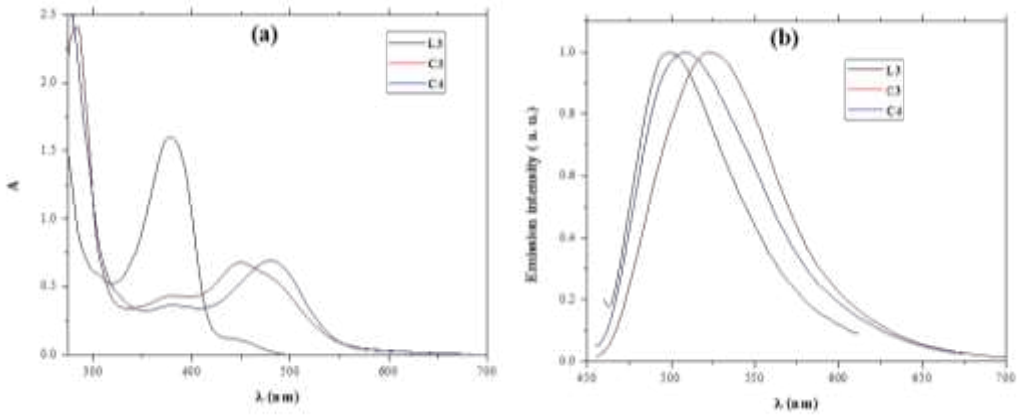

Figure 2-8. (a) Absorption and (b) emission spectra of **L3** ligand, **C3** and **C4** complexes in degassed DMSO solution (100 μM).

Table 2-5. Maximum absorption and emission data for **L3**, **C3** and **C4**.

Compound	Abs.[a], λ/nm (ε/L·mol^{-1}·cm^{-1})	Em.[b], λ/nm
L3	378 (16050)	496
C3	284(24100), 451 (6780)	522
C4	480 (6970)	508
[a]DMSO degassed solution, 100 μM; [b]DMSO degassed solution.		

The absorption spectra combined with the FT-IR analysis showed the specific electron donor of the flavonoid ligand involved in chelation, respectively it was demonstrated the involvement of the more acidic 3-OH and 4-oxo groups, while the 3', 4 and 5-hydroxyl groups are not involved. The luminescence properties of complexes **C3** and **C4** enables them for further biological studies, for example to investigate their interactions with DNA without the need of external luminescent agents.

Stability in solution by UV-Vis spectroscopy

One of the most important chemical properties of flavonols is the sensitivity to oxygen. Quercetin, belonging to flavonols class, readily oxidizes in water or ethanol solution close to the pH value of physiological media (~ 7.4). The mechanism involves oxidative decarboxylation, oxygen cleaving initially from the γ-pyrone fragment of the quercetin.[302] It was reported that the chemical stability of quercetin is influenced by a variety of factors (*e.g.* pH value, temperature, solvent and by presence of metal ions).[303] The oxidation reaction is considered as one of the main biotransformation routes of flavonols, catalyzed by presence of metal centres like Cu(II),[297,304] therefore we further studied the decomposition of ligand **L3** and of the **C3** and **C4** complexes in air equilibrated DMSO solution at a constant temperature of 30°C, by following the decrease of the cynammoil absorption band in time. No changes were detected for **L3** dissolved in DMSO solution recorded over 1 hour, in agreement with other reports in polar solvents.[297,304] However, for the **C3** and **C4** complexes, the intensity of the lower energy absorption band from 451 nm and 480 nm, respectively, gradually decays over time (Figure 2-10). Plotting the normalized absorbance intensity at 451 nm for **C3** and at 480 nm for **C4** *vs*. time, a smooth exponential curve is obtained as depicted in **Figure 2-9**, therefore the decomposition rate constants, listed in **Table 2-6**, were calculated assuming a first order kinetic.

The rate of a first-order reaction is directly proportional with the concentration of one of the reactants, the differential rate constant (k) being calculated using the exponential equation [**eq**.**1**].

$$[C] = [C]_0 \cdot e^{-k \cdot t} \text{ [eq. 1]}$$

where: $[C]$ – concentration at time t = 60 minutes, [mol/L];

$[C]_0$ - initial concentration at t = 0, [mol/L].

The concentrations were calculated on the basis of the absorbance intensities at λ = 451 nm for complex **C3** and 480 nm for **C4** respectively.

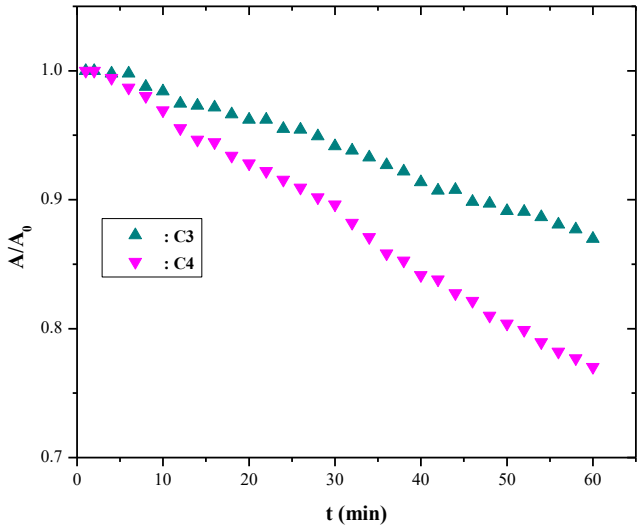

Figure 2-9. The curve of A/Ao vs time for **C3** and for **C4**.

Table 2-6. Decomposition rate constants of **C3** and **C4**.

Compound	$k \cdot 10^{-3}$, min^{-1}
C3	2.3
C4	4.3

The oxidation of the free quercetin ligand in ethanol- phosphate buffered saline solution (PBS) under physiological conditions takes place with the decrease of the absorption band centred at 380 nm and the formation of a new absorption band at *ca*. 330 nm attributed to the formation of a substituted benzofuranone structure.[304] The presence of this band was evidenced also during the study of decomposition process of Cu(II) analogues coordination complexes,[305] suggesting a similar oxidative mechanism. However, regarding complexes **C3** and **C4**, only a decrease in the absorption maxima of the cinnamoyl band is observed (**Figure 2-10**), probably due to a different oxidation mechanism. Comparatively, both Zn(II) complexes show a higher sensitivity to oxidation with respect to the free quercetin ligand in solution, while the presence of the *phen* co-ligand increases the decomposition rate constant of complex **C4** showing a higher sensitivity towards oxidation with respect to its *bpy*-based analogue **C3**.

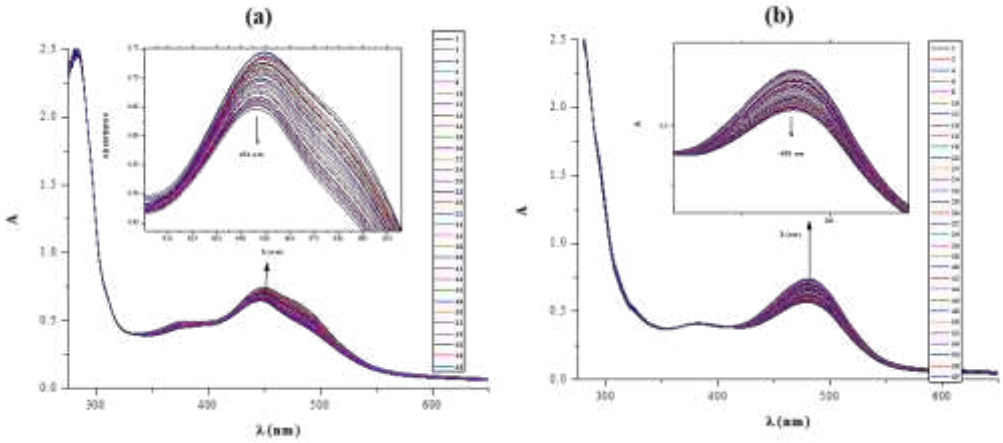

Figure 2-10. Absorption spectra of (a) **C3**, (b) **C4** in DMSO air saturated solutions (100 μM). Scan speed was set at 2 min intervals for 60 min; the arrows in the inset designate the evolution of the band.

Antioxidant activity

The antioxidant activity of quercetin (**L3**) plays an important role in the prevention and treatment of osteoporosis, cancer, tumours, cardiovascular diseases, etc. Additionally, recent studies have revealed that after coordination, the antioxidant capacity of quercetin is kept or even enhanced.[298] Therefore, the oxidation and coordination influence of quercetin in presence of the co-ligand (*bpy* or *phen*) and Zn(II) ion were investigated using the radical scavenging 2,2-diphenyl-1-picrylhydrazyl (DPPH$^{\bullet}$) method (see Experimental part). Briefly, a solution of **L3**, **C3** and **C4** in degassed DMSO of different concentrations was added a freshly prepared solution of DPPH in methanol.[306,307] The reduction of the DPPH was followed by monitoring the decrease in absorbance at 515 nm by UV–Vis spectroscopy.

The reaction between **L3**, **C3** and **C4** and DPPH occurred in two steps, as seen in **Figure 2-11**: (i) a fast decay of DPPH absorbance (between 60–120 s) and (ii) a slow decay of DPPH absorbance until it reached a constant value (∼1 h).

The fast step of 60 – 120s was corelated to the abstraction of the most labile H-atoms from the antioxidant. In the case of quercetin these are 3'-OH, 4'-OH and 3-OH (see **Scheme 2-3**).[308]

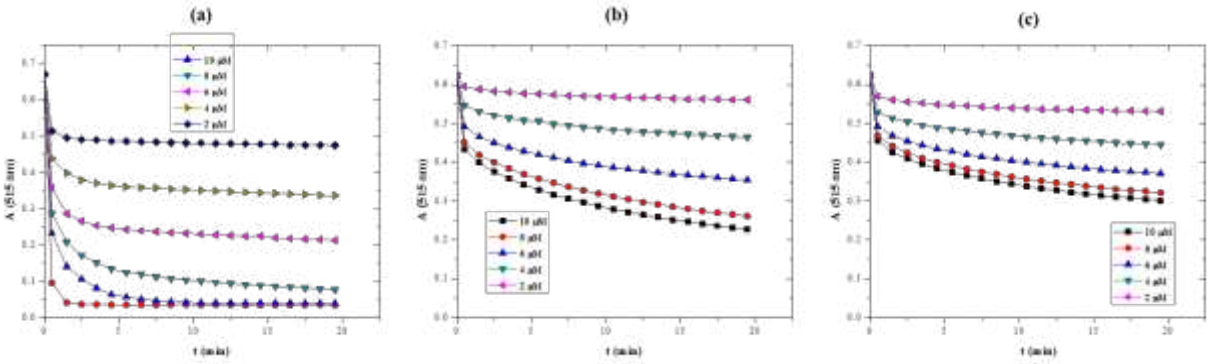

Figure 2-11. Decrease in absorbance of DPPH methanolic solution in presence of different concentration of: (a) quercetin, (b) **C3** and c) **C4** in DMSO solution.

The DPPH• scavenging activity of the **C3** and **C4** complexes are presented in **Figure 2-12** and in **Table 2-7**. The experimental value of IC_{50} of quercetin (4.94 μM) is higher than reported in literature (2.79 μM) and is related to the change of the experimental conditions. It can be concluded that **C3** and **C4** showed antioxidant activity comparable with those of the free **L3**. A possible mechanism for the antioxidant activity was proposed by de Souza *et al.*,[145] for homoleptic complexes of quercetin with Cu(II) centre which was chelated to the cathecol moiety, and the oxidation pathway was described via semiquinone radical intermediate. Herein, the antioxidant activity of the complexes is influenced by the different chelation site and the presence of the N^N chelating ligand.

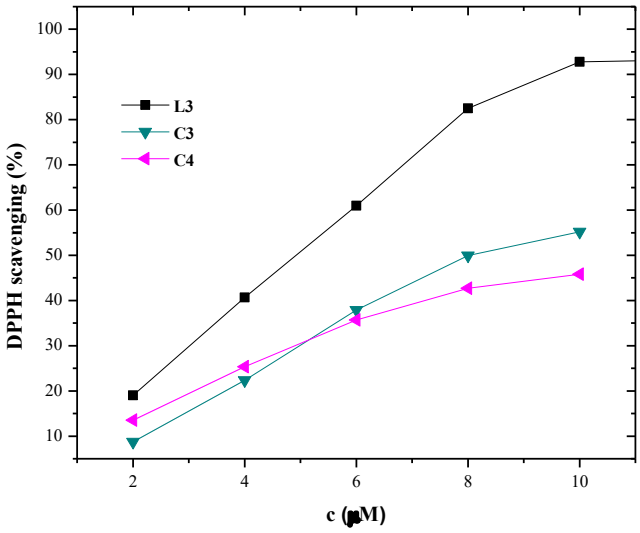

Figure 2-12. Scavenging activities evaluated through the absorbance decrease of **C3** and **C4**, plotted against **L3**.

Table 2-7. IC_{50} values of **L3**, **C3** and **C4**.

Compound	IC_{50}
L3	4.94 μM
C3	8.10 μM
C4	12.17 μM

Conclusions

Two new complexes, **C3** and **C4**, based on Zn(II) bio-metallic centre containing two biologically relevant chelating ligands - *N^N* (*bpy* or *phen*) and quercetin as O^O unit, and a monodentate chlorine ligand were synthesized and structurally characterized by analytical and spectroscopical methods. The FT-IR and UV spectroscopies revealed that quercetin coordinates through the carbonyl group and one of the two hydroxyl groups namely 3-OH or 5-OH from the vicinity of carbonyl.

Under aerobic conditions the complexes are oxygen-sensitive, resulting in the degradation of the complexes in several minutes after dissolution, and several hours in solid state. However, in solid state, the complexes can be kept without decomposition for several weeks under argon atmosphere. The higher oxygen sensitivity compared with the free quercetin was evidenced by TGA-DTA analysis in solid state and by UV-Vis absorption spectroscopy in DMSO solution. The high sensitivity to oxygen and the comparable scavenging activity of the heteroleptic complexes **C3** and **C4** show a good potential to be used for further investigations in biomedical fields.

2.2.2 Zn(II) complex with L4 bq ligand

In order to increase the solubility of Zn(II) complexes in protic solvents, the N^N ligand was functionalized with two hydrophilic chains. Therefore, the N^N-chelating biquinoline (*bq)* ligand, **L4** was complexed with $ZnCl_2$, yielding the new complex **C5** presented in **Scheme 2-4**. **C5** complex was published with ligand **L4** in reference **288**.

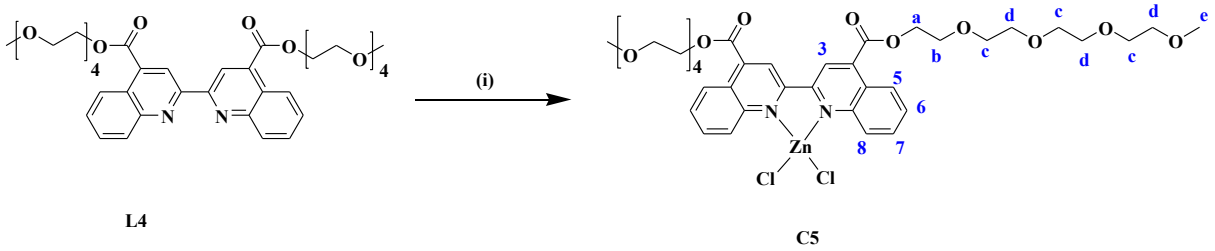

Scheme 2-4. Reaction pathway of **C5** and the atom labelling (blue). Reagents and conditions: (i) $ZnCl_2$, EtOH, r.t, 4h;

The synthesis of complex **C5** was performed – as described in the experimental chapter, following a procedure reported for similar *bq* derivatives.[207] In particular, the reaction between the ligand **L4** and a small excess of the corresponding zinc chloride yielded the desired product in 95% yield. The compound was characterized by elemental analysis, FT-IR and ^{1}H-NMR spectroscopies. The results of elemental analysis support the chemical nature and is in agreement with the proposed formula. The proposed structure it is also sustained by information further obtained from the FT-IR and ^{1}H-NMR spectroscopies.

FT-IR spectroscopy

The FT-IR spectra of **L4** and **C5** were recorded on KBR pellets and are presented in **Figure 2-13**. The comparative FT-IR spectroscopy was used to gain information regarding the shifts in the characteristic absorption bands of the functional groups after the coordination of Zn(II) salt to the ligand. The vibrational modes of the coordinated **L4**, in complex **C5** (**Figure 2-13**), are shifted upwards with respect to the free molecule, having a $\Delta = 14$ cm^{-1} for $\nu_{C=O}$ and a $\Delta = 7$ cm^{-1} for $\nu_{C=N}$, thus indicating the formation of complex **C5**.[289] The wavenumber values of the characteristic absorption bands are summarized in **Table 2-8**.

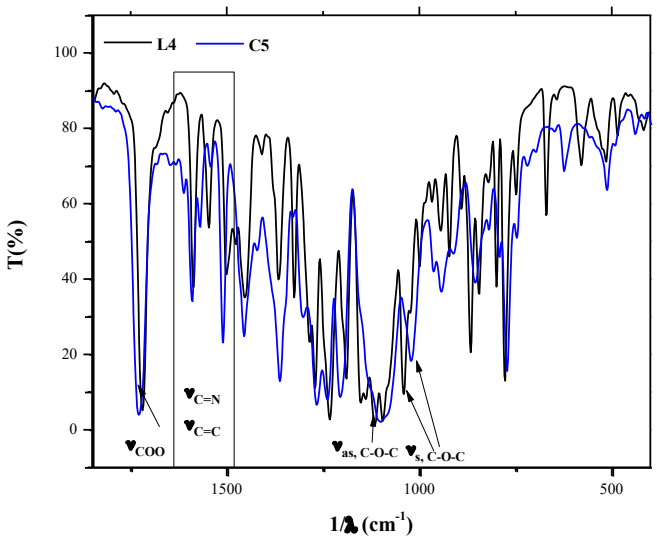

Figure 2-13. FT-IR spectra of complex **C5,** plotted against the free ligand **L4**.

Table 2-8. Assignment of the characteristic absorption bands of **L4** and **C5** (wavenumber values in cm^{-1})

Assignment of the characteristic absorption bands (wavenumber values in cm^{-1})					
Compound	$\nu_{as,(-CH_2-)}$	$\nu_{as,(COO^-)}$	$\nu_{(C=N \text{ and } C=C)}$	$\nu_{as,(C-O-C)}$	$\nu_{s,(C-O-C)}$
L4	2876	1719	1588 - 1459	1152 - 1095	1040
C5	2886	1736	1595 - 1462	1096	1026

^{1}H-NMR spectroscopy

In order to obtain information regarding the structure of **C5**, the NMR spectrum was considered. The spectrum was recorded on $CDCl_3$ solution and compared with that of the free **L4** as seen in **Figure 2-14**. Examination of the spectra of **L4** and Zn(II) complex confirms the formation of the complex by the shift of all aromatic protons (**Figure 2-14**).[309] The highest chemical shift could be observed in the case of H^8 and H^3 protons. Proton H^8 presented a downfield shift from 8.32 ppm to 8.83 ppm, whereas of protons H^3 were upfield shifted from 9.33 to 9.11 ppm with respect to the free ligand. **Table 2-9** summarizes the chemical shifts of **L4** and **C5**.

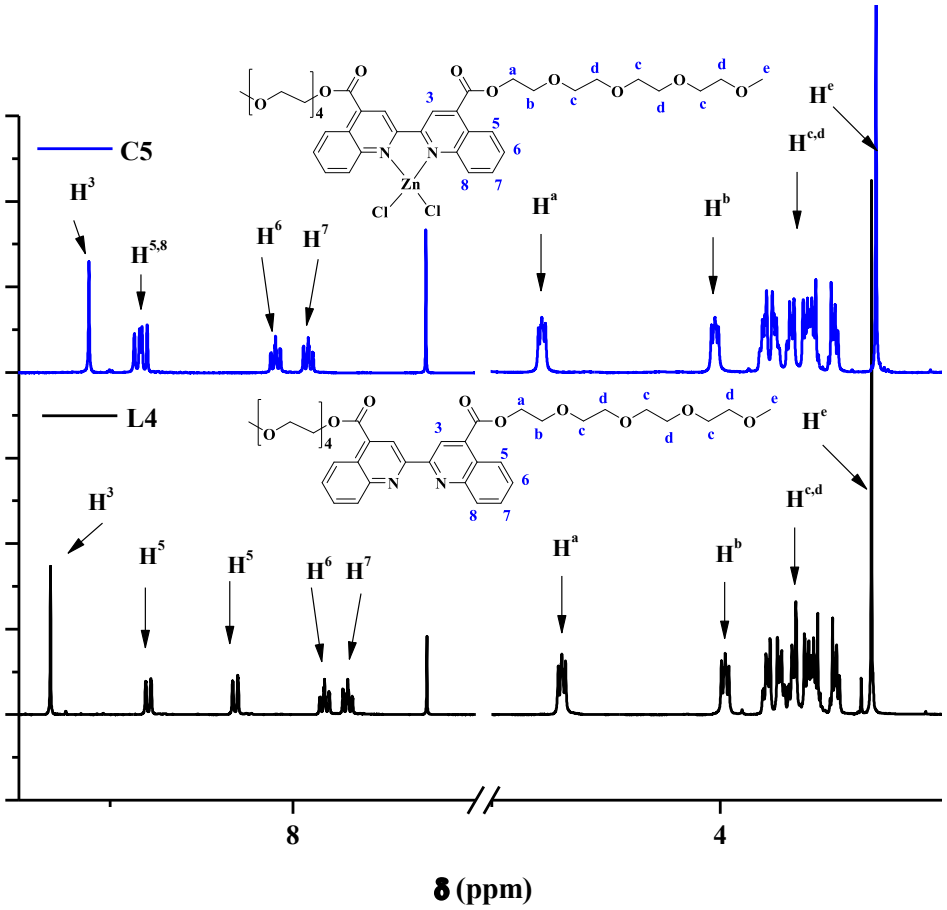

Figure 2-14. ^{1}H-NMR spectra of **C5** complex plotted against the free ligand **L4**.

Table 2-9. Chemical shifts (in δ/ppm) of **L4** and **C5**, recorded in $CDCl_3$.

Chemical shifts (in δ/ppm)									
Compound	H^3	H^5	H^6	H^7	H^8	H^a	H^b	H^{c-d}	H^e
L5	9.33	8.79	7.91	7.09	8.32	4.78	4.02	3.85 - 3.45*	3.31
C5	9.11	8.83*	7.83	7.70	8.83*	4.69	3.98	3.85 - 3.45*	3.34
* overlapped peaks									

From the spectrum of complex **C5** the shift of all aromatic protons indicated the successful coordination of Zn(II) salt to the ligand **L4**.

The insufficient solubility of the Zn(II) coordination complexes in water and biologically relevant solvents is one of the major drawbacks in using them in medicinal fields. Grafting hydrophilic substituents on the ligand may be a valuable strategy to induce solubility in water and/or polar solvents for the resulting Zn(II) coordination complexes. Nonetheless, the dissolution may occur in several steps, while the competition of coordinating solvents with the bidentate ligand may induce the following of different equilibrium reactions.[310] Indeed, a change in the geometry of the metal centre may occur with similar coordination strength

solvents, while strong donor solvents may induce the formation of solvated metal chlorides by a stepwise dissociation of complex.

Based on this background, the investigations of the species formed by dissolution in different solvents of complex **C5** was carried out by absorption and fluorescence spectroscopies and conductivity measurements. The complex is soluble in polar solvents (CH_3CN, DMF, EtOH and MeOH), scarcely soluble in water and insoluble in nonpolar solvents. However, the addition of water to the polar solutions does not cause precipitation of the complex even at high-water content (95% volume).

Ionic conductivity measurements

Conductivity measurements performed at a concentration of 10^{-3} mol•L^{-1} showed a neutral character, except for MeOH, where a value of 83 $\Omega^{-1}\cdot mol^{-1}\cdot cm^2$ revealed the presence of a monovalent specie.[311] However, with the addition of water, monovalent or even bivalent species are formed, as shown in Figure 2-15. As documented in literature,[310] the dissolution of complexes of this type can occur in several steps, following different equilibrium reactions triggered by the competition of the coordinating solvent with the bidentate ligand (**Figure 2-15**).

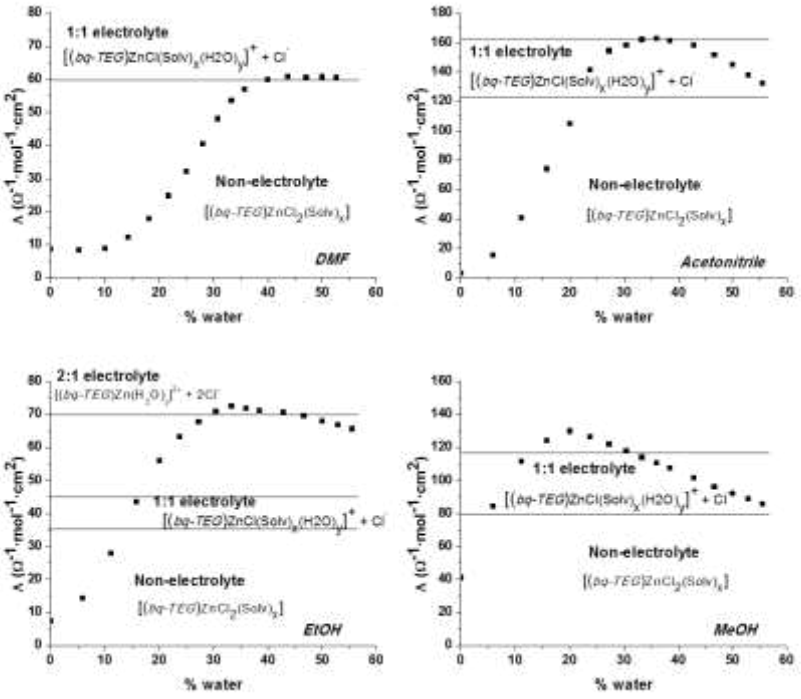

Figure 2-15. Conductivity measurements of complex **C5** in mixtures of solvent/water.

No suitable single crystals could be obtained in order to elucidate the structure of complex **C5**, therefore, based on the above results and on literature data reported for similar complexes,[289,312] the proposed chemical structure of the complex is a tetracoordinated species, as seen in **Scheme 2-4**, with one *N^N* chelating and two chloride ligands completing the coordination sphere of the metal.[312]

Absorption and emission spectroscopies

The absorption spectra of complex **C5** (**Figure 2-16**) was recorded in 5 different solvents and the data are summarized in **Table 2-10**.

Table 2-10. Maximum absorption data of **C5** in different solvents.

Solvent	**CH_2Cl_2**	**CH_3CN**	**DMF**	**EtOH**	**MeOH**
	λ_{max}/nm (ε/$M^{-1}\cdot cm^{-1}$)				
L1_bq-TEG	279 (31500) 340 (15550)				
C5	277 (46300) 310 (5800) 318 (5900) 371 (19050) 380 (21550)	229 (26550) 272 (54400) 319 (10750) 357 (16050) 377 (17000)	340 (21850)	270 (41050) 340 (21250)	268 (40750) 340 (20450)

Figure 2-16 presents the absorption spectra of **C5** in 5 different solvents. By comparison with that of the ligand **L4** (**Figure 2-16 a**), in case of the spectra of **C5** recorded in EtOH, the absorption band of lower energy corresponding to $\pi-\pi*$ transition presents a small hypsochromic shift from 279 nm to 270 nm.

When different solvents were used (**Figure 2-16 b**), the spectra presented hypsochromic (CH_3CN and MeOH) or bathochromic shifts (CH_2Cl_2 and DMF), compared to those recorded in EtOH. These shifts may appear due to the polarity of the solvents, *i.e* a blue shift of UV-Vis absorption band with increasing solvent polarity, whereas bathochromic shifts are typical for non-polar solvents.[313] After the dissolution of the complex, a change of the geometry may be induced by coordinating solvents yielding penta- or hexacoordinated species. Strong donor solvents may induce in steps the complete dissociation of the complex to form solvated metal chlorides, as evidenced by spectrophotometric studies and ESI-mass spectrometric measurements.[310] When using a mixture of solvent/water 5:95 volume, no significant changes were seen in the absorption spectra of **C5**.

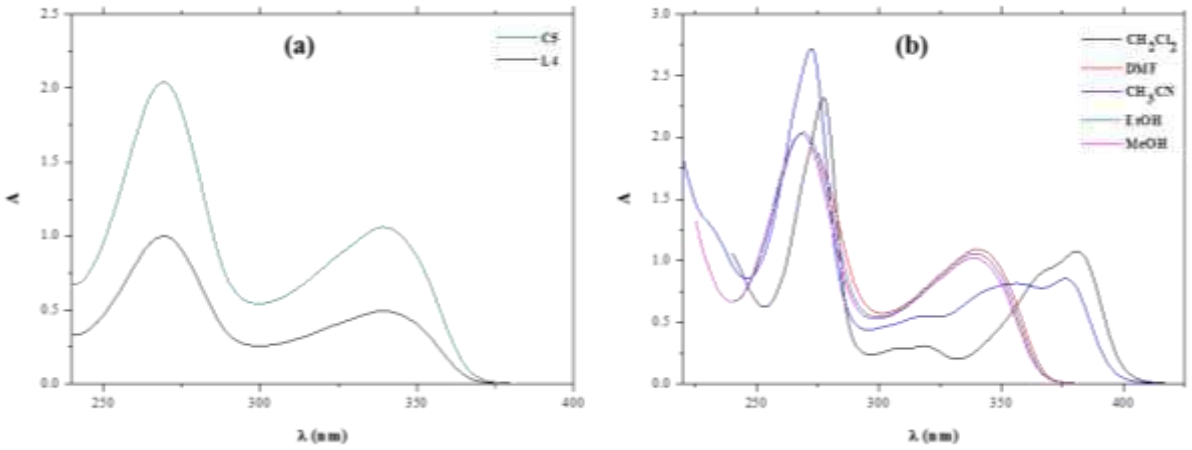

Figure 2-16. Absorption spectra of: (a) **C5** in EtOH plotted against **L4** and (b) **C5** in CH_2Cl_2, DMF, CH_3CN, EtOH and MeOH solutions.

When the emission spectra were recorded only in the pure above-mentioned solvents, **C5** complex did not emit in all solvents, but when water was added into the system, similar emission as the ligand **L4** with small blue shifts in CH_3CN and EtOH and red shift in MeOH were observed (**Figure 2-17**).

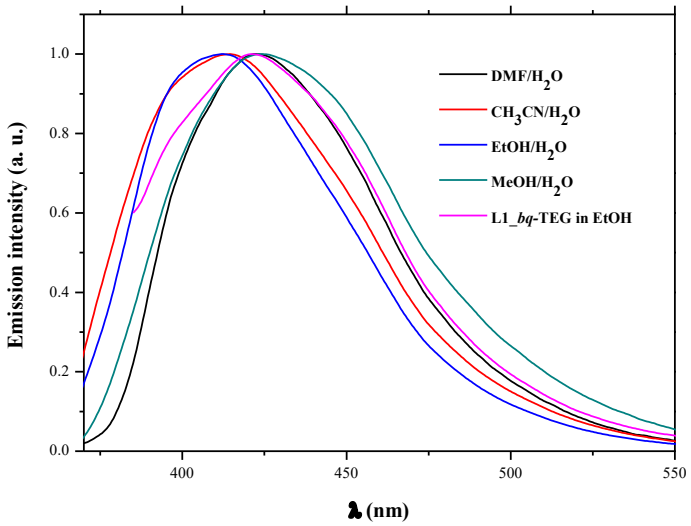

Figure 2-17. Emission spectra of complex **C5** in a mixture of solvent/water, where solvent is DMF, CH_3CN, EtOH and MeOH.

Antioxidant activity

Because bioactive compounds have the ability to prevent, delay, and protect against oxidation of various substrates such as DNA and lipid materials in living organisms,[314] the antioxidant activity of the ligand **L4** and that of the **C5** complex was investigated using DPPH

in methanolic solution, according to the Brand-Williams method.[306,307] However, no scavenging effect was evidenced for neither of compounds.

Conclusions

The new compound **L4** capable to act as a N^N donor ligand functionalized with hydrophilic chains has been synthesized and characterized. The new compound **C5** is soluble in polar solvents. The complex is tetrahedral, with a chelating N^N ligand and two monodentate chlorine ligands completing its coordination sphere.

2.3. Synthesis and characterization of Cu(I) complexes

Copper is a low cost biometal, readily available, finding applications in several domains, from electrooptics[315,316] to catalysis[317] and biomedicine.[318,319] Cu(I) complexes containing bis-chelated N^N-donor ligands are strongly subjected to oxidation. Cu(I) complexes are stabilized by a tetrahedral geometry. Homoleptic Cu(I) coordination complexes with N^N ligands are susceptible to distortions both in the ground and excited states, facilitating the attack of a nucleophile (coordinating solvent or anion) as reported by Scaltrito *et al.*[320] in the review of a series of $[Cu(N^N)_2]^+$ systems, where N^N is *phen* or *bpy* ligand derivatives. The stability of the Cu(I) complexes is given by the bulky substituents from the adjacent position to nitrogen atom, but also by the nature of the counterion.[321,322,323,324,325] Our studies are based on the influence of the counterion using *phen* and *bq* ligands.

2.3.1 Cu(I) complexes with phen ligand

The influence of the counterion was only studied on complexes with substituted *phen* and mostly with non-coordinating ions. Herein, we investigated the influence of the counterion on the stability of Cu(I) complexes based on unsubstituted *phen* (**L2**) with different counterions

The structures of the synthesized complexes $[(phen)_2Cu(I)]^+Y^-$, where Y^-= ClO_4^-, I^-, SCN^- and BF_4^-) are presented in **Scheme 2-5**.

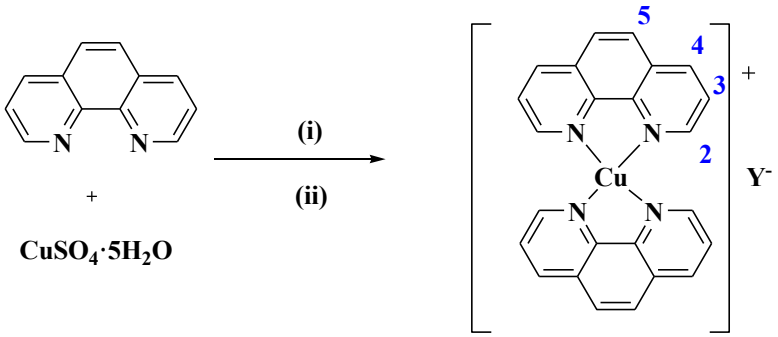

C6, Y^-= ClO_4^-;
C7, Y^-= I^-;
C8, Y^-= SCN^-;
C9, Y^-= BF_4^-;

Scheme 2-5. Reaction pathway of **C6** – **C9** and the atom labelling (blue); Reagents and conditions: (i) $NH_2OH{\cdot}HCl/NH_3$, H_2O, ΔT; (ii) MY (M = Na or K).

The synthesis of copper complexes was carried out following a reported procedure: $CuSO_4{\cdot}5H_2O$ was reduced in water solution with $NH_2OH{\cdot}HCl/NH_3$, heated to the boiling point and then **L2** was added in the reaction mixture.[296] Then, a metathesis reaction with a slight excess of an inorganic salt containing the appropriate counterion yielded the desired products as purple solids, complexes **C6** – **C9**. Cu(I) complexes resulted by the reduction of the Cu(II) salt, instantaneously precipitated out from the water media due to their low solubility. Complex **C6** was already reported in literature,[296,326] The complexes **C7** – **C9** were first published in the frame of this thesis.[327]

The nature of the complexes is proved by the elemental analysis and atomic absorption spectroscopy (AAS). The molar conductivity values of Cu(I) complexes, recorded in freshly prepared DMSO solutions (10^{-3} M), fall in the range of 1:1 electrolyte,[311] thereby supporting the presence of the counter ion outside the coordination sphere.

Structural information has been obtained from FT-IR and ^{1}H-NMR spectroscopy. The recording of the ^{1}H-NMR spectrum supports the presence of diamagnetic Cu(I). The thermal stability and behaviour were studied by thermal analyses.

FT-IR spectroscopy

The characteristic absorption bands of the ligands can be noticed in the FT-IR spectra of **C6** – **C9** complexes and are summarized in **Table 2-11**. They are shifted, thus proving the presence of the coordinated ligands. The bands attributed to $\nu_{C=C}$ and $\nu_{C=N}$ are shifted with respect to the vibration bands in the free *phen* ligand. The shift to lower frequencies of the characteristic bands in the 700 – 900 cm^{-1} regions assigned to *phen* rings shows a significant deformation of the heterocyclic rings due to coordination to Cu(I) ion. Moreover, the presence of the counterion is proven by the corresponding strong vibrational bands: **C6**: ν_{ClO4} = 1098, 623 cm^{-1}; **C8**: ν_{SCN} = 2051 cm^{-1}; **C9**: ν_{BF4} = 1060 cm^{-1}.[296,328,329]

Table 2-11. Assignment of the characteristic absorption bands of **C6** – **C9** (wavenumber values in cm^{-1}).

Assignment of the characteristic absorption bands (wavenumber values in cm^{-1})					
Complex	ν_{H2O}	$\nu_{C=N}$	$\nu_{C=C}$	ν_{Y^-}	ν_{C-H}
C6		1622	1588, 1508, 1430	1090, 622	851, 724
C7		1619	1576, 1504, 1420		839, 722
C8	3309	1623	1575, 1507, 1423	2051	739, 723
C9		1622	1588, 1508, 1424	1060	842, 724

^{1}H-NMR spectroscopy

In order to prove the purity and the molecular structure **C6** – **C9** complexes, ^{1}H-NMR spectroscopy was used. The signal shifts of the Cu(I) complexes with respect to the corresponding free ligand demonstrate their successful coordination. By keeping constant the concentration of complexes **C6** – **C9**, their spectra were recorded in DMSO-d_6. As **Figure 2-18** shows, the signals of the aromatic protons in the spectra of the complexes are broad, and their relative intensity and broadening with respect to the signal of the solvent, are different as a function of the counterion. Due to the sharpness of the solvent signals, it is possible to exclude that the broadening of the aromatic proton signals is related to the concomitant presence of small amounts of Cu(II) species. A similar signal broadening was observed by Barrientos *et al.*[330] on the ^{1}H-NMR spectra of analogues complexes recorded at room temperature and explained by a possible "internal paramagnetism" as a consequence of a fluxional process toward distorted "Cu(II)-like" preferred geometries about the Cu(I) ion. Herein, protons adjacent to the copper centre (H^2 and H^3) are more broaden and less intense than the protons located further away (H^4 and H^5). The observed aromatic signal broadening can be attributed reasonably therefore to a fluxional process due to structural variations of the Cu(I) ion pseudo-

tetrahedral environment, implying distortion towards geometries generally preferred by pentacoordinated Cu(II) complexes. The broadening of the proton signals is higher in the case of complexes **C7** and **C8** with respect to complexes **C6** and **C9** (**Figure 2-18**). Thus, it can be envisaged that counterions with higher coordination strength, I^- and SCN^-, favour in the fluxional process the more distorted "Cu(II)-like" preferred geometry, while non coordinating anions, ClO_4^- and BF_4^-, contribute to the stabilization of the Cu(I) geometry. Although in the crystalline solid state, only ionic and pseudo-tetrahedral four coordinated Cu(I) complexes of *phen* ligands are known, even in presence of coordinating counterions such as the I^-,[331] it is not possible to exclude in solution the fluxional rearrangement of the complex structure towards a neutral five-coordinated Cu(I) centre, favoured by the presence of coordinating counterions. The chemical shifts for aromatic region of the *phen* Cu(I) homoleptic complexes (**C6** – **C9**) are summarized in **Table 2-12**. No major chemical shifts were observed when using different counterions.

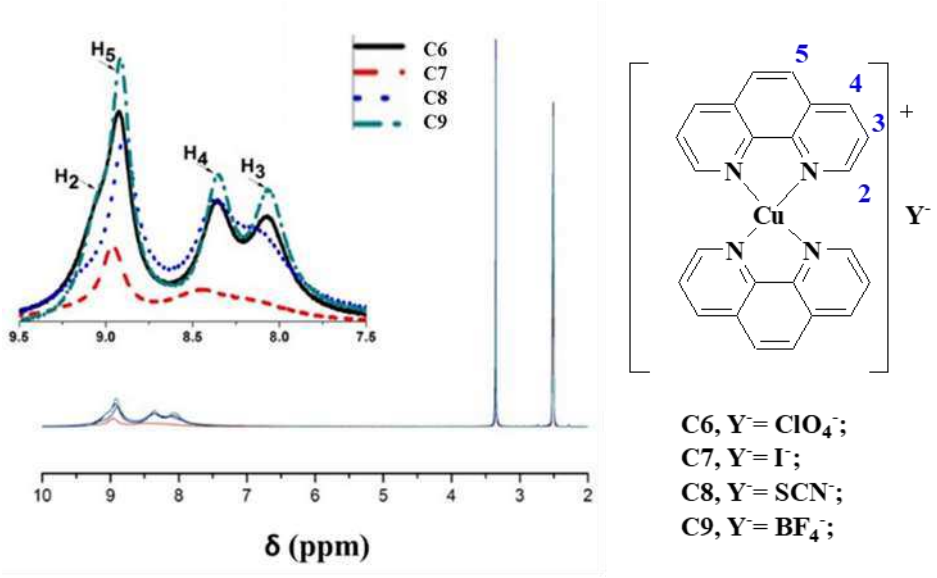

Figure 2-18. ^{1}H-NMR spectra of **C6** – **C9** complexes (the aromatic region is shown in the inset).

Table 2-12. Chemical shifts (in δ/ppm) of the aromatic region of **C6** – **C9,** recorded in DMSO-d_6.

Chemical shifts (in δ/ppm				
Compound	H^2	H^5	H^4	H^3
C6	9.06- 8.92 *		8.36	8.07
C7	8.96 *		8.47	
C8	8.90 *		8.36	8.16
C9	9.03	8.92	8.36	8.08

* overlapped signals

TGA analysis

The thermal analysis of complexes **C7 - C9** was conducted in air atmosphere and is presented in **Figure 2-19**. In particular, no thermal processes were detected up to 250°C. The thermograph of complex **C8** showed at low temperature a loss of weight corresponding to ½ water molecules over a broad temperature range of 50°C to 125°C. The experimental percentage of CuO residue obtained for the Cu(I) complexes **C7 - C9** is close to the theoretical ones. The results of thermogravimetric analysis are summarized in **Table 2-13**.

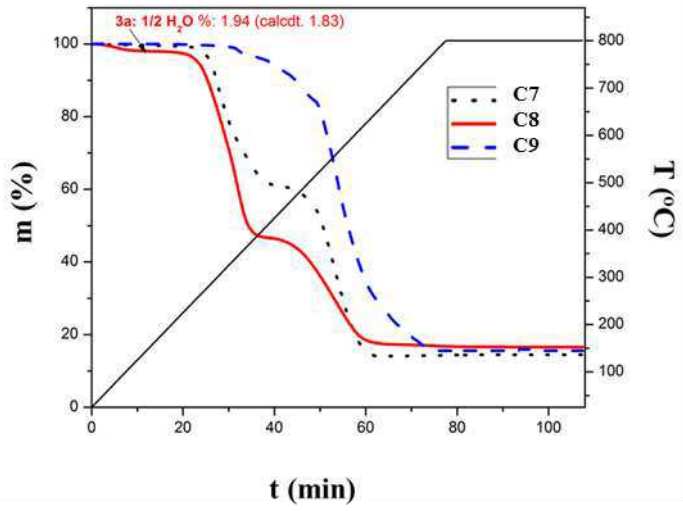

Figure 2-19. TGA traces for **C7** – **C9** complexes.

Table 2-13. Thermogravimetric analysis results of **C6 - C9** complexes.

Complex	Thermal process* (temperature range/ ºC)	calcd/ found CuO residue (%)
C6	*	
C7	no thermal processes detected	14.44/ 14.49
C8	weight loss: ½ · H_2O (50°C- 125°C)	16.20/ 16.60
C9	no thermal processes detected	15.57/ 15.87
*reported in literature[296,326]		

Absorption spectroscopy

The electronic spectra of **C7 - C9** recorded in DMSO solution at 10^{-4} M, show the usual ligand centred π-π* and n-π* bands between 300 - 350 nm, and bands in the 400-600 nm range originating from MLCT, centred at 445 nm, with a weak shoulder at longer wavelengths, related to either a static or dynamic flattening distortion ($D_{2d} \rightarrow D_2$).[332,333,334] The spectra are nearly identical and do not show solvatochromic effect by changing the solvents (CH_3CN or CH_2Cl_2). The effect of the counterion is not observed, explained by less interaction between the counterions with the cationic chromophore at low concentration (10^{-4} M). Moreover, the observed spectral shape is similar to that reported in the literature, suggesting a structure in solution with approximate D_{2d} symmetry.[333]

Figure 2-20 shows the solid-state UV-Vis diffuse-reflectance spectra of **C6 - C9**, similar to the solid-state absorption spectra already reported for complex **C6**.[335] All spectra consist of strong MLCT bands in the region 450-900 nm, with a shoulder more pronounced in the case of complexes **C7** and **C8**. If the intensity of the shoulder is taken as a measure of the flattening distortion in the ground state,[335,336] the degree of distortion is greater in the case of complexes **C7** and **C8** than for complexes **C6** and **C9,** a similar trend to that is evidenced by ^{1}H NMR analysis in concentrated solution. It can be highlighted that the influence of the counterion on the geometry of the complex cation $[(phen)_2Cu]^+$, seems to be determined probably by different direct or indirect interactions as well as by donor strength of the counterions.

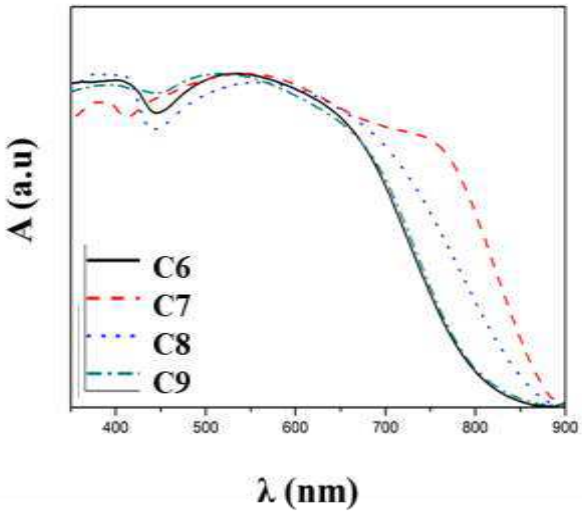

Figure 2-20. Solid-state UV-VIS diffuse-reflectance spectra of **C6 - C9**.

Conclusions

Complex **C6** was already reported in literature,[296,326] whereas **C7** – **C9** complexes were synthesized and reported by our group herein.[327] Based on literature and our experiments, the formula of the complexes **C6** – **C9** is proposed to be $[(phen)_2Cu]^+Y^-$, where $Y^- = ClO_4^-$, I^-, SCN^- and BF_4^-. Both in solution and in the solid state, the nature of the counterion affects the tetrahedral environment of the Cu(I) ion: a flattening of the complexes symmetry ($D_{2d} \rightarrow D_2$) is evidenced both by ^{1}H-NMR analysis in concentrated solution and UV-Vis absorption spectroscopy in the solid state. In both cases a greater structural distortion is observed when the Cu(I) salts are build up with more coordinating strength counterions (I^- and SCN^-) with respect to ones having non coordinating counterions (ClO_4^- and BF_4^-).

2.3.2 Cu(I) complexes with bq ligands

The design, synthesis and characterization of metallomesogens based on Cu(I) metal centres was carried out according to **Scheme 2-6**. In order to obtain stable Cu(I) species, *bq* derivatives that contain a fused aromatic ring closed to the chelation centre as ligands and the non-coordinating ClO_4^- and BF_4^- which showed in our study the best abilities in stabilising the tetracoordination as counterions were chosen.

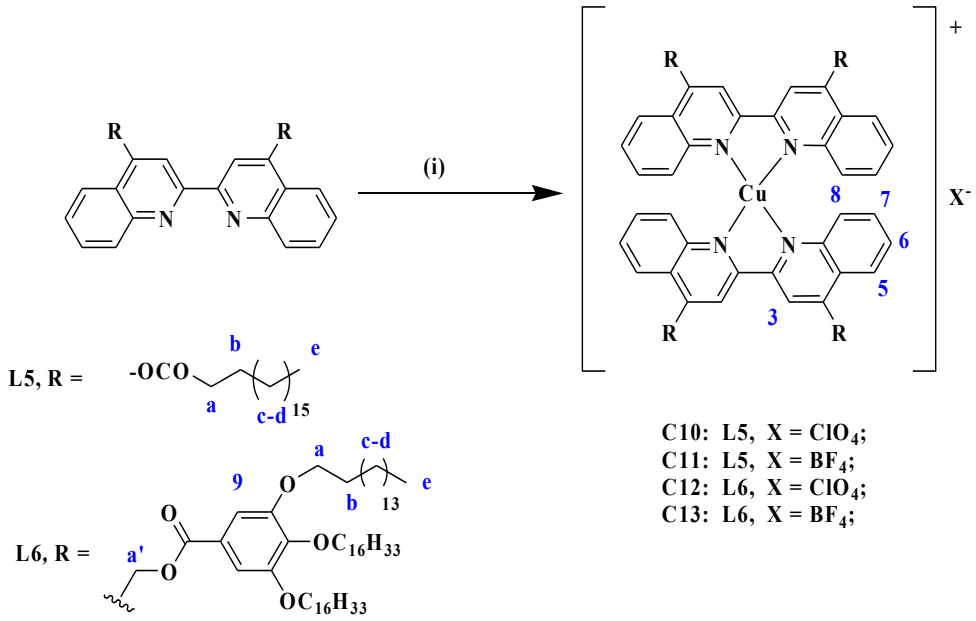

Scheme 2-6. Reaction pathway of the **C10** – **C13** and their atom labelling (blue). Reagents and conditions: (i) $[Cu(CH_3CN)_4]X$, $CHCl_3$, r.t, 15 min.

The synthesis of the complexes **C10** – **C13** as presented in the experimental chapter was realized in two steps; the first step involved the synthesis of Cu(I) precursor of type $[Cu(CH_3CN)_4]X$ (X = ClO_4 and BF_4) were obtained from appropriate CuX_2 salt and Cu(0), as previously reported.[337] In the second step the precursor $[Cu(CH_3CN)_4]X$ was reacted with the *bq* derivative ligands, **L5** and **L6** in a 1:2 ligand-to-metal ratio, to form the new Cu(I) complexes **C10** – **C13** in good yields.

The complexes were characterized by **C10** – **C13** by FT-IR and ^{1}H-NMR spectroscopies and the ionic nature was established by conductivity measurements. Their thermal behaviour was studied by TGA and differential scanning calorimetry (DSC) and the mesomorphic behaviour were studied by and SWAXS.

FT-IR spectroscopy

FT-IR spectroscopy was employed to gain information regarding the shifts in the characteristic absorption bands of the functional groups of **C10** – **C13** complexes. FT-IR spectra presents the characteristic bands of the ClO_4^- and BF_4^- as intense absorption bands around 1085 – 1100 cm^{-1} and 620 – 625 cm^{-1} for ClO_4^-,[338] and 1060 – 1065 cm^{-1} for BF_4^- counterions.[339] The spectra of the complexes contain also the $\nu_{C=O}$ absorption band characteristic for the carboxylate

unit at 1715 - 1730 cm^{-1}.[291] In **Figure 2-21** the spectra of **C10** and **C11** complexes are plotted against the free ligand **L5**, and **Figure 2-22** presents the spectra of **C12** and **C13** complexes are plotted against the free ligand **L6**, and the main absorption bands are summarized in **Table 2-14**.

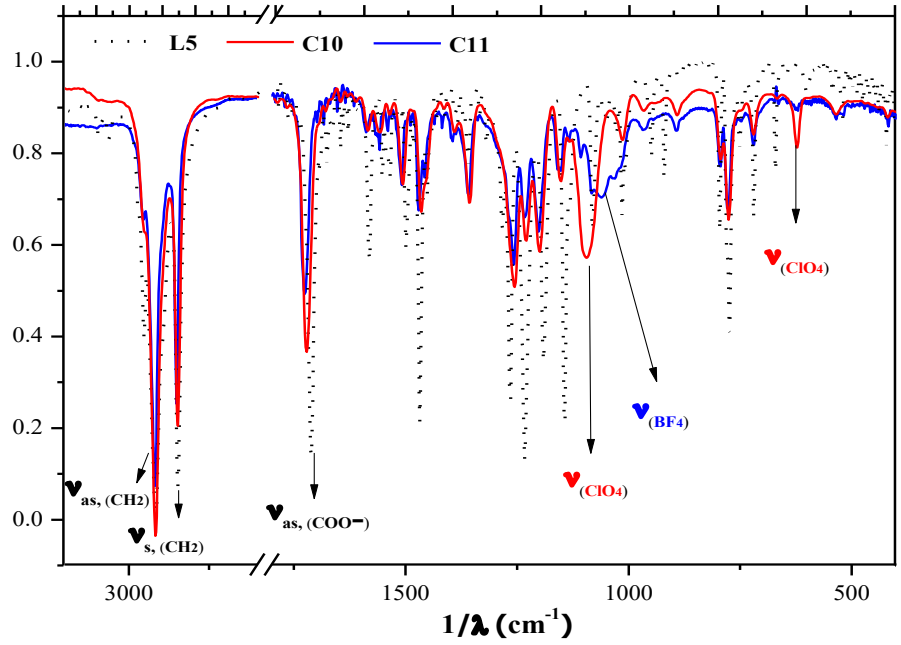

Figure 2-21. FT-IR spectra of **C10** and **C11** complexes**,** plotted against the free ligand **L5**.

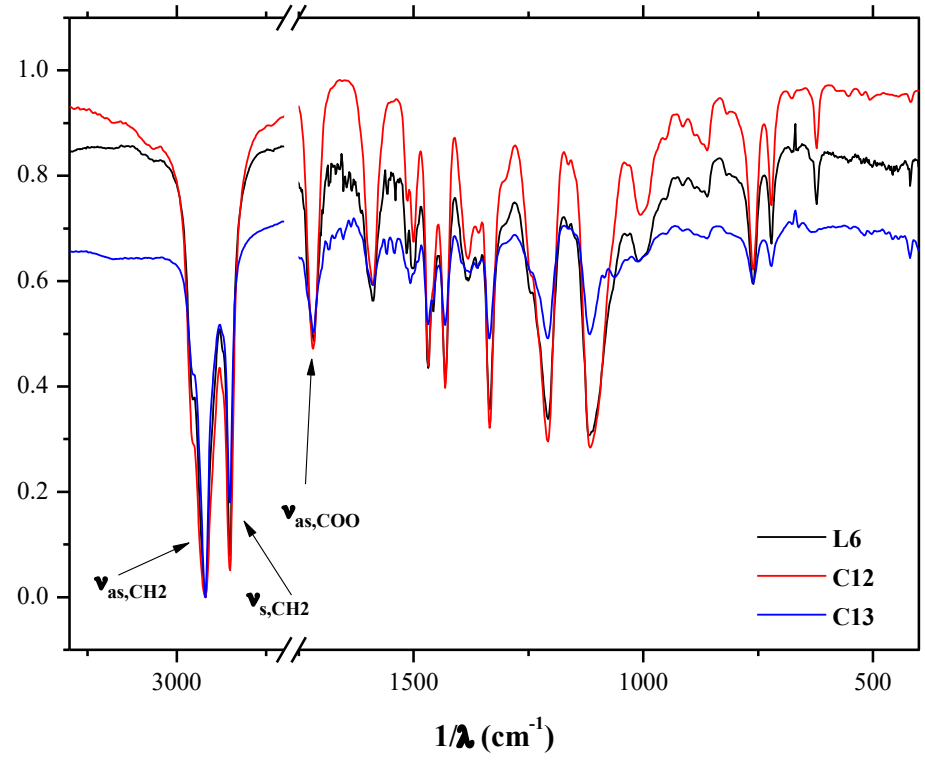

Figure 2-22. FT-IR spectra of **C12** and **C13** complexes**,** plotted against the free ligand **L6**.

Table 2-14. Assignment of the characteristic absorption bands of **C10** – **C13** complexes (wavenumber values in cm^{-1}).

Assignment of the characteristic absorption bands (wavenumber values in cm^{-1})							
Complex	$\nu_{as,CH2}$	$\nu_{s,CH2}$	ν_{COO}	$\nu_{C=N}$, $\nu_{C=C}$	$\nu_{as,(C-O-C)}$	$\nu_{s,(C-O-C)}$	ν_{X*}
C10	2920	2844	1713	1604 - 1435	1115	1053	1103
C11	2920	2844	1713	1604 - 1435	1115	1053	1043
C12	2922	2849	1716	1590 - 1430	1115		1109, 622
C13	2924	2854	1721	1591 - 1421	1149	1053	1053
∗X= ClO_4 for **C12** complex and BF_4 for **C13** complex							

^{1}H-NMR spectroscopy

By comparing the NMR chemical shifts of the complexes **C10** – **C13** with those of the free *bq* ligands,[286] the significant shifts observed for the aromatic protons proves the successful coordination, as seen in **Figure 2-23** and **Figure 2-24**. The fine structure and sharpness of the proton signals associated to the *bq* ligands of the Cu(I) complexes is an indication of the absence of Cu(II) species.

In particular, after complexation, proton H^8, presents a small chemical shift to higher frequencies, from 8.79 for free **L5** ligand to 8.85 and 8.83 ppm for **C10** and **C11**, respectively. Also, protons H^5, H^6 and H^7 were shielded to lower frequencies with respect to the free ligand (**Figure 2-23**).

By comparing the spectra of complexes **C12** and **C13**, with that of the free ligand **L6** (**Figure 2-24**) it can be observed that protons H^3 of the complexes are shielded by 0.24 ppm with respect to H^3 in the free ligand. A significant shift was observed for proton H^8, by as much as 0.35 ppm with respect to H^8 in the free ligand.

The ^{1}H-NMR chemical shifts for the complexes are summarized in **Table 2-15**.

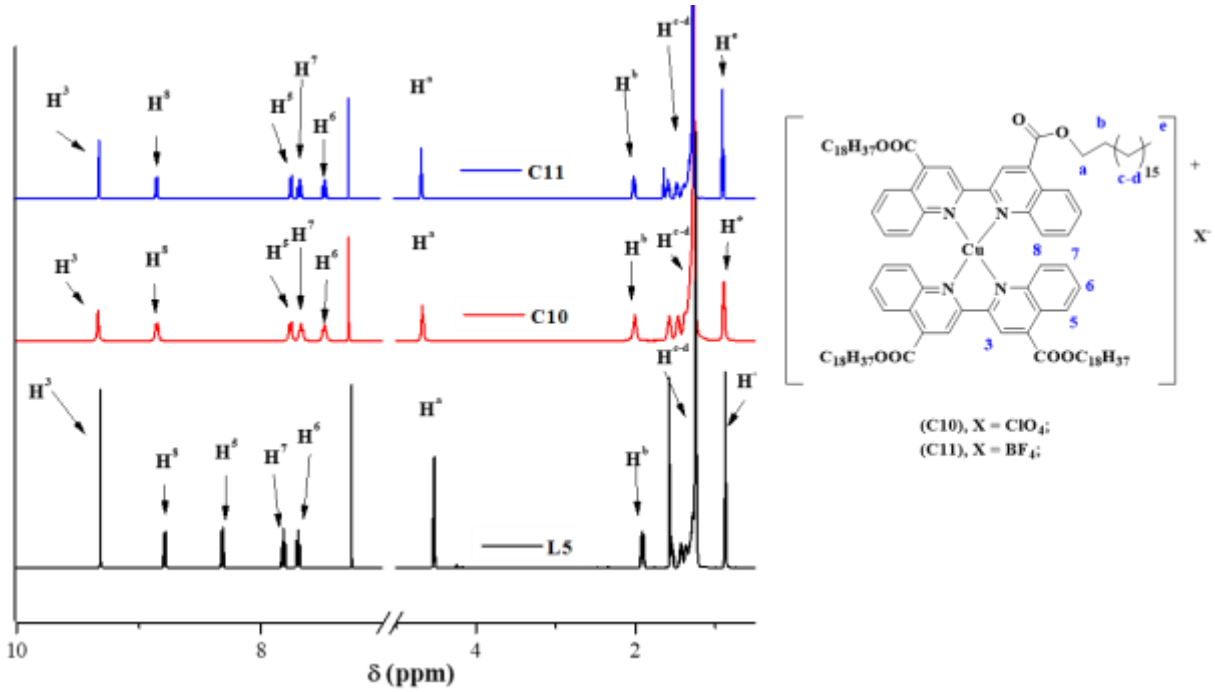

Figure 2-23. ^{1}H-NMR spectra of **C10** and **C11** complexes, plotted against the free ligand **L5**.

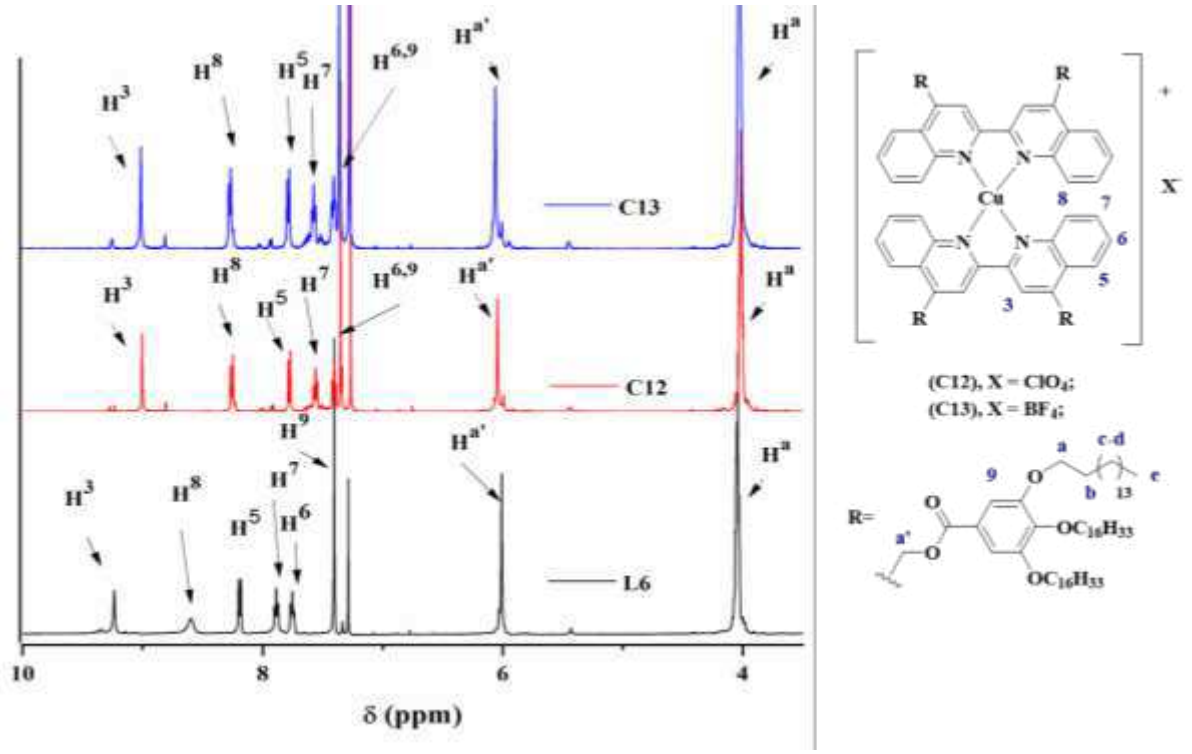

Figure 2-24. ^{1}H-NMR spectra of **C12** and **C13** complexes, plotted against the free ligand **L6**.

Table 2-15. Chemical shifts (δ/ppm) of **C10** – **C13** recorded in $CDCl_3$.

Chemical shifts (δ/ppm)				
	C10	**C11**	**C12**	**C13**
H^3	9.33	9.30	9.00	9.00
H^5	7.76	7.73	7.77	7.77
H^6	7.48	7.46	7.40	7.39
H^7	7.67	7.66	7.56	7.56
H^8	8.85	8.83	8.24	8.25
H^9			7.34	7.34
$H^{a'}$			6.04	6.02
H^a	4.67	4.65	4.01	4.01
H^b	2.00	1.99	1.93 – 1.69	1.74
H^{c-d}	1.77 – 1.19	1.65 – 1.12	1.53 – 1.15	1.52 – 1.25
H^e	0.87	0.87	0.87	0.87

Absorption and emission spectroscopy in solution

The absorption and emission properties of the complexes have been investigated in CH_2Cl_2 solution. Coordination to Cu(I) modifies the absorption bands of both ligands in a similar manner: regardless of the counterion, complexes **C10** - **C13** show with respect to the corresponding ligand spectrum, a red-shift of the ligand-centred (LC) and ILCT bands, and a more defined vibrational structure of the ILCT bands, due to the rigidity conveyed to the ligand by coordination of Cu(I) (**Figure 2-25**). In case of the complexes corresponding to the same ligand, spectra perfectly overlap. The principal effect of the copper coordination is the presence, of a band with a medium-low intensity, with a series of shoulders at 578 nm (for complexes **C10** and **C11**) and at 560 nm (for complexes **C12** and **C13**), assigned to MLCT electronic transitions.[340]

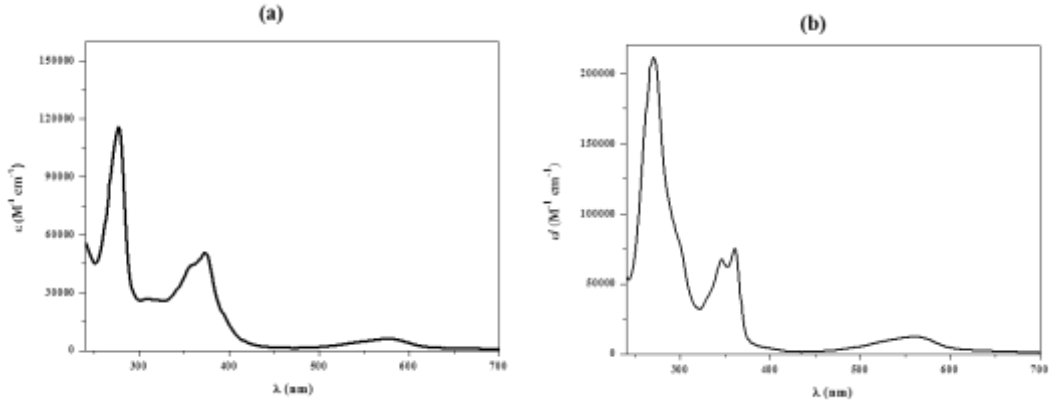

Figure 2-25. Absorption spectra of: (a) complex **C10** and (b) complex **C12** in CH_2Cl_2 solution.

The emission spectra of complexes **C10** – **C13** were recorded in air-equilibrated and in degassed CH_2Cl_2 solutions. No emission was detected for neither of the complexes. The non-emissive deactivation paths can be assigned to a flattened coordination geometry, moving towards a planar geometry, by changing its formal oxidation state from Cu(I) to Cu(II). Therefore, a fifth coordination site becomes available, which can be occupied by solvent molecules or counterions, leading to a non-emissive pentacoordinated exciplexes.[341]

Mesomorphic properties

The mesomorphic properties of the coordination complexes **C10** – **C13** were investigated by POM, DSC and powder X-Ray scattering (PXRD).

The mesomorphic properties of the complexes **C10** – **C13** were first assessed by POM observation. The POM images in **Figure 2-26**, show a fan-like texture with features pointing towards a lamellar phase for complexes **C10** and **C11**. **Figure 2-26** presents the POM textures of **C12** and **C13** complexes. A long annealing does not help to develop a texture whose identification was not unequivocal. herefore, the mesophases were identified based on PXRD experiments.

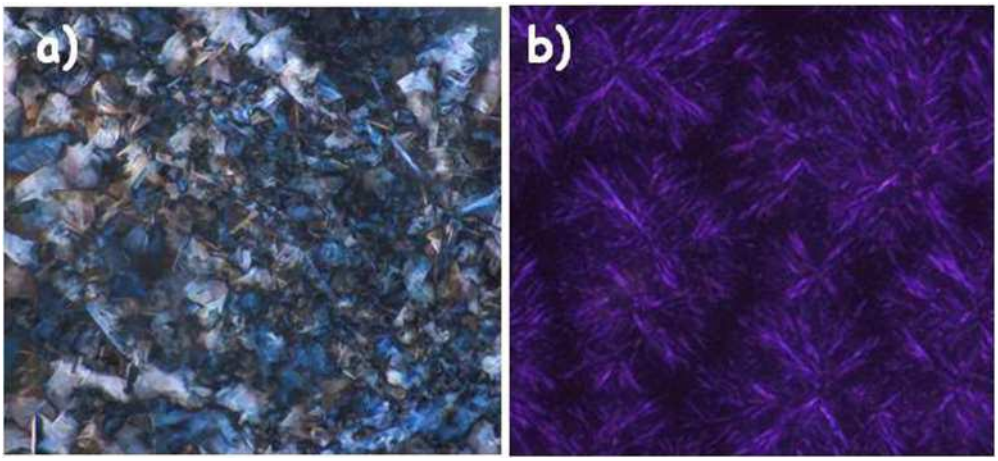

Figure 2-26. POM micrograph of the textures exhibited by: (a) complex **C11** at 70ºC on cooling, magnification 20x and (b) complex **C13** at 60ºC on cooling, magnification 50x.

Figure 2-27 shows DSC thermograms of all four complexes. The transition temperatures and the enthalpies associated are determined by DSC measurements and are shown in **Figure 2-27** and the data summarized in **Table 2-16**. The high thermal stability of the complexes was proved by running two heating – cooling cycles, without changes of the isotropisation points.

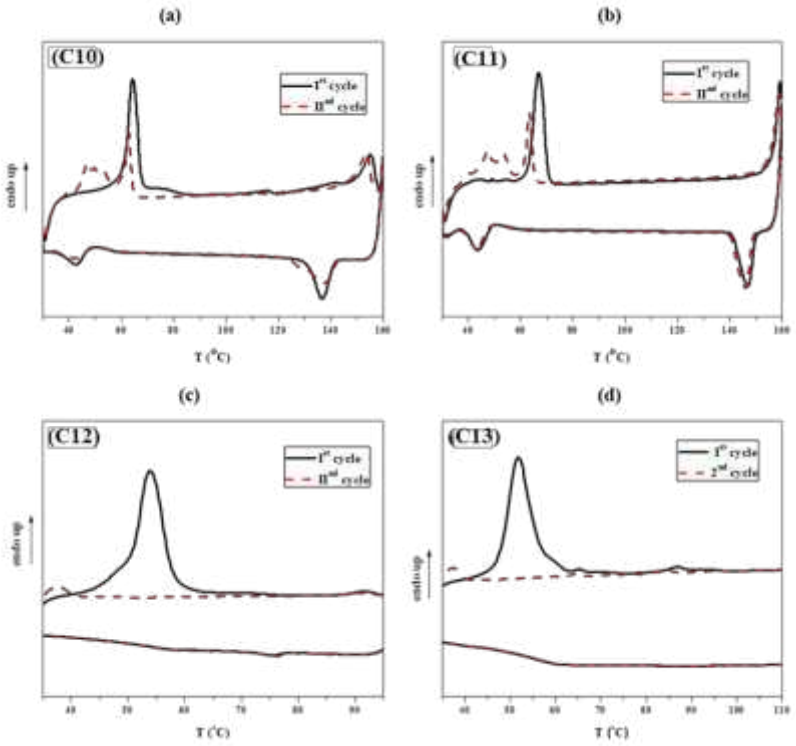

Figure 2-27. First and second cycle DSC traces of complexes: a) **C10**, b) **C11**, c) **C12** and d) **C13** obtained with a heating-cooling rate of 10°C/min.

Table 2-16. Phase transition temperatures and associated enthalpy changes of complexes **C10** – **C13**.

Complex	Transition[a]		T^b (°C)	ΔH (kJ·mol^{-1})
C10	Ist cycle	Cr-L_{col}	61.1	49.2
		L_{col}- I	150.3	31.3
		I-L_{col}	141.4	24.1
		L_{col} -L_{colg}	47.7	11.0
	IInd cycle	L_{colg}-L_{colg}	43.8	18.1
		L_{colg}-L_{col}	60.1	13.8
		L_{col} -I	147.2	26.7
		I-L	141.4	23.7
		L-L_{colg}	53.7	9.1
C11	Ist cycle	Cr-L_{col}	62.4	63.7
		L_{col}-I	156.2	38.0
		I-L_{col}	150.1	35.6
		L_{col}-L_{colg1}	47.3	16.7
	IInd cycle	L_{colg}- L_{colg}	45.6	20.5
		L_{colg} -L_{col}	60.4	22.6
		L_{col}-I	155.15	36.5
		I-L_{col}	150.9	35.1
		L_{col}-L_{colg1}	48.7	13.7
C12	Ist cycle	Cr-Col_h	48.6	133.5
		Col_h -I	89.9	3.1
		I- Col_h	77.0	2.3
	IInd cycle	Col_h -I	88.2	2.2
		I- Col_h	79.7	2.4
C13	Ist cycle	Cr- Col_h	47.0	146.5
		Col_h -I	83.4	2.4
		I- Col_h	-	-
	IInd cycle	Col_h-I	80.6	2.0
		I-Col_h	-	-0.5

a: Cr – crystalline phase; L_{col} – lamello columnar phase; L_{colg} – frozen lamello columnar phases; Col_h – columnar hexagonal phase; b: onset peak

The tetra-catenar complexes **C10** – **C11**, exhibit a rather complicated thermal behaviour: the first heating cycle consists of distinct transitions indicating the melting to liquid crystalline phase and clearing to isotropic phase, whereas the cooling trace shows transitions

corresponding to the formation of a liquid crystalline state and around 50ºC a transformation to a more rigid and/or ordered state. The optical texture of the mesophase is preserved as seen on POM, which is consistent with the formation of anisotropic liquid crystalline glass states. On further heating several transitions appear before the melting into LC state as shown in **Figure 2-27** a and b, accompanied by substantial enthalpy change, but again without any textural changes.

Complexes **C12** – **C13** isolated as amorphous solids melt to a liquid crystalline state around 50ºC whereas the clearing to isotropic liquid occurs at around 90ºC. On cooling crystallisation is not observed, although the mesophase appears not fluid at r. t. as observed on POM. On further heating-cooling cycles, no transition could be detected by DSC.

The nature of the mesophases was clarified by SWAXS experiments carried out at variable temperatures. Complexes **C10** and **C11** (**Figures 2-28** a and b) showed an ordered lamello-columnar mesophase, L_{col}, as proved by the PXRD patterns recorded both on heating in the IInd heating cycle at 70°C and 75°C, respectively for **C10** and **C11**. Indeed, in the small angle region of the X-ray diffraction patterns, four diffraction peaks with reciprocal spacings in the ratio 1 : 2 : 3 : 5 and indexed as (001), (002), (003) and (005) are observed. These peaks indicate the presence of a layered structure, with a repetition distance d_L of 37.8 Å for **C10** and 37.1 Å for **C11**. Since the calculated molecular longer dimension, with the alkyl chains in all *trans* conformation, is about 37 Å, comparable with the *d* spacing periodicity, it is reasonable to suppose that the smectic layers are parallel to the *ab* plane and the alkyl chains highly interdigitated.

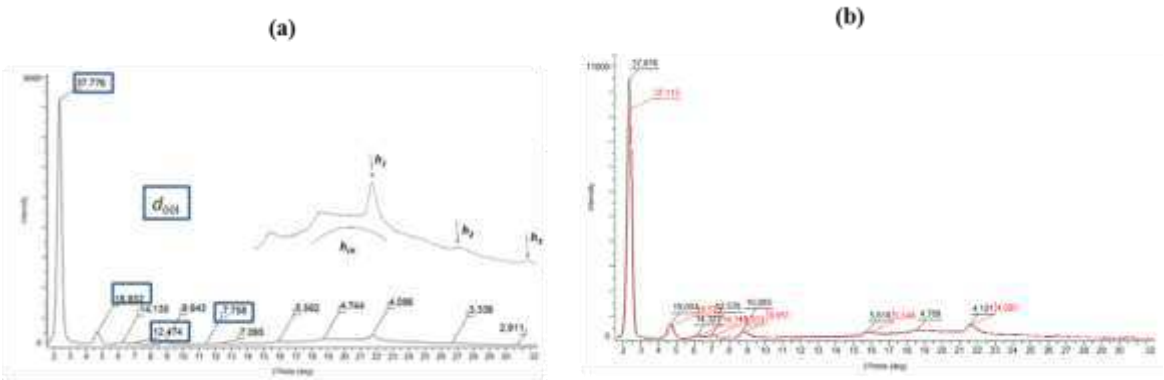

Figure 2-28. X-ray powder diffraction pattern of: (a) complex **C10** recorded on heating in the IInd cycle at 70°C and (b) complex **C11** recorded on heating in the IInd cycle at 75°C (red trace) and at 135°C (black trace).

In both cases, only variation of the structural parameters is observed in the PXRD patterns recorded on the heating/cooling cycles, otherwise registered in the DSC measurements

with relevant transition ΔH values. In particular, following the IInd heating cycle from room temperature to 130°C, the most relevant difference in the PXRD patterns recorded for complex **C10** lies in the position of the (00l) diffraction peaks. The interplanar distance constantly increases moving from 35.6 Å recorded at room temperature up to of 38.3 Å at 130°C. No significant differences are found in the position of the reflection peaks not correlated to the layered structure, meaning that the variation in temperature within the mesophase is only able to affect the most fluid portion of the aggregation, which is the paraffinic layer. Similar change in the layer spacings accompanied by enthalpy changes was reported for ionic liquid crystals as SmA to SmA polymorphic transitions,[342] due to different space requirements of the alkyl chains as a function of their specific conformations.

The columnar sub-structure of the lamellar mesophase is, in both cases, proved by the presence of diffraction peaks in the middle angle region of the PXRD patterns, reflecting the 2D organization of the molecules within each layer, and the presence, in the wide-angle region, of the typical π-π stacking interaction at about 3.5 Å.[343] Indeed, along with the broad halo observed in the wide angle part of the PXRD spectra, centred at 4.4 Å corresponding to the liquid-like order of the molten chains (h_{ch}), two broad peaks (h_2 and h_3 in **Figure 2-28**) centred at about 3.3 and 2.9 Å, in both complexes, are associated with a degree of columnar stacking within the layers, at due the presence of π–π stacking interactions between the large biquinoline aryl surfaces. Moreover, one sharp wide-angle peak is observed at 4.1 Å (h_1), that can be attributed to additional aromatic interactions with correlation found at long-range distance. The indexation of the peaks in the middle-angle region, performed by using the LCDixRay program,[344] is in agreement with a 2D columnar rectangular organization within layers, with calculated unit cell parameters corresponding to the minimum value of the RMSD (root-mean-square-difference) index obtained along the optimization processes (**Table 2-17**). Finally, in both cases the lamello-columnar organization is kept at room temperature just after the first heating/cooling cycle.

Table 2-17. Indexation of X-ray powder diffraction patterns of complexes **C10** – **C11**.

Complex	d_{obs} (Å)	d_{hkl}	d_{calcd} (Å)	Cell parameters
C10	37.78	d_{001}	37.78	
	18.83	d_{002}	18.89	d_{00l} = 37.8 Å
	14.14	d_{010}	14.14	
	12.47	d_{003}	12.59	
	9.94	d_{100}	9.94	L_{col}, T = 70°C
	7.76	d_{005}	7.56	a_r = 9.94 Å
	7.10	d_{020}	7.07	b_r = 14.14 Å
	5.60	d_{120}	5.76	$RMSD_{index}$ = 0.12
	4.74	d_{030}	4.71	
	4.10	h_1		
	3.34	h_2		
	2.91	h_3		
C11	37.13	d_{001}	37.13	
	18.59	d_{002}	18.57	d_{00l} = 37.1 Å
	14.32	d_{010}	14.32	
	12.32	d_{003}	12.38	
	9.95	d_{100}	9.95	L_{col}, T = 75°C
	7.87	d_{005}	7.43	a_r = 9.95 Å
	7.19	d_{020}	7.16	b_r = 14.32 Å
	5.70	d_{120}	5.81	$RMSD_{index}$ = 0.12
	4.74	d_{030}	4.77	
	4.10	h_1		
	3.35	h_2		
	2.91	h_3		

The structural change due to the different substituents on the *bq* ligands on going from **L5** to **L6**, causes a different overall molecular organization within the mesophases of the derived complexes. Indeed, proper columnar phases are formed with temperature in the case of both **C12** and **C13** complexes. The X-ray pattern of complex **C12** (**Figure 2-29**) recorded on cooling in the IInd cycle at 65°C consists, in the small angle region, of three reflections in the ratio 1 : √3 : √4 : characteristic of a two-dimensional lattice of a hexagonal columnar phase (**Table 2-16**), with cell parameter a = 45.5 Å. The fluid-like nature of the phase is confirmed by the diffuse and broad-scattering halo h centred at 4.4 Å at wide angles of the X-ray pattern. On cooling at r.t., the hexagonal columnar arrangement is kept in a kind of glassy state. The

same liquid crystalline behaviour is observed in the case of complex **C13** (**Table 2-18**). The small variation of the structural hexagonal parameter a_h is an indication of the fact that the counter ion is irrelevant in the mesophase supramolecular organization.

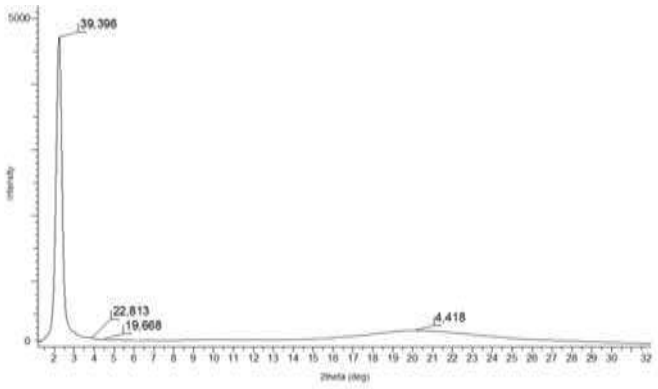

Figure 2-29. X-ray powder diffraction pattern of complex **C12** recorded on cooling in the IInd cycle at 65°C.

Table 2-18. Indexation of X-ray powder diffraction patterns of complexes **C12** – **C13**.

Complex	d_{obs} **(Å)**	d_{hkl}	d_{calcd} **(Å)**	**Cell parameters**
C12	39.40	d_{10}	39.40	Col_h, T = 65°C
	22.81	d_{11}	22.75	a_h = 45.50 Å
	19.69	d_{20}	19.70	$RMSD_{index}$ = 0.06
	4.42	-		
C13	40.18	d_{10}	40.18	Col_h, T = 60°C
	23.04	d_{11}	23.20	a_h = 46.4 Å
	19.93	d_{20}	20.09	$RMSD_{index}$ = 0.3
	13.23	d_{30}	13.39	
	4.36	-		

Emission in condensed state

Regarding the emission of complexes **C10** – **C13** in the solid state at room temperature, a very weak luminescent band was observed at 760 nm for complexes **C10** and **C11** and at 750 nm for complexes **C12** and **C13**. **Table 2-19** reports the absolute emission quantum yields of the solid samples at various temperatures, obtained by using an integrating sphere. By heating, the solid samples evolve towards liquid-crystalline phases that, regardless of the mesophase type, retain the luminescence displayed in the solid state, confirming that the intramolecular

interactions responsible of the emission are still present in the liquid crystalline state. Nevertheless, by increasing temperature, the intensity of the luminescence band decreases, and over 120°C, luminescence is completely quenched; by cooling the samples, luminescence is restored. The decrease of luminescence by increasing temperatures (and vice versa) is attributed to the gain of the non-radiative kinetic constants when vibrational modes are enhanced by heating the samples.

Table 2-19. Emission quantum yields of **C10** – **C13** complexes in different condensed phases at various temperatures.

Complex	Room temperature	50°C	80°C	100°C
C10	2.4%	0.7%	0.2%	0.06%
C11	2.2%	0.5%	0.2%	0.04%
C12	1.5%	0.4%	0.1%	<0.01%
C13	1.1%	0.4%	0.2%	<0.01%

Conclusions

Promesogenic *bq* ligands **L5** and **L6** were used to induce liquid crystalline properties in ionic bis-chelated Cu(I) complexes having ClO_4^- and BF_4^- counterions. The presence of long alkyl chains as substituents on the *bq* ligand, induced thermotropic low temperature liquid crystalline behaviour on the resulting Cu(I) complexes, the type and symmetry depending on the number of the alkyl chains grafted. The dicatenar ligand **L5** induces lamello-columnar mesophases, whereas the hexacatenar **L6** ligand induces columnar hexagonal mesophases in the final complexes.

No emission was found in solution, which is probably due to a flattening of the coordination geometry, arising in the ^{3}MLCT excited state, with a possible variation of the formal oxidation state from Cu(I) to Cu(II), moving towards a planar geometry. However, both in the solid and in the liquid crystalline states, all of the complexes were found to emit weakly in the red region, with emission quantum yields varying depending on the type of aggregation state.

2.4 Conclusions

Chapter 2 presented the original results regarding the synthesis of TMCs based on oligopyridine ligands (*phen, bpy, bq*) having Zn(II) and Cu(I) metal centres.

The new Zn(II) TMCs with *phen* or *bpy* and bioactive ligand quercetin, complexes **C3** and **C4** presented antioxidant activity comparable to that of the free quercetin ligand. The high sensitivity to oxygen was related to antioxidant potency due to a direct trapping of reactive oxygen species (ROS) mechanism. The results of this study were published by our group.[305]

The luminescent new Zn(II) complex, **C5**, with *bq* derivative with hydrophylic chains was reported. Although this complex presented a higher solubility in polar solvents (except water) than Zn(II) complexes with *phen* or *bpy*, the complex nor the ligand did not have any antioxidant activity. The results of this study were disseminated in a paper.[288]

The influence of the counterion (Y^-= ClO_4^-, I^-, SCN^- and BF_4^-) on to the stability of the **C6** – **C9** Cu(I) complexes with the formula $[(phen)_2Cu]^+Y^-$ was investigated and reported here.[327]

Promesogenic *bq* ligands **L5** and **L6** were used to induce liquid crystalline properties in ionic bis-chelated Cu(I) complexes having ClO_4^- and BF_4^- counterions, complexes **C10** – **C13.**

The presence of long alkyl chains as substituents on the *bq* ligand, induced low-temperature thermotropic liquid crystalline behaviour on the resulting Cu(I) complexes, the type and symmetry depending on the number of the alkyl chains grafted. The dicatenar ligand **L5** induces lamello-columnar mesophases, whereas the hexacatenar **L6** ligand induces columnar hexagonal mesophases in the final complexes. The original results of this study were published by our group.[345] Recently, complex **C6** was used as a precursor to modify a carbon nanofiber paste electrode, which generated in-situ copper oxides within carbon nanofiber matrix in alkaline medium for glucose detection, which could be promising electrode material for developing a non-enzymatic electrochemical glucose sensor.[346]

Chapter 3. Zn(II) complexes with terpyridine ligands

Based on the promising results obtained in the previous chapter and higher stability of the Zn(II) complexes, with respect to Cu(I) complexes, we further considered Zn(II) to obtain metallomesogens with terpyridine (*tpy*) derivatives, as shown in **Figure 3-1**. Firstly, to assess the liquid crystalline properties, we used the commercially available **L7** ligand. The terpyridine derivatives **L8**, **L9 and L10**, functionalized with groups important for future applications of the complexes were obtained. These compounds allow derivatization, potentially usable to link the complexes on functionalized metallic and/or oxide nanoparticles or mesoporous silica structures for theranostic purposes. To lower the melting temperatures of the final metallomesogens, ligand **L11** functionalized with a gallate unit was synthesized.

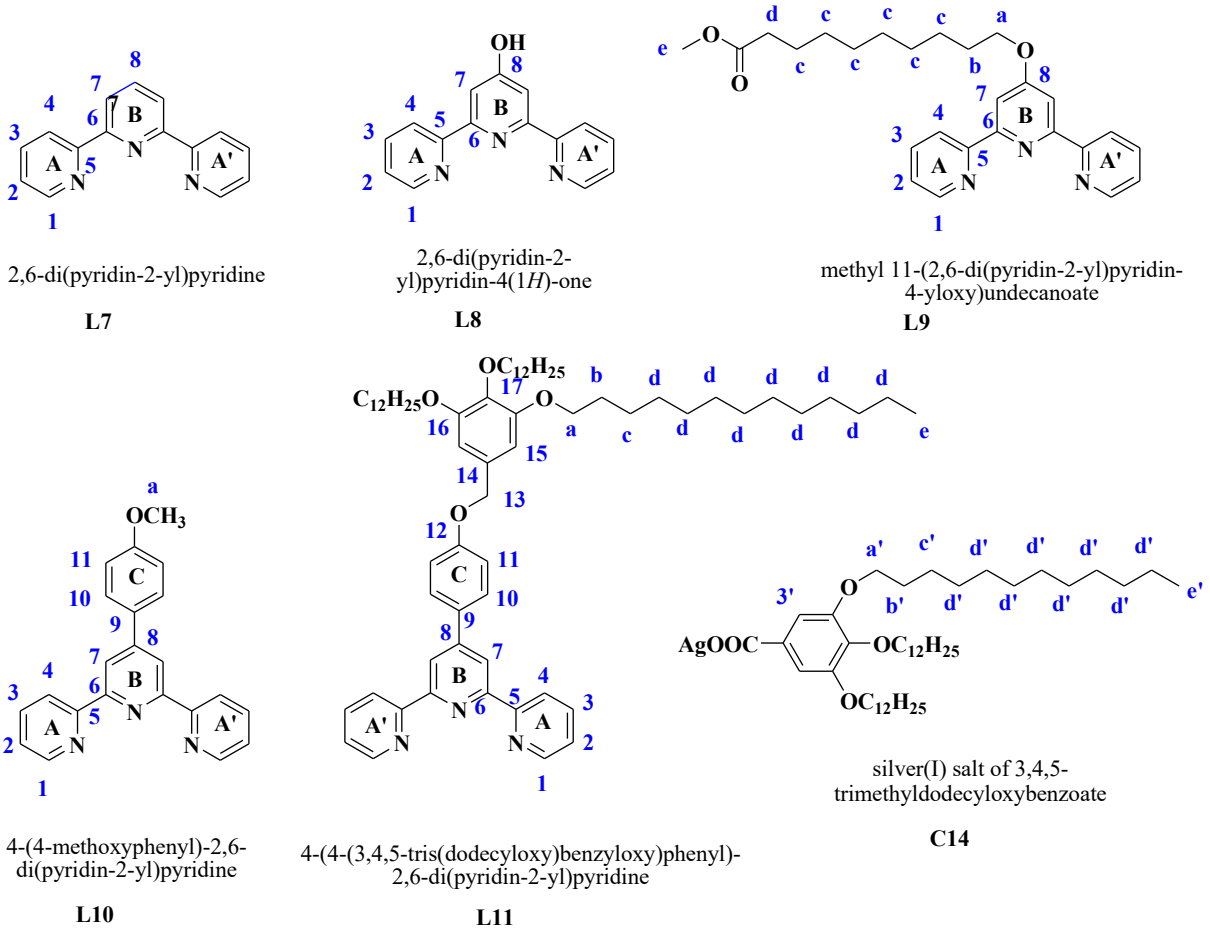

Figure 3-1. Schematic representation of the precursors used in this chapter, their nomenclature and atom labelling.

Zn(II) complexes were prepared by a versatile and straightforward synthesis that permits a facile molecular engineering, by the displacement of Cl ligands with the silver(I) salt of 3,4,5-trimethyldodecyloxybenzoate (**C14**). This strategy allowed us to induce to induce liquid

crystallinity into Zn(II) complexes avoiding the several steps necessary to precisely functionalize the ligands.

3.1 Synthesis and characterization of tpy ligands

This subchapter describes the synthesis and characterization of several 4-substituted *tpy* ligands, which were further employed to synthesize luminescent Zn(II) metal complexes. All of the *tpy* derivatives are already reported in literature.

Ligand **L7** was commercially available whereas the other ligands, **L8** – **L11**, presented in **Figure 3-1** were synthesized as described in the experimental chapter, based on literature methods reported for similar derivatives.[347,348] **Scheme 3-1** and **Scheme 3-2** show the synthesis pathway of the *tpy* derivatives.

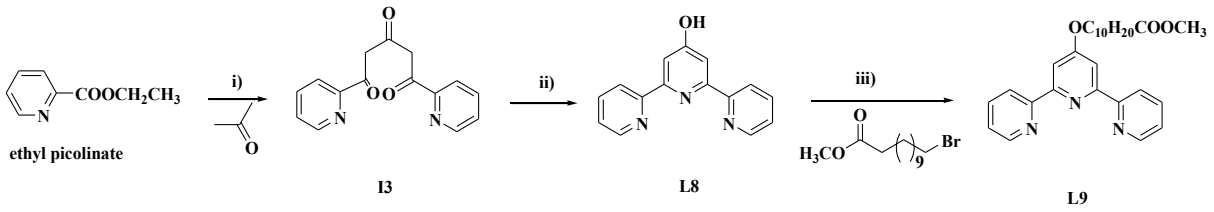

Scheme 3-1. Reaction pathway of ligands **L8** and **L9**. Reagents and conditions: i) NaH, THF, ΔT, 6h; ii) NH_4OAc, EtOH, ΔT, 24h; iii) KOH, DMF dry, Ar, 80ºC, 6h.

Ligand **L8** is a useful starting material for the synthesis of 4'-substituted terpyridine ligands. The synthesis of **L8** implies a double Claisen condensation reaction between two equivalents of 2-ethyl picolinate and one of acetone, leading to triketone intermediate formation (**I3**), which is then reacted with ammonium acetate for the middle ring closure to form **L8** (**Scheme 3-1**).[349] The tautomeric form 4'-hydroxy-2,2':6',2"-terpyridine is obtained by a simple recrystallization from ethanol.[347]

The use of a base leads to the deprotonation of hydroxyl group of **L8**, and the resulting nucleophile can be further reacted with compounds containing a good leaving group (e.g alkyl halides). This method was successfully applied to obtain ligand **L9** following a reported procedure for similar derivatives.[350]

First, ligand **L8** was dissolved in DMF, under argon, and was deprotonated at room temperature using potassium hydroxide as base. The reaction mixture was heated at 80°C and after half an hour, the halogenated compound, methyl 11-bromoundecanoate was added and the stirring continued for 6 hours at 80°C. During this time, a nucleophilic substitution reaction

occurred, which implies the nucleophilic attack of the deprotonated form of ligand **L8** at the halogenated position of the bromo-derivative, leading to the formation **L9** in high yields (>90 %).

In case of the phenyl-substituted *tpy,* **L10** and **L11** (**Figure 3-1**), a different method was approached. Ligand **L10** was synthesized as described in **Scheme 3-2** and it involved a one-pot Kröhnke condensation between 4-methoxybenzaldehyde and 2-acetylpyridine, in a basic media.[351] The pure compound was isolated after a recrystallization from methanol.[348]

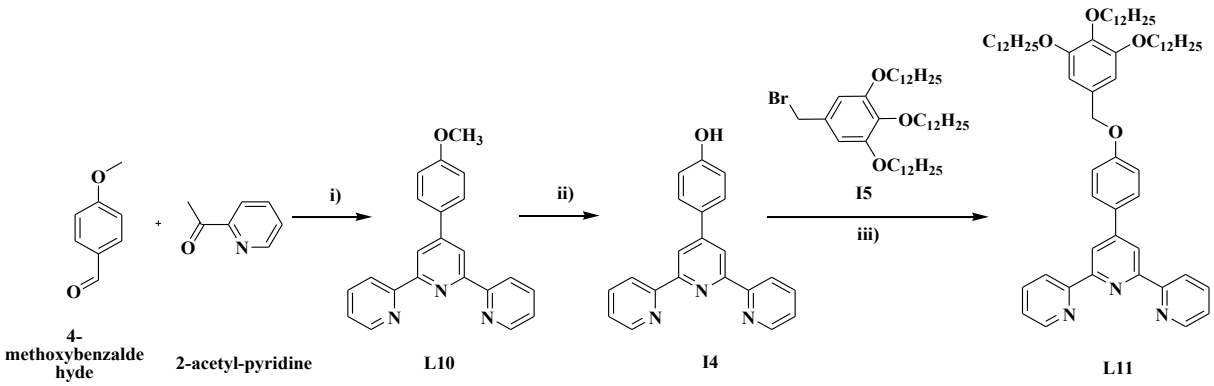

Scheme 3-2. Reaction pathway of ligands **L10** and **L11**. Reagents and conditions: i) KOH, NH_4OH, EtOH, ΔT, 24 h; ii) CH_3COOH/HBr, ΔT, 24 h; iii) K_2CO_3, DMF, 80ºC, 24 h.

In order to obtain **L11**, the terpyridine derivative **L10** was demethoxylated to the hydroxyl form (**I4**), under strong acidic conditions. After the isolation of this intermediate a similar Williamson etherification procedure was applied,[352] as the one described for ligand **L9**: 5-(bromomethyl)-1,2,3-tris(dodecyloxy)benzene (**I5**), 4-([2,2':6',2"-terpyridin]-4'-yl)phenol (**I4**) and K_2CO_3 were ssuspended in 20 mL of DMF. The reaction mixture was stirred at 80ºC under argon for 24 h. The pure product was obtained after a recrystallization from CH_2Cl_2/MeOH.

The nature of the synthesized ligands was established by ^{1}H-NMR and FT-IR spectroscopies.

FT-IR spectroscopy

The main characteristic absorption bands are summarized in **Table 3-1**. For all ligands the signals between 1635 cm^{-1} and 1420 cm^{-1} were atributed to the stretching of the aromatic carbon-carbon $\upsilon_{C=C}$ and carbon-nitrogen bonds, $\upsilon_{C=N,}$ in the pyridyl and phenyl groups of the *tpy* derivatives. The presence of the carboxylic group is evidenced from the FT-IR of ligand **L9**

by an intense absorbtion band at 1745 cm^{-1}, corresponding to the stretching vibration $\nu_{as,(COO^-)}$.[291] In case of ligands **L9** and **L11**, the bands between 2950 - 3000 cm^{-1} $\nu_{as,(CH_3)}$, between 2950 - 3000 cm^{-1}, $\nu_{as,(-CH_2-)}$, and around 2850 cm^{-1}, $\nu_{s,(-CH_2-)}$, are characteristic for the carbon-hydrogen bond from the aliphatic chains.[353]

Table 3-1. Assignment of the characteristic absorption bands of the *tpy* ligands (wavenumber values in cm^{-1}).

Compound	**Assignment of the characteristic absorption bands (wavenumber values in cm^{-1})**				
	$\nu_{as}(CH_3)$	ν_{as} $(-CH_2-)$	ν_s $(-CH_2-)$	$\nu_{as}COO^-$	υ(C=C), υ(C=N)
L7					1422- 1581
L8					1450- 1629
L9	2997	2917	2853	1745	1445- 1585
L10	2993				1432 - 1599
L11	2958	2920	2851		1438- 1604

^{1}H-NMR spectroscopy

All of the synthesized *tpy*-based ligands were characterized by ^{1}H-NMR spectroscopy in $CDCl_3$ solution and their spectra are presented in **Figure 3-2**. The resonances assigned to the aromatic protons of *tpy* derivatives sugest that N-heterocycle rings A and A' are equivalent in the NMR timescale.

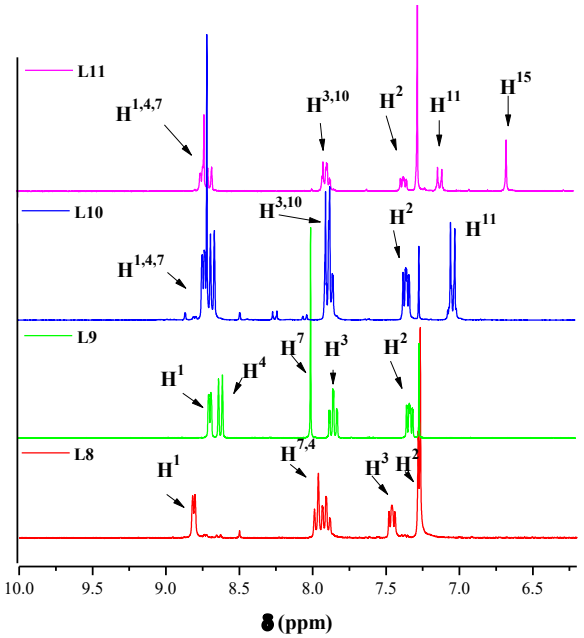

Figure 3-2. ^{1}H-NMR spectra (aromatic region) of *tpy* derivatives **L8** – **L11**.

In case of the substituted *tpy* ligands – as **Figure 3-3** shows, the chemical shifts for aliphatic region of the *tpy* ligands are different, depending on the nature of the substituents used and the number of methylene (CH_2) groups. Due to its proximity to the electronegative oxygen atom directly bound to the terpyridine unit, protons H^a for **L9**, **L10** and H^{13} for **L11** presented the most significant downfield shifting.

In case of ligand **L11** the signals for *tpy* and for the gallate unit can be identified in the aromatic region. Also, protons H^{15} and H^{13} are downfield shifted due to their close proximity to either the terpyridine (H^{15}) or to the gallate unit (H^{13}) oxygen atom.

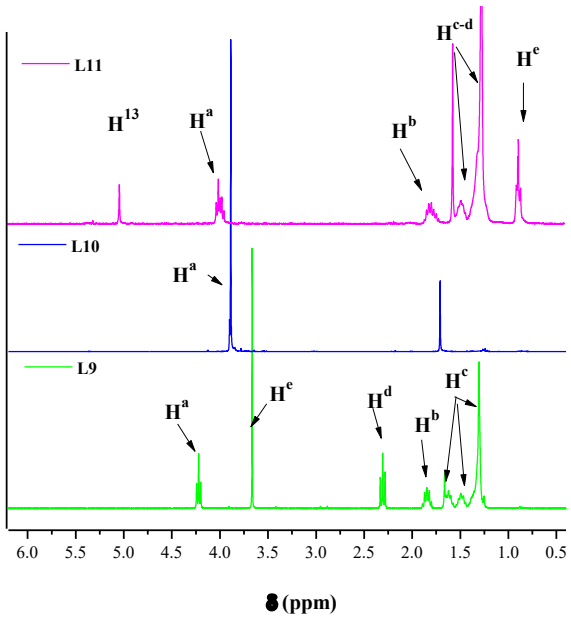

Figure 3-3. ^{1}H-NMR spectra (aliphatic region) of *tpy* derivatives **L9** – **L11**.

Table 3-2. Chemical shifts (δ/ppm) of ligands **L8** – **L11** recorded in $CDCl_3$.

Chemical shifts (in δ/ppm)				
	L8	**L9**	**L10**	**L11**
H^1	8.80	8.69	8.76-8.61[b]	8.77 – 8.63[d]
H^2	7.28	7.33	7.32	7.34
H^3	7.44	7.85	7.95-7.68[c]	7.93 – 7.78[e]
H^4	7.92[a]	8.62	8.76-8.61[b]	8.77 – 8.63[d]
H^7	7.92[a]	8.00	8.76-8.61[b]	8.77 – 8.63[d]
H^{10}			7.95-7.68[c]	7.93 – 7.78[e]
H^{11}			7.03	7.12
H^{13}				5.02
H^{15}				6.66
H^a		4.22	3.89	3.99
H^b		1.85		1.80
H^c		1.66-1.30		1.57 – 1.17[f]
H^d		2.31		1.57 – 1.17[f]
H^e		3.66		0.89
[a-f] protons appear overlapped in the ^{1}H-NMR spectra				

The as-synthesized ligands were further used to obtain metallomesogens based on Zn(II) metal centre. For this, the silver(I) salt of 3,4,5-trimethyldodecyloxybenzoate (**Figure 3-1**) was synthesized and it is described henceforward.

3.2 Synthesis and characterization of the silver(I) salt of 3,4,5-trimethyldodecyloxybenzoate.

The silver(I) salt of 3,4,5-trimethyldodecyloxybenzoate, complex **C14**, was synthesized in a two-step procedure and it involved the reaction of 3,4,5-trimethyldodecyloxy benzoic acid (**I6**) with an excess of NaOH to yield the corresponding sodium salt, and then the exchange of Na^+ ions with Ag^+, using silver nitrate, as depicted in **Scheme 3-3**. The final compound was isolated by filtration and it was obtained in a good yield (80 %). **C14** was characterized by FT-IR and ^{1}H-NMR spectroscopies.

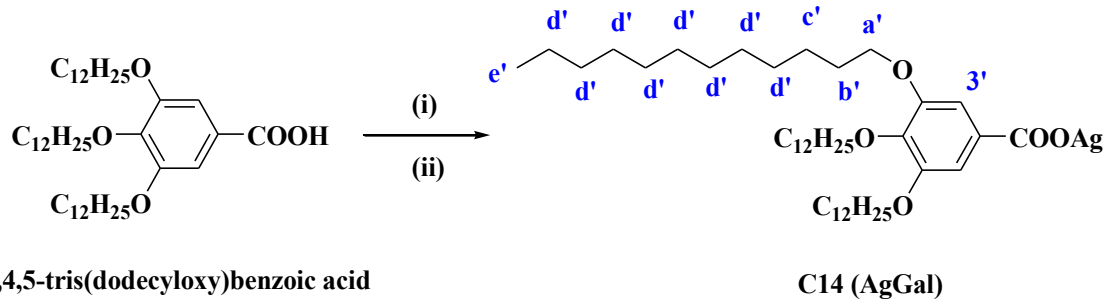

3,4,5-tris(dodecyloxy)benzoic acid **C14 (AgGal)**

Scheme 3-3. Reaction pathway of **C14** complex. Reagents and conditions: i) NaOH, EtOH, r.t, 2 hours; ii) $AgNO_3$, 2 hours.

FT-IR spectroscopy

Figure 3-4 presents the FT-IR spectra of **C14** complex plotted vs. its precursor **I6**. The the bands between 2950 - 3000 cm^{-1} $\nu_{as,(CH3)}$, between 2950 - 3000 cm^{-1}, $\nu_{as,(-CH2-)}$, and around 2850 cm^{-1}, $\nu_{s,(-CH2-)}$, are characteristic for the carbon-hydrogen bond from the aliphatic chains.[353] Also, in case of **C14** the characteristic bands for COO^- group appeared at 1588 cm^{-1}, and were shifted with respect to the precursor **I6**, indicating the successful formation of the silver salt

complex. The wavenumber values of the characteristic absorption bands are summarized in **Table 3-3**.

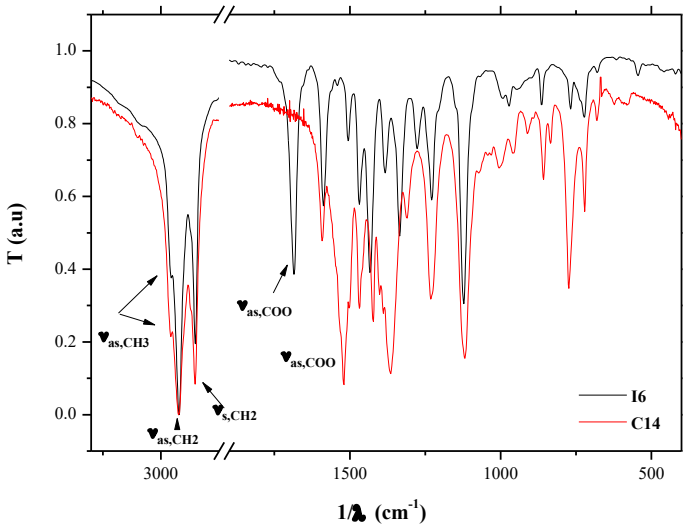

Figure 3-4. FT-IR spectra of Ag(Gal) **C14** plotted against its precursor **I6**.

Table 3-3. Assignment of the characteristic absorption bands of **C14** and **I6** (wavenumber values in cm^{-1}).

Compound	**Assignment of the characteristic absorption bands (wavenumber values in cm^{-1})**			
	$\nu_{as}(CH_3)$	ν_{as} (-CH_2-)	ν_s (-CH_2-)	$\nu_{as}COO^-$
I6	2960	2924	2855	1682
C14	2960	2923	2850	1588

^{1}H-NMR spectroscopy

In order to determine the purity and the molecular structure of **C14**, ^{1}H-NMR spectroscopy was used. For a clearer view, the spectra of the complex **C14** was plotted against its precursor **I6**, as seen in **Figure 3-5**. It can be noticed that after complexation to Ag(I) the aromatic proton $H^{3'}$ presented an upfield shift from 7.32 ppm to 7.22 ppm, suggesting the successful coordination. Also, a significant shift was observed in case of the aliphatic proton $H^{a'}$, which shifted from 4.03 ppm to 3.90 ppm.

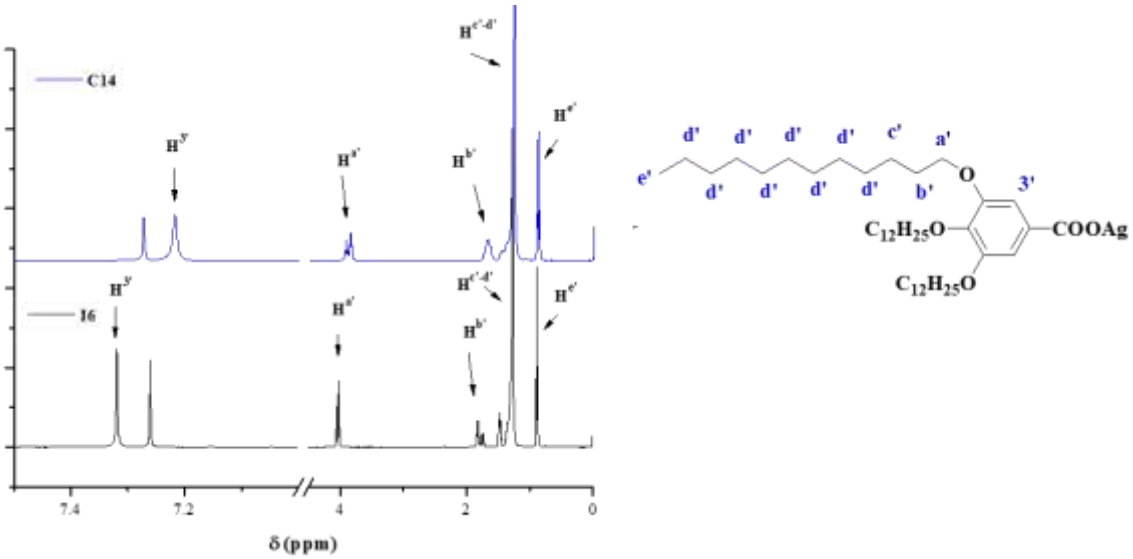

Figure 3-5. ^{1}H-NMR spectra of **C14** complex plotted against its precursor **I6**.

Table 3-4. Chemical shifts (δ/ppm) of complexes **I6** and **C14** recorded in $CDCl_3$.

Chemical shifts (in δ/ppm)		
	I6	**C14**
H$^{3'}$	7.32	7.22
H$^{a'}$	4.03	3.90
H$^{b'}$	1.78	1.66
H$^{c'}$	1.52 – 1.16[a]	1.51 – 1.19[b]
H$^{d'}$	1.52 – 1.16[a]	1.51 – 1.19[b]
H$^{e'}$	0.88	0.89
[a-b] protons appear overlapped in the ^{1}H NMR spectra.		

3.3 Synthesis and characterization of Zn(II) tpy complexes

Ligands **L7**, **L9** – **L11**, were reacted with a small excess of $ZnCl_2$, to yield $[Zn(Ln)Cl_2]$.[126] These precursors were further reacted with silver(I) salt of 3,4,5-trimethyldodecyloxybenzoate, Ag(Gal), to yield the new complexes $[Zn(Ln)(Gal)_2]$, as depicted in **Scheme 3-4**. The synthesis and characterization of the new Zn(II) complexes with ligand **L9**, were reported by our group.[354]

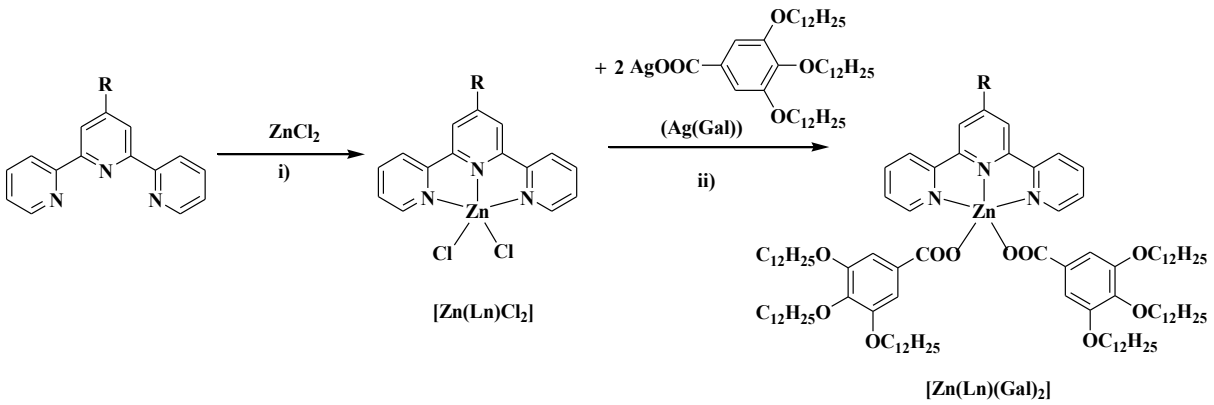

Ligand	R =	[Zn(Ln)Cl$_2$]	[Zn(Ln)(Gal)$_2$]
L7	-H	C15	C16
L9	-OC$_{10}$H$_{20}$COOMe	C17	C18
L10	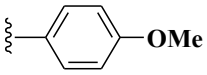	C19	C20
L11	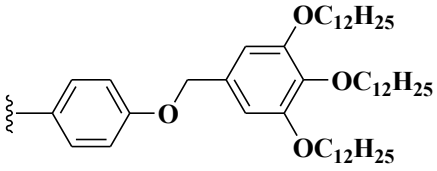	C21	C22

Scheme 3-4. Reaction pathway of Zn(II) *tpy* complexes. Reagents and conditions: i) MeOH/$CHCl_3$, r. t., 1.5 hours; ii) $CHCl_3$, r. t., 2 hours.

The complexes were obtained as white or pale rosy powders in relatively good yields (45 – 90%). The as synthesized complexes were characterized through FT-IR and ^{1}H NMR spectroscopies and their photophysical properties were investigated both in solution and in condensed states. Moreover, the thermal behaviour and liquid-crystalline self-assemblies were fully characterized by POM, DSC, TGA and SWAXS.

3.3.1 Synthesis and characterization of Zn(II) tpy complexes with L7 ligand

The reaction of the *tpy* ligand **L7** with $ZnCl_2$ afforded the neutral complex **C15**, **Figure 3-6**, with the metal centre penta-coordinated by the tridentate terpyridine and two monodentate chlorine ligands. Further reaction of **C15** with 2 equivalents of Ag(Gal) yielded the neutral **C16** with two gallate ligands saturating the coordination sphere of the Zn(II) metal centre in 47 % yield. The complexes were characterized by FT-IR and ^{1}H-NMR spectroscopies and their

photophysical properties were investigated both in solution and in condensed states. Moreover, the thermal behaviour and liquid-crystalline self-assemblies were fully characterized by POM, DSC, TGA and SWAXS.

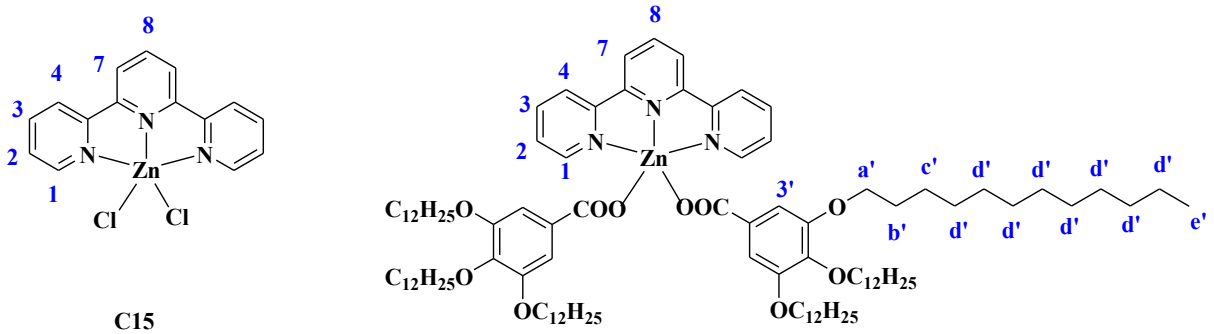

Figure 3-6. The proposed structures of the complexes **C15** and **C16** with **L7** and their atom labelling.

FT-IR spectroscopy

Figure 3-7 presents the FT-IR spectra of the complex **C15** plotted against **L7** ligand. By comparing these two spectra, the $\upsilon_{C=C}$ and $\upsilon_{C=N}$ characteristic bands present a significant shift to higher frequencies compared to the *tpy* ligand which indicates the coordination via the nitrogen atoms of the ligand.[355] In case of complex **C16** the FT-IR spectra shows the presence of the symmetric and antisymmetric stretching modes of the methylene [–$(CH_2)_n$–] groups corresponding to aliphatic chains $\upsilon_{(CH2)}$ of the gallate unit.[356] Moreover, the exclusively coordinating mode of the gallate unit is demonstrated by the separation of the stretching vibrations of COO^- group.[357] Indeed, the asymmetric stretching vibration for $\nu_{as(COO^-)}$ is found at 1623 cm^{-1}, while the symmetric one is observed at 1359 cm^{-1}, giving a separation (Δ) of 264 cm^{-1}. **Table 3-5** presents the assignment of the main characteristic absorption bands.

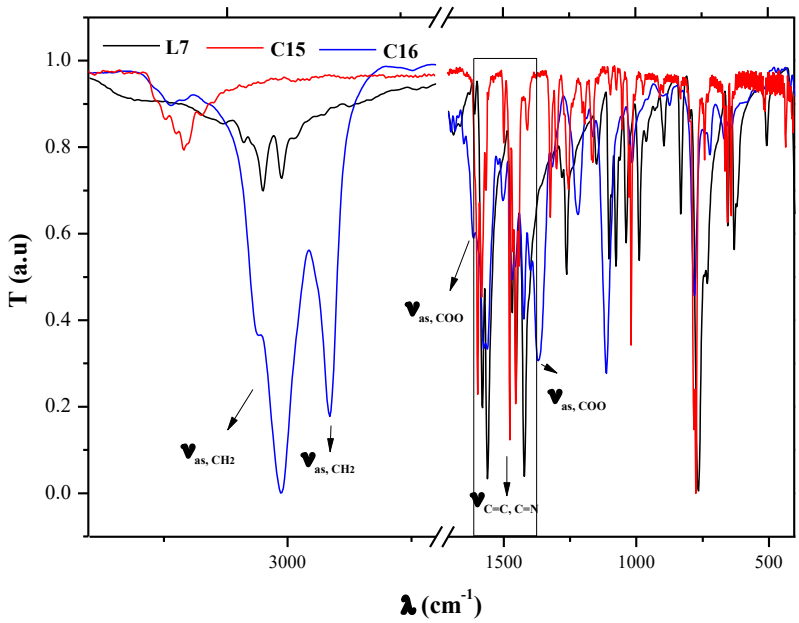

Figure 3-7. FT-IR spectra of complexes **C15** and **C16**, plotted against the free ligand **L7**.

Table 3-5. Assignment of the characteristic absorption bands of **C15** and **C16** (wavenumber values in cm^{-1}).

Assignment of the characteristic absorption bands (wavenumber values in cm^{-1})					
Complex	$\nu_{as,(-CH2-)}$	$\nu_{s,(-CH2-)}$	$\nu_{as,(COO^-)}$	$\nu_{s,(COO^-)}$	$\upsilon_{C=C}$, $\upsilon_{C=N}$
C15					1594-1448
C16	2924	2854	1623	1359	1567-1428

^{1}H-NMR measurements

Due to the different solubilities the NMR spectra of complex **C15** was recorded in DMSO-d_6, and for **C16** in $CDCl_3$. Also, the spectra of **L7** was not recorded. However, the aromatic proton signal of the gallate unit, $H^{3'}$ is observed at 7.27 ppm (overlapped with $CDCl_3$ signal), suggesting that the ligand exchange took place (**Figure 3-8**). Another proof of the ligand exchange was given by the chemical shift of $H^{a'}$ protons corresponding to Ag(Gal) from 4.01 ppm to 3.94 ppm. The chemical shifts of the protons of complexes **C15** and **C16** are summarized in **Table 3-6**.

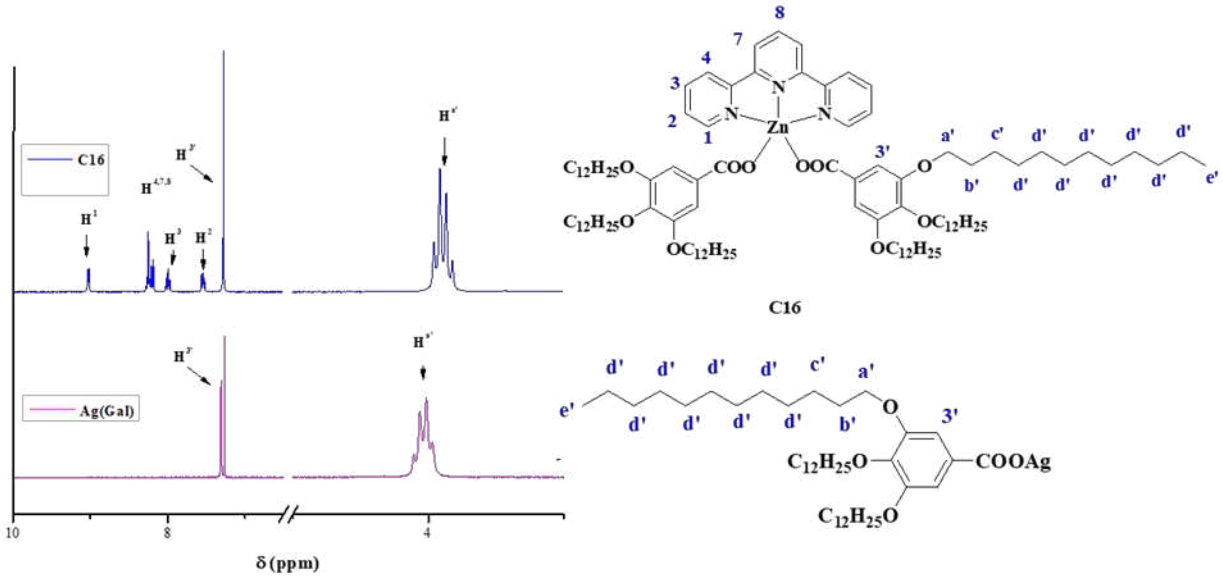

Figure 3-8. ^{1}H-NMR spectra of **C16** complex plotted against Ag(Gal).

Table 3-6. Chemical shifts (δ/ppm) of complexes **C15** (in DMSO-d_6) and **C16** (in $CDCl_3$).

Chemical shifts (in δ/ppm)		
	C15	**C16**
H^{1}	8.84	9.02 [a]
H^{2}	7.88	7.54
H^{3}	8.34	7.99
H^{4}	8.84	8.39 – 8.12[a]
H^{7}	8.60	8.39 – 8.12[a]
H^{8}	8.60	8.39 – 8.12[a]
H$^{3'}$		7.27 [c]
H$^{a'}$		3.94
H$^{b'}$		1.75
H$^{c'}$		1.47 – 1.27[b]
H$^{d'}$		1.47 – 1.27[b]
H$^{e'}$		0.88
[a-b] protons appear overlapped in the ^{1}H NMR spectra, [c]- overlapped with the signal of $CDCl_3$		

Absorption and emission spectroscopy in solution

The absorption and emission properties of the complexes **C15** and **C16** were investigated in $CHCl_3$. All samples appear colourless in diluted solutions and absorb in the UV region of the electromagnetic spectra. The complexes do not follow the Lambert-Beer Law: the molar absorptivity (ε (λ)) of a dilute solution (10^{-6} M) results greater than a concentrated one (10^{-5} M) for all the samples.

The absorption spectra of **C15** and **C16** complexes registered in $CHCl_3$ solution (**Figure 3-9**) show a series of bands (**Table 3-7**) in the UV portion of the electromagnetic spectrum, all originating from *tpy* LC transitions.[358,359]

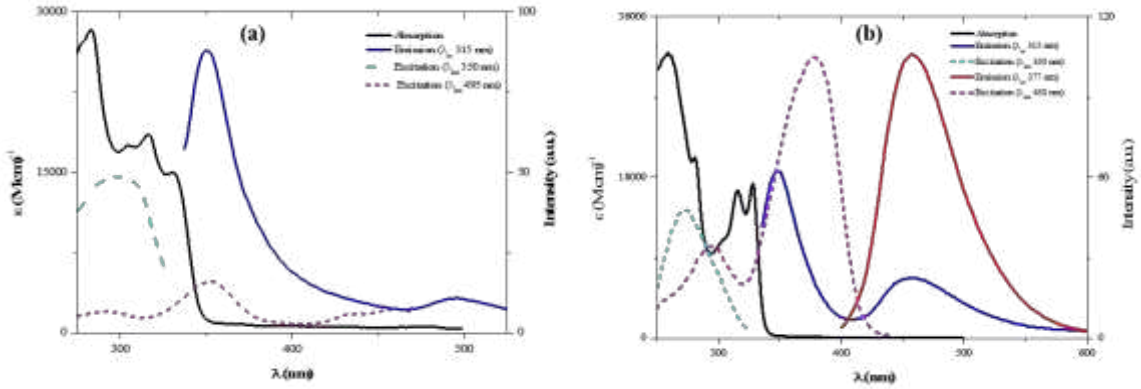

Figure 3-9. Absorption, emission and excitation spectra of: (a) **C15** in diluted DMSO solution (1.4 10^{-5} M) and (b) **C16** in diluted $CHCl_3$ solution (8.3 10^{-5} M).

The emission spectra of **C15** and **C16** shows a double emission band: a blue-shifted one centred at 350 nm and a red-shifted one centred 495 and 455 nm, respectively. The excitation spectra registered on these emission maximums are different with respect to the absorption spectra of the relative complex.

Table 3-7. Absorption and emission data of **C15** and **C16** complexes in dilute solution.

Complex	**Absorption, λ_{max}/nm (ε/M^{-1} cm^{-1})**	**Emission, λ_{max}/nm**	**Lifetime,τ /ns (α_i/%)**		
C15	283 (28390), 305 (17520), 316 (18550), 330 (15000)	350	5.1 (45)	31 (30)	0.9 (25)
		495	7.5		
C16	254 (57070), 264 (56070), 283 51950), 299 (39680), 322 (41700), 333 (37580)	350			
		455			

Thermal and mesomorphic behaviour

The thermal behaviour of **C15** and **C16** was first investigated by POM, TGA and DSC. The complex without Gal unit, **C15** was obtained as amorphous solid with high melting point, and, as expected, deprived of liquid crystalline properties much due to the absence of aliphatic chains. The introduction of lipophilic gallate units as monodentate ligand **C16**, resulted in the drastic lowering of the melting points and in the induction of mesomorphism (**Table 3-8**).

TGA analysis of complex **C15** revealed weight loss from water or solvent release above 150°C and the compound decomposed at $T_{5\%}$ = 388°C, whereas complex **C16** was found to be stable up to 245°C.

The mesomorphic behaviour was firstly investigated by POM observation. As expected, complex **C15** did not present LC properties, whereas complex **C16** transits into the isotropic phase at 122^0C. However, a birefringent fan-shaped LC texture was observed on both heating and cooling cycles, pointing towards a lamellar structure (**Figure 3-10**). The complex kept its texture up until room temperature.

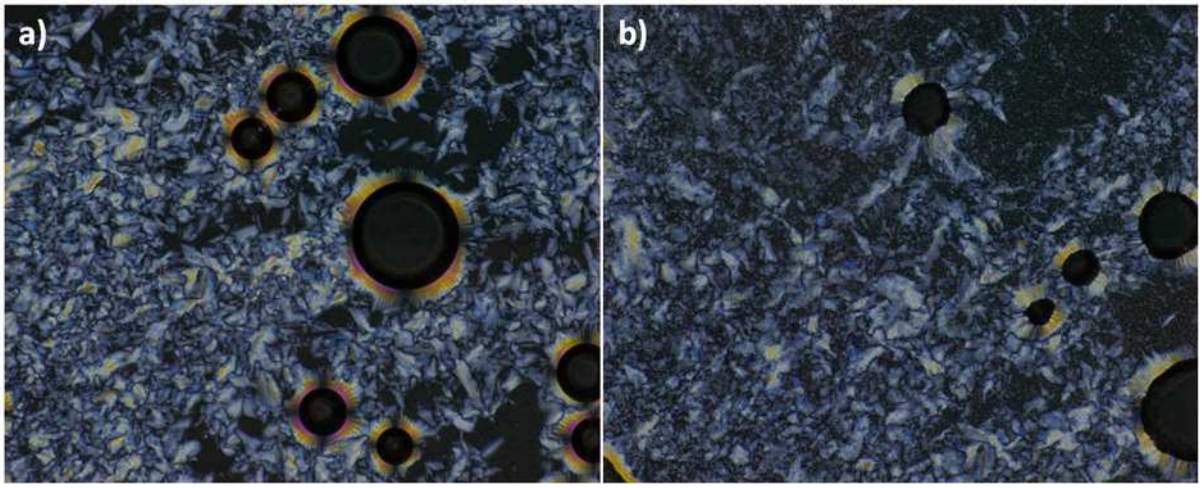

Figure 3-10. POM micrographs of the textures exhibited by complex **C16** on cooling from the isotropic liquid at: (a) 118^0C and (b) 65^0C.

Table 3-8 summarizes the thermal and mesomorphic behaviour of complexes **C15** and **C16**. SWAXS analysis combined with POM observations, revealed a smectic A organisation (SmA) at higher temperatures, and at lower temperatures the coexistence of crystal (Cr) and smectic (Sm) phases for **C16**.

Table 3-8. Thermal behaviour of complex **C15** and **C16**.

Complex	**$T_{dec\ 5\%}$ /°C[a]**	**Thermal properties: mesophases, [b] transitions temperatures[c] (in°C) and enthalpies (ΔH in kJ mol^{-1})**
C15	358°C	Dec[d]
C16	245°C	[Cr+Sm] 95 (7.3), SmA 95.5 (1.5), Iso Iso 109.7 (1.62), SmA 70.5 (6.1), [Sm+Cr] (-)
[a] Significant weight loss (5%) from degradation from TGA trace; [b] Determined on first cooling and second heating (for mesomorphous compounds), and only first heating for the other: Cr, crystalline phase; Sm and SmA, smectic mesophases; Iso, isotropic liquid. [c] onset peaks; [d] decomposition before melting.		

Characterization of the mesophases by Small- and Wide- Angle X-ray Scattering (SWAXS)

The SWAXS patterns were recorded at various temperatures and are presented in **Figure 3-11**. The data collected from various temperatures allowed the calculation of the main

geometrical phase parameters (**Table 3-9**). The benzoate ligands consist of gallate units substituted with long alkyl chains, whose rejection into adjacent molten aliphatic layers generates a smectic A-like organization, as presented in **Figure 3-12**. The formation of such lamellar structure supposes that the molecular packing within the aromatic layer matches the high overall cross-sectional area of the six pending chains ($6\times\sigma_{ch}$ » 130 Å^2). This condition is realized through a monolayer configuration alternating terpyridine rings and gallate segments in the layer plane. This arrangement, which is also found in CSD-BETWOO[158] and otherwise explains the in-plane periodicity D_{ar}, offers a high molecular cross-section (S_{ZnAr} = 87 Å^2 in CSD-BETWOO and S_{ZnAr} ≈ 95 Å^2 in **C16**). Above all, it allows sharing alkyl substituents between both adjacent layers and thus elevating the molecular area to A_{mol} ≈ 190 Å^2, which even exceeds the requirement for alkyl chains. This discrepancy is however easily compensated by a higher degree of folding of the chains, to the cost of more diffuse interfaces and of a lower efficient nanosegregation between antagonistic moieties. This effect should contribute to the narrowness of the smectic range and to the difficulty to detect the lamellar higher order reflections.

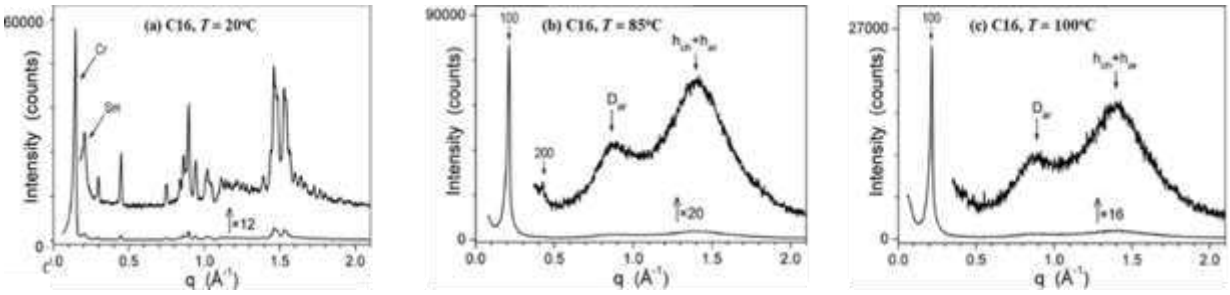

Figure 3-11. SWAXS patterns of **C16**: (a) at room temperature in the pasty states of the crystal and mesophase, and in the fluid smectic mesophase (b) at 85°C and (c) at 100 ^{0}C.

Table 3-9. Mesophases parameters of complex **C16**.

Phase $T^{[a]}$	V_{mol} $\rho^{[b]}$	d_{lam}[c]	N_{molL}[d] A_{mol}	N_{arL}[e] S_{ZnAr}	N_{chL}[f] S_{ch}	q_{ch}[g]
Sm$_A$, 85	2753 0.99	29.31	2 188	1 94	2 31.3	1.41
Sm$_A$, 100	2781 0.98	28.91	2 192	1 96	2 32.1	1.43

[a] temperature of the measurement (°C). [b] V_{mol}, calculated molecular volume (Å^3); ρ, density (g/cm^3). [c] d_{lam}, lamellar periodicity (Å); [d] N_{molL}, number of molecular layers per lamella; $A_{mol} = N_{molL}\times V_{mol}/d$, molecular area (Å^2); [e] N_{arL}, number of aromatic layers per lamella (N_{arL} = 1 for monolayer arrangement); $S_{ZnAr} = (N_{arL}/N_{molL})\times A_{mol}$, surface per Zinc complex (Å^2); [f] N_{chL}, number of chain layers per lamella (N_{chL} = 2 for non-interdigitated chains); $S_{ch} = (N_{chL}/N_{molL})\times A_{mol}/n_{ch}$, surface per chain (Å^2), n_{ch} = 6 being the number of peripheral chains per molecule; [g] $q_{ch} = S_{ch}/\sigma_{ch}$, chain packing ratio, σ_{ch} = 21.2 (1+7.5E-4 (T-20)) (Å^2) being the cross-sectional area of a molten chain;

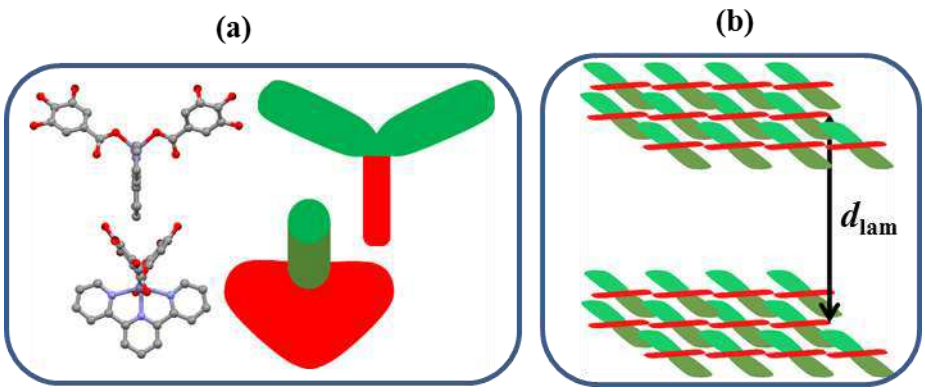

Figure 3-12. (a) Two rotated side-views of the aromatic moiety of **C16**, as deduced from structure CSD-BETWOO,[158] and schematic representation of the molecular architecture; and (b) molecular organization of **C16** in the SmA phase through self-assembly of aromatic moieties into monolayers alternating with molten chains (not represented).

Emission spectroscopy in condensed state

Accurate structural and photophysical investigations in condensed state was realized to study how the mesophase organization has an influence on the emitting states. It is known that Zn(II) prefers tetrahedral or higher coordination number geometries, advantageous for luminescence properties (blocking excimer formation), but detrimental for inducing low temperature mesomorphism. Thus, for obtaining luminescent Zn(II)-based MMs, a luminescent ligand functionalized with several alkyl chains is preferred, which upon coordination with Zn(II) ions stabilizes the excited states, whereas the alkyl chains give fluidity to the system.[360] **Figure 3-13** shows the emission spectra recorded in the solid state at room temperature of complexes **C15** and **C16.** It was found that both complexes were luminescent in the visible region of electromagnetic spectra. By comparing the spectral features of **C15** and **C16** in solution (**Table 3-7**), with those in the pristine state at room temperature (**Table 3-10**), a red shift of the emission maxima was observed in case of both complexes. The emission maxima, quantum yields and lifetimes are reported in **Table 3-10**.

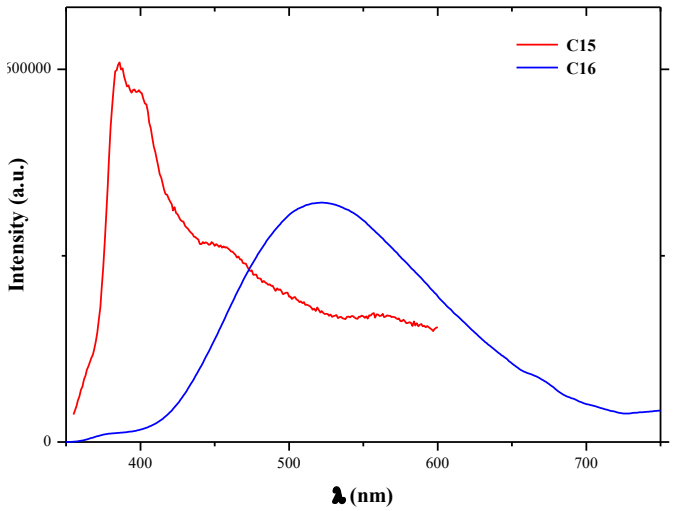

Figure 3-13. Emission spectra of **C15** and **C16** in the solid state at room temperature.

Table 3-10. Photophysical data of **C15** and **C16** in solid state at room temperature.

Complex	Emission, λ_{max} /nm [λ_{ex}]	Quantum yields, ϕ /%	Lifetime,τ /ns (α_i/%)		
C15	400 [340 nm]	n.d.	0.8 (72)	2.2 (21)	94.9 (7)
	460 [340 nm]		11 (48)	69.2 (4)	4.1 (48)
	580 [340 nm]		5.45 (36.5)	15.7 (63)	0.45 (0.5)
C16	520 [335 nm]	n.d.	12.7 (30)	37.3 (65)	0.88 (5)

For complex **C16**, the effect of the mesogenic arrangement on the emission properties was investigated by measuring the quantum yields with temperature variation and the results are summarized in **Table 3-11**. Because it was not possible to measure the quantum yields at room temperature, hence the quantum yields on varying temperature were measured assuming a reference value (R) equal to one for the emission at 30°C. It can be noticed that the quantum yield decreases, with the increase of the temperature, due to the non-radiative deactivations raise triggered by the high temperature. Trends are reversible by decreasing temperature, but the initial higher values are never restored in relation with structural changes on first heating.

The lamellar structure of the **C16** complex is indeed initially disordered (**Figure 3-11**), and the regular arrangement only develops with the softening of the sample on first heating. Such a transformation obviously creates interactions between the compounds which stabilize the excited state, as indicated by the red-shift of the emission band.

Table 3-11. Quantum yields for **C16** by varying the temperature (λ_{ex} = 360 nm).

Ist cycle						IInd cycle					
Heating			Cooling			Heating			Cooling		
T/°C	λem/ nm	ϕ (%)	T/°C	λem/ nm	ϕ (%)	T/°C	λem/ nm	ϕ (%)	T/°C	λem/ nm	ϕ (%)
30	523	R= 1	100	539	0.08	30	508	0.42	100	529	0.07
50	521	0.97	50	510	0.3	50	n.d.	n.d.	50	513	0.27
110	524	0.09	30	508	0.42	110	532	0.07	30	514	0.31
130	544	0.05				130	525	0.04			

3.3.2 Synthesis and characterization of Zn(II) tpy complexes with L9 ligand

The reaction of the *tpy* ligand **L9** with $ZnCl_2$ afforded the neutral complex **C17**, **Figure 3-14**, with the metal centre penta-coordinated by the tridentate terpyridine and two monodentate chlorine ligands. Further reaction of **C17** with 2 equivalents of Ag(Gal) yielded the neutral complex with two benzoate ligands saturating the coordination sphere of the Zn(II) metal centre. The AgCl formed was removed by filtration, and the pure product was obtained from the filtrate by recrystallization from $CHCl_3$/MeOH, with a yield of 75%.

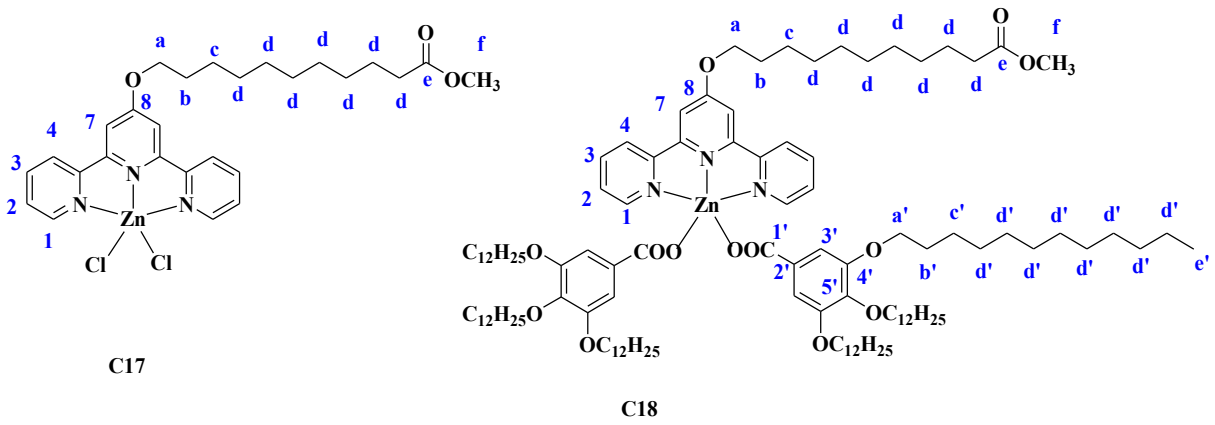

Figure 3-14. The proposed structures off the complexes **C17** and **C18** with **L9** and their atom labelling.

FT-IR spectroscopy

The FT-IR spectra of complexes **C17** and **C18**, shown in **Figure 3-15** presented a shift to higher frequencies of the characteristic absorption bands corresponding to $\upsilon_{C=C}$ and $\upsilon_{C=N}$. **C17** presented a broad band from *ca.* 3400 to 2800 cm^{-1}, which was attributed to the presence of H_2O. Also in case of both complexes the stretching vibration for $\nu_{as(COO^-)}$ corresponding to methanoate group was identified at 1752 cm^{-1}. Moreover, the exclusively coordinating mode of the gallate unit is demonstrated by the separation of the stretching vibrations of COO^- group.

Indeed, the asymmetric stretching vibration for $\nu_{as(COO^-)}$ is found at 1630 cm^{-1}, while the symmetric one is observed at 1304 cm^{-1} , giving a separation (Δ) of 326 cm^{-1}.[357] The assignments of the characteristic absorption bands for complexes **C17** and **C18** are summarized in **Table 3-12**.

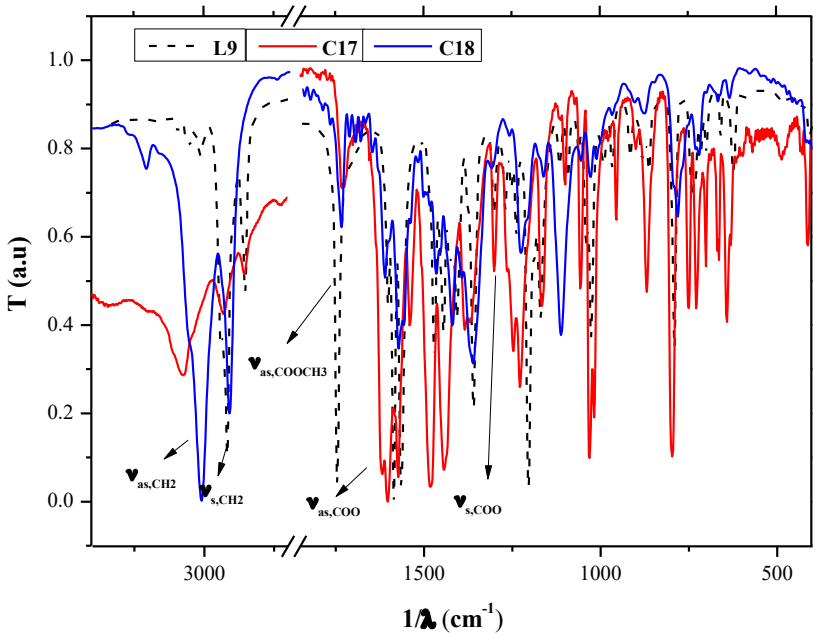

Figure 3-15. FT-IR spectra of **C17** and **C18** complexes, plotted against the free ligand **L9**.

Table 3-12. Assignment of the characteristic absorption bands of **C17** and **C18** complexes (wavenumber values in cm^{-1}).

Assignment of the characteristic absorption bands (wavenumber values in cm^{-1})						
Complex	$\nu_{as,(-CH2-)}$	$\nu_{s,(-CH2-)}$	$\nu_{as,(COOCH3)}$	$\nu_{as,(COO^-)}$	$\nu_{s,(COO^-)}$	$\upsilon_{C=C}$, $\upsilon_{C=N}$
C17	2860	2804	1752			1571-1439
C18	2864	2807	1752	1630	1304	1571-1439

^{1}H-NMR spectroscopy

Due to the different solubilities, the NMR spectra of complex **C17** was recorded in DMSO-d_6, while the spectra of ligand and complex **C18** were registered in $CDCl_3$. The proton assignments of **C17** and **C18** are summarized in **Table 3-13**. By comparing the spectra of **C18** and of the free *tpy* ligand, **Figure 3-16**, significant changes in the aromatic region can be observed: protons H^1 presented a shift to higher frequency, from 8.69 ppm to 8.94 ppm, whereas those belonging to H^4 presented a shift to lower frequencies, from 8.46 ppm to 8.15 ppm. In

particular, the spectra of **C18** shows the signals corresponding to the aromatic proton of Gal unit ($H^{3'}$) at 7.31 ppm.

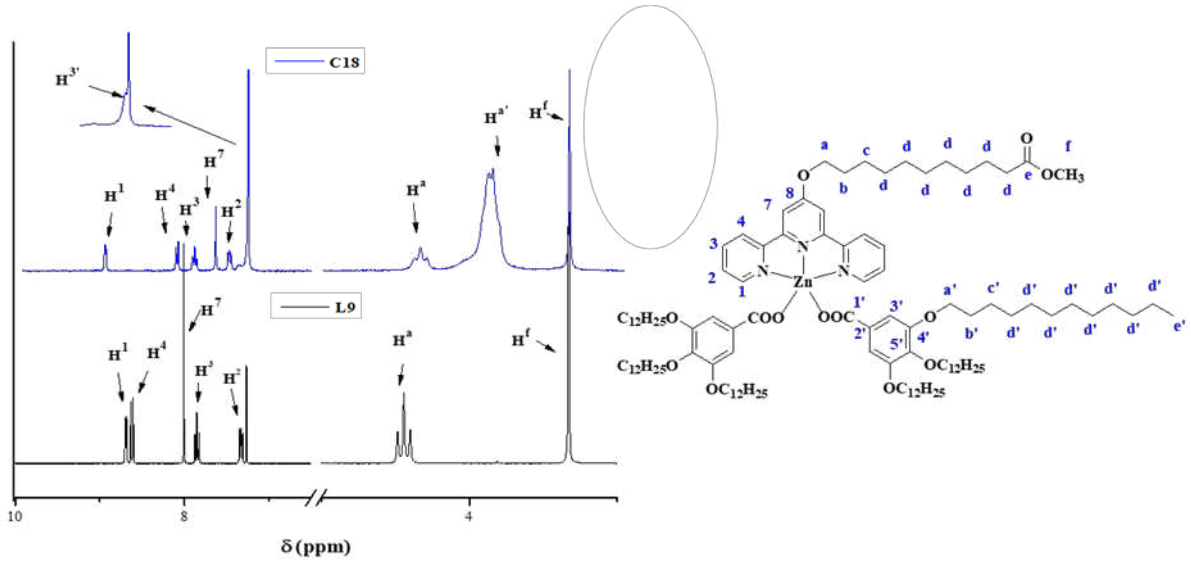

Figure 3-16. ^{1}H-NMR spectra of complex **C18** and of the free ligand **L9**.

Table 3-13. Chemical shifts (δ/ppm) of complexes **C17** (in DMSO-d_6) and **C18** (in $CDCl_3$).

	Chemical shifts (in δ/ppm)	
	C17	**C18**
H^1	8.82	8.94
H^2	7.87	7.41
H^3	8.37 – 8.30[a]	7.73
H^4	8.72	8.15
H^7	8.37 – 8.30[a]	7.65
$H^{3'}$		7.31
H^a	4.34	4.17
H^b	1.76	1.70
H^c	1.59 - 1.01	1.60 – 1.26 [b]
H^d	2.27	2.31
H^f	3.57	3.68
$H^{a'}$		3.91
$H^{b'}$		1.60 – 1.26
$H^{c'}$		1.60 – 1.26 [b]
$H^{d'}$		1.60 – 1.26 [b]
$H^{e'}$		0.88
[a-d]: protons appear overlapped in the ^{1}H NMR spectra		

Absorption and emission spectroscopy in solution

The absorption spectra of **C17** and **C18** complexes registered in CH_2Cl_2 solution (**Figure 3-17 a**) show a series of bands (**Table 3-14**) in the UV portion of the electromagnetic spectrum, all originated from *tpy* LC transitions.[358,361] In particular, for **C18**, these transitions overlap with those localized on benzoate ligand, giving rise to a broad band below 300 nm. By

comparing the absorption spectra of the **C18**, **Figure 3-17 a**, with that of the *tpy* ligand, **Figure 3-17 b**, it can be noted that in this last one the bands above 300 nm are very low in intensity, while in the absorption spectra of the complexes these bands have an intensity comparable with those of the other bands. This different spectral behaviour is due to the different symmetry of the free and zinc-bonded *tpy*; the free *tpy* shows the nitrogen atoms of the lateral pyridines both facing from the opposite side with respect to the nitrogen atom of the central pyridine,[359] while when the *tpy* binds zinc ion all the nitrogen atoms are facing the same side.

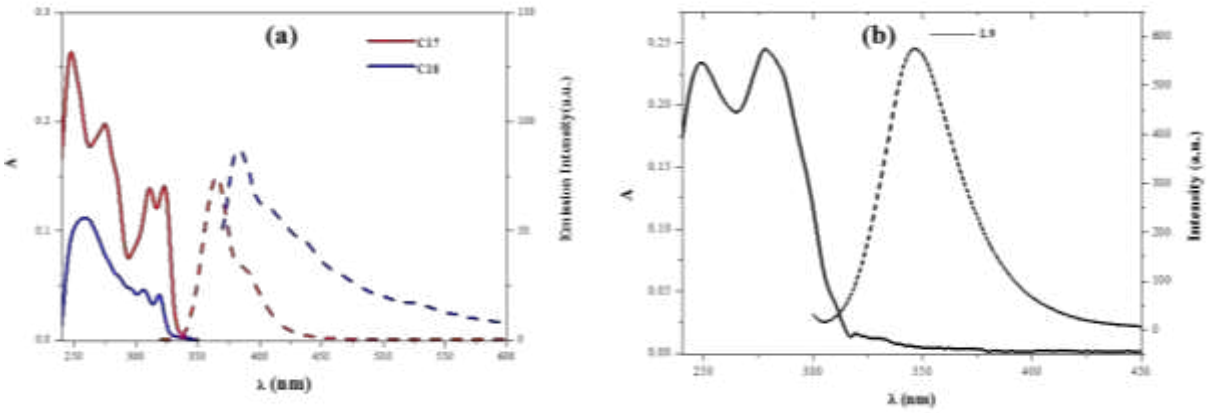

Figure 3-17. Absorption (continuous line) and emission (dashed line) spectra of (a) **C17** and **C18** complexes and of (b) **L9** ligand in CH_2Cl_2 solutions at room temperature.

Both complexes resulted to be fluorescent, showing asymmetric emission band at 365 nm (with a vibronic shoulder at 386 nm) for **C17**, and at 379 nm (and a long tail extending towards the green spectral range) for **C18** (**Figure 3-17 a**).

Table 3-14. Photophysical data of **C17** and **C18** complexes in dilute solutions.

Complex	**Absorption, λ_{max}/nm (ε/M^{-1} cm^{-1})**	**Emission, λ_{max}/nm**	**Lifetime,τ /ns**	
C17	248,275,311,323	365	6.4	
C18	258 (28030), 285 (15150),306 (11620), 319 (10100)	379	24.5	2.7

The luminescence intensity is quite high, with an emission quantum yield of 6.4 % for **C17** and 24.5 % for **C18**; time-resolved measurements give a mono-exponential decay of the excited states, with lifetimes of respectively of 1.2 and 2.7 ns (**Table 3-14**). By comparing the emission spectra of the two zinc complexes, it is evident that the substitution of the two chlorine atoms with two electron-donor benzoate groups involves a lowering of the energy of the

emitting state, an increase of the Stokes-shift and, above all, a considerable increase in the emission quantum yield.

Thermal and mesomorphic behaviour

The thermal behaviour was first investigated by POM, TGA and DSC. Complex **C17** had high melting point, and, as expected, deprived of liquid crystalline properties much due to the absence of aliphatic chains. The introduction of lipophilic gallate units as monodentate ligand to yield **C18** resulted in the drastic lowering of the melting point and induction of mesomorphism. (**Table 3-15**).

Table 3-15. Thermal behaviour of complex **C17** and **C18**.

Complex	**$T_{dec\ 5\%}$ /°C[a]**	**Thermal properties: mesophases,[b] transitions temperatures[c] (in°C) and enthalpies (ΔH in kJ mol^{-1})**
C17	246	Cr 243 (-)[e] Iso
C18	309	Col_{hex} 101 (2.2) Iso Iso 108 (-2.0) Col_{hex}

[a] Significant weight loss (5%) from degradation from TGA trace; [b] Determined on first cooling and second heating (for mesomorphous compounds), and only first heating for the other: Cr, crystalline phase; Col_{hex}, hexagonal columnar mesophase; Iso, isotropic liquid; [c] onset peaks; [d] decomposition before melting; [e] POM observations.

C18 is mesomorphous at room temperature up to a reversible but broad clearing transition at 101°C. POM textures at 80°C in the mesophase and at room temperature, obtained on cooling from the isotropic state, display pseudo-focal-conic defects and homeotropic zones, which indicate the formation of an untilted Col_{hex} mesophase (**Figure 3-18**). The texture was preserved at room temperature.

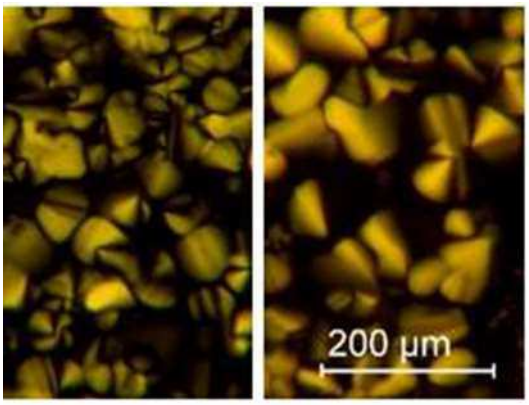

Figure 3-18. POM micrographs of the textures exhibited by complex **C18** on cooling from the isotropic liquid at: (a) 80°C and (b) room temperature.

Characterization of the mesophases by Small- and Wide- Angle X-ray Scattering (SWAXS)

Combined with SWAXS investigation, a hexagonal mesophase was confirmed for **C18**. The SWAXS patterns, recorded at various temperatures, revealed several sharp and intense reflections in the small-angle range characteristic of the various two-dimensional arrangements of mesogenic columns separated in space by a molten aliphatic continuum (**Figure 3-19**). Up to four reflections in the ratio 1:√3:2:√7 were observed, unambiguously characterizing a hexagonal *p6mm* lattice.

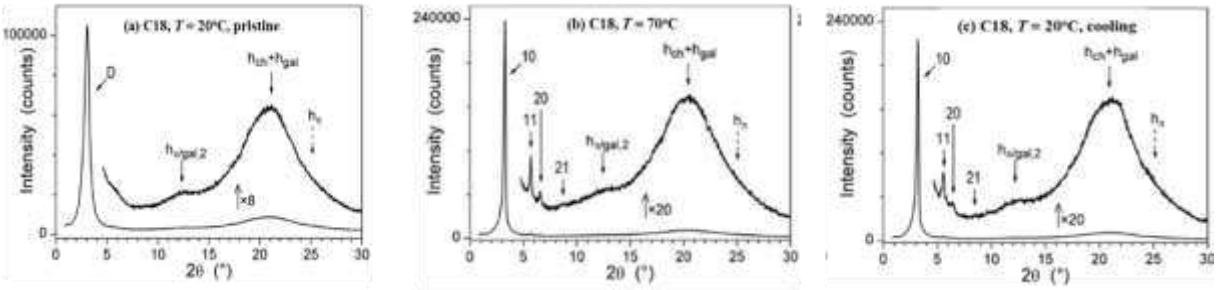

Figure 3-19. SWAXS pattern of **C18**: (a) in the pristine state at 20°C; (b) in the Col_{hex} mesophase and (c), on Ist cooling at 20°C.

The columns of the Col_{hex} phase of **C18** are constituted by a core of piled complexes and a crown of irregularly closed-packed gallate units, whose average lateral distances give rise to scattering maximums h_{gal} and h_{ch}, which are not resolved from the scattering contribution h_{ch} from the molten chains in the periphery of columns. The distribution of gallate units and chains around piled complexes results in the appearance of a scattering maximum from a two-cores periodicity $h_{\pi/gal,2}$, in relation with the change of in-plane orientation of successive cores. For this compound, it turns out that the number of chains and the size of the cores are well adapted, so that molecules self-assemble in an untilted Col_{hex} phase, with h_{mol} close to the natural stacking distance of *tpy*-zinc(II) (**Figure 3-19**) and with a chain packing ratio,[362] q_{ch}, slightly above unity (**Table 3-16**). The stacking distance of the *tpy* rings is indeed of 3.2945 Å at 25°C in the single crystal structure CSD-TPYZNC[363] of the dichloro-terpyridyl-zinc(II) complex, thus nearly the same as in the frozen Col_{hex} state of **C18**. The q_{ch} values around 1.1 correspond to almost stretched chains favouring the formation of sharp nanosegregation interfaces with piled cores and thus the columnar mesomorphism.

Table 3-16. Mesophases parameters of complex **C18**.

Phase $T^{[a]}$	V_{mol}[b] ρ	a[c] $A[Z]$	h_{mol}[d]	χ_{Vch}[e] A_{core}	$D_{core,cyl}$[f]	$S_{ch,cyl}$[g] $q_{ch,cyl}$
Col_{hex}, 70	3025 1.04	31.32 850[1]	3.56	0.778 189	15.5	24.8 1.12
Col_{hex}, 30	2946 1.07	32.08 891[1]	3.31	0.775 200	16.0	23.7 1.11

[a] T, temperature of the measurement (°C). [b] V_{mol}, calculated molecular volume (Å^3); ρ, density (g/cm^3). [c] a, lattice parameter (Å); $A = a^2\sqrt{3}/2$, lattice area (Å^2); Z, number of columns per lattice. [d] $h_{mol} = V_{mol}/A$, molecular slice thickness (Å). [e] χ_{Vch}, calculated aliphatic volume fraction; $A_{core} = (1-\chi_{Vch})\times(A/Z)$, cross-sectional area of columnar cores (Å^2). [f] $D_{cyl} = \sqrt{(4/\pi\ A_{core})}$, diameter (Å) of equivalent cylinder of cross-sectional area A_{core}. [g] $S_{ch,cyl} = \pi D_{cyl} \times h_{mol}/n_{ch}$: cylinder area per chain (Å^2), $n_{ch} = 7$ being the number of chains per molecule. [h] $q_{ch,cyl} = S_{ch,cyl}/\sigma_{ch}$, chain packing ratio, $\sigma_{ch} = 21.2$ (Å^2) being the cross-sectional area of a molten chain at 20°C.

Emission spectroscopy in condensed states

In the pristine condensed states both samples are fluorescent as seen in **Figure 3-20**. Comparing the luminescence properties of **C17** in solution with those measured in condensed state (**Table 3-17**), emission maximum remained almost unchanged (365 vs 360 nm, respectively), while the quantum yield doubles from 6.4 % to 15.8 %, and the lifetime increased from 1.2 ns to 78.5 ns. This behaviour is attributable to the reduction of non-radiative de-excitation pathways that occur in the solid phase, where the vibronic modes of the single molecule are somewhat reduced.

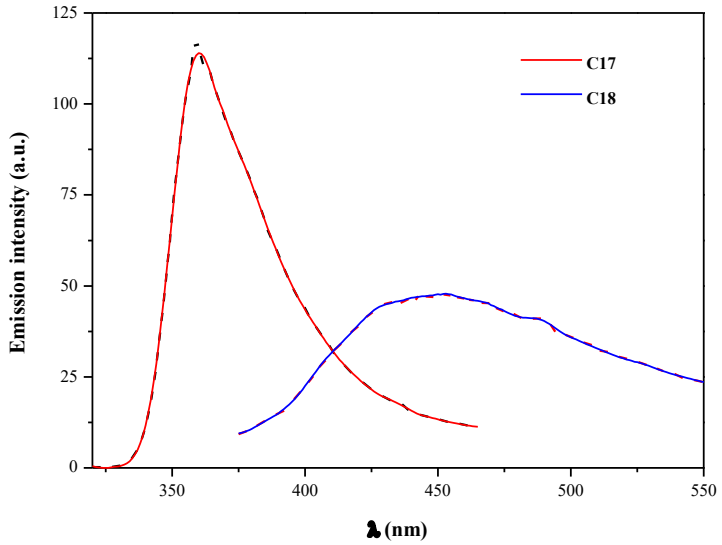

Figure 3-20. Emission spectra of **C17** and **C18** in the solid state at room temperature.

Table 3-17. Photophysical data of **C17** and **C18** in solid state at room temperature.

Complex	Emission, λ_{max}/nm	Quantum yields, ϕ /%	Lifetime,τ /ns (α_i/%)		
C17	360	15.8	78.5		
C18	450	7.1	0.4 (23)	3 (69)	11 (8)

If we compare the behaviour of **C18** in solution (**Table 3-14**) with respect to the pristine condensed phase (**Table 3-17**), we first notice a consistent red-shift of the emission band (379 nm in solution vs 450 nm in condensed phase), a drastic reduction of the quantum yield passing from 24.5 % to 7.1 %, and a different kinetics of the excited-state decay: mono-exponential in solution (with a lifetime of 2.7 ns) and multi-exponential in the pristine condensed phase, with a relevant percentage of short lifetimes. The effect of temperature variation on the emission properties of **C18** is reported in **Table 3-18**. The temperature increase (both during the first and the second heating / cooling cycle) involves a red-shift of the emission band and a decrease of quantum yield.

Table 3-18. Quantum yields for **C18** by varying the temperature.

Ist cycle						**IInd cycle**					
Heating			**Cooling**			**Heating**			**Cooling**		
T/°C	λ_{em}/ nm	ϕ (%)	T/°C	λ_{em}/ nm	ϕ (%)	T/°C	λ_{em}/ nm	ϕ (%)	T/°C	λ_{em}/ nm	ϕ (%)
30	450	7.1	80	497	1.92	30	478	2.98	80	493	1.63
80	478	4.97	30	478	2.98	80	500	1.35	30	482	3.27
140	507	0.71				140	509	0.50			

Trends are reversible by decreasing temperature, but the initial higher values are never restored in relation with structural changes on first heating. The columnar structure of the **C18** is indeed initially disordered, with only average distances between irregularly arranged columns and the regular hexagonal arrangement only develops with the softening of the sample on first heating (**Figure 3-19**). Such a transformation obviously creates interactions between the compounds, which help stabilizing the excited state, as indicated by the red-shift of the emission band, while the quantum yield decreases due to the non-radiative deactivations raise triggered by the high temperature.

3.3.3 Synthesis and characterization of Zn(II) tpy complexes with L10 ligand

Complexes **C19** and **C20,** form **Figure 3-21**, were synthesized as described in the chapter containing the experimental procedures. The complexes were isolated as amorphous

solids in 90 % and respectively 70 %. The complexes were characterized through FT-IR and ^{1}H-NMR spectroscopies and their photophysical properties were investigated both in solution and in condensed states. Moreover, the thermal behaviour and liquid-crystalline self-assemblies were fully characterized by POM, DSC, TGA and SWAXS.

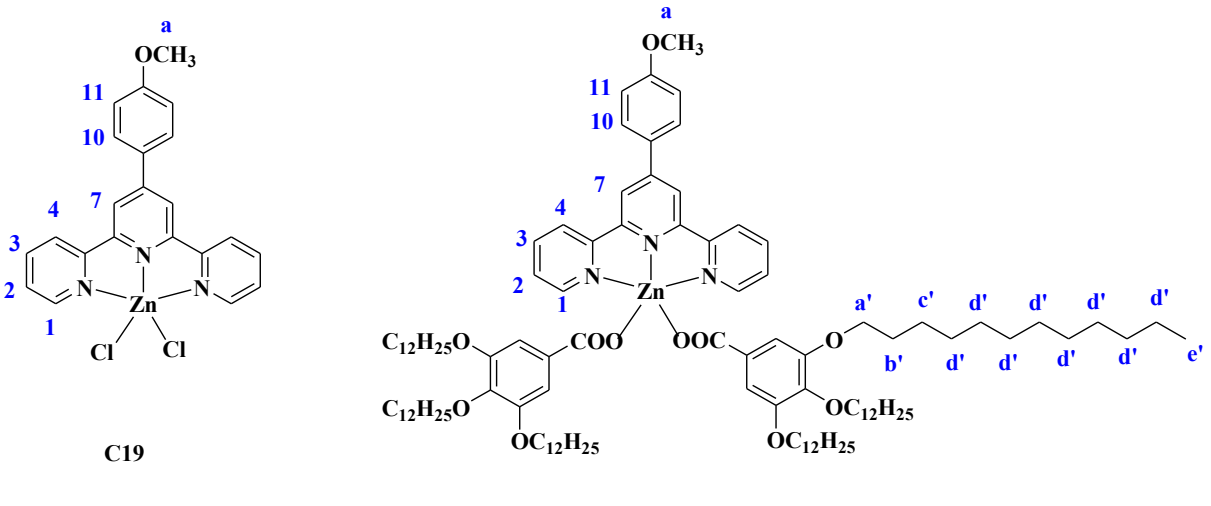

Figure 3-21. The proposed structures of the complexes **C19** and **C20** with **L10** and their atom labelling.

FT-IR spectroscopy

The FT-IR spectra of complexes **C19** and **C20** are presented in **Figure 3-22**. The assignments of the characteristic absorption bands for complexes **C19** and **C20** are summarized in **Table 3-19**. By comparing the spectra of C19 with that of the free ligand **L10**, no significant changes can be observed between 3400 - 1650 cm^{-1} wavenumber region. In the 1650 – 1400 cm^{-1} wavenumber region, **C19** presents a significant shift to higher frequencies of $\upsilon_{C=C}$ and $\upsilon_{C=N}$ characteristic bands compared to the free *tpy* ligand, which indicates the coordination via the nitrogen atoms of the ligand.[355] As for the other Zn(II) complexes with gallate units as co-ligands, the exclusively coordinating mode of the gallate unit is demonstrated by the separation of the stretching vibrations of COO^- group: the asymmetric stretching vibration for $\nu_{as(COO^-)}$ appeared at 1616 cm^{-1}, while the symmetric one of the coordinated carboxylate at 1368 cm^{-1} , giving a separation (Δ) of 248 cm^{-1}.[357]

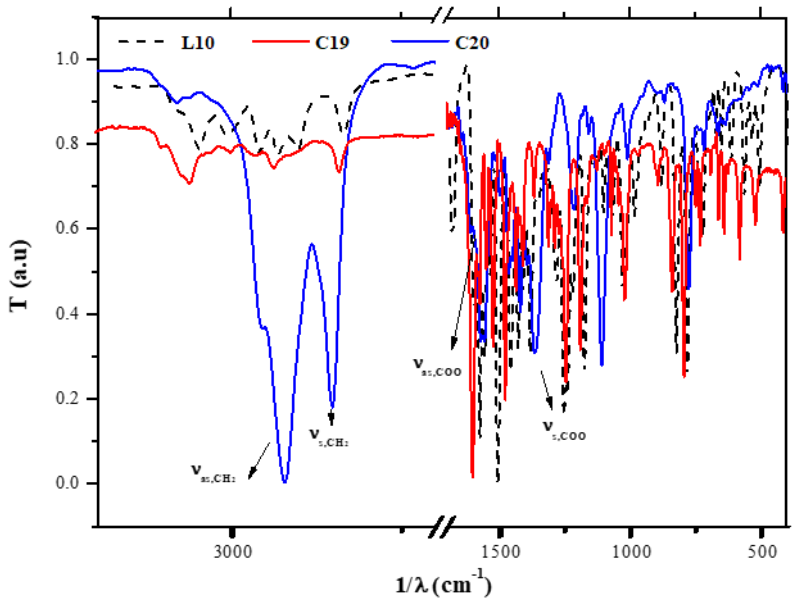

Figure 3-22. FT-IR spectra of complexes **C19** and **C20**, plotted against the free ligand **L10**.

Table 3-19. Assignment of the characteristic absorption bands of complexes **C19** and **C20** (wavenumber values in cm^{-1}).

Assignment of the characteristic absorption bands (wavenumber values in cm^{-1})					
Complex	$\nu_{as,(-CH2-)}$	$\nu_{s,(-CH2-)}$	$\nu_{as,(COO^-)}$	$\nu_{s,(COO^-)}$	$\upsilon_{C=C}$, $\upsilon_{C=N}$
C19					1601 - 1435
C20	2922	2851	1611	1368	1562 - 1436

^{1}H-NMR spectroscopy

Due to the different solubilities the NMR spectra of complex **C19** was recorded in DMSO-d_6, while the ligand and complex **C19** were obtained in $CDCl_3$. The proton assignments of **C19** and **C20** are summarized in **Table 3-20**.

By comparing the spectra of **C20** and of the free *tpy* ligand, **Figure 3-23**, the shift of the aromatic protons belonging to *tpy* unit indicated the successful formation of the complex, giving a well-resolved spectrum. In particular, the spectra of **C20** shows the signals corresponding to the aromatic proton of Gal unit ($H^{3'}$) at 7.32 ppm. Moreover, proton H^1 shifted from 8.72 ppm to 9.01 ppm, solving the overlapped peaks, which appear for the free ligand. The protons H^7 and H^4 presented a chemical shift from 8.72 ppm (overlapped peaks) to *ca.* 8.31 ppm and 7.73 ppm, respectively.

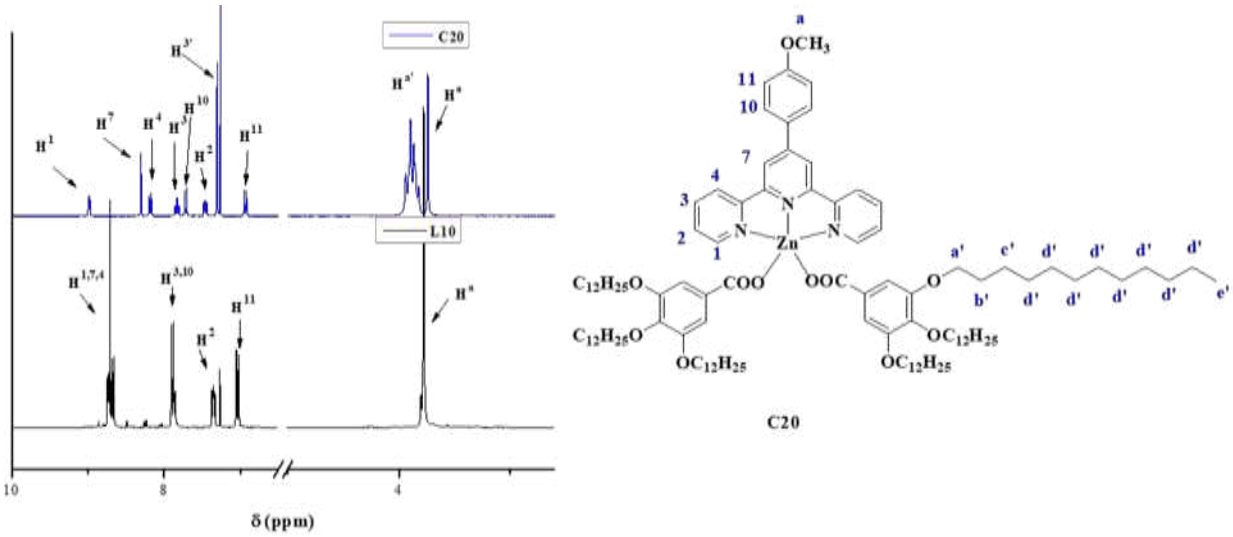

Figure 3-23. ^{1}H-NMR spectra of complex **C20** plotted against the free ligand **L10**.

Table 3-20. Chemical shifts (δ/ppm) of complexes **C19** (in DMSO-d_6) and **C20** (in $CDCl_3$).

	Chemical shifts (in δ/ppm)	
	C19	**C20**
H^{1}	8.83[a]	9.00
H^{2}	7.91 – 7.76	7.84
H^{3}	8.31 – 8.18[b]	8.19
H^{4}	8.83[a]	7.73
H^{7}	8.93	8.31
H^{10}	8.31 – 8.18[b]	7.50 – 7.42
H^{11}	7.12	6.95
H$^{3'}$		7.32
H^{a}	3.87	3.87
H$^{a'}$		4.03 – 3.88
H$^{b'}$		1.73
H$^{c'}$		1.43 – 1.26[c]
H$^{d'}$		1.43 – 1.26[c]
H$^{e'}$		0.89
[a - c]: protons appear overlapped in the ^{1}H NMR spectra		

Absorption and emission spectroscopy in solution

The photophysical properties of the complexes **C19** and **C20** were investigated in $CHCl_3$ and are presented in **Figure 3-24**. As for the other Zn(II) analogues, the two samples appear colourless in diluted solutions and absorb in the UV region of the electromagnetic spectra. The absorption spectra of **C19** and **C20** complexes show a series of bands (**Table 3-21**) in the UV portion of the electromagnetic spectrum, all originated from *tpy* LC transitions.[358,361]

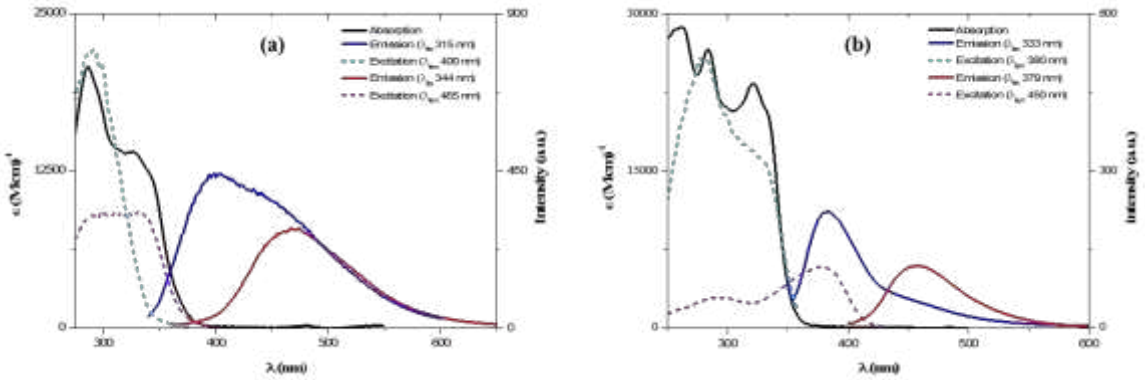

Figure 3-24. Absorption, emission and excitation spectra of: (a) **C19** in diluted DMSO solution (1.2 10^{-5} M) and (b) **C20** in diluted $CHCl_3$ solution (6.1 10^{-5}).

The emission spectra of complexes **C19** and **C20** presents a double emission band: a blue-shifted one centred around 400 and 380 nm, and a red-shifted one centred around 465 and 460 nm (**Table 3-21**). The excitation spectra registered on these emission maximums are different with respect to the absorption spectra of the complexes.

Table 3-21. Photophysical data of **C19** and **C20** complexes in dilute solutions.

Complex	**Absorption, λ_{max}/nm (ε/M^{-1} cm^{-1})**	**Emission, λ_{max}/nm**	**Lifetime, τ /ns (α_i/%)**		
C19	286 (20800), 312 (14250), 326 (14030), 340 (12490)	400	n.a.		
		465	2.43 (67)	0.79 (27)	4.88 (6)
C20	255 (28440), 263 (28730), 284 (26600), 321 (23360), 333 (20550)	380			
		460			

Thermal and mesomorphic behaviour

The thermal behaviour was first investigated by POM, TGA and DSC. Complex **C19** was deprived of liquid crystalline properties much due to the absence of aliphatic chains. The introduction of lipophilic gallate units as monodentate ligand to yield **C20** resulted in the drastic lowering of the melting point and induction of mesomorphism.

TGA analysis of complex **C19** revealed a weight loss from degradation above 358°C, whereas complex **C20** was found to be stable up to 295°C. According to POM observation, complex **C20** went into the isotropic phase at 240°C. While cooling a mosaic like texture was identified at 235°C, which was kept until room temperature, pointing towards a hexagonal-like

organization (**Figure 3-25**). During the heating cycle, the compound started to soften at 60°C and at 72°C a transition to a more ordered state was noticed (not seen in DSC).

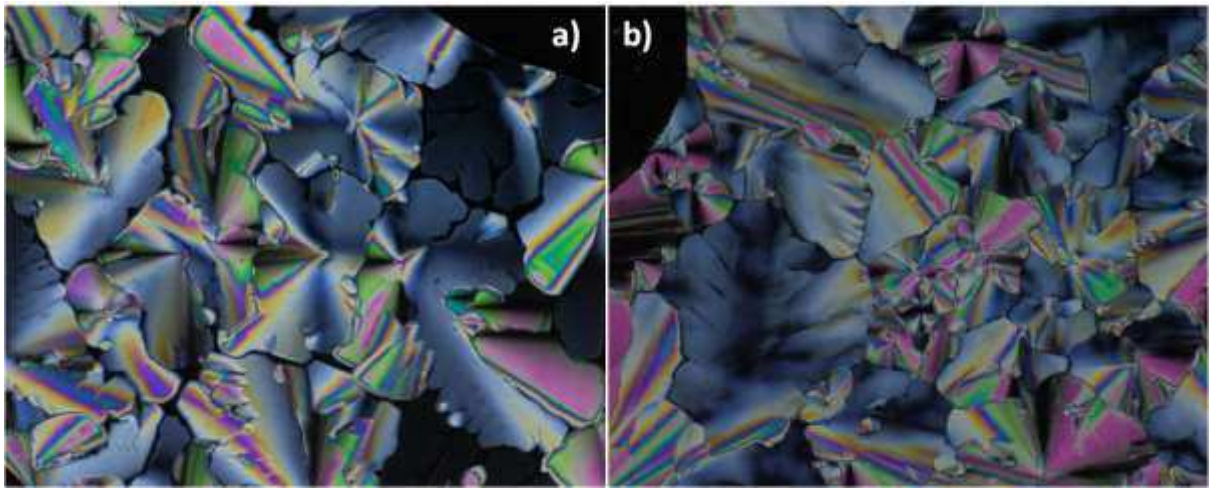

Figure 3-25. POM micrographs of the textures exhibited by complex **C20** on cooling from the isotropic liquid at: (a) 230^0C and (b) room temperature.

Table 3-22 summarizes the thermal and mesomorphic behaviour of complexes **C19** and **C20** determined by DSC analysis combined with POM observations. For complex **C20** an unidentified three-dimensional mesophase but with a hexagonal 2D sublattice (M_{hex}) was deduced by SWAXS.

Table 3-22. Thermal behaviour of complexes **C19** and **C20**.

Complex	$\mathbf{T_{dec\ 5\%}}$ **/°C**[a]	**Thermal properties: mesophases,** [b] **transitions temperatures**[c] **(in°C) and enthalpies (ΔH in kJ mol^{-1})**
C19	358°C	Dec[d]
C20	295°C	M_{hex} 231.8 (13) Iso (-) Iso 227.8 (16.1) M_{hex} (-)
[a] Significant weight loss (5%) from degradation from TGA trace; [b] Determined on first cooling and second heating (for mesomorphous compounds), and only first heating for the other; M_{hex}: unidentified hexagonal mesophase; Iso: isotropic liquid; [c] onset peaks; [d] decomposition before melting.		

Characterization of the mesophases by Small- and Wide- Angle X-ray Scattering (SWAXS)

The SWAXS patterns, presented in **Figure 3-26**, of complex **C20** were recorded at various temperatures. The data collected allowed the calculation of the geometrical phase parameters, which are summarized in **Table 3-23**.

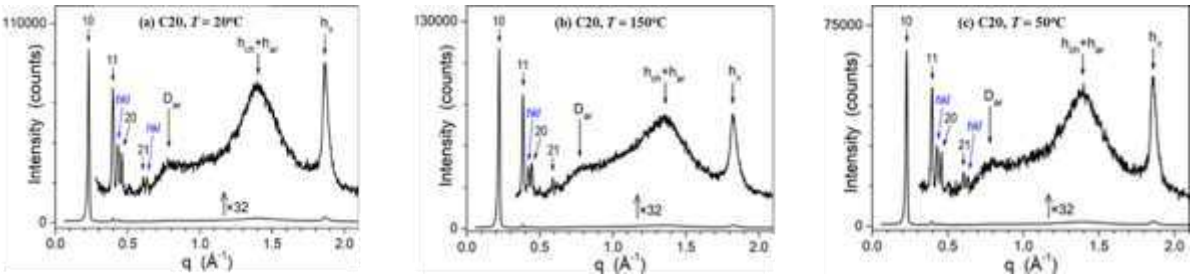

Figure 3-26. SWAXS patterns of **C20**: (a) at room temperature in the pristine mesomorphous state, (b) in the fluid state of the mesophase, and (c) at 50^{0}C on cooling from the isotropic liquid.

Table 3-23. Mesophases parameters of complex **C20**.

Phase $T^{[a]}$	V_{mol}[b] ρ	a[c] $A[Z]$	h_{mol}[d] h_p	χ_{Vch}[e] A_{core}	$D_{core,cyl}$[f] $S_{ZnAr,cyl}$	$S_{ch,cyl}$[g] $q_{ch,cyl}$
M_{hex}, 20	2758 1.06	31.44 856[1]	3.22 3.36	0.714 245	17.7 179	25.5 1.20
M_{hex}, 50	2817 1.03	31.66 868[1]	3.24 3.37	0.715 248	17.8 181	25.8 1.19
M_{hex}, 150	3012 0.97	32.42 910[1]	3.31 3.45	0.717 257	18.1 188	26.9 1.15

[a] Temperature of the measurement (°C). [b] V_{mol}, calculated molecular volume (Å^3); ρ, density (g/cm^3).
[c] a, hexagonal lattice parameter (Å); $A = a^2\sqrt{3}/2$, lattice area (Å^2); Z, number of columns per lattice; $h_{mol} = V_{mol}/A$, molecular slice thickness (Å); [d] h_π, π-stacking distance from peak position (Å); [e] χ_{Vch}, calculated aliphatic volume fraction; $A_{core} = (1-\chi_{Vch})\times(A/Z)$, cross-sectional area of columnar cores (Å^2); [f] $D_{core,cyl} = \sqrt{(4/\pi\ A_{core})}$, diameter (Å) of equivalent cylinder of cross-sectional area A_{core}; $S_{ZnAr,cyl} = \pi D_{core,cyl}\times h_{mol}$, cylinder surface per Zinc complex (Å^2); [g] $S_{ch,cyl} = S_{ZnAr,cyl}/n_{ch}$, cylinder surface per chain (Å^2), n_{ch} being the number of peripheral substituents per molecule ($n_{ch} \approx 7$, the interface area requirement of the methoxyphenyl branch being approximated to that of a chain); $q_{ch,cyl} = S_{ch,cyl}/s_{ch}$, chain packing ratio for the average cylindrical interface.

Pattern composition and geometrical parameters indicate that the compound self-organizes through π-stacking of terpyridine rings and decoration by gallate and extender segments. However, the high $q_{ch,cyl}$ (1.2 if extender is counted as a chain, 1.4 if only long chains are considered) reveals a loose aliphatic shell, explaining that molecules from neighbouring π-stacked assemblies interact and form a three-dimensional structure. The few crossed reflections (blue (*hkl*) labels) do not allow unambiguous determination of the emerging structure, but the symmetry of the sublattice and the birefringent, mosaic-like POM textures indicate that cell is more likely trigonal or hexagonal. Missing information for the complete crystallographic analysis could be brought by oriented GIWAXS patterns, which will be performed in due course.

Photophysical properties in condensed state

Accurate structural and photophysical investigations in condensed state were realized to study how the mesophase organization influences on the emitting states. The emission recorded in the solid state at room temperature for complexes **C19** and **C20,** presented in **Figure 3-27**,

showed that both of complexes were luminescent in the visible region of electromagnetic spectra with narrow emission bands centred at 445 nm for **C19** and at 417 nm for **C20**. In the solid state, a blue shift of the emission maxima was observed for both complexes with respect to the spectra recorded in solution. The emission maxima, quantum yields and lifetimes are summarized in **Table 3-24**.

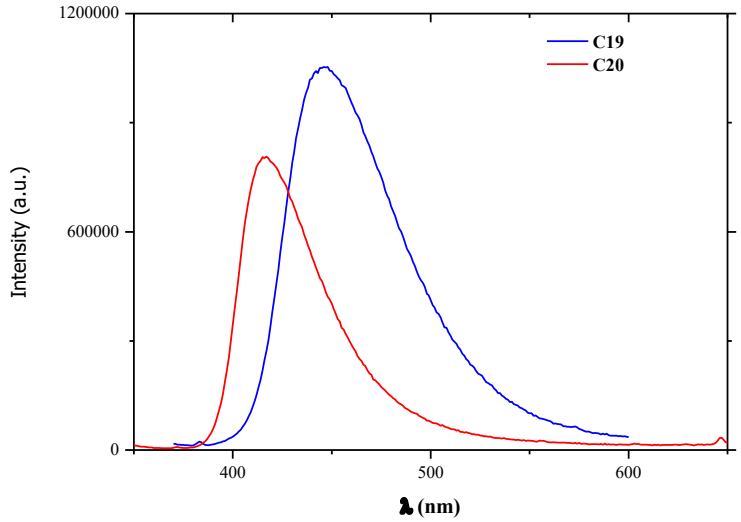

Figure 3-27. Emission spectra of **C19** and **C20** in the solid state at room temperature.

Table 3-24. Photophysical data of **C19** and **C20** in solid state at room temperature.

Complex	**Emission, λ_{max} /nm [λ_{ex}]**	**Quantum yields, ϕ /%**	**Lifetime, τ /ns (α_i/%)**		
C19	445 [350 nm]	26.3	82.8 (3)		6.1 (55)
C20	417 [340 nm]	9.1	8.8 (70)	33.4 (13)	1.9 (17)

For complex **C20**, which is mesomorphic, the quantum yields in the solid state have also been measured with varying the temperature and the results are summarized in **Table 3-25**. Because the transition to the isotropic state happens at a temperature out of the working range of the instrument normally used for the heating of the sample in the fluorometer (T_{max} = 190°C), this transition was induced with a conventional heating plate hence the cooling emission spectra and the corresponding quantum yields could not be measured.

It can be noticed that the emission quantum yield decreases, with the increase of the temperature, due to the increase in thermal agitation, which favours the non-radiative deactivation pathway, except at 80°C, when the transition from amorphous solid to the unidentified M_{hex} phase takes place.

As for the above Zn(II) MMs, trends are reversible by decreasing temperature, but the initial higher values are never restored in relation with structural changes on first heating. Also, the temperature increase leads to a red-shift of the emission maxima.

Table 3-25. Quantum yields for **C20** by varying the temperature (λ_{ex} = 360 nm).

Ist cycle			**IInd cycle**		
Heating			**Heating**		
T/°C	λem/ nm	ϕ (%)	T/°C	λem/ nm	ϕ (%)
30	416	9.1	30	435	4
80	436	15.2	80	433	2.9
150	438	9.2	150	434	1.7
190	437	6.4	188	435	1.35

3.3.4 Synthesis and characterization of Zn(II) tpy complexes with L11 ligand

Complexes **C21** and **C22** (**Figure 3-28**) were synthesized as described in previous subchapters. The complexes were obtained as amorphous solids in 90 % and respectively 70 %. The complexes were characterized through FT-IR and ^{1}H-NMR spectroscopies and their photophysical properties were investigated both in solution and in condensed states. Moreover, the thermal behaviour and liquid-crystalline self-assemblies were fully characterized by POM, DSC, TGA and SWAXS.

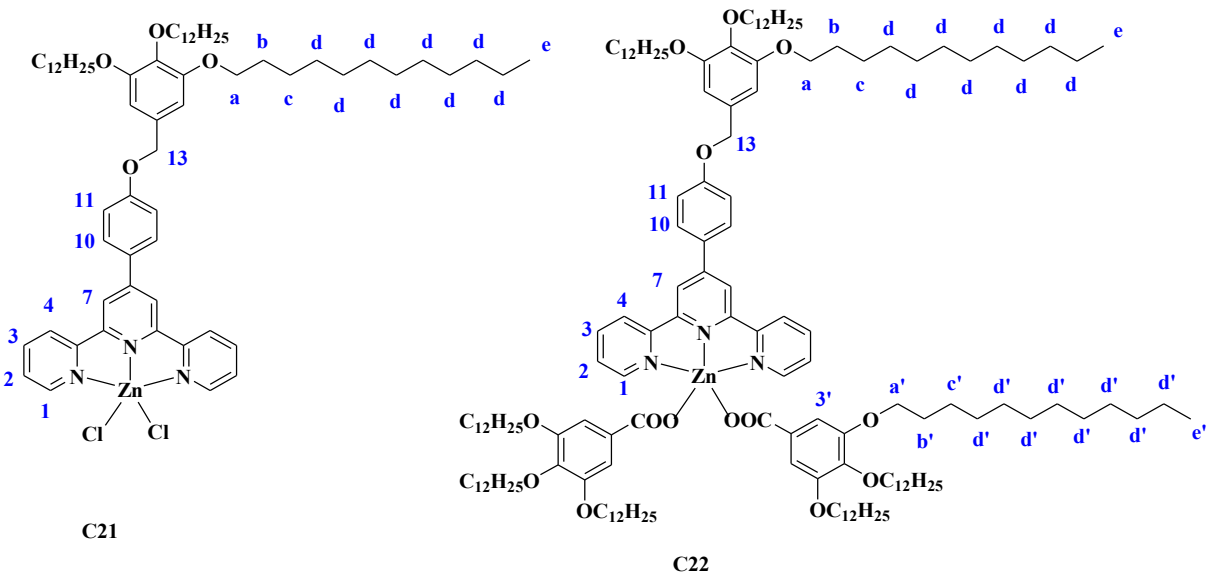

Figure 3-28. The proposed structures of the complexes **C21** and **C22** with **L11** and their atom labelling (in blue).

FT-IR spectroscopy

The FT-IR spectra of complex **C22** revealed the characteristic absorption bands of the carbon-hydrogen bond from the aliphatic chains at 2923 cm^{-1} corresponding to the asymmetric stretching vibration $\nu_{as,(-CH_2-)}$, and around 2853 cm^{-1}, corresponding to the symmetric stretching vibration $\nu_{s,(-CH_2-)}$.[353] By comparing the FT-IR spectra of the complex **C22** with that of the free tpy ligand, **L11** (**Figure 3-29**), the characteristic absorption bands corresponding to the carboxylate unit from gallate could be identified: ν_{as} at 1575 cm^{-1} and ν_s at 1371 cm^{-1} (Δ = 204 cm^{-1}). The big separation value between the asymmetric and symmetric carboxylate absorption bands indicates that the gallate unit is coordinated to Zn(II).[357] The main characteristic absorption bands are summarized in **Table 3-26**.

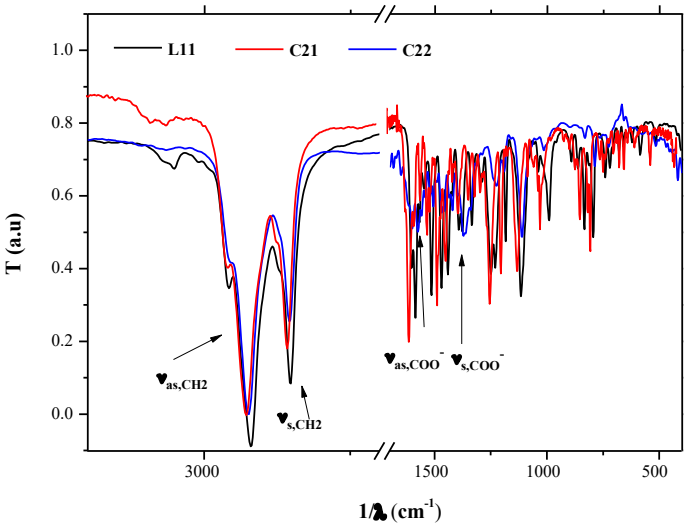

Figure 3-29. FT-IR spectra of complexes **C21** and **C22** plotted against the free ligand **L11**.

Table 3-26. Assignment of the characteristic absorption bands of complexes **C21** and **C22** (wavenumber values in cm^{-1}).

Assignment of the characteristic absorption bands (wavenumber values in cm^{-1})					
Complex	$\nu_{as,(-CH2-)}$	$\nu_{s,(-CH2-)}$	$\nu_{as,(COO^-)}$	$\nu_{s,(COO^-)}$	$\upsilon_{C=C}$, $\upsilon_{C=N}$
C21	2926	2851			1608 - 1422
C22	2923	2853	1570	1370	1598-1422

^{1}H NMR spectroscopy

By comparing the spectra of **C21** precursor with that of the free ligand **L11**, small shifts were observed for the aliphatic protons, while the aromatic protons presented important shift confirming the effective coordination of Zn(II) salt to *tpy* unit (**Figure 3-30**). The ligand

exchange with Ag(Gal) was confirmed by the presence of $H^{3'}$ at 7.31 ppm. In case of both complexes, proton H^1 shifted from 8.71 to 9.01 ppm, solving the overlapped peaks, which appear for the free ligand. In case of complex **C21**, the protons H^7 and H^4 presented a chemical shift from 8.67 (overlapped peaks) to *ca.* 8.03, whereas for complex **C22** to 8.33 and 8.24.

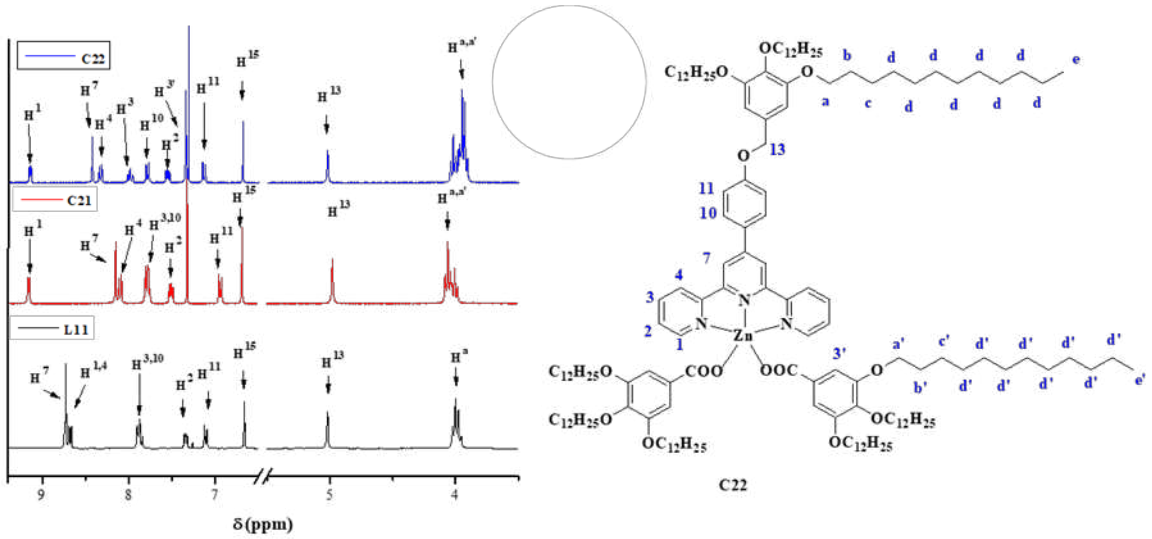

Figure 3-30. ^{1}H-NMR spectra of complex **C21**, **C22** and of the free ligand **L11**.

Table 3-27. Chemical shifts (in δ/ppm) of complexes **C21** and **C22** recorded in $CDCl_3$.

	Chemical shifts (in δ/ppm)	
	C21	**C22**
H^1	9.01	9.01
H^2	7.45	7.50
H^3	7.74 – 7.68[b]	7.92
H^4	8.09 – 7.97[a]	8.24
H^7	8.09 – 7.97[a]	8.33
H^{10}	7.74 – 7.68[b]	7.73
H^{11}	6.91	7.11
H^{13}	4.98	5.03
H^{15}	6.68	6.68
$H^{3'}$		7.31
$H^{a,a'}$	4.06, 4.00	4.08 – 3.88
$H^{b,b'}$	1.83	1.96 – 1.67
$H^{c,c'}$	1.40 – 1.28[c]	1.53 – 1.26[d]
$H^{d,d'}$	1.40 – 1.28[c]	1.53 – 1.26[d]
$H^{e,e'}$	0.89	0.89
[a-d]: protons appear overlapped in the ^{1}H NMR spectra		

Absorption and emission spectroscopy in solution

The *absorption and emission* properties of the complexes **C21** and **C22** were investigated in $CHCl_3$ in diluted solutions and are presented in **Figure 3-31**. Both complexes absorb in the UV region of the electromagnetic spectra. The results are summarized in **Table 3-28**.

The emission spectra of all the complexes present a double emission band: a blue-shifted one centred around 380 nm and a red-shifted one centred at 550 nm (**C21**) and 455 nm (**C22**) as seen in **Table 3-28**. The emission maximum for complex **C22** is different with respect to the absorption spectra of the relative complex, while for complex **C21** the absorption and excitation bands are overlapped.

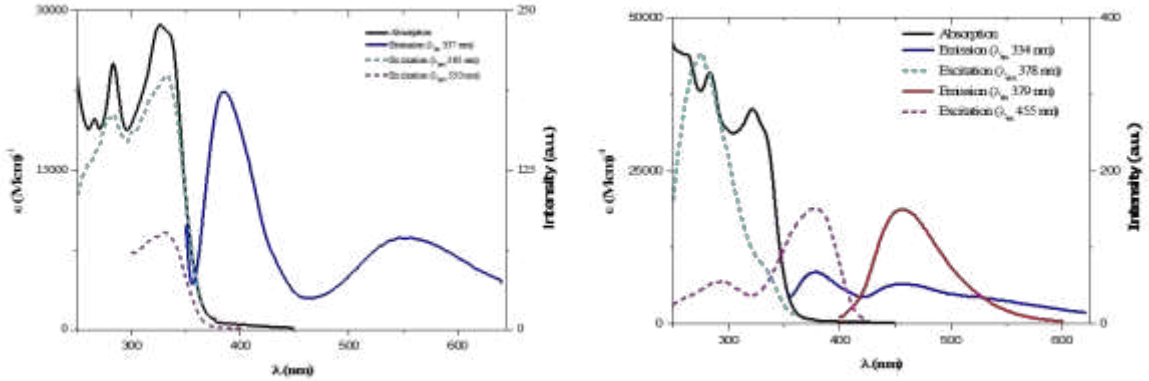

Figure 3-31. Absorption, emission and excitation spectra of: **C21** in diluted $CHCl_3$ solution (1.1 10^{-5} M, left) and **C22** in diluted $CHCl_3$ solution (1.8 10^{-5} M, right).

Table 3-28. Photophysical data of **C21** and **C22** complexes in dilute solution.

Complex	**Absorption, λ_{max}/nm (ε/M^{-1} cm^{-1})**	**Emission, λ_{max}/nm**	**Lifetime,τ /ns (α_i/%)**		
C21	266 (19860), 283 (25050), 325 (28650), 335 (27890)	385	2.46 (65)	33.7 (8)	0.81 (27)
		550	8.85		
C22	254 (57070), 264 (56070), 283 51950), 299 (39680), 322 (41700), 333 (37580)	378			
		455			

Thermal and mesomorphic behaviour

TGA analysis of complex **C21** revealed a weight loss due to degradation above 288°C, whereas complex **C22** was found to be stable up to 315°C. The mesomorphic behaviour was firstly investigated by POM observation and two of the most representative images are presented in **Figure 3-32**. Complex **C22** having three gallate units, one as substituent in *tpy* molecule, and the other two as co-ligands, was found to be liquid crystal from room temperature up to 177ºC when it reached the isotropic phase. When cooling, it quickly returned at 172ºC into a mesophase with focal conic textures and homeotropic zones pointing toward a columnar hexagonal mesophase. The texture was kept on cooling until room temperature. **C21** was not mesomorphous and decomposed before reaching the isotropic liquid.

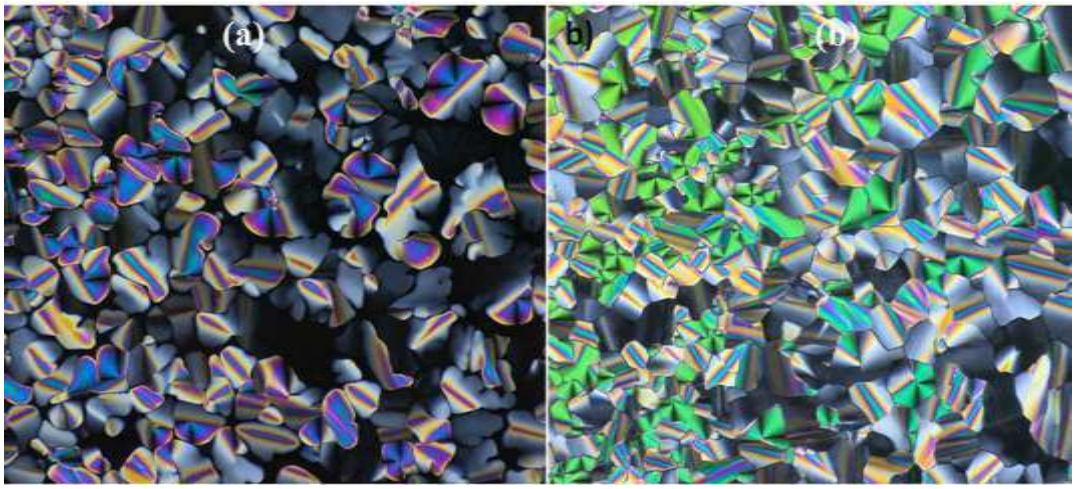

Figure 3-32. POM micrographs of the textures exhibited by complex **C22** on cooling from the isotropic liquid at: (a) 167 ^{0}C and (b) 45 ^{0}C.

Table 3-29 summarizes the thermal and mesomorphic behaviour of complexes **C21** and **C22**. The DSC analysis combined with POM observations revelead that **C22** exhibited a two-dimensional hexagonal columnar mesophase (Col_{hex}).

Table 3-29. Thermal behaviour of complex **C21** and **C22**.

Complex	**$T_{dec\ 5\%}$ /°C[a]**	**Thermal properties: mesophases, [b] transitions temperatures[c] (in°C) and enthalpies (ΔH in kJ mol^{-1})**
C21	288°C	Dec[d]
C22	315°C	Col_{hex} 169 (8.3) Iso (-) Iso 165 (8.3) Col_{hex} (-)
[a] Significant weight loss (5%) from degradation from TGA trace; [b] Determined on first cooling and second heating (for mesomorphous compounds), and only first heating for the other: Cr, crystalline phase; Col_{hex},columnar hexagonal mesophase; Iso, isotropic liquid; [c] onset peaks; [d] decomposition before melting;		

Characterization of the mesophases by Small- and Wide- Angle X-ray Scattering (SWAXS)

The SWAXS patterns of complex **C22** were recorded at various temperatures and are presented in **Figure 3-33**. The data collected confirmed the existence of the columnar hexagonal mesomorphism and allowed the calculation of the main geometrical phase parameters, which are summarized in **Table 3-30**.

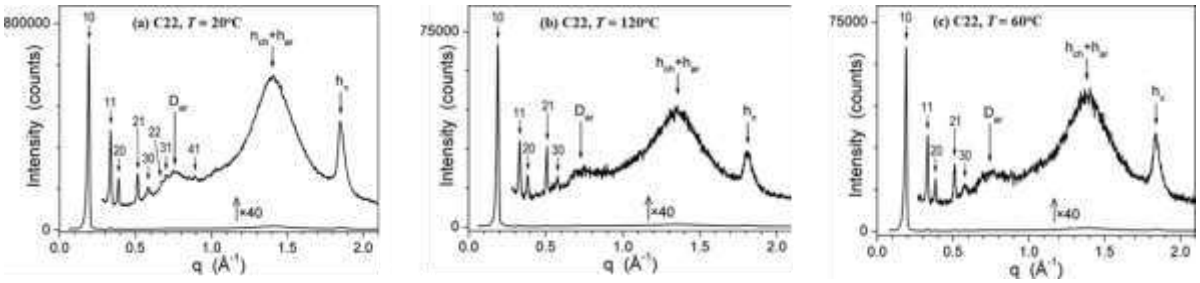

Figure 3-33. SWAXS patterns of **C22** (a) at room temperature, (b) at 120°C and (c) at 60 ^{0}C on cooling.

Table 3-30. Mesophases parameters of complex **C22**.

Phase T[a]	**V_{mol}[b] ρ**	***a*[c] *A*[*Z*]**	***h*$_{mol}$[d] *h*$_{p}$**	**χ_{Vch}[e] A_{core}**	***D*$_{core,cyl}$[f] *S*$_{ZnAr,cyl}$**	***S*$_{ch,cyl}$[g] *q*$_{ch,cyl}$**
Col_{hex}, 20	3862 1.02	37.23 1200[1]	3.22 3.38	0.754 295	19.4 196	21.8 1.02
Col_{hex}, 50	3973 1.00	37.58 1223[1]	3.25 3.42	0.755 297	19.5 199	22.1 1.01
Col_{hex}, 120	4141 0.96	37.75 1234[1]	3.36 3.47	0.756 301	19.6 206	22.9 1.00
[a] Temperature of the measurement (°C). [b] V_{mol}, calculated molecular volume (Å^3); ρ, density (g/cm^3). [c] a, hexagonal lattice parameter (Å); $A = a^2\sqrt{3}/2$, lattice area (Å^2); Z, number of columns per lattice; $h_{mol} = V_{mol}/A$, molecular slice thickness (Å); [d] h_π, π-stacking distance from peak position (Å); [e] χ_{Vch}, calculated aliphatic volume fraction; $A_{core} = (1-\chi_{Vch})\times(A/Z)$, cross-sectional area of columnar cores (Å^2); [f] $D_{core,cyl} = \sqrt{(4/\pi\ A_{core})}$, diameter (Å) of equivalent cylinder of cross-sectional area A_{core}; $S_{ZnAr,cyl} = \pi D_{core,cyl}\times h_{mol}$, cylinder surface per Zinc complex (Å^2); [g] $S_{ch,cyl} = S_{ZnAr,cyl}/n_{ch}$, cylinder surface per chain (Å^2), n_{ch} being the number of peripheral substituents per molecule ($n_{ch} = 9$); $q_{ch,cyl} = S_{ch,cyl}/s_{ch}$, chain packing ratio for the average cylindrical interface.						

In complex **C22**, three further peripheral alkyl chains are introduced through a benzyloxyphenyl extender of the terpyridine ligand. This implies an expansion of the interface between antagonistic aromatic and alkyl chains segments and the changeover from lamellar

(**C16**) to columnar (**C18** and **C22**) structures through the aggregation of aromatic segments into columns surrounded by an aliphatic shell. The appearance of the characteristic π-stacking signature h_{π} and the matching of the stacking distance with the molecular slice thickness h_{mol} further reveals that columnar cores consist of a single molecular strand of π-stacked terpyridine rings. This strand is decorated with the gallate segments and benzyloxyphenyl extenders of the individual complexes, whose average distances explain the additional broad scattering signals D_{ar} and h_{ar}. This decoration preserves the hexagonal lattice symmetry and the average interface with the aliphatic periphery is therefore a cylinder. Chain packing ratio $q_{ch,cyl}$ is close to unity, i.e. nearly ideal for an efficient nanosegregation, which improves the cohesion of the structure and obviously contributes to the extended Col_{hex} range.

Photophysical properties in condensed state

Accurate structural and photophysical investigations in condensed state was realized to study how the mesophase organization has an influence on the emitting states.

The emission recorded in the solid state at room temperature, presented in **Figure 3-34**, showed that both complexes were fluorescent in the visible region of electromagnetic spectra, with broad emission bands centred at 510 nm for **C21** and at 440 nm for **C22**. In the solid state (**Table 3-31**), a red shift of the emission maxima was observed for both complexes with respect to the spectra recorded in solution (**Table 3-32**).

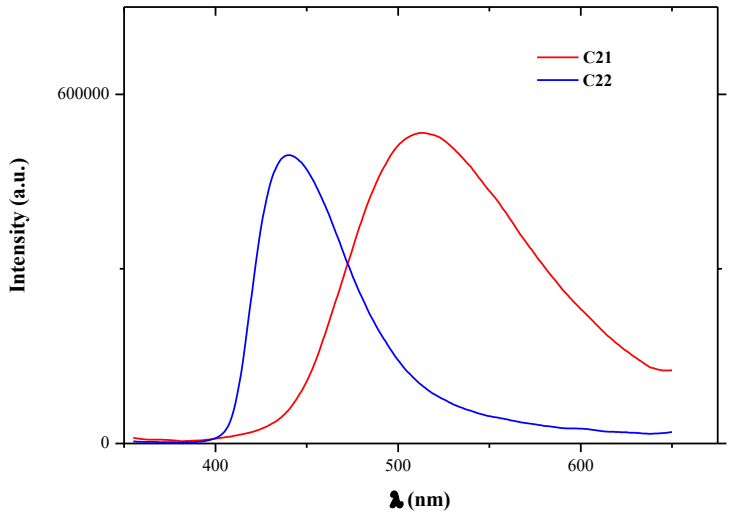

Figure 3-34. Emission spectra of **C21** and **C22** in the solid state/mesophase at room temperature.

Table 3-31. Photophysical data of **C21** and **C22** in solid state at room temperature.

Complex	Emission, λ_{max} /nm [λ_{ex}]	Quantum yields, ϕ /%	Lifetime,τ /ns (α_i/%)		
C21	510 [340 nm]	17	15.1 (88)	32.4 (12)	
C22	440 [340 nm]	8.2	7.8 (49)	33.5 (34)	1.5 (17)

The emission of complex **C22**, which presented LC behaviour, was also measured as a function of temperature. **C22** mesophase was found to be emissive showing a broad emission band. By heating, the emission quantum yield of **C22** decreased as the temperature increased due to the increase in thermal agitation, which favours the non-radiative deactivation pathway (**Table 3-32**). Also, the temperature increase (both during the first and the second heating / cooling cycle) involves a blue-shift of the emission band and a decrease of quantum yield.

Table 3-32. Quantum yields for **C22** by varying the temperature (λ_{ex} = 350 nm).

Ist cycle						**IInd cycle**					
Heating			**Cooling**			**Heating**			**Cooling**		
T/°C	λem/ nm	ϕ (%)	T/°C	λem/ nm	ϕ (%)	T/°C	λem/ nm	ϕ (%)	T/°C	λem/ nm	ϕ (%)
26	443	8.2	150	435	0.4	26	435	2.3	150	435	0.4
80	443	4.5	80	435	1.2	80	435	1.2	80	437	1.1
150	438	0.7	26	435	2.3	150	434	0.3	26	434	1.5
185	436	0.08				185	432	0.07			

3.4 Conclusions

The goal of this chapter was to synthesize luminescent liquid crystalline Zn(II) complexes and to study the structure-photophysical property in condensed states.

All Zn(II) complexes were successfully obtained in high yields. The substitution of the chloride ancillary ligands with the gallate unit led to new neutral pentacoordinated complexes **C16**, **C18**, **C20** and **C22** with the general formula [Zn(Ln)$(Gal)_2$] with liquid crystalline properties. TGA analysis revealed that the complexes were stable up to the melting into isotropic state. The temperature range of the mesophase existence and the nature of the mesophases was determined by a systematic characterization through POM observations, DSC and SWAXS analysis. As the number of lateral chains increases, the nature and the thermal stability of the mesophases evolves logically from SmA in case of complex with **L7** (**C16**), to Col_{hex} mesophase (**C18**, **C22**) in case of complexes with **L9** and **L11**, via an intermediate 3D-like hexagonal M_{hex} mesophase for **L10** (**C20**), respectively. This is a good example of the high

sensitivity of the system and its ability to adapt the aliphatic periphery to self-organize in the most optimum way.

All of the studied complexes were found to be luminescent in solution and in the pristine condensed states. Furthermore, the luminescent properties of the liquid crystalline Zn(II) complexes were measured by temperature variation. As expected, in all cases, the emission quantum yields decreased, with raising of temperature, due to the increase in thermal agitation, which favours the non-radiative deactivation pathway An interesting behaviour was observed for the complex with **L10**, in which case while heating the sample from room temperature to 80ºC (at the transition to a 3D phase), the yield increased from 9.1 % to 15.2 %. Further heating led to a decrease of the yield. **Figure 3-35** presents the phase diagram of the Zn(II) metallomesogens on first cooling, and the values of the emission quantum yields in the different states on first heating.

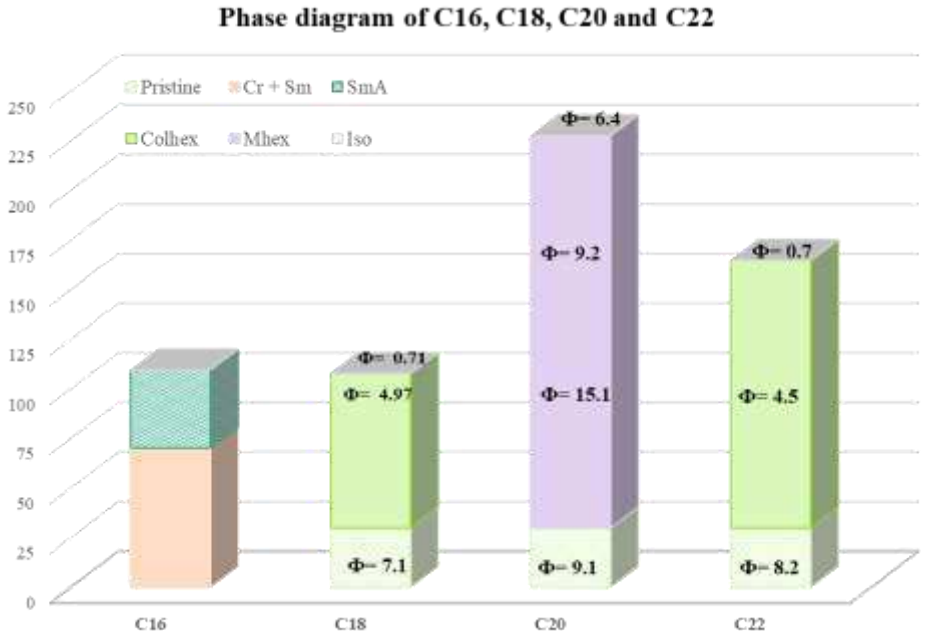

Figure 3-35. Phase diagram of **C16**, **C18**, **C20** and **C22** and emission quantum yields in the different phases.

Complex **C16** was used to modify a carbon nanofiber paste electrode and it is currently tested as sensor for the electrochemical detection for glucose, ascorbic acid and uric acid.

The promising results motivated us to synthesize Pt(II) complexes, although not in the scope of this thesis, using these *tpy*-based ligands **L7** – **L11.**

Pt(II) complexes with ligand **L9** were already reported by our group together with the Zn(II) analogues (**complexes C17 and C18**).[354] Their mesomorphic and luminescent properties make them good candidates for biological investigations in perspective.

Chapter 4. Supramolecular architectured gold nanoparticles as carriers for a potential active coordination compound

A possible route to deliver appropriate coordination compounds (a medicine, or an imagistic relevant compound) to a specific target in biological systems is to fix this compound on a carrier which can be externaly monitorised. Such a carrier has been recognized to be gold nanoparticles. In these cases, an appropriate binding system between the biological active complex compound and gold nanoparticles (Au NPs) is necessary to be constructed. In order to increase and control the efficiency, dendritic moieties were considered in our studies as binding system. The dendritic moieties are connected to the Au NPs through some anchors. An active shell around Au NPs will be thus created as the dendritic moieties act as appropriate system to bind more active TMC at the external rim. The number of dendritic moieties around Au NPs as well as the number of dendritic branches can be correlated with the specific doses of necessary TMC at the target. **Figure 4-1** shows the schematic representation of the targeted structures, where in **(a)** the simplest structure is represented with a single TMC unit binding to a zero dendritic unit (no bifurcation). The **Figure 4-1 (b)** shows a system with a first-generation dendritic branch (first bifurcation), and – as a consequence, two biological active TMCs units can be delivered to the desired target.

Thus, three fundamental classes of materials and their specific properties will be merged: i) 3d transition metal complexes (luminescence); ii) dendrimers (conformational flexibility, nano-scale dimensions, periodic 3D branched architectures, hyperfunctionalisation and multivalency); and iii) noble metal NPs (localized surface plasmon resonance).

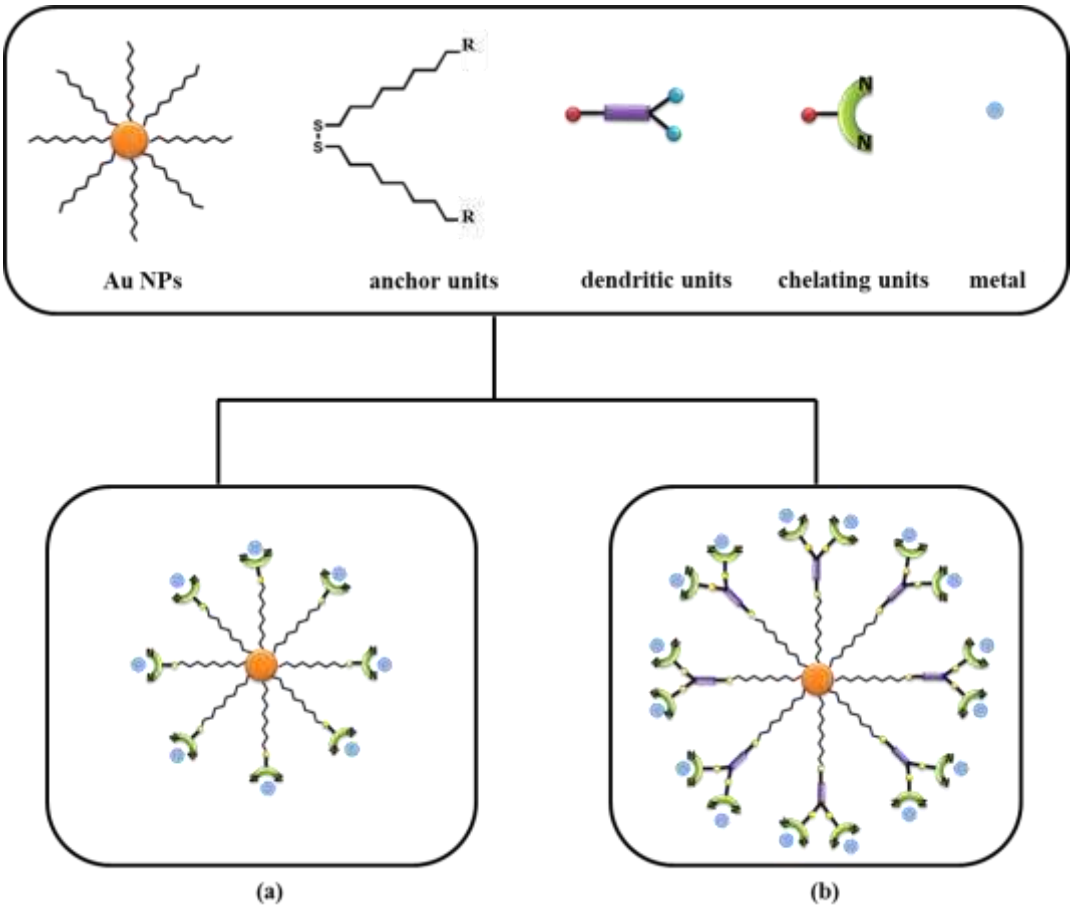

Figure 4-1. Schematic representation of the NP dendronization with end-N-donor ligands concept: basic elementary units (top) used to obtain the targeted structures (bottom).

The assembling of the above-mentioned moieties would lead to potential efficient multifunctional nanoplatforms for theranostic purposes.

To obtain such Au NPs coated with metallodendritic branches, several synthetic steps are required, which were realized in parallel modules:

- (4.1) Synthesis of the Au NPs,
- (4.2) Synthesis of the N-donor chelating units,
- (4.3) Synthesis of the dendritic branches,
- (4.4) Metal chelation of the dendritic branches containing N-donor ligands,
- (4.5) Ligand exchange between Au NPs and metallodendritic branches.

Using the four basic elementary units from **Figure 4-1,** several synthetic strategies can be envisaged for the synthesis of the aimed advanced materials, such as: i) building the dendritic structures around the oleylamine capped Au NPs or ii) synthesis of the dendritic branches and then their subsequent attachment on to the Au NPs.

The first step may be the attachment of the anchor unit around the oleylamine coated Au NPs surface, afterwards the attachment of the dendrons on the terminal groups R (R= OH, COOH, N_3, etc.) of Au NPs. Once the dendritic Au NPs are obtained, the next step would be the attachment of the metal chelating unit, followed by the coordination to a *3d* metal ion, as seen in **Scheme 4-1**.

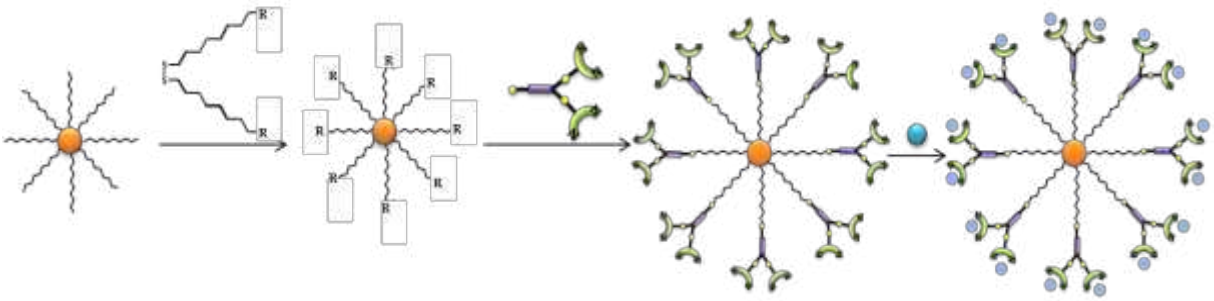

Scheme 4-1. Schematic synthetic route of the dendritic structure around Au NPs.

Another strategy may be the synthesis of the dendritic branches with the corresponding N-donor chelating units, following by the attachment of the anchor unit, and coordination of the desired *3d* metal ions. Finally, the dendronization of the Au NPs by solvent-mediated ligand exchange will be performed, as seen in **Scheme 4-2**.

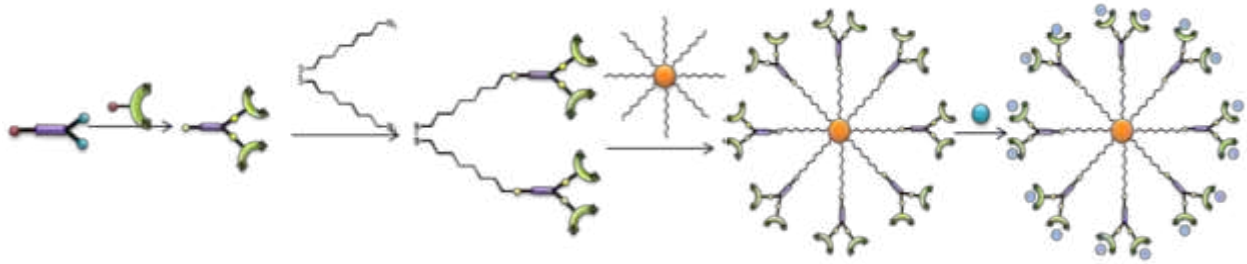

Scheme 4-2. Schematic synthetic route of dendritic branches and then their attachment on to the Au NPs.

In both of the cases, the coordination of the metal centre to the chelating unit can be performed in different steps of the described strategy: initially, in the synthesis of the dendritic branch step, or finally, after the dendritic branches were attached to the Au NPs.

4.1 Gold nanoparticles

Due to their unique physical and chemical properties, functionalized Au NPs with controlled geometrical and optical properties are highly researched for their potential biomedical applications (e.g.: targeted delivery of drugs, laser phototherapy of cancer cells and tumours, biosensorics, immunoassays, optical bioimaging, etc.).[364] The optical properties of Au NPs are influenced by the plasmon resonance, which is associated with the collective excitation of conduction electrons and localized from the Vis to the IR region, and depends on the particle size, shape, and structure.[365]

The synthesis of Au NPs – according to a method described by Peng *et al.*[366] is presented in the experimental chapter. The as synthesized Au NPs were characterized by FT-IR spectroscopy, UV-Vis spectroscopy and TEM microscopy.

The FT-IR spectrum, represented in **Figure 4-2**, presents the characteristic absorption bands of oleylamine at 3422 cm^{-1} corresponding to the stretching of the N-H bond, 2919 cm^{-1} and 2850 cm^{-1} which are characteristic for the C-H stretching, 1631 cm^{-1} which is attributed to the C=C stretching vibration.[367]

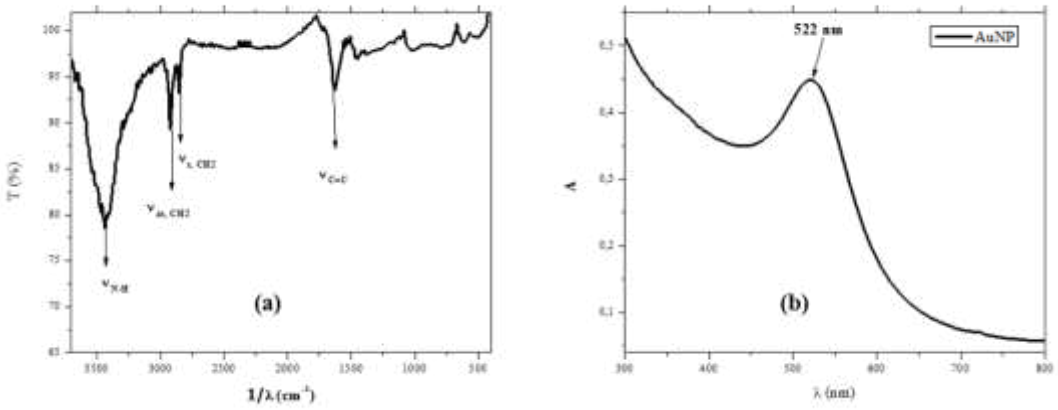

Figure 4-2. (a) FT-IR spectra of Au NPs and (b) UV-Vis spectra of Au NPs in CH_2Cl_2.

The UV-Vis spectrum was recorded in CH_2Cl_2 and it shows the presence of the surface plasmon resonance (SPR) band, having a maximum at λ_{max}=522 nm.

To determine the physical size and structural morphology of gold nanoparticles, TEM micrographs were recorded. The micrographs from **Figure 4-3** indicate the formation of spherical nanoparticles, with the average size diameter of 6.6 nm.

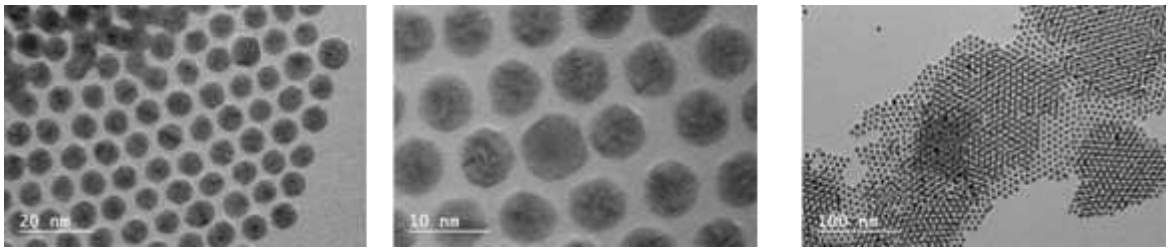

Figure 4-3. TEM images of the oleylamine coated Au NPs.

Subchapters 4.2 and 4.3 are highly interconnected. First, we choose a *bpy* derivative as the N-donor ligand. However, the repeated failures of the synthesis of this ligand, forced us to substitute *bpy* for *tpy* ligand whose synthesis is more straightforward and where less steps are required. When we finally obtained the desired *tpy* derivative, the carboxylic acid of ligand **L9** used in Chapter 3, further reaction with the dendritic branches led to the only monosubstituted dendrimers. Therefore, the generation growth was ensured by using a phenyl unit.

4.2 Synthesis of the N-donor chelating units

In order to sustain our concept regarding the synthesis a supramolecular architectured gold nanoparticles as carriers for a potential active coordination compound, we considered the several *bpy* and *tpy* derivatives, amongst which the intermediate **I4** has already been presented in Chapter 3. The structures of the targeted *bpy* and *tpy* derivatives are presented in **Figure 4-4**.

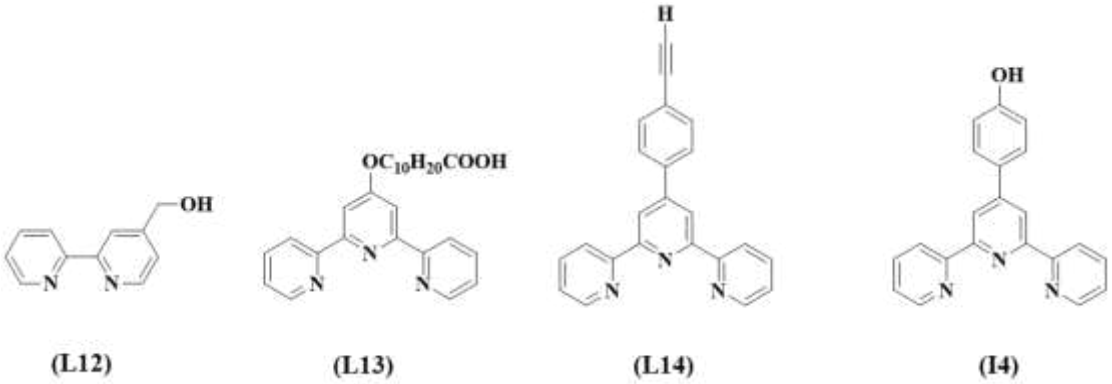

Figure 4-4. The structures of the substituted *bpy* and *tpy* derivatives used in this chapter.

N-heterocycles are one of the most studied classes of ligands in coordination chemistry, due to their ability to readily integrate in more than two donor atoms and aromatic N-containing heterocycles in a single molecule, which led to several chelating and bridging ligands.[368,369]

As highlighted in the introduction part, TMCs containing nitrogen chelating ligands, such as *bpy* and *tpy*, have also interesting physicochemical properties and important biological activities.[370]

The first report on *bpy* is dated in 1888, when F. Blau synthesized the first bipyridine iron complex.[371] Since then, numerous reports regarding the synthesis of *bpy* derivatives and/ or their metal complexes have been made,[372] with applications ranging from analytical chemistry, energy conversion, catalysis to medical chemistry etc. Over the past few years, the *bpy* motif has been developped in polymer and dendrimer chemistry, used as targeting materials with novel photo-, electrochemical, or catalytic features, and considered as an important novel architectures in supramolecular chemistry.[373] Therefore, the synthesis of dendrimers containing *bpy* units is of current interest.

Due to their ease of synthesis and functionalization, *tpy* derivatives, especially those substituted in the 4'-position, have also gained increasing interest as functional templates in the fields of supramolecular and coordination chemistry.[374]

Tpy was first reported in 1932 by Morgan and Burstall,[375] as one of the 20 products from the reaction of pyridine with anhydrous $FeCl_3$. Since then other synthetic routes have been developed with higher yields and more specific results. Nowadays there are different synthetic routes to form substituted terpyridines, generally based on two different methods, ring closure and ring coupling (Ullmann, Stille or Suzuki coupling reactions),[351,376] the latter approach is not preferred due the poor availability of the required starting materials, severe reaction conditions and low yields.

An example of the ring closure method is the Kröhnke condensation,[351] briefly described in **Scheme 4-3**, and which involves the reaction between derivatives of 2-acetylpyridine and an aromatic aldehyde.[377] Using this method, various substituted aryl groups can be easily incorporated at the *tpy* 4'-position and it is widely applied for the preparation of functional *tpy* for self-assembly studies.[378]

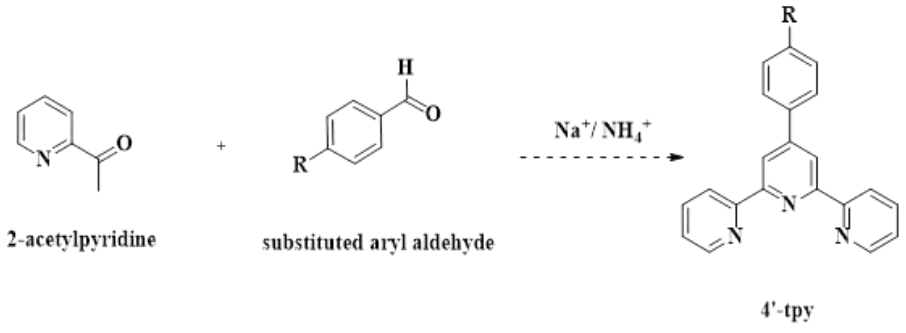

Scheme 4-3. Schematic synthetic route of 4'-substituted *tpy* through Kröhnke condensation.

Switching from 2-acetylpyridine to ethyl picolinate generates 4'-hydroxy-*tpy* (see **Scheme 3-1**, Chapter 3, ligand **L8**), which can be easily converted into other *tpy* derivatives simply through etherification or esterification reactions.

Both of the above-mentioned approaches allow the incorporation of various functional groups at the 4'-position of the central pyridine ring, including hydroxy, thiol, carboxylic acid and amino groups.[378]

Due to their high binding affinity towards a variety of metal ions and their interesting properties (electrochemical, catalytic, magnetic properties and photophysical) imparted upon coordination, *bpy* and *tpy* have been employed as building blocks for the preparation of numerous metallo-supramolecular architectures.[379] Also, because metal-ligand interactions are essential in the self-assembly strategies used in supramolecular chemistry,[380] the design of metallodendrimers bearing *bpy* or *tpy* derivatives, could lead to new functional materials.[374]

Moreover, by attaching metallodendritic structures to Au NPs, the resulting conjugated systems could be employed as biomaterials for the investigation of biological systems.**233**

Based on this background, the design and synthesis of hybrid nanostructures containing Au NPs and TMCs linked by dendritic structures will result in the obtaining advanced materials.

4.2.1 Bipyridine chelating units

4.2.1.1 (2-(Pyridin-2-yl)pyridin-4-yl)methanol

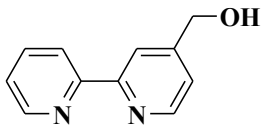

(L12)

Figure 4-5. Targeted *bpy* unit.

Using 2-bromopyridine as starting material, two synthetic routes were planed: one involved to obtain the targeted *bpy* unit through a Suzuki coupling procedure (**Scheme 4-4**) and the other through C-H bond activation (**Scheme 4-5**).

Strategy 1. Suzuki coupling synthetic route

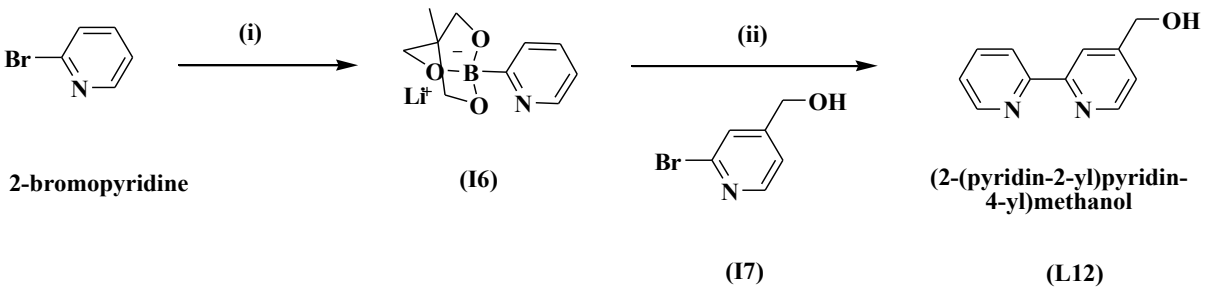

Scheme 4-4. Reaction pathway of **L12** through Suzuki coupling. Reagents and conditions: (i) BuLi, $B(OBu)_3$, THF, -78 °C, (ii) $Pd(Ph_3P)_4$, DMF/H_2O, Na_2CO_3.

Compound **I7** was obtained in very good yield following a multi-step procedure (see experimental chapter), but the desired compound **L12**, was obtained in a very low yield (< 4%) and moreover the product was difficult to isolate (some impurities were still detected after laborious purification steps).

Strategy 2. The C-H arylation synthetic route

We followed a synthetic procedure reported by S. Duric *et al.*[381] which involves the direct coupling between pyridine N-oxides and bromopyridines using a palladium catalyst, to yield compound **L12**, as depicted in **Scheme 4-5**. This method was also unsatisfactory, producing on average less than 5 % yield of the targeted *bpy*.

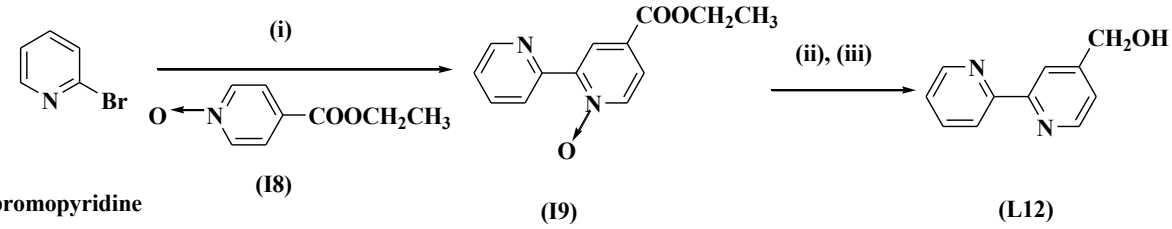

Scheme 4-5. Synthetic pathway of **L12** by C-H coupling. Reagents and conditions: (i) $Pd(OAc)_2$, K_2CO_3, toluene, ΔT, (ii) Pd/C, $HCOONH_4$, MeOH, (iii) $NaBH_4$, MeOH.

The difficulty and low-yields syntheses of **L12** were clearly two major drawbacks for the continuity and success of the project. We therefore decided to move forward and we envisaged another strategy based on the derivatization of terpyridine deriatives. Indeed, we have

showed in the previous chapter that 4-substituted *tpy* derivatives were relatively easy to synthesize, and that such systems could be perfectly adapted to the project.

4.2.2 Terpyridine chelating units

4.2.2.1 11-(2,6-di(Pyridin-2-yl)pyridin-4-yloxy)undecanoic acid

The synthesis of **L13** was realized by the hydrolysis of ligand **L9** as described in **Scheme 4-6**. The compound was characterized by ^{1}H-NMR (**Figure 4-5**).

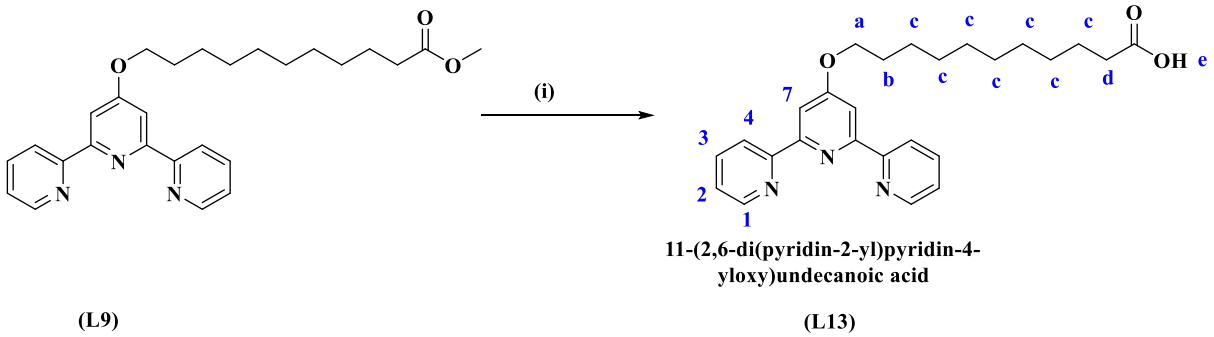

Scheme 4-6. Reaction pathway of **L13** (and its atom labelling) starting from ligand **L9**. Reagents and conditions: (i) NaOH, MeOH, ΔT.

^{1}H-NMR spectroscopy

The successful hydrolysis of the methoxylate group was confirmed by ^{1}H- NMR spectroscopy, **Figure 4-6**, and the presence of the signal corresponding to H^{e} proton at 11.96 ppm, corresponding to the proton of the carboxylic group. A summary of the chemical shifts it is realized in **Table 4-1.**

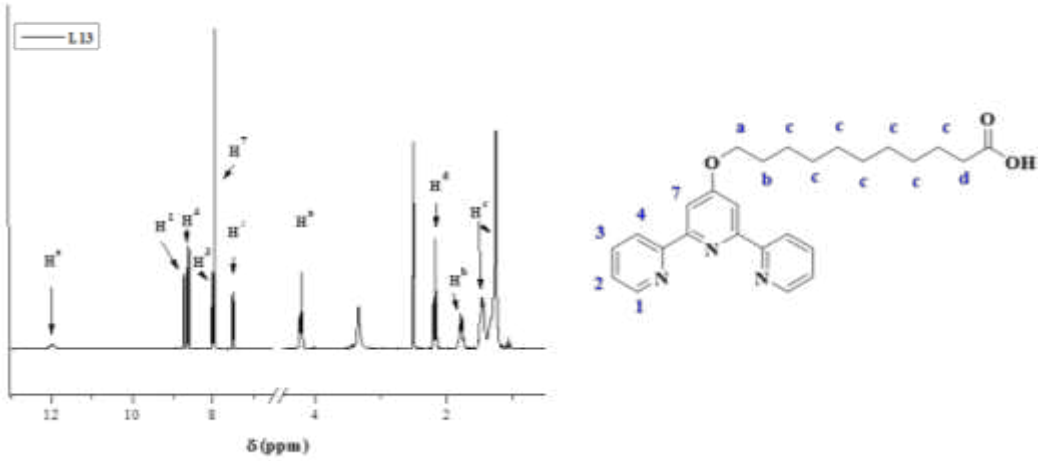

Figure 4-6. ^{1}H NMR spectra of **L13**.

Table 4-1. Chemical shifts (in δ/ppm) of ligand **L13** recorded in $CDCl_3$.

Chemical shifts (in δ/ppm)									
Compound	H^1	H^2	H^3	H^4	H^7	H^a	H^b	H^c	H^d
L13	8.71	7.51	8.00	8.61	7.96	4.23	1.78	1.56 – 1.22	11.96

4.2.2.2 4'-(4-Ethynylphenyl)-2,2':6',2''-terpyridine

The second option was the synthesis of a *tpy* derivative with an acetylene linker, compound **L14**, which was obtained through Sonogoshira coupling starting from the intermediary compound **I10**, according to **Scheme 4-7**.[382,383] The intermediary compound **I10** and the targeted compound **L14** were characterized by ^{1}H-NMR spectroscopy.

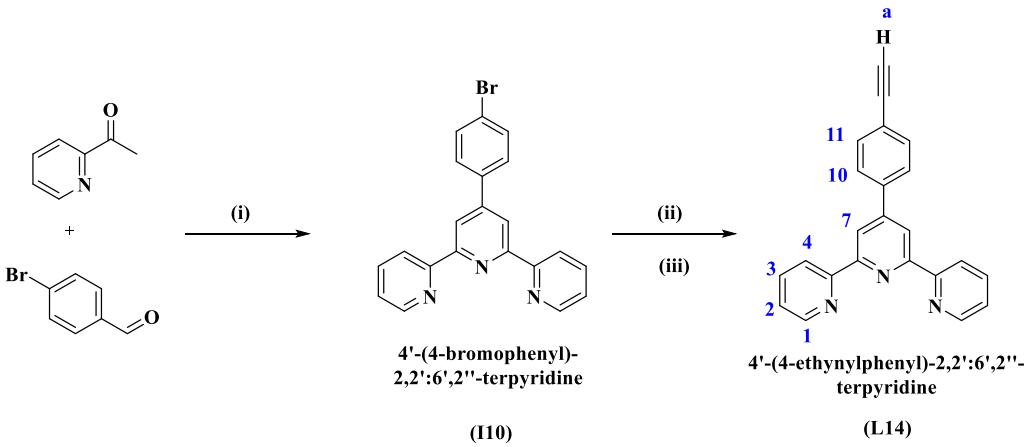

Scheme 4-7. Reaction pathway of **L14** and atom labelling (blue). Reagents and conditions: i) KOH, NH_4OH, ETOH, ΔT, 24 h; ii) TMSA, $PdCl_2(PPh_3)_2$, CuI, NEt_3/ THF, 70°C, 12h; iii) K_2CO_3, $CHCl_3$/ MeOH, r.t, 3h.

^{1}H-NMR spectroscopy

The purity of the targeted compound was checked by ^{1}H NMR and is presented in **Figure 4-7**. Also, from the NMR spectra the proton belonging to the acetylene linker could also be identified by the singlet at 3.20 ppm (H^{a}). A summary of the chemical shifts is realized in **Table 4-2**.

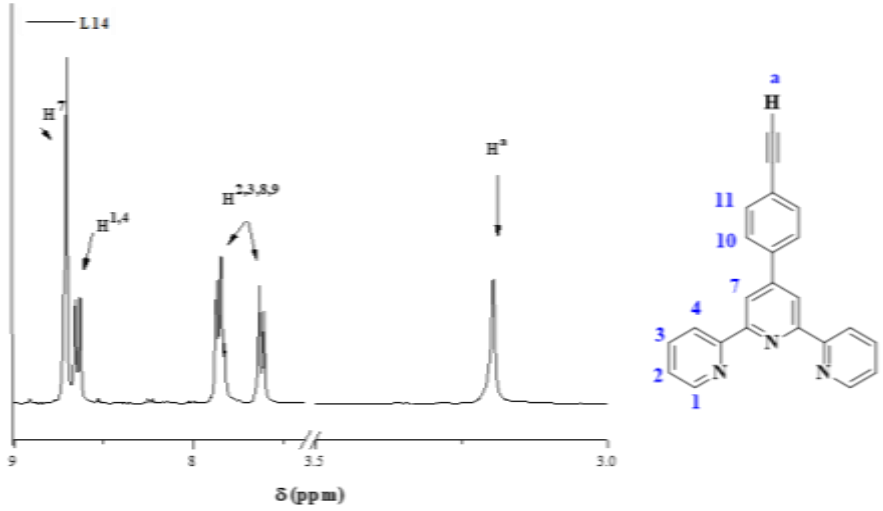

Figure 4-7. ^{1}H NMR spectra of **L14**.

Table 4-2. Chemical shifts (in δ/ppm) of ligand **L14** recorded in $CDCl_3$.

Chemical shifts (in δ/ppm)								
Compound	H^{1}	H^{2}	H^{3}	H^{4}	H^{7}	H^{8}	H^{9}	H^{a}
L14	8.81-8.58[a]			8.81-8.58[a]	8.81-8.58[a]			3.19

*4.2.2.3 4-([2,2':6',2''-Terpyridin]-4'-yl)phenol **I4***

The third *tpy* derivative taken into consideration was compound **I4**, which was obtained from ligand **L10**, by a demethoxylation reaction, as described in **Scheme 4-8**. The targeted compound **I4** was characterized by ^{1}H-NMR spectroscopy.

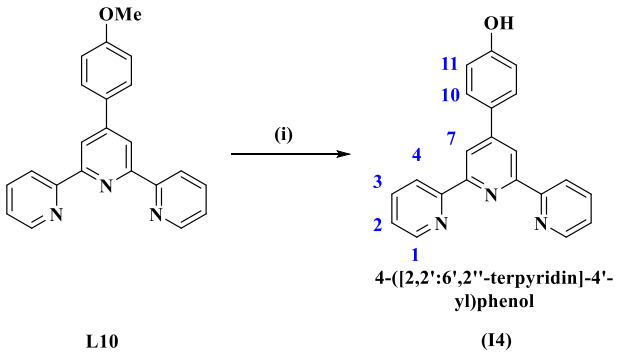

Scheme 4-8. Reaction pathway of **I4** and its atom labelling (blue). Reagents and conditions: i) CH_3COOH/HBr, ΔT, 24 h.

Table 4-3. Chemical shifts (in δ/ppm) of ligand **I4** recorded in DMSO-d_6.

Chemical shifts (in δ/ppm)							
Compound	H^1	H^2	H^3	H^4	H^7	H^{10}	H^{11}
I4	8.78- 8.70	7.58- 7.43	8.07- 7.95	8.68-8.59	8.68-8.59	6.95	7.82

More details regarding the synthesis and characterization of targeted *tpy* derivatives can be found in the experimental chapter.

4.3 Dendritic branches functionalized with tpy derivatives

In order to increase and control the efficiency, and also to bind more active TMCs, dendritic moieties were considered in the design of the assemblies. Therefore, we decided to synthesize two types of dendritic branches, either using 3-hydroxy-2-(hydroxymethyl)-2-methylpropanoic acid (**G_A**) or 3,5-dihydroxy methyl benzoate (**G_B** and **G_C**) as starting materials, as described in **Figure 4-8**.

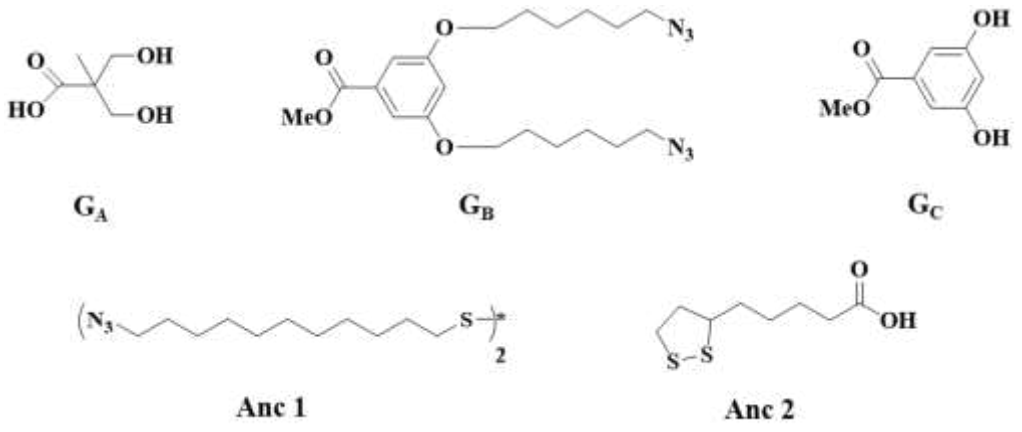

Figure 4-8. The structures of the dendritic branches and of the anchoring units used in this chapter.

The dendritic branches of type $\mathbf{G_A}$, derived from 3-hydroxy-2-(hydroxymethyl)-2-methylpropanoic acid (bis-MPA), were functionalized with with *tpy* derivative **L13** and the anchoring unit **Anc 1** was taken into consideration. For the synthesis of dendritic branches of type $\mathbf{G_B}$ ligand **L14** was used, whereas for those of type $\mathbf{G_C}$ ligand **I4** was considered. In case of the dendritic branches derived from 3,5-dihydroxy methyl benzoate ($\mathbf{G_B}$ and $\mathbf{G_C}$), the commercially available thioctic acid or lipoic acid (**Anc 2**) was used.

Following, this subchapter was divided in two parts depending on the starting materials used to synthesize the dendritic branches.

4.3.1. Dendritic branches with $\mathbf{G_A}$ with ligand **L13**.

For the synthesis of $\mathbf{G_A}$ functionalized with ligand **L13** several synthetic steps were taken into account, which are described in **Scheme 4-9**.

4.3.1.1 Synthesis of dendritic branches of type $\mathbf{G_A}$

The dendritic branches of various generations were synthesized according to methods described in literature, through anhydride coupling, using 3-hydroxy-2-(hydroxymethyl)-2-methylpropanoic acid as starting material. Two generations, presented in **Scheme 4-9**, were synthesized and characterized by ^{1}H-NMR spectroscopy. Their NMR data were in agreement with the ones reported in the literature (see experimental chapter).[384]

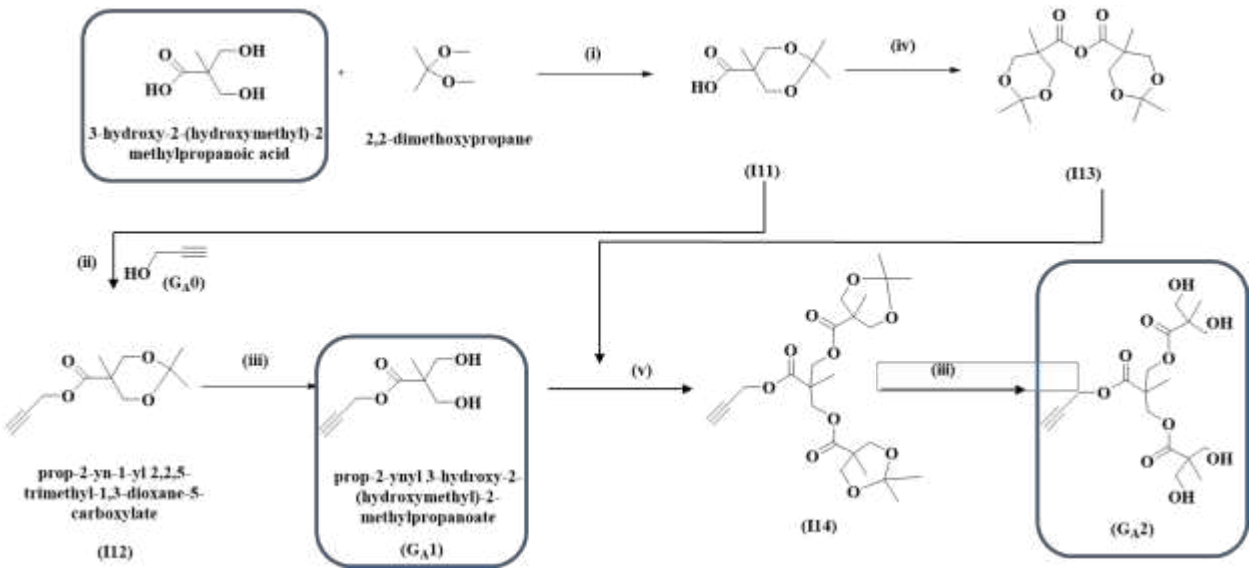

Scheme 4-9. Reaction pathway of **G_A1** and **G_A2** dendrons derived from 3-hydroxy-2-(hydroxymethyl)-2-methylpropanoic acid. Reagents and conditions: (i) dry acetone, PTSA, 2h, r.t (ii) dry CH_2Cl_2, DMAP, DCC, r.t, 24 h, (iii) Dowex H^+, MeOH, 40ºC, 2h, (iv) dry CH_2Cl_2, DCC, r.t., (v) dry CH_2Cl_2, DMAP, pyridine, r.t, 24 h;

*4.3.1.1 Synthesis of **G_A1** and **G_A2***

The **G_A1** compound was obtained in three steps following a reported procedure as described in **Scheme 4-9**.[385] Briefly, the hydroxyl groups of 3-hydroxy-2-(hydroxymethyl)-2-methylpropanoic acid, were protected using 2,2 -dimethoxy-propane (compound **I11**), then the carboxylic acid was esterified through a Steiglich method with propargyl alcohol. The hydroxyl groups were deprotected using an ion-exchange resin (Dowex H^+) to yield targeted compound **G_A1**.

In order to synthesize the next generation dendron, starting from compound **I11**, 2,2,5-trimethyl-1,3-dioxane-5-carboxylic anhydride, **I13** was first synthesized, as described in **Scheme 4-9**. The dendritic branches of **G_A2** were synthesized according to a method described in literature,[384] through anhydride coupling, using **G_A1** and **I13**, to yield compound **I14**. The hydroxyl groups were deprotected, thus obtaining **G_A2**.

*4.3.1.2 Synthesis of **Anc_1***

The anchoring unit **Anc_1** from **Figure 4-8** was synthesized according to a published procedure, in a three-step, high-yield synthesis from commercially available 11-bromoundecanol, as described in **Scheme 4-10**.[384] The intermediary compounds and the final

product were characterized by ^{1}H-NMR spectroscopy. Their NMR data is in agreement with the ones reported in the literature.[384]

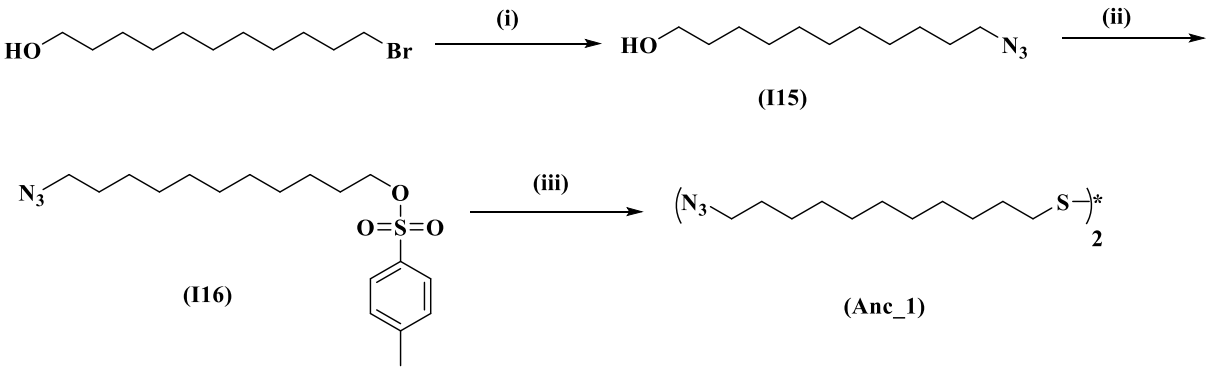

Scheme 4-10. Reaction pathway of **Anc_1**. Reagents and conditions: (i) NaN_3, DMF, 70ºC, (ii) CH_2Cl_2, TsCl, NEt_3, 0ºC, r.t, 12 h, argon, (iii) thiourea, EtOH, 80ºC, 20 h.

*4.3.1.3 Functionalization of **G_A0** and **G_A1** with ligand **L13***

The functionalization of dendritic branches **G_A0** and **G_A1**, derived from 3-hydroxy-2-(hydroxymethyl)-2-methylpropanoic acid, with *tpy* derivative **L13**, involved a two-step procedure. Firstly, the terminal azide group of **Anc_1** and the acetylenic units of **G_A0** (propargyl alcohol) and **G_A1**, were reacted through a Cu(I) catalysed cycloaddition, to yield the intermediary compounds **I17** and **I18**, respectively, whose hydroxylic groups were further esterified with *tpy* derivative **L13** as described in **Scheme 4-11**.

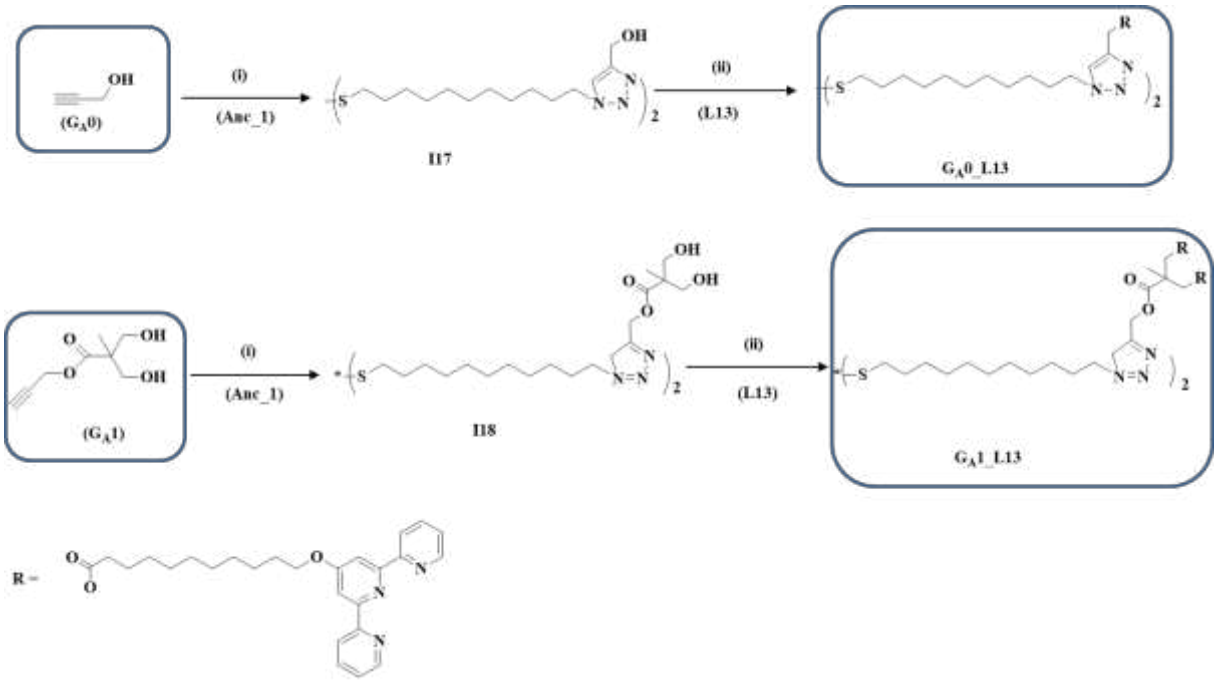

Scheme 4-11. Reaction pathway of **G_A0_L13** and **G_A1_L13**. Reagents and conditions: (i) $CuSO_4$ x $5H_2O$, THF/H_2O, 80ºC, 24 h, (ii) DCC, DMAP, CH_2Cl_2, Ar, r.t., 2 days.

As mentioned above, the first step to obtain the targeted compound **G_A0_L13** was the Cu(I) "click" reaction between the terminal azide group of **Anc_1** and the acetylenic units of propargyl alcohol, to yield **I17**. This reaction proceeded in high yields (72 %) and the compound was separated by filtration from the reaction media, and successive washing with H_2O, THF and CH_2Cl_2. Compound **I17** was further reacted with **L13** using DCC as coupling agent, which resulted in compound **G_A0_L13** in low yields (**Scheme 4-11**). The NMR analysis also revealed the presence of impurities.

Compound **G_A1_L13** was synthesized in a similar manner to **G_A0_L13**, as described in **Scheme 4-11**. The pure compound **I18** was obtained in high yields by extraction with CH_2Cl_2. When it was further reacted with **L13**, no reaction took place.

Because both targeted compounds were obtained in low yields, a different synthetic approach was attempted. Because acyl chlorides are known to readily react with an alcohol,[386] first the *tpy* derivative **L13** was converted to the corresponding acyl chloride (**I19**) and then reacted with compounds **I17** and **I18**, using pyridine as a base to neutralize the HCl formed in the reaction, as seen in **Scheme 4-12**.

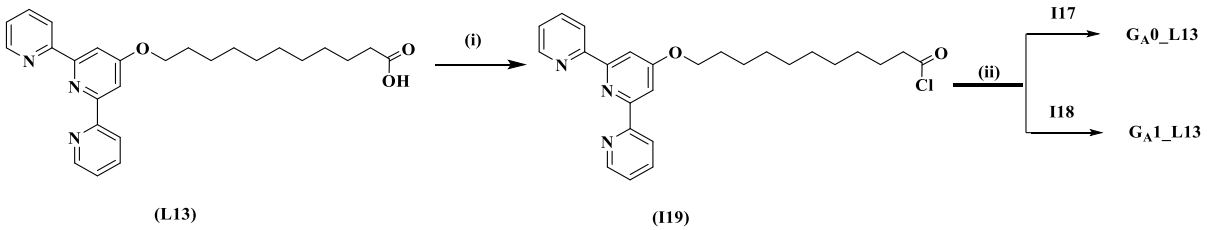

Scheme 4-12. Alternative route to obtain **G_A0_L13** and **G_A1_L13**. Reagents and conditions: (i) $SOCl_2$, ΔT, 12 h, (ii) pyridine, CH_2Cl_2, Ar, r.t., 2 days.

The dendritic branches bearing the N-donor ligands **G_A0_L13** and **G_A1_L13** were obtained in low yields, regardless of the synthetic approach. Therefore, we undertook the synthesis of other *tpy* derivatives, with different anchoring and branching units.

4.3.2 Synthesis of dendritic branches of type G_B with ligand L14

To obtain more sites able to bind active species, the dendritic moiety can be expanded. Therefore, to ensure the dendritic growth, another junction was designed, using 3,5-dihydroxy methyl benzoate as starting material (**Figure 4-8**).

4.3.2.1 Synthesis of dendritic branches of type G_B

Compound **G_B1** was easily synthesized according to published procedure, by a Williamson etherification reaction between 1-azido-6-bromohexane compound **I20** and 3,5-dihydroxy methyl benzoate as depicted in **Scheme 4-13**. The purity and nature of the compound was determined by ^{1}H-NMR analysis. The results are in agreement with the literature data.[387]

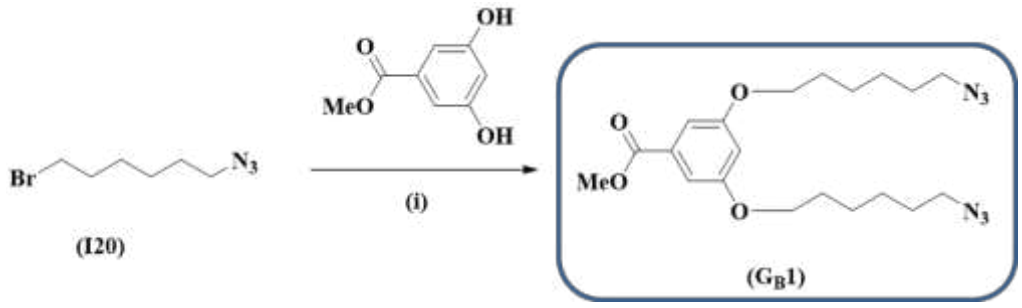

Scheme 4-13. Reaction pathway of **G_B1**. Reagents and conditions: (i) DMF, K_2CO_3, KI, 80 ^{0}C.

4.3.2.2 Functionalization of G_B0 and G_B1 with ligand L14

The synthetic approach to obtain **G_B0_L14** and **G_B1_L14** with *tpy* derivative **L14**, involved a multi-step procedure, as described in **Scheme 4-14** and **Scheme 4-15**. To reduce the number of steps we have also used thioctic acid (**Anc_2**) which is commercially available.

To obtain the final compounds **G_B0_L13** and **G_B1_L13**, some steps are still under work, as marked with blue in the corresponding schemes.

4.3.2.2.1 Synthesis of G_B0_L14

To obtain the **G_B0_L13**, firstly the *tpy* derivative **L13** was reacted with 6-azidohexanoic acid (**I21**) by Cu(I) "click reaction". Following, compound **I22** will be reacted with N-Boc-ethylenediamine (N-Boc) by an amidation reaction, then deprotected and esterified with **Anc_2** as depicted in **Scheme 4-14**. At this stage, the targeted compound has not yet been obtained, and the synthesis of compounds **I23**, **I24** and **G_B0_L14** are still in progress.

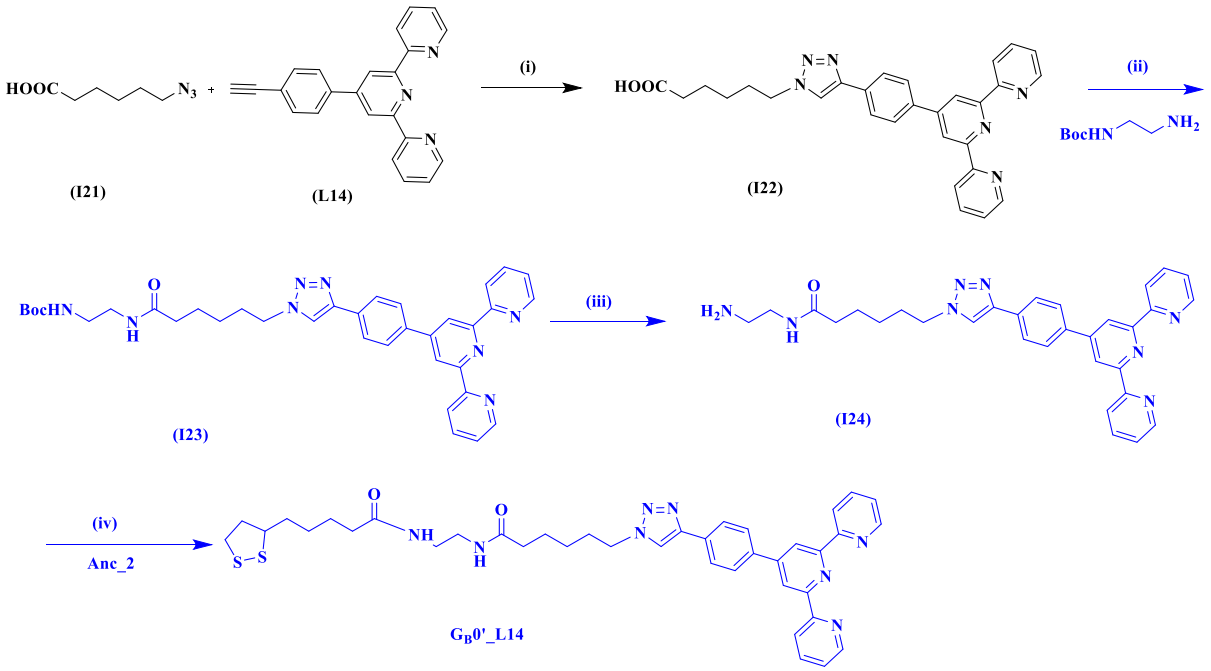

Scheme 4-14. Reaction pathway of **G_B0_L14**. Reagents and conditions: (i) $CuSO_4$ x $5H_2O$, L-Na asc., THF/H_2O, 80°C, 24h; (ii) DCC, DMAP, CH_2Cl_2, r.t, 14 h; (iii) CF_3COOH, CH_2Cl_2, r.t, 24 h; (iv) DCC, DMAP, CH_2Cl_2, r.t.

4.3.2.2.2 Synthesis of ***G_B1_L14***

To obtain the **G_B1_L14** compound (**Scheme 4-15**), firstly the terminal azide groups of **G_B1** and the acetylenic units of ligand **L14**, were reacted through a Cu(I) "click" cycloaddition, to yield **I25**, followed by the hydrolysis of the methyl ester, to obtain the acid **I26**. The corresponding acid will be further linked to N-Boc-ethylenediamine by an amidation reaction, followed by a deprotection of BOC and then esterified with thioctic acid, **Anc_2**.

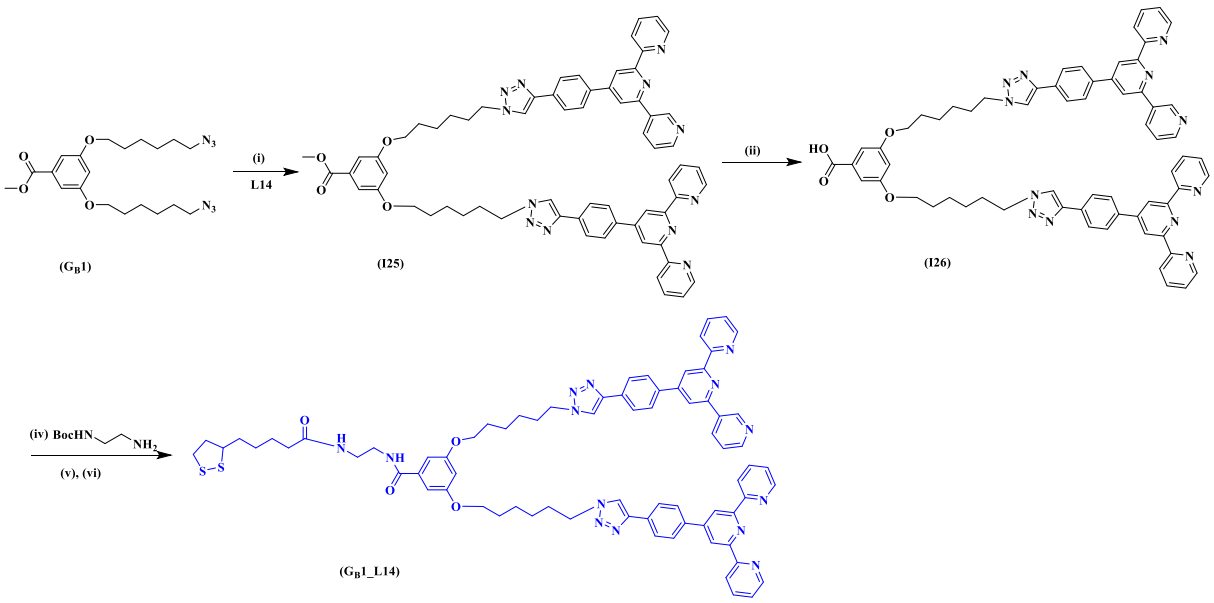

Scheme 4-15. Reaction pathway of **G_B1_L14**. Conditions: (i) $CuBr(PPh_3)_3$, THF, 65°C, 24 h, (ii) KOH, H_2O/THF, ΔT; (iv) DCC, 4-DMAP, THF. r.t, 24 h, (v) 1N HCl in THF, overnight, (vi) DCC, 4-DMAP, THF. r.t, 24 h.

4.3.3 Synthesis of dendritic branches of type G_C with ligand I4.

To reduce the number of synthetic steps, a different approach was taken into consideration, which allowed us to synthesize **G_C0_I4** generation in one step, whereas the synthesis of **G_C1_I4** requires four steps, as described in **Scheme 4-16**. Briefly **G_C0_I4** was obtained in 67 % yield through an esterification reaction between the anchoring unit **Anc_2** and **I4**, and for the synthesis of compound **G_C1_I4** some steps are still needed, which are currently in progress.

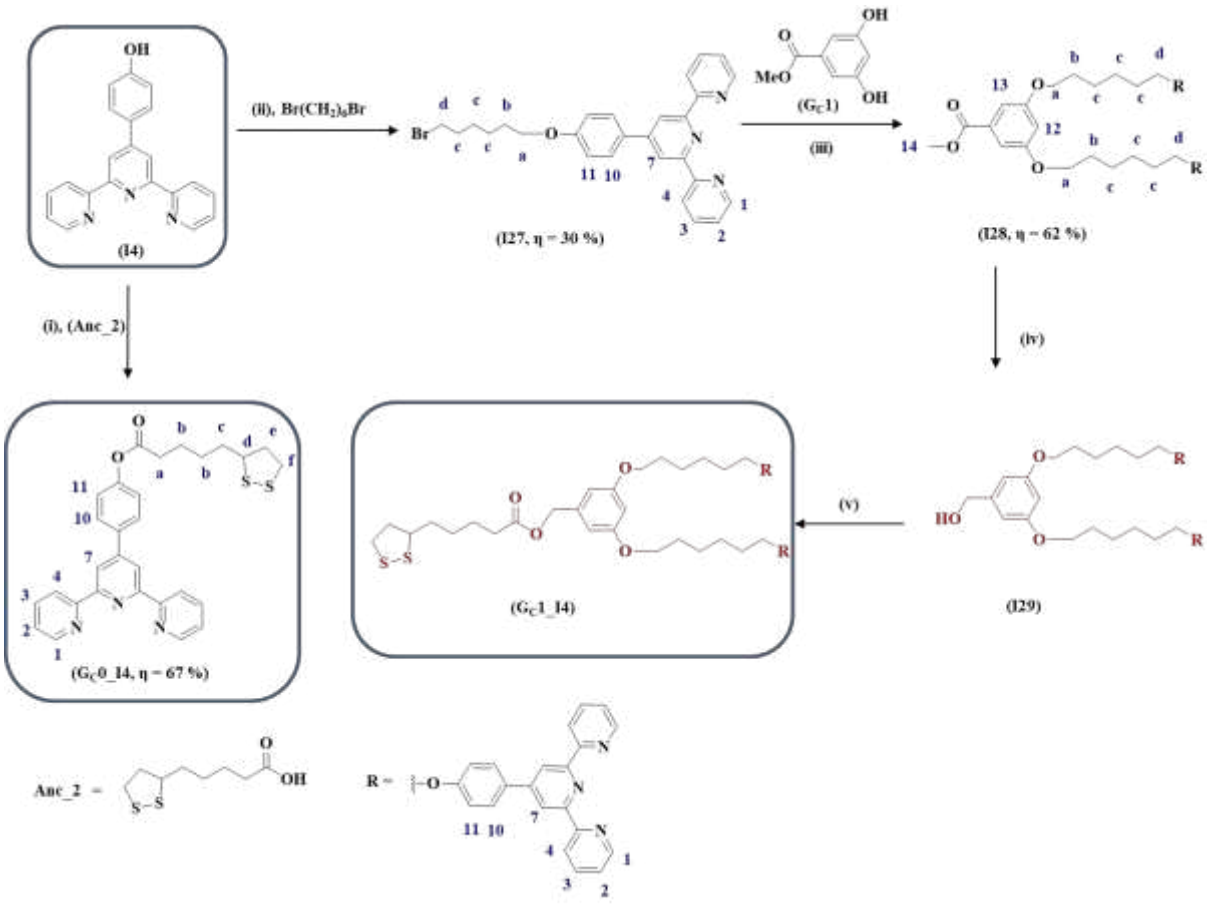

Scheme 4-16. Reaction pathway of **GC0_I4** and **GC1_I4** (atom labelling in blue). Reagents and conditions: (i) = (v) DCC, 4-DMAP, THF. r.t, 7 days, (ii) = (iii) K_2CO_3, DMF, 80ºC, 24 h, (iv) $LiAlH_4$, THF, r.t.

*4.3.3.1 Synthesis of **GC0_I4***

As mentioned above, compound **GC0_I4** was synthesized through a Steiglich esterification reaction and was isolated as a pale-yellow powder after recrystallization from EtOAc/EtOH in 67 % yield. The compound was characterized through FT-IR and ^{1}H-NMR spectroscopies.

FT-IR spectroscopy

Figure 4-9 shows the FT-IR spectra of **GC0_I4** plotted *vs.* **I4** and **Anc2**. **GC0_I4** presents the characteristic absorption bands corresponding to the *tpy* unit shifted with respect to **I4**.[388] The formation of **I4** was confirmed by the disappearance of the carbonyl absorption

and at 1694 cm^{-1}. The low intensity bands at 668 cm^{-1} (ν (C–S)) and 453 cm^{-1} (ν (S–S))[389,390,391] appear overlapped with the in-plane and out-of-plane deformation vibrations of *tpy* unit.[388]

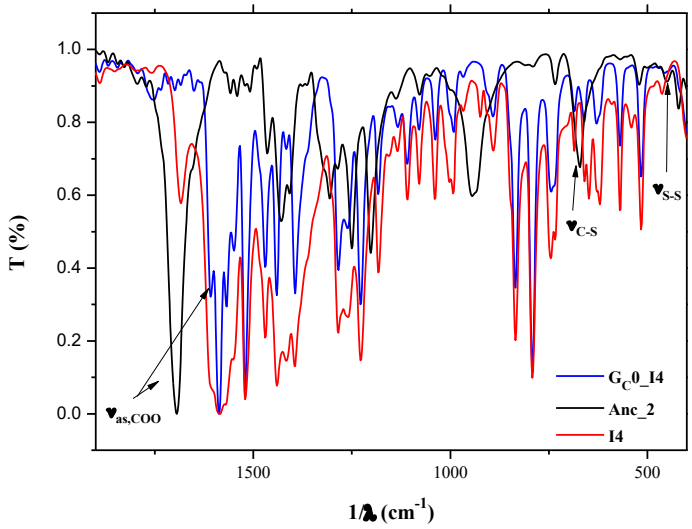

Figure 4-9. FT-IR spectra of **GC0_I4** plotted against its precursors **I4** and **Anc_2**.

Table 4-4. Assignment of the characteristic absorption bands of **I4**, **Anc_2** and **GC0_I4**.

Compound	**Assignment of the characteristic absorption bands (wavenumber values in cm^{-1})**			
	ν_{as}(COO)	$\nu_{(C=N \text{ and } C=C)}$	ν_{C-S}	ν_{S-S}
I4		1591-1442		
Anc_2	1694		668	453
GC0_I4	1605	1586-1437	659	469

^{1}H-NMR spectroscopy

Figure 4-10 presents ^{1}H-NMR spectra of **GC0_I4** plotted vs. **Anc_2.** By comparing the the two spectra, it can be seen that it presents the aromatic protons of the *tpy* unit. Also, the aliphatic protons H^{a} and H^{d} corresponding to presented a downfield shift with respect to the thioctic acid, from 3.16 ppm to 3.19 ppm for H^{a} and from 3.58 ppm to 3.64 ppm for H^{d}.

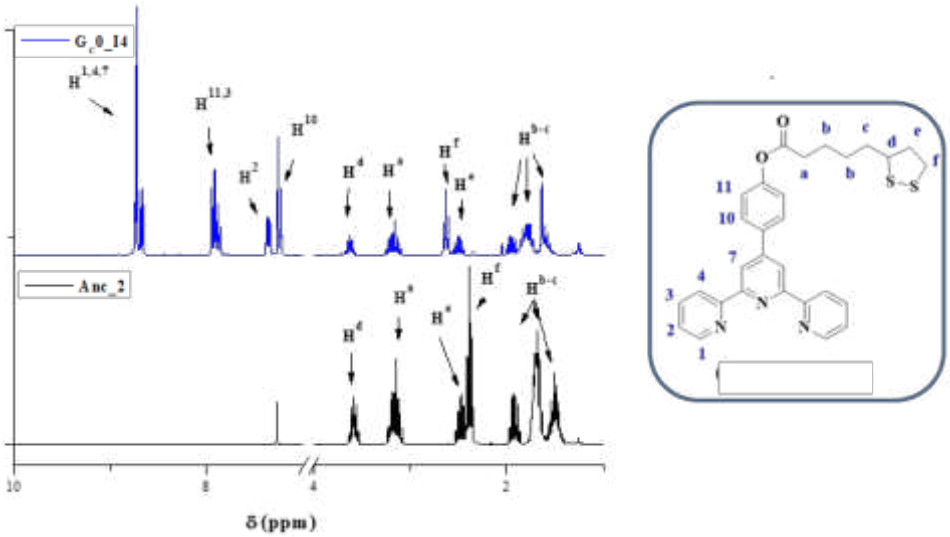

Figure 4-10. ^{1}H NMR spectra of **G_C0_I4** and of **Anc2**.

Table 4-5. Chemical shifts (in δ/ppm) of the aromatic region of **G_C0_I4** recorded in $CDCl_3$.

Chemical shifts (in δ/ppm)							
Compound	H^1	H^2	H^3	H^4	H^7	H^{10}	H^{11}
G_C0_I4	8.86 – 8.59	7.37	8.21 – 7.71	8.86 – 8.59	8.86 – 8.59	7.28	8.21 – 7.71

Table 4-6. Chemical shifts (in δ/ppm) of the aliphatic region of **G_C0_I4** and of **Anc_2** recorded in $CDCl_3$.

Chemical shifts (in δ/ppm)					
Compound	H^a	H^{b-c}	H^d	H^e	H^f
Anc_2	3.16	2.01 – 1.42	3.58	2.66 – 2.33	
G_C0_I4	3.19	2.08 – 1.48	3.64	2.72 – 2.55	

4.3.3.2 Synthesis of G_C1_L14

To obtain the final compound **G_C1_I4**, some steps are still in progress, which are marked with red in the corresponding **Scheme 4-16**, but the overall synthesis will be explained. The intermediary compounds **I27** and **I28** have been synthesized by etherification reactions. Compound **I29** will be obtained by the reduction of the carboxylate group to the hydroxyl group, using $LiAlH_4$ as catalyst, afterwards it will be esterified with **Anc_2** to yield the final desired compound **G_C1_I4**.

^{1}H-NMR spectroscopy

Figure 4-11 represents the ^{1}H-NMR spectra of the two intermediary compounds synthesized so far. By comparing the NMR spectra of **I27** with that of **I28**, very small shifts of

the aromatic protons corresponding to *tpy* unit could be noticed, whilst the aliphatic protons H^d presented a downfield shift from 3.44 ppm to 4.01 ppm. **Table 4-7** and **Table 4-8** summarize the chemical shifts of the two compounds.

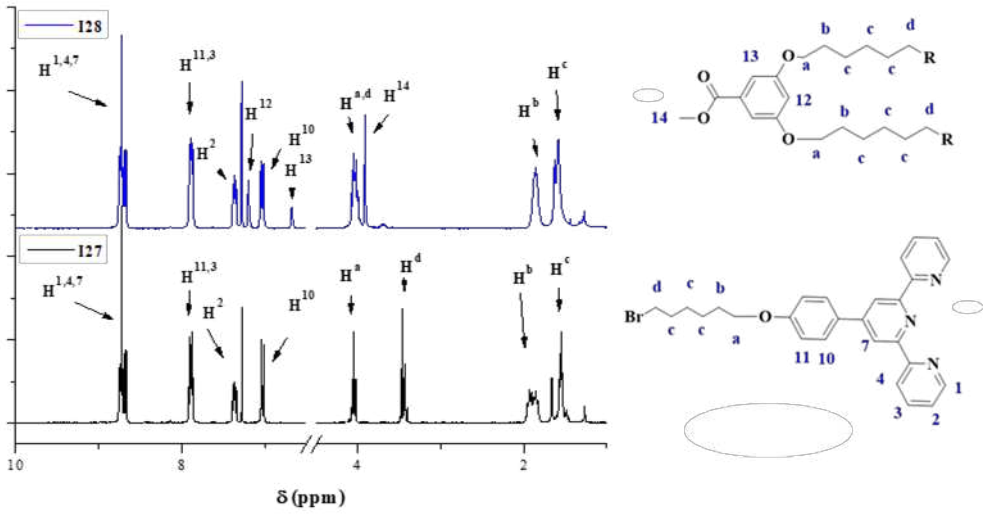

Figure 4-11. ^{1}H NMR spectra of **I27** and **I28**.

Table 4-7. Chemical shifts (in δ/ppm) of the aromatic region of **I27** and **I28** recorded in $CDCl_3$.

Chemical shifts (in δ/ppm)									
Compound	H^1	H^2	H^3	H^4	H^7	H^{10}	H^{11}	H^{12}	H^{13}
I27	8.92 – 8.54	7.35	8.04 – 7.78	8.92 – 8.54	8.92 – 8.54	7.03	8.04 – 7.78		
I28	8.88 – 8.59	7.57 – 7.32	7.89	8.88 – 8.59	8.88 – 8.59	7.03	7.89	6.67	7.19

Table 4-8. Chemical shifts (in δ/ppm) of the aliphatic region of **I27** and **I28** recorded in $CDCl_3$.

Chemical shifts (in δ/ppm)					
Compound	H^a	H^b	H^c	H^d	H^{14}
I27	4.15 – 3.91	1.89	1.39	3.44	
I28	4.24 – 3.81	1.86	1.73	4.24 – 3.81	4.24 – 3.81

Based on the fact that *tpy* with Zn(II) leads to luminescent TMCs, and on the fact that Zn(II) is less toxic and less expensive, we have decided to use Zn(II) as metal centre in our synthesis. Therefore, in order to perform the ligand exchange between **Au NPs** and the **G_C0_I4** generation, firstly we have obtained the Zn(II) complex with **G_C0_I4_Zn**, then we realized the ligand exchange obtain the functionalized **Au@G_C0_I4_Zn**, which are described hereafter.

4.4 Metal chelation of the dendritic branches containing N-donor ligands

The metal chelation of Zn(II) to the N-donor ligand was realized by reacting a small excess of $ZnCl_2$ with the corresponding **G_C0_I4_Zn** as described in **Scheme 4-17**. The final compound was characterized by FT-IR and UV-Vis spectroscopies. The low solubility of the complex ($<10^{-3}$ M) prevented recording of NMR experiments.

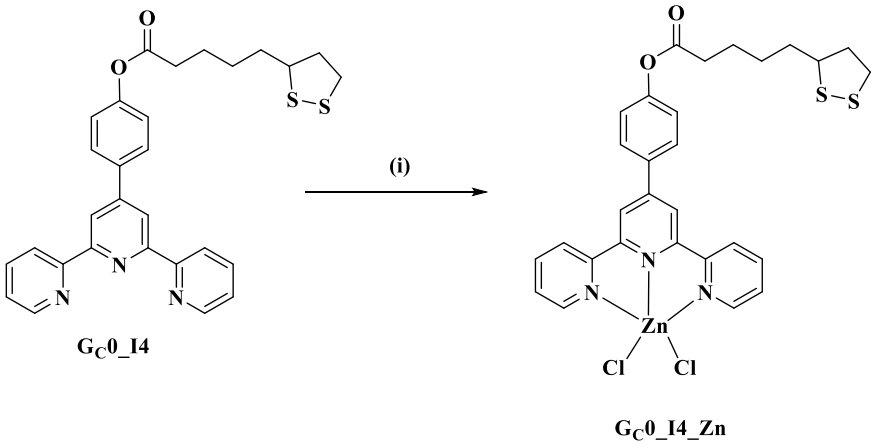

G_C0_I4 **G_C0_I4_Zn**

Scheme 4-17. Reaction pathway of **G_C0_I4_Zn**. Reagents and conditions: (i) $ZnCl_2$, EtOH/$CHCl_3$, r.t., 2h.

FT-IR spectroscopy

Figure 4-12 presents the FT-IR spectra of **G_C0_I4_Zn** plotted against its **G_C0_I4** precursor. By comparing these two spectra, the $\upsilon_{C=C}$ and $\upsilon_{C=N}$ characteristic bands present a significant shift to higher frequencies compared to the *tpy* ligand which indicates the coordination via the nitrogen atoms of the ligand.[355]

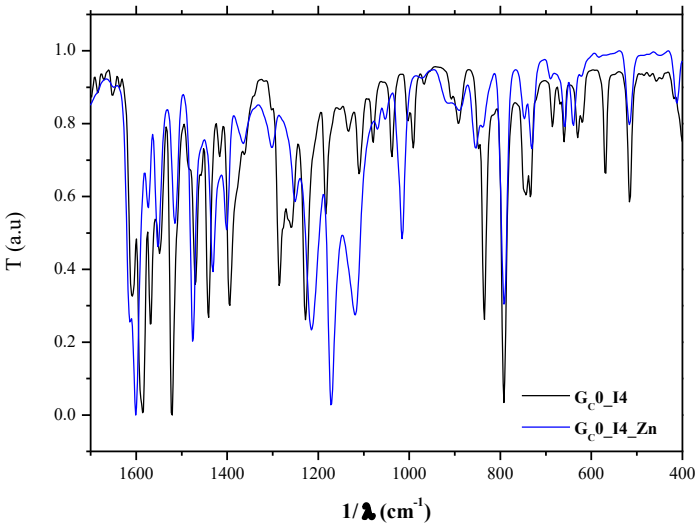

Figure 4-12. FT-IR spectra of **G_C0_I4_Zn** plotted against its **G_C0_I4** precursor.

4.5 Ligand exchange between Au NPs and metallodendritic branches

The ligand exchange was carried out according to a literature procedure.[384] Briefly, a solution of oleylamine-capped Au@OA in chloroform was added dropwise to a solution of **G_C0_I4_Zn** in DMF. A brown precipitate was formed in time which was isolated by filtration. The resulting compound **Au@G_C0_I4_Zn**. The compound was characterized by FT-IR and UV-Vis spectroscopies. Due to their low dispersity in any solvents, no NMR spectrum could be recorded. The presence of the *tpy* complex **G_C0_I4_Zn** was confirmed by EDX analysis.

FT-IR spectroscopy

Figure 4-13 presents the FT-IR spectra of **Au@OA**, **G_C0_I4_Zn** and **Au@G_C0_I4_Zn**. By comparing the spectra of the oleylamine capped **Au@OA** with that of **Au@G_C0_I4_Zn**, the successful ligand exchange could be confirmed by the disappearance of the characteristic absorption bands $\nu_{as(N-H)}$ corresponding to oleylamine. Moreover, another sign of the formation of the targeted compound was given by the shifts of the $\upsilon_{C=C}$ and $\upsilon_{C=N}$ characteristic bands to higher frequencies compared to **G_C0_L14_Zn**.[355]

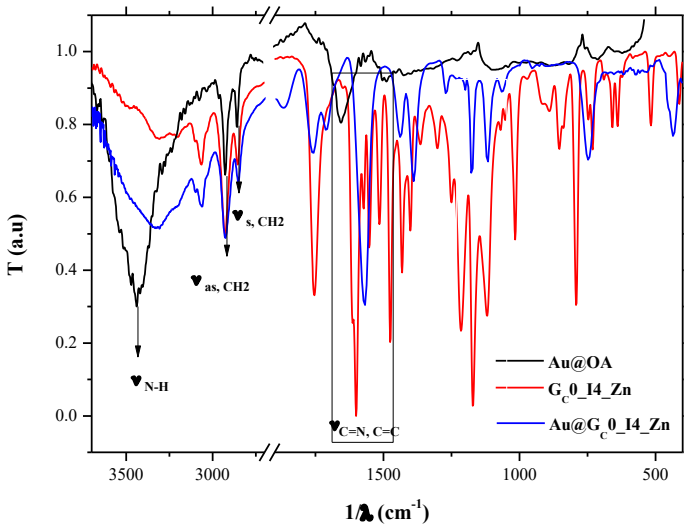

Figure 4-13. FT-IR spectra of **Au@OA**, **G$_C$0_I4_Zn** and **Au@G$_C$0_I4_Zn**.

Table 4-9. Assignment of the characteristic absorption bands of **Au@OA**, **G$_C$0_I4**_Zn, and **Au@G$_C$0_I4_Zn**.

Compound	**Assignment of the characteristic absorption bands (wavenumber values in cm^{-1})**			
	$\nu_{as(N-H)}$	$\nu_{as(CH2)}$	$\nu_{s(CH2)}$	$\nu_{(C=N,\ C=C)}$
Au@OA	3435	2925	2834	1627
G$_C$0_I4_Zn		2933	2866	1607 - 1426
Au@G$_C$0_I4_Zn		2933	2866	1590 - 1436

Absorption spectroscopy

Figure 4-14 shows the absorption spectra of **G$_C$0_I4_Zn** and **Au@G$_C$0_I4_Zn** recorded in AcN solutions. The absorption spectra of **G$_C$0_I4_Zn** shows a series of bands in the UV portion of the electromagnetic spectrum at 251, 284, 324 and 338 nm, all originating from *tpy* LC transitions.[358,359] After the ligand exchange, the absorption bands presented a red shift of the absorption bands with respect to **G$_C$0_I4_Zn** complex. The **Au@G$_C$0_I4_Zn** compound was found to be scarcely soluble, therefore, the ε-values could not be evaluated.

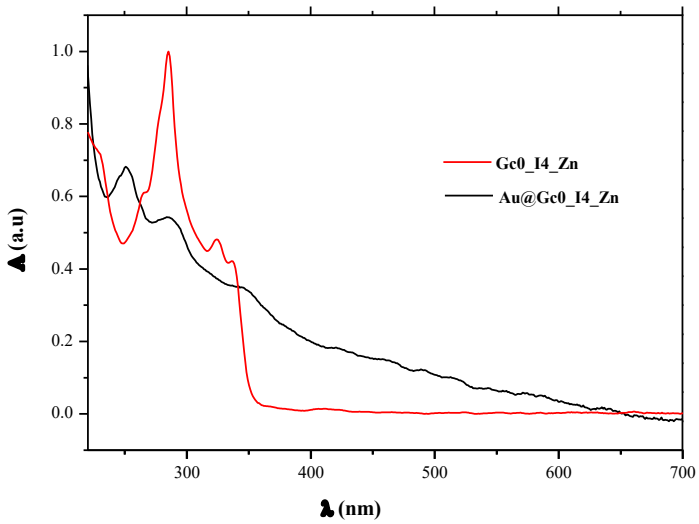

Figure 4-14. UV-Vis spectra of **G$_C$0_I4_Zn** and **Au@G$_C$0_I4_Zn**.

4.6 Conclusions

The goal of this project was to obtain Au NPs functionalized with dendritic shells that contain *bpy* or *tpy* derivatives, which will be coordinated to various metal centres.

After several trials, by altering the nature of the chelating unit and/or of the dendritic branches, promising results were obtained for the dendrons functionalized with *tpy* derivative **I4**. Therefore, **Au@G$_C$0_I4_Zn** was obtained by the ligand exchange reaction between **G$_C$0_I4_Zn** and **Au@OA.**

Chapter 5. Experimental procedures

5.1 Materials and methods

All commercially available starting materials and the solvents used in this thesis were of analytical reagent grade and were used as received without further purification. Spectrofluorimetric grade solvents were used for the photophysical investigations in solution, at room temperature.

1. Fourier-transform infrared spectroscopy (FT-IR)

The FT-IR spectra were recorded on a Cary 630 FT-IR spectrophotometer, as KBr pellet, in the 400– 4000 cm^{-1} range.

2. Nuclear magnetic resonance spectroscopy (NMR)

The ^{1}H-NMR spectra were recorded either on a Bruker Fourier 300 MHz spectrometer or Bruker Avance 300 (300 MHz). 1D and 2D NMR experiments were recorded on Bruker Avance III HD – 500 MHz spectrometer in $CDCl_3$ or DMSO-d_6, using tetramethylsilane (TMS) as internal standard.

3. Elemental analysis (EA)

The elemental analysis C, H and N was performed on a Flash 2000 analyzer, by ThermoFisher Scientific, using 1 mg of sample. Two determinations were performed and the average value was used.

The metal content was determined using a SensAA flame atomic absorption spectrometer (GBC Scientific Equipment, Australia). The flame used was an air-acetylene mixture. For each complex, two determinations were made and the average absorbance value was further used.

To study the elemental composition of Au NPs assemblies, scanning electron microscopy (SEM: Quanta FEG 250, FEI, The Netherlands) using back scattered electron detector (BSD) and by energy dispersive X-ray spectroscopy (EDX using an Apolo SSD detector, EDAX Inc. US), were used. The microstructure and EDX analysis were performed at about 10 mm working distance (WD) in high vacuum mode using BSD (back scattered detector).

4. Thermogravimetric analysis (TGA)

The thermogravimetric analysis of complexes synthesized in Chapter 2, was carried out using a TGA/SDTA 851-LF 1100 Mettler Toledo thermo-gravimetric analyzer. The samples with mass of about 10-20 mg were placed in alumina crucible of 150 µL. The experiments were

conducted in air or nitrogen flow of 50 mL min^{-1}, in the temperature range of 25–800°C with a heating rate of 10°C min^{-1} and a final isothermal heating at 800°C for 30 min.

In case of complexes synthesized in Chapter 3 TGA was carried out with a Q50 apparatus of TA Instruments, at a scanning rate of 5°C min^{-1} and with air as purge gas.

5. Polarized optical microscopy (POM)

The optical textures of mesophases were carried out using an Olympus BX53M polarizing microscope (POM) equipped with Linkam hot-stage. Images of the various phases were recorded using an Olympus UC90 camera.

6. Differential scanning calorimetry (DSC)

The transition temperatures and enthalpies of complexes synthesized in subchapter 2.1 were measured on a Discovery DSC 25 differential Scanning Calorimeter, whereas for those synthesized in subchapter 2.2 on a Q1000 from TA Instruments. In both cases, the heating and cooling rates were of 10°C/min. The apparatus was calibrated with indium. Three heating/cooling cycles were performed on each sample.

7. Powder X-ray diffraction (P- XRD)

The powder X-ray diffraction patterns of complexes Cu_5 – Cu_8 at variable temperature were obtained using a Bruker AXS General Area Detector Diffraction System (D8 Discover with GADDS) with Cu-Ka radiation (λ = 1.54056 Å). Measurements were performed by placing samples in Lindemann capillary tubes with an inner diameter of 0.05 mm. The highly sensitive area detector was placed at a distance of 20 cm from the sample (2θ detector placed at 14°) and equipped with a CalCTec (Italy) heating stage. The samples were heated at a rate of 5.0°C min^{-1} to the appropriate temperature.

The SWAXS patterns of Pt(II) and Zn(II) complexes were obtained with a transmission Guinier-like geometry. A linear focalized monochromatic Cu Kα1 beam (λ = 1.5405 Å) was obtained using a sealed-tube generator (600 W) equipped with a bent quartz monochromator. In all cases, the crude powder was filled in Lindemann capillaries of 1 mm diameter and 10 μm wall-thickness. The diffraction patterns were recorded with a curved Inel CPS120 counter gas-filled detector linked to a data acquisition computer (periodicities up to 90 Å) and on image plates scanned by Amersham Typhoon IP with 25 μm resolution (periodicities up to 120 Å).

8. Ultraviolet visible spectroscopy (UV-VIS)

For complexes **C1** – **C5** the absorption spectra were recorded using an Agilent Cary 60 spectrophotometer equipped with a Cell Holder Single Peltier Thermostatted - Carry G6870A.

For complexes **C6** – **C9** and all of the complexes with *tpy* derivatives a PerkinElmer Lambda 900 spectrophotometer was used to obtain the UV/vis absorption spectra.

9. Emission spectroscopy

For complexes **C1** – **C5** the emission spectra were recorded on a Perkin Elmer LS 55 spectrometer, whereas for the other complexes presented in this work a Perkin-Elmer LS 50B spectrofluorimeter was used to obtain the emission spectra in solution, in both cases quartz cuvettes of a 1 cm path length were used.

Steady-state emission spectra were recorded on a HORIBA Jobin-Yvon Fluorolog-3 FL3-211 spectrometer equipped with a 450 W xenon arc lamp, double-grating excitation and single-grating emission monochromators (2.1 nm/mm dispersion; 1200 grooves/mm), and a Hamamatsu R928 photomultiplier tube. Emission and excitation spectra were corrected for source intensity (lamp and grating) and emission spectral response (detector and grating) by standard correction curves. Luminescence from solid samples and mesophases were obtained by placing microcrystalline powder between two quartz windows positioned on a customized temperature-controlled hot stage realized in Teflon by CaLCTec s.r.l. (Rende, Italy), within the sample holder of the spectrofluorimeter in a front-face geometry.

10. DPPH radical-scavenging activity:

The antioxidant activities were determined using DPPH as a free radical as follows: 0.2 mL solution of complexes in degassed DMSO of different concentrations was added to 3.8 mL of freshly prepared solution of DPPH in methanol. The final concentrations were: 59.1 μM DPPH and 10 μM, 8 μM, 6 μM, 4 μM and 2 μM of L3, L4, C3, C4 and C5. The reduction of the radical was followed by monitoring the decrease in absorbance at 517 nm at 30ºC, until the reaction reached a plateau. A blank solution of DPPH was screened to estimate the decomposition of DPPH radical during the measurements. The initial DPPH concentration $(C_{DPPH})_0$ was calculated from a calibration curve with the equation:

$$Abs_{517nm} = 0.01134 \cdot 10^{-6} \cdot (C_{DPPH})_0 - 0.00406 \qquad (1)$$

as determined by linear regression, $r^2 = 0.99994$.

5.2 Experimental procedures

Synthesis of L4

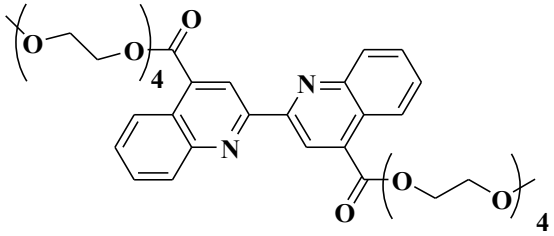

A mixture of 2,2′-biquinoline-4,4′-dicarboxylic acid (0.50 g, 1.452 mmol) and thionyl chloride (50 mL) were refluxed under nitrogen until a clear yellow solution was obtained. Excess thionyl chloride was removed and the residue was dried under vacuum for 2 h. The acid chloride was suspended in toluene (30 mL) and treated with an excess of tetraethyleneglycol monomethylether (0.70 mL, 3.49 mmol). The mixture was heated under reflux for 24 h. The solvent was evaporated before the addition of chloroform (40 mL) and the mixture was washed with a solution of saturated $NaHCO_3$ (40 mL), H_2O(100 mL), dried over anhydrous Na_2SO_4, filtered, and evaporated to dryness. The pure product was obtained by column chromatography (SiO_2: EtOAc/MeOH = 9:1), obtaining a waxy white solid (0.93 mmol, 680 mg, 63%). m.p. 76-78°C.

Anal. calcd. for $C_{38}H_{48}N_2O_{12}$ (724.79 g·mol^{-1}): C, 62.97; H, 6.68; N, 3.87; found: C, 63.14; H, 6.60; N, 3.99.

FT-IR (KBr): 2922 (ν_{as} (CH_2)), 2876 (ν_s (CH_2)), 1719 (ν (C=O)), 1587 (ν (C=N)), 1547, 1501, 1453 (ν (C=C)), 1270, 1233, 1189 (ν (C=O)-O), 1152, 1116, 1095 (ν_{as} (C-O-C)), 1040 (ν_s (C-O-C)).

^{1}H NMR (300 MHz, $CDCl_3$, δ–ppm): = 9.33 (s, 2H), 8.79 (d, ^{3}J = 8.5 Hz, 2H), 8.32 (d, ^{3}J = 8.4 Hz, 2H), 7.83 (t, ^{3}J = 8.3 Hz), 7.70 (t, ^{3}J = 8.4 Hz, 2H), 4.69 (m, 4H), 3.98 (m, 4H), 3.85 – 3.45 (overlapped peaks, 24H), 3.34 (s, 6H).

Synthesis of L5

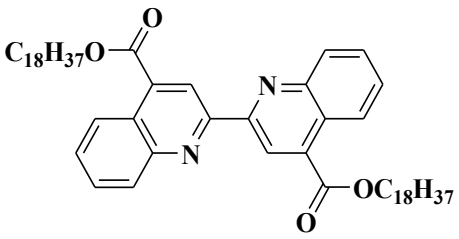

A mixture of 2,2′-biquinoline-4,4′-dicarboxylic acid (0.50 g, 1.452 mmol) and thionyl chloride (50 mL) were refluxed under inert atmosphere until a clear yellow solution was obtained. Excess thionyl chloride was removed and the residue was dried under vacuum for 2 h. The acid chloride was suspended in toluene (30 mL) and treated with an excess of n-octadecanol (0.942 g, 3.485 mmol). The mixture was stirred under reflux for 24 h. The solvent was evaporated before the addition of chloroform (40 mL) and the mixture was washed with a solution of saturated $NaHCO_3$ (40 mL), H_2O (100 mL), dried over anhydrous Na_2SO_4, filtered, and evaporated to dryness. The pure product was obtained after recrystallisation from $CHCl_3$/MeOH, resulting in a waxy white solid (1.16 mmol, 986 mg, 80 %).

FT-IR (KBr): 2921 (ν (CH_3)), 2849 (ν (CH_2)), 1719 (ν (C=O)), 1586 - 1472 (ν (C=N) and ν (C=C)), 1151 (ν_{as} (C-O-C)), 1040 (ν_s (C-O-C)).

^{1}H NMR (300 MHz, $CDCl_3$, δ–ppm): 9.31 (s, 2H), 8.79 (dd, J = 8.5, 0.8 Hz, 2H), 8.38 – 8.25 (m, 2H), 7.82 (ddd, J = 8.3, 6.9, 1.4 Hz, 2H), 7.70 (ddd, J = 8.4, 6.8, 1.3 Hz, 2H), 4.53 (t, J = 6.8 Hz, 6H), 2.02 – 1.72 (m, 6H), 1.72 – 1.13 (overlapped peaks, 54H), 0.87 (m, 9H).

Synthesis of L6

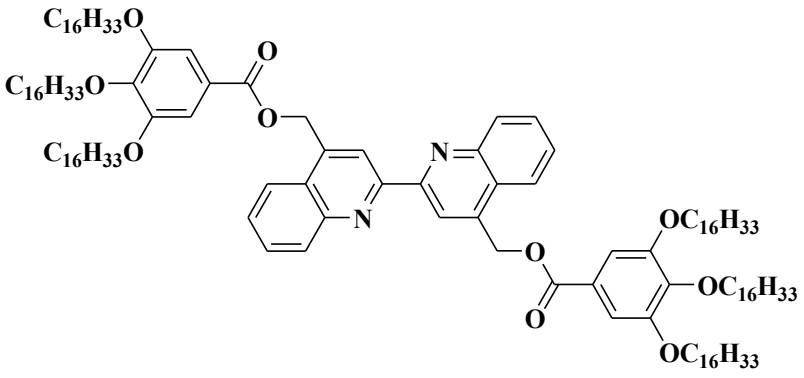

I2 (0.8 g, 1.452 mmol), and 4,4'- bis(hydroxymethyl)-2,2'-*bq* (0.209 g, 0.66 mmol) and a catalytic amount of 4-DMAP (0.033 g, 0.66 mmol) were dissolved in the minimum volume of dry THF under inert media. The reaction mixture was cooled down to 0ºC and stirred for 30 min. Then, DCC (0.300 g, 1.452 mmol) dissolved in the minimum amount of dry THF was added dropwise. The reaction mixture was stirred at room temperature under inert atmosphere for four days. The DCU formed was filtered off and the pure product was isolated by recrystallisation from $CHCl_3$/MeOH (0.231 mmol, 0.447 g, yield 35 %).

FT-IR (KBr): 2921 (ν (CH_3)), 2849 (ν (CH_2)), 1719 (ν (C=O)), 1586 - 1472 (ν (C=N) and ν (C=C)), 1150 (ν_{as} (C-O-C)), 1043 (ν_s (C-O-C)).

^{1}H NMR (500 MHz, $CDCl_3$, δ–ppm): 9.24 (s, 2H), 8.60 (s, 2H), 8.19 (d, *J* = 8.5 Hz, 2H), 7.89 (t, *J* = 7.5 Hz, 2H), 7.75 (t, *J* = 7.4 Hz, 2H), 7.40 (s, 4H), 6.02 (d, *J* = 10.3 Hz, 4H), 4.21 – 3.76 (m, 12H), 1.97 – 1.69 (m, 12H), 1.65 – 1.16 (m, 156H), 0.90 (t, *J* = 6.9 Hz, 18H).

Synthesis of C1 and C2

General method: To a solution of *N^N* ligand (0.591 mmol) in 10 mL EtOH was added 20 mL H_2O solution containing $ZnCl_2$ (0.200 g, 0.591 mmol). The product formed instantly as white solid and was stirred for 4 hours at r.t. Then it was filtrated out, washed repeatedly with ethanol and dried under vacuum.

Synthesis of C1

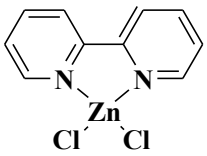

C1: [*bpy*$ZnCl_2$]: 0.415 g (94%).

FT-IR (KBr, cm^{-1}): 3433, 3076 ($\nu_{O-H)}$, 1600 (ν_{CC} + ν_{NC}), 1566 (ν_{CC}+ ν_{NC} +δ_{CCH}), 1443 (ν_{CC}+ ν_{NC} +δ_{NCH}), 1169 (ν_{CC}+δ_{CCH}), 764, 735 (Γ_{NCCH}+ Γ_{CCCH}).

Synthesis of C2

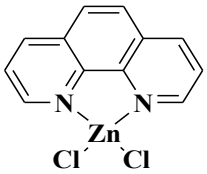

C2: [*phen*ZnCl$_2$]: 0.501 g (95%).

FT-IR (KBr, cm^{-1}): 3415, 3063 (ν_{O-H}), 1594 (ν_{CC} + ν_{NC}), 1518 (ν_{CC}+ ν_{NC} +δ_{CCH}), 1427 (ν_{CC}+ ν_{NC} +δNCH), 1167 (ν_{CC}+δ_{CCH}), 845, 726 (Γ_{NCCH}+ Γ_{CCCH}).

Synthesis of C3 and C4

General method: To a solution of (*N*^*N*)MCl$_2$ (0.591 mmol) in 10 mL degassed H$_2$O was added 20 mL degassed ethanol solution containing quercetin (0.200 g, 0.591 mmol) and NEt$_3$ (0.16 mL, 1.182 mmol). The product formed instantly as orange solid and was filtrated out, washed repeatedly with water and ethanol and dried under vacuum.

Synthesis of C3

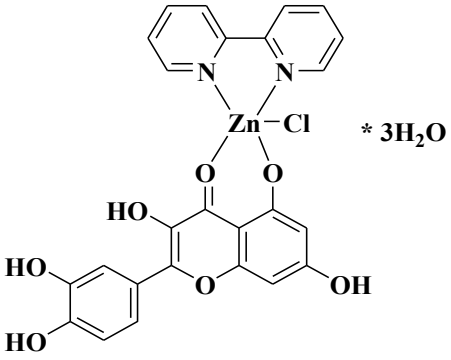

C3: [*bpy*ZnQCl]·3H$_2$O: 0.315 g (92%).

Anal. calcd. for $C_{25}H_{23}ClN_2O_{10}Zn$ (612.30 g·mol^{-1}): C, 49.04; H, 3.79; N, 4.58; found: C, 49.25; H, 3.70; N, 4.86. AAS: Zn % calcd.: 10.41, found: 10.19.

FT-IR (KBr, cm^{-1}): 3433, 3076 (ν_{O-H}), 1643 ($\nu_{C=O}$), 1600 (ν_{CC} + ν_{NC}), 1566 (ν_{CC}+ ν_{NC} +δ_{CCH}), 1476 (ν_{COH}), 1443 (ν_{CC}+ ν_{NC} +δ_{NCH}), 1269 (ν_{COC}), 1169 (ν_{CC}+δ_{CCH}), 764, 735 (Γ_{NCCH}+ Γ_{CCCH}).

TGA: (70.3ºC – onset peak) experimental mass loss 8.37% corresponds to 3 H$_2$O molecules (calcd. 8.82%); residue ZnO: experimental 13.65% (calcd. 13.29%).

Synthesis of C4

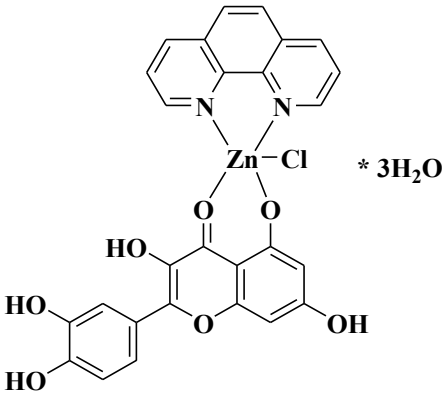

C4: [*phen*ZnQCl]·3H$_2$O: 0.334 g (94%).

Anal. calcd. for $C_{27}H_{23}ClN_2O_{10}Zn$ (636.32 g·mol^{-1}): C, 50.36; H, 3.64; N, 4.40; found: C, 50.01; H, 3.53; N, 4.72. AAS: Zn % calcd.: 10.28, found: 10.59.

FT-IR (KBr, cm^{-1}): 3415, 3063 (ν_{O-H}), 1645 ($\nu_{C=O}$), 1594 (ν_{CC} + ν_{NC}), 1518 (ν_{CC}+ ν_{NC} +δ_{CCH}), 1489 (ν_{COH}), 1427 (ν_{CC}+ ν_{NC} +δ_{NCH}), 1269 (ν_{COC}), 1167 (ν_{CC}+δ_{CCH}), 845, 726 (Γ_{NCCH}+ Γ_{CCCH}).

TGA: (63.9ºC – onset peak) experimental mass loss 8.90% corresponds to 3 H_2O molecules (calcd. 8.49%); residue ZnO: experimental 12.35% (calcd. 12.79%).

Synthesis of C5

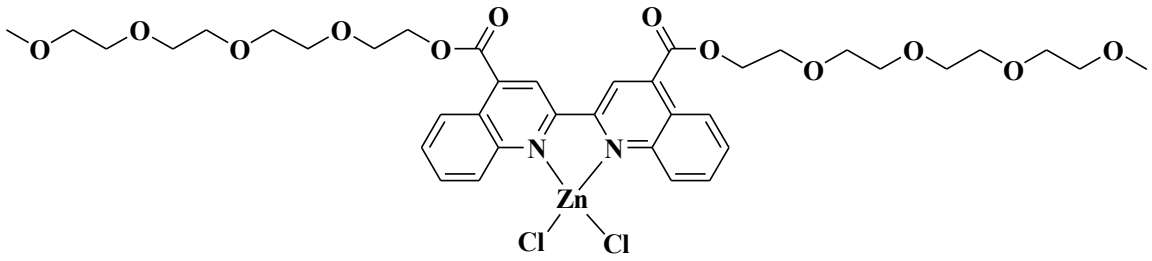

A solution of **L4** (0.200 g, 0.276 mmol) in ethanol (20 mL) was added to a solution of $ZnCl_2$ (0.564 mg, 0.414 mmol) in EtOH (10 mL) and the reaction mixture was stirred for 4 hours at r.t. Then the solvent was evaporated, the residue was dissolved in chloroform, filtrated and recrystallized with hexane.

C5: yellowish waxy solid (95% yield), m. p. 107-109ºC.

Anal. calcd. for $C_{38}H_{48}Cl_2N_2O_{12}Zn$ (861.09 g·mol^{-1}): C, 53.00; H, 5.62; N, 3.25; found: C, 52.81; H, 5.83; N, 3.01. AAS: Zn % calcd.: 7.59, found: 7.68.

FT-IR (cm^{-1}, KBr): 3083 (ν (CH_3)), 2894 (ν (CH_2)), 1733 (ν (C=O)), 1594, 1545, 1513, 1459 (ν (C=N)) and ν (C=C)), 1270, 1243, 1209 (ν (C=O)-O), 1152, 1104, 1095 (ν_{as} (C-O-C)), 1025 (ν_s (C-O-C)).

^{1}H-NMR (300 MHz, $CDCl_3$, δ–ppm): 9.11 (s, 2H, $H^{3,3'}$), 8.83 (overlapped peaks, 4H, $H^{5,5'}$, $H^{8,8'}$), 7.09 (t, ^{3}J = 8.3 Hz, 2H $H^{7,7'}$), 7.91 (t, ^{3}J = 8.4 Hz, 2H, $H^{6,6'}$), 4.78 (m, 4H, $H^{a,a'}$), 4.02 (m, 4H, $H^{b,b'}$), 3.85 – 3.45 (overlapped peaks, 24H, $H^{c\text{-}h,\ c'\text{-}h'}$), 3.31 (s, 6H, $H^{i,i'}$).

Synthesis of C6

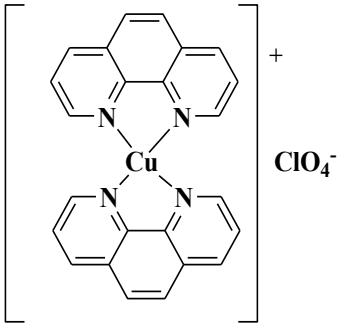

C6: 0.20 g (2.9 mmol) $NH_2OH{\cdot}HCl$ and 1 mL aqueous ammonia 25% (dropwise) were added to a hot solution of 0.25 g (1 mmol) $CuSO_4{\cdot}5H_2O$ in 100 mL water. After the mixture has reached the boiling point, 0.40 g (2 mmol) *phen* in 25 mL ethanol was added dropwise, resulting a dark red solution. The mixture was treated with a slight excess of $NaClO_4$ (0.14 g, 1.1 mmol) and boiled for 1h. The compound was obtained as dark purple precipitate was washed with water and dried at r.t.. Yield: 84 %.

Anal. Calcd. $C_{24}H_{16}ClCuN_4O_4$ (523.41 g/mol): C, 55.07; H, 3.08; N, 10.70; found: C, 54.89; H, 3.14; N, 10.83. AAS: Cu % calcd.: 12.14, found: 12.46.

FT-IR [KBr, cm^{-1}]: 1622 ($\nu_{C=N}$), 1588, 1508, 1424 ($\nu_{C=C}$), 1098, 623 (ν_{ClO4}), 841, 724 ($\nu_{C\text{-}H}$).

^{1}H-NMR (300 MHz, DMSO-d6, δ-ppm): 9.06 - 8.92 (overlapped peaks, 4H, H_2, H_5); 8.36 (2H, H_4); 8.07 (2H, H_3).

Λ_M (c =10^{-3} M, DMSO) = 34.9 Ω^{-1}mol^{-1}cm^2.

Synthesis of C7

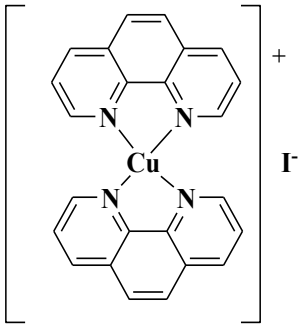

C7: was obtained using the same synthesis as for complexes **C6,** but a slight excess of KI (0.18 g, 1.1 mmol) was added instead of $NaClO_4$. Yield: 85.3 %.

FT-IR [KBr, cm^{-1}]: 1619 ($\nu_{C=N}$), 1576, 1504, 1420 ($\nu_{C=C}$), 839, 722 (ν_{C-H}).

^{1}H-NMR (300 MHz, DMSO-d^6, δ-ppm): 8.96 (overlapped peaks, 4H, H_2, H_5); 8.47 (4H, H_3, H_4).

Λ_M ($c = 10^{-3}$ M, DMSO) = 32.5 $\Omega^{-1}mol^{-1}cm^2$.

Anal. Calcd. $C_{24}H_{16}CuIN_4$ (550.87 g/mol): C, 52.33; H, 2.93; N, 10.17; found: C, 52.41; H, 2.80; N, 10.34. AAS: Cu % calcd.: 11.54, found: 11.89.

TGA (CuO residuum %) calcd.: 14.44; found: 14.49.

Synthesis of C8

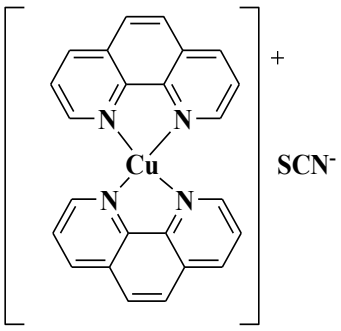

C8: was obtained using the same synthesis as for complexes **C6,** but using a slight excess of KSCN (0.11 g, 1.1 mmol) instead of $NaClO_4$. Yield: 74.5 %.

Anal. Calcd. $C_{25}H_{16}CuN_5S \cdot 1/2H_2O$ (491.05 g/mol): C, 61.15; H, 3.49; N, 14.26; found: C, 61.58; H, 3.28; N, 13.99. AAS: Cu % calcd.: 12.94, found: 13.21.

FT-IR [KBr, cm^{-1}]: 3309 (ν_{H2O}), 2051 (ν_{SCN}), 1623 ($\nu_{C=N}$), 1575, 1507, 1423 ($\nu_{C=C}$), 839, 723 (ν_{C-H}).

^{1}H-NMR (300 MHz, DMSO-d^6, δ-ppm): 8.90 (overlapped peaks, 4H, H_2, H_5); 8.36 (2H, H_4); 8.16 (2H, H_3).

Λ_M ($c = 10^{-3}$ M, DMSO, δ-ppm) = 33.3 $\Omega^{-1}mol^{-1}cm^2$.

TGA (CuO residuum %) calcd.: 16.20; found: 16.60; desolvation process of 1/2 water molecule: calcd.: 1.83%; found: 1.94%.

Synthesis of C9

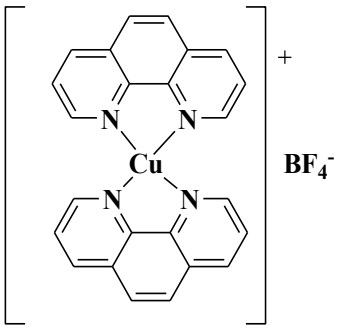

C9: was obtained using the same synthesis as for complexes **C6,** but using a slight excess of KBF_4 (0.14 g, 1.1 mmol) instead of $NaClO_4$. Yield: 75 %.

Anal. Calcd. $C_{24}H_{16}BCuF_4N_4$ (510.76 g/mol): C, 56.44; H, 3.16; N, 10.97; found: C, 56.18; H, 3.21; N, 11.23. AAS: Cu % calcd.: 12.44, found: 12.43.

FT-IR [KBr, cm^{-1}]: 1622 ($\nu_{C=N}$), 1588, 1508, 1424 ($\nu_{C=C}$), 1060 (ν_{BF4}), 842, 724 (ν_{C-H}).

^{1}H-NMR (300 MHz, DMSO-d^6, δ-ppm): 9.03 (2H, H_2); 8.92 (2H, H_5); 8.36 (2H, H_4); 8.08 (2H, H_3).

Λ_M ($c = 10^{-3}$ M, DMSO) = 37.8 $\Omega^{-1}mol^{-1}cm^2$.

TGA (CuO residuum %) calcd.: 15.57; found: 15.87.

Synthesis of C10 – C13.

C10 – **C13** were obtained through reaction between 2 equivalents of the corresponding *bq* ligands dissolved in $CHCl_3$ with 1 equivalent of $[Cu(CH_3CN)_4]X$, where X = ClO_4 and BF_4, dissolved in CH_3CN solution for 15 min., at r.t. and inert conditions. The purple solution was evaporated to dryness under vacuum and the obtained solid was recrystallized with chloroform and diethyl ether.

Synthesis of C10

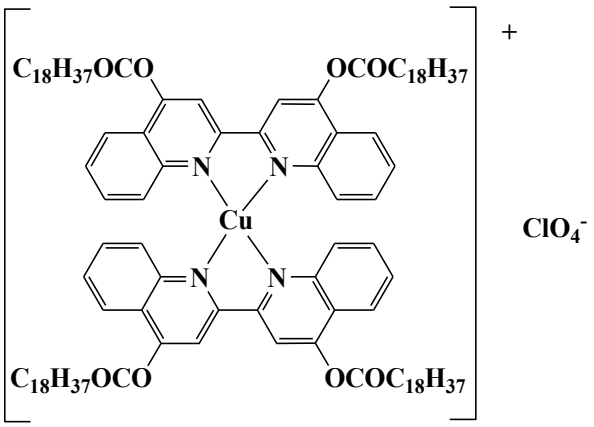

C10: 93.4 % yield;

Anal. calcd. for $C_{112}H_{168}ClCuN_4O_{12}$ (1861.55 g·mol^{-1}): C, 72.26; H, 6.10; N, 3.01. Found: C, 72.49; H, 5.97; N, 3.34%;

FT-IR (KBr, cm^{-1}): $\nu_{(C=O)}$ 1725, $\nu_{(ClO4)}$ 1107, 623;

^{1}H-NMR (500 MHz, $CDCl_3$, δ-ppm): 9.31 (s, 1H, *H3*), 8.79 (d, *J* = 8.5 Hz, 1H, *H7*), 8.32 (d, *J* = 7.8 Hz, 1H, *H4*), 7.82 (t, *J* = 7.0 Hz, 1H, *H5*), 7.72 – 7.67 (m, 1H, *H6*), 4.53 (t, *J* = 6.8 Hz, 2H, *Ha*), 1.96 – 1.87 (m, 2H, *Hb*), 1.47 – 1.19 (m, 30H,*Hc*), 0.87 (t, *J* = 7.0 Hz, 3H,*Hd*).

Λ_M ($CHCl_3$, 10^{-4}M): 34 Ω^{-1}mol^{-1}cm^2.

Synthesis of C11

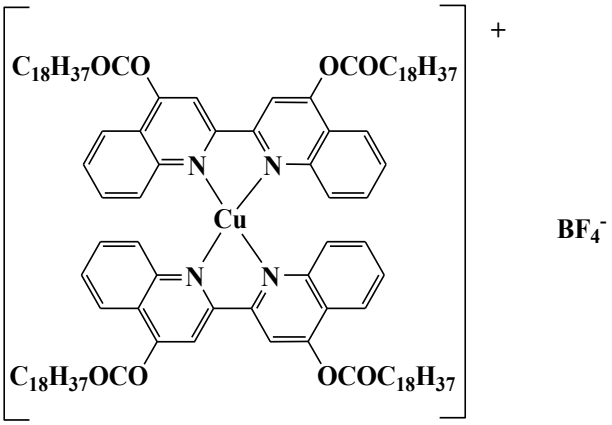

C11: 93.4 % yield;

Anal. calcd. for $C_{112}H_{168}BCuF_4N_4O_8$ (1848.90 g·mol^{-1}): C, 72.76; H, 9.16; N, 3.03. Found: C, 72.58; H, 9.51; N, 3.44%;

FT-IR (KBr, cm^{-1}):$\nu_{(C=O)}$ 1728, $\nu_{(BF4)}$ 1061;

^{1}H-NMR (500 MHz, $CDCl_3$, δ-ppm): 9.30 (s, 2H, *H3*), 8.83 (d, *J* = 8.5 Hz, 2H, *H7*), 7.73 (d, *J* = 8.5 Hz, 2H, *H4*), 7.70 – 7.63 (m, 2H, *H5*), 7.46 (t, *J* = 7.1 Hz, 2H, *H6*), 4.65 (t, *J* = 7.0 Hz, 4H, *Ha*), 2.03 – 1.94 (m, 4H, *Hb*), 1.59 – 1.52 (m, 4H,*Hc*), 1.48 – 1.20 (m, 56H,*Hc*), 0.87 (t, *J* = 7.0 Hz, 6H,*Hd*).

Λ_M ($CHCl_3$, 10^{-4}M): 37 Ω^{-1}mol^{-1}cm^2.

Synthesis of C12

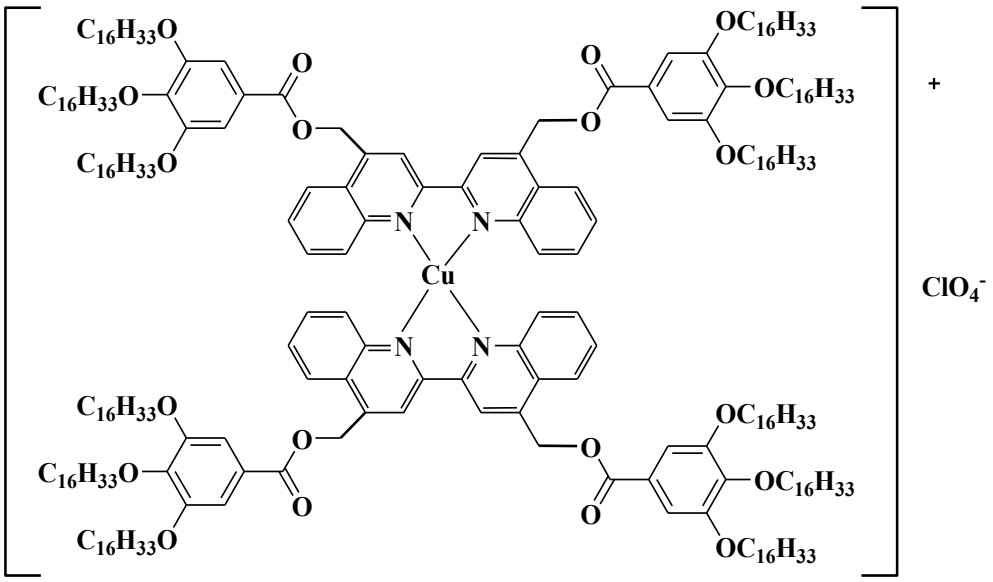

C12: 91.8% yield;

Anal. calcd. for $C_{260}H_{432}ClCuN_4O_{24}$ (4127.99 g·mol^{-1}): C, 76.22; H, 10.63; N, 1.37. Found: C, 76.43; H, 10.22; N, 1.81%;

FT-IR (KBr, cm^{-1}):$\nu_{(C=O)}$ 1717, $\nu_{(ClO4)}$ 1108, 622, 623;

^{1}H NMR (500 MHz, $CDCl_3$, δ-ppm): 9.00 (s, 1H, *H3*), 8.25 (d, *J* = 8.5 Hz, 1H, *H7*), 7.77 (d, *J* = 8.6 Hz, 1H, *H4*), 7.56 (t, *J* = 7.7 Hz, 1H, *H5*), 7.40 (t, *J* = 7.8 Hz, 1H, *H6*), 7.34 (d, *J* = 7.2 Hz, 2H, *H8,*8'), 6.04 (s, 2H, *Ha*), 4.01 (dd, *J* = 10.9, 6.3 Hz, 6H, *Hb*), 1.86 – 1.69 (m, 6H, *Hc*), 1.25 (d, *J* = 4.9 Hz, 78H, *Hd*), 0.87 (t, *J* = 6.9 Hz, 9H, *He*).

Λ_M ($CHCl_3$, 10^{-4}M): 17 Ω^{-1}mol^{-1}cm^2.

Synthesis of C13

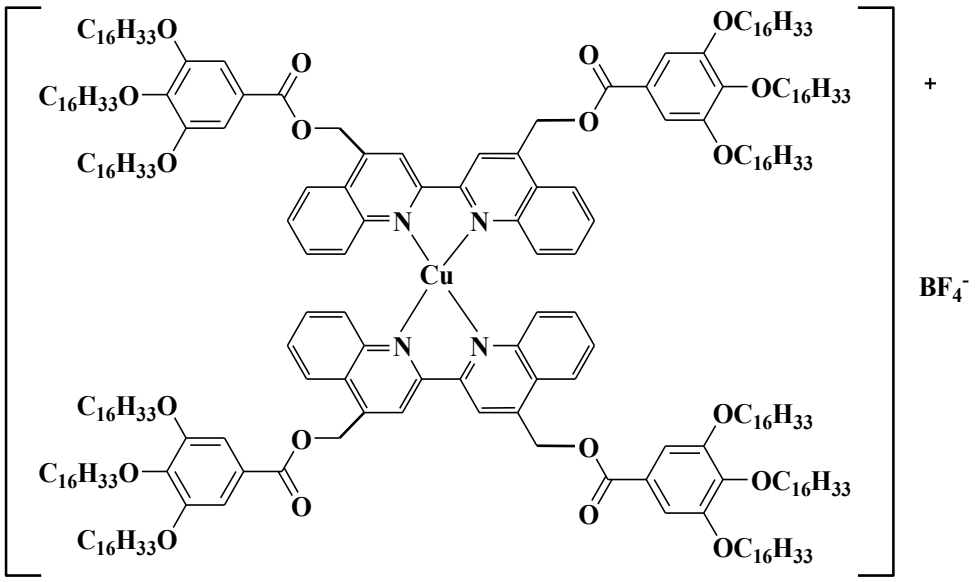

C13: 88.0% yield;

Anal. calcd. for $C_{260}H_{432}BCuF_4N_4O_{20}$ (4084.58 g·mol^{-1}): C, 76.45; H, 10.66; N, 1.37. Found: C, 76.58; H, 10.41; N, 1.58%;

FT-IR (KBr, cm^{-1}): $\nu_{(C=O)}$ 1717, $\nu_{(BF4)}$ 1063;

^{1}H NMR (500 MHz, $CDCl_3$, δ-ppm): 9.00 (s, 1H, *H3*), 8.25 (d, *J* = 8.4 Hz, 1H, *H7*), 7.77 (d, *J* = 8.4 Hz, 1H, *H4*), 7.56 (t, *J* = 7.4 Hz, 1H, *H5*), 7.42 – 7.31 (m, 3H, *H6,8,8'*), 6.04 (s, 2H, *Ha*), 4.01 (s, 6H, *Hb*), 1.76 (d, *J* = 29.8 Hz, 6H, *Hc*), 1.31 (t, *J* = 53.0 Hz, 78H, *Hd*), 0.87 (t, *J* = 5.6 Hz, 9H, *He*).

Λ_M ($CHCl_3$, 10^{-4}M): 18 Ω^{-1}mol^{-1}cm^2.

Synthesis of ligands L8 – L11

Synthesis of L8

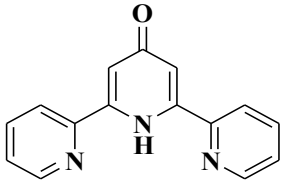

The ligand **L8** was synthesized in a two-step procedure, using acetone and ethyl picolinate as starting materials:

To a solution of 12 g of ethyl-picolinate (79.4 mmol) and 4.32 g of NaH (60%, 108 mmol) in 145 ml dry THF, 2.92 ml acetone 2 (39.7 mmol) in 40 ml dry THF were added slowly during 1.5 h under reflux. After stirring the reaction mixture under reflux for additional 6 h the solvent was evaporated under reduced pressure. The remaining orange paste was dissolved in 250 ml water and was filtered over celite. The product was precipitated upon neutralization with CH_3COOH 2M as a yellow solid. The crude product was filtered off and dissolved in chloroform. Upon standing, an aqueous phase separated. The organic phase was dried over Na_2SO_4 and the solvent was removed under vacuum, yielding 3.95 g of yellow powder (14.72 mmol, 37%), which was refluxed in 50 mL EtOH with an excess ammonium acetate for 24h. During this time, a dark brown solution formed, which was concentrated to half volume and kept at 4°C overnight. A pale grey precipitate was formed which was filtered and washed with cold EtOH. (2.06 g, 8.26 mmol, 56.1%)

^{1}H NMR (300 MHz, 300 MHz, $CDCl_3$, δ- ppm): 8.81 (dt, J = 4.9, 1.4 Hz, 2H), 7.93 (dddd, J = 15.3, 8.0, 6.9, 1.5 Hz, 4H), 7.45 (ddd, J = 7.4, 4.8, 1.4 Hz, 2H), 7.24 (s, 2H).

FT-IR (cm^{-1}, KBr): 1629 – 1450 (ν (C=N)) and (ν (C=C)).

Synthesis of L9

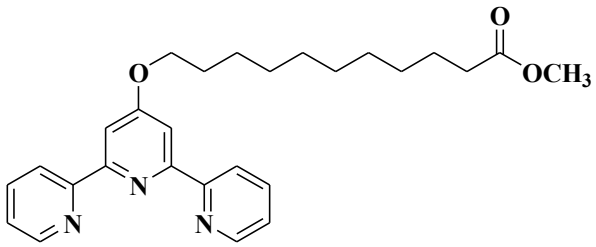

2.327 mmol of 2,6-bis-(2'-pyridyl)-4-pyridone (0.580 g) were added, under argon, to a suspension of powdered KOH in 20 mL dry DMF. The mixture was stirred for 30 min at 80°C, after which 2.792 mmol of methyl 11-bromoundecanoate (0.780 g) was added drop wise. The reaction mixture was stirred at this temperature for 6h. After cooling down to room temperature, the reaction was quenched by the addition of H_2O (200 mL). The water phase was extracted with EtOAc and the organic phase was dried over anhydrous Na_2SO_4. The pure product was precipitated from hexane, yielding 2.141 mmol of white precipitate (0.955 g, 92 %). M. p. = 91-93°C.

FT-IR (KBr, cm^{-1}): 2997, 2917, 2854 (C-H stretch); 1745 ($\nu_{(COO)}$).

^{1}H-NMR (300 MHz, $CDCl_3$, δ- ppm): 8.69 (d, ^3J = 5.5 Hz, 2H, H^1), 8.62 (d, ^3J = 8.0 Hz, 2H, H^4), 8.00 (s, 2H, H^5), 7.85 (td, ^3J = 7.8 Hz, ^4J = 1.8 Hz, 2H, H^3), 7.33 (m, 2H, H^2), 4.22 (t, ^3J = 6.4 Hz, 2H, H^a), 3.66 (s, 3H, H^e), 2.31 (t, ^3J = 7.5 Hz, 2H, H^d), 1.85 (m, 2H, H^b), 1.66-1.30 (overlapped peaks, 14H, H^c).

Synthesis of L10

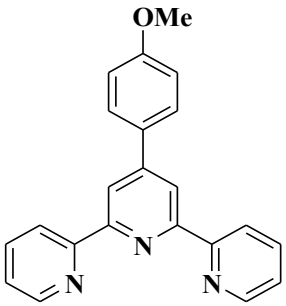

A solution of acetylpyridine (12.1 g, 99.08 mmol), KOH (8.5 g, 151.5 mmol) and 4-methoxybenzaldehyde (6.8 g, 49.94 mmol) in 150 mL EtOH were stirred at room temperature for 30 min, then 75 mL NH_4OH were added dropwise. The reaction mixture was stirred at 50 ^oC for 12 h, cooled to room temperature and stirred for an additional hour. The precipitate was filtered and washed with cold MeOH. The crude product was recrystallized from hot MeOH, yielding a white solid (11.1 g, 32.7 mmol, 66 %).

FT-IR (KBr, cm^{-1}): 2993 (C-H stretch); 1599 – 1432 (ν (C=N)) and (ν (C=C)).

^{1}H-NMR (300 MHz, $CDCl_3$, δ- ppm): 8.76 - 8.61 (m, 6H), 7.95-7.68 (m, 4H), 7.42-7.25 (m, 2H), 7.13-6.92 (m, 2H), 3.89 (s, 3H);

Synthesis of I4

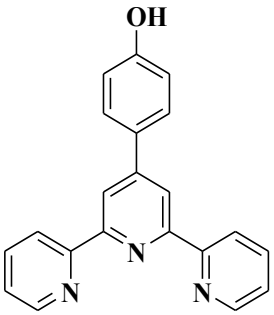

4'-(4-methoxyphenyl)-2,2':6',2''-terpyridine (10.9 g, 32.1 mmol) were refluxed in an excess of 48% HBr/ CH_3COOH for 24 h, then cooled to room temperature and neutralized with NaOH 20 %. The precipitate was filtered off and washed with water, resulting in a pale grey solid (10.21 g, 31.3 mmol, 95 %).

^{1}H-NMR (300 MHz, DMSO-d_6, δ- ppm): 8.78- 8.70 (d, 2H), 8.68-8.59(d, 4H), 8.07- 7.95 (td, 2H), 7.82 -7.61(m, 2H), 7.58- 7.43 (m, 2H), 7.00- 6.95(dd, 2H).

Synthesis of I5

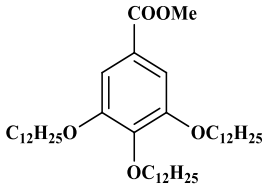

A mixture of methyl 3,4,5-trihydroxybenzoate (30 g, 54.30 mmol) and K_2CO_3 (75.0 g, 542.26 mmol) in 100 mL DMF was heated to 65ºC, then n-bromododecane (48.8 g, 195.8 mmol) in 50 mL DMF was quickly added to the mixture. The reaction mixture was stirred at 80ºC for 24 hours, cooled to room temperature and filtered over celite. The mixture was diluted with water (300 mL) and extracted with DCM (4 x 100 mL). The combined organic layers were washed with H_2O (5 x 100 mL), NH_4Cl (100 mL) saturated and NaCl saturated (100 mL). Recrystallization from acetone afforded the pure product as a white powder (28.81 g, 41.79 mmol, 87%).

^{1}H-NMR (300 MHz, $CDCl_3$, δ- ppm): 7.29 (s, 2H), 4.02 (td, J=6.5, 1.9 Hz, 6H), 3.90 (s, 3H), 1.76 (m, 6H), 1.48- 1.28 (m, 64H), 0.88 (m, 6H);

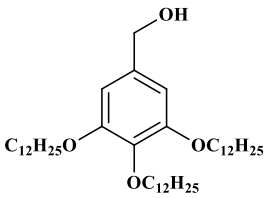

Methyl 3,4,5-tris(dodecyloxy)benzoate (11.72 g, 17.01 mmol) in THF was added dropwise to a cooled suspension of $LiAlH_4$ (1.29 g, 0.034 mmol) in dry THF. The reaction mixture was

allowed to reach room temperature and stirred overnight. Methanol was then added dropwise, filtered over celite and washed with DCM. The solvent was removed under vacuum, and crude product was purified by column chromatography (SiO_2: DCM), yielding the desired compound as a white solid (10.19 g, 16.50 mmol, 97%).

^{1}H-NMR (300 MHz, $CDCl_3$, δ- ppm): 6.56 (s, 2H), 4.59 (d, J=5.9 Hz, 2H), 3.95 (m, 6H), 1.76 (m, 6H), 1.64 - 1.15 (m, 64H), 0.89 (m, 6H);

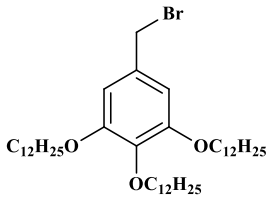

TMSBr (3.74 mL, 28.74 mmol) was added dropwise to a cooled solution of (3,4,5-tris(dodecyloxy)phenyl)methanol (10 g, 15.12 mmol) in dry DCM (150 mL). The reaction mixture stirred for 2 hours while gradually reaching room temperature. The volatiles were removed under vacuum, yielding the compound as a pale brown solid (10.85 g, 14.99 mmol, 99%). The product was used without further purification.

^{1}H-NMR (300 MHz, $CDCl_3$, δ- ppm): 6.56 (s, 2H), 4.45 (d, J=5.9 Hz, 2H), 3.95 (m, 6H), 1.76 (m, 6H), 1.64- 1.15 (m, 64H), 0.94- 0.75 (m, 6H);

Synthesis of L11

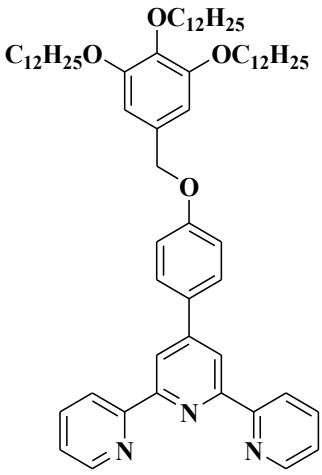

I5 (1.76 g, 2.43 mmol), **I4** (0.792 g, 2.43 mmol) and K_2CO_3 (2.02 g, 14.64 mmol) were ssuspended in 20 mL of DMF. The reaction mixture was stirred at 80°C, under argon, until the completion of the reaction (followed by TLC: Al_2O_3: hexane: EtOAC= 3: 2). The reaction mixture was then cooled to room temperature, 100 mL H_2O were added and the aqueous phase was extracted with DCM (3 x 100mL). The combined organic layers were washed with H_2O (2 x 100 mL), NaCl sat. (100 mL), NH_4Cl sat. (100 mL) dried over Na_2SO_4 anhydrous. The product was recrystallized from DCM/ MeOH, resulting in a pale grey precipitate (1.61 g, 1.66 mmol, 68,4%).

FT-IR (KBr, cm^{-1}): 2958, 2920, 2851 (C-H stretch); 1608 – 1438 (ν (C=N)) and (ν (C=C)).

^{1}H NMR (300 MHz, $CDCl_3$, δ- ppm): 8.77 – 8.63 (m, 6H), 7.93 – 7.78 (m, 4H), 7.34 (dd, *J* = 7.4, 4.9 Hz, 2H), 7.17 – 7.06 (m, 2H), 6.66 (s, 2H), 5.02 (s, 2H), 3.99 (q, *J* = 6.7 Hz, 6H), 1.92 – 1.69 (m, 6H), 1.57 – 1.17 (m, 56H), 0.89 (td, *J* = 6.7, 2.2 Hz, 9H).

^{13}C NMR (126 MHz, $CDCl_3$, δ- ppm): 156.73, 156.21, 153.72, 149.45, 137.18, 128.90, 124.11, 121.70, 118.62, 115.58, 106.52, 73.81, 70.88, 69.50, 32.33, 32.31, 30.75, 30.15, 30.13, 30.09, 30.04, 30.02, 29.82, 29.80, 29.75, 26.54, 26.50, 23.07, 14.50.

Synthesis of C14

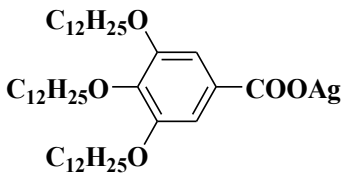

A solution of **I6** (1.43 g, 2.118 mmol) in EtOH and NaOH (0.085 g, 2.118 mmol) in H_2O was stirred at room temperature for 2 hours. Then a solution of AgNO3 (0.360 g, 2.118 mmol) in EtOH was added dropwise and the reaction mixture was stirred for another 2 hours. The white precipitate formed was washed with water and EtOH, to yield 1.70 g of **C14**.

^{1}H NMR (300 MHz, $CDCl_3$, δ- ppm): 7.22 (s, 2H), 3.90 (q, *J* = 6.7 Hz, 6H), 1.86 – 1.58 (m, 6H), 1.47 – 1.17 (m, 56H), 0.89 (td, *J* = 6.7, 2.2 Hz, 9H).

Synthesis of C15

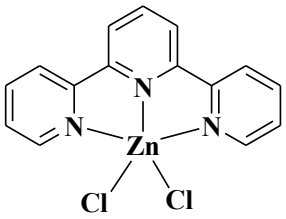

A solution of $ZnCl_2$ (0.292 g, 2.143 mmol) in 10 mL of MeOH was added dropwise to a solution of ligand **L7** (0.500 g, 2.143 mmol) in 20 mL MeOH. During the addition of the Zn(II) salt, a pale-yellow precipitate formed. The reaction mixture was stirred for 2 h at r. t. Then, the yellowish precipitate was filtered off washed with MeOH and dried under vacuum to yield 0.785 g (2.122 mmol, 99 %) of the desired compound.

FT-IR (KBr, cm^{-1}): 1594 - 1448 ($\upsilon_{C=C}$, $\upsilon_{C=N}$);

^{1}H-NMR (DMSO-d_6, δ/ppm): 8.84 (overlapped peaks, 4H), 8.60 (overlapped peaks, 3H), 8.34 (t, 2H), 7.86 (t, 2H).

Synthesis of C16

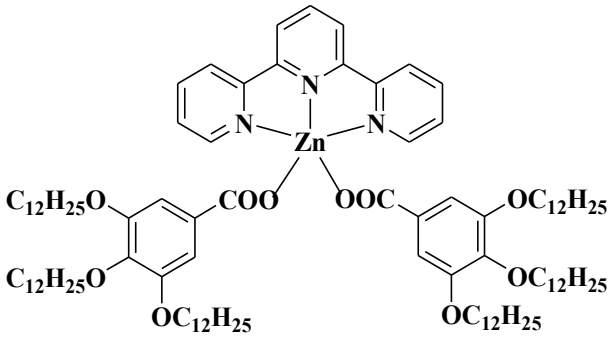

A solution of **C14** (0.698 g, 0.893 mmol) in 25 mL $CHCl_3$ was added dropwise to a solution of **C15** (0.150 g, 0.4054 mmol) in 40 mL of CHCl3. The reaction mixture was stirred at room temperature for 6h. After the removal of AgCl by filtration, the mother liquor was evaporated under reduced pressure. The residue was dissolved in Et_2O and acetone was added. The

precipitate formed was filtrated out, and the pure product was obtained from the mother solution by recrystallization from $CHCl_3$/ACN (0.315 g, 47%).

FT-IR (KBr, cm^{-1}): 2924 ($\nu_{as,(-CH_2-)}$), 2854 ($\nu_{s,(-CH_2-)}$), 1623 ($\nu_{as,(COO^-)}$), 1567 – 1428 ($\upsilon_{C=C}$, $\upsilon_{C=N}$) 1359 ($\nu_{s(COO^-)}$);

^{1}H-NMR ($CDCl_3$-d, δ/ppm): 9.02 (m, 2H), 8.23 (overlapped peaks, 5H), 7.99 (t, 2H), 7.54 (dd, J = 7.6, 5.0 Hz, 2H), 3.94 (overlapped peaks, 12H), 1.75 (m, 12H), 1.69 – 1.26 (overlapped peaks, 108H), 0.89 (m, 18H).

Synthesis of C17

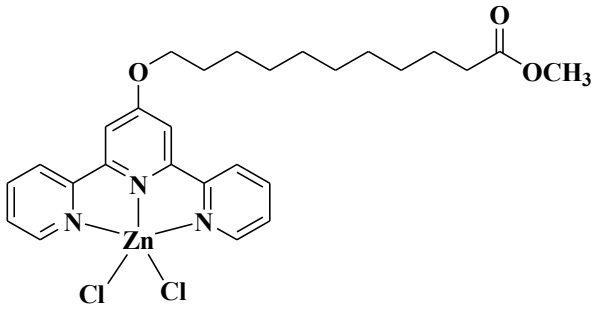

A solution of $ZnCl_2$ (0.061 g, 0.447 mmol) in 20 mL of MeOH was added dropwise to a solution of **L9** (0.200 g, 0.447 mmol) in 20 mL $CHCl_3$. The reaction mixture was stirred for 1.5 h at r. t. Then, the yellowish solution was filtered. Over the mother liquor diethyl ether was added, resulting a white precipitate which was filtered out, washed with diethyl ether and dried under vacuum to yield complex C17 (0.238 g, 0.407 mmol, 91%).

Anal. Calcd. for C27H33Cl2N3O3Zn (583.87 g/mol): C, 55.54; H, 5.70; N, 7.20. Found: C, 54.92; H, 5.68; N, 7.14%.

FT-IR (KBr, cm^{-1}): 2928 ($\nu_{as,(-CH_2-)}$), 2855 ($\nu_{s,(-CH_2-)}$), 1735 ($\nu_{as,(COOCH3)}$), 1623 ($\nu_{as,(COO^-)}$), 1571–1439 ($\upsilon_{C=C}$, $\upsilon_{C=N}$) 1359 ($\nu_{s(COO^-)}$);

^{1}H-NMR ($CDCl_3$-d, δ/ppm): 8.82 (d, ^{3}J = 6.4 Hz, 2H,), 8.72 (d, 2H), 8.37 – 8.30 (overlapped peaks, 4H), 7.87 (m, 2H), 4.34 (t, ^{3}J = 6.7 Hz, 2H), 3.37 (s, 3H), 2.27 (t, ^{3}J = 7.4 Hz,2H), 1.76 (m, 2H), 1.59 – 1.01 (overlapped peaks, 14H).

Synthesis of C18

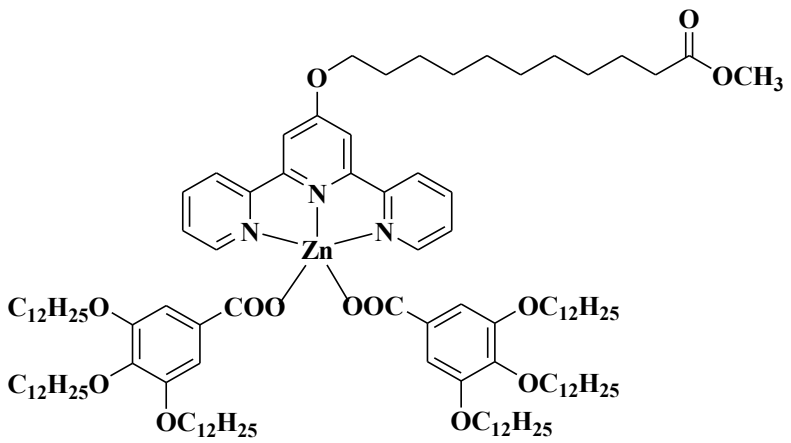

A solution of complex **C14** (0.268 g, 0.342 mmol) in 25 mL $CHCl_3$ was added drop wise to a solution of **C17** (0.100 g, 0.171 mmol) in 40 mL of CHCl3. The reaction mixture was stirred at room temperature for 2h. After the removal of AgCl by filtration, the solution was concentrated under vacuum and acetone was added. The precipitate formed was filtrated out, and the pure product was obtained from the mother solution by recrystallization from $CHCl_3$/MeOH (0.239 g, 75%).

Anal. Calcd. for C113H187N3O13Zn (1861.1 g·mol-1): C, 72.93; H, 10.13; N, 2.26. Found: C, 72.65; H, 10.32; N, 1.70%.

FT-IR (KBr, cm^{-1}): 3063, 2924, 2854 (C-H stretch); 1740 (ν(C=O)); 1615 (νas(COO-)), 1365 (νs(COO-));

^{1}H-NMR ($CDCl_3$-d, δ/ppm): 8.94 (d, ^{3}J = 5.1 Hz, 2H), 8.15 (d, ^{3}J = 8.1 Hz, 2H), 7.73 (m, 2H), 7.65 (s, 2H), 7.31 (s, 4H), 3.91 (overlapped peaks, 14H), 3.68 (s, 3H), 2.31 (t, ^{3}J = 7.6 Hz, 2H), 1.70 (m, 2H), 1.60 – 1.57 (overlapped peaks, 136H), 0.88 (t, 18H).

Synthesis of C19

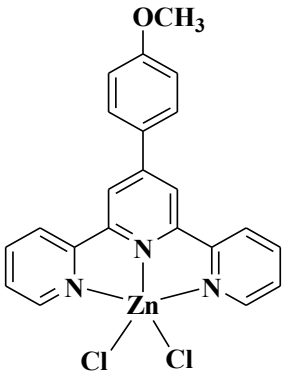

A solution of $ZnCl_2$ (0.145 g, 1.06 mmol) in 20 mL of MeOH was added dropwise to a solution of **L10** (0.300 g, 0.884 mmol) in 20 mL $CHCl_3$. The reaction mixture was stirred for 1.5 h at r. t. A yellow precipitate was formed, which was filtered out and washed with MeOH. The precipitate was dried under vacuum to yield complex **C19** (0.379 g, 0.796 mmol, 90 %).

FT-IR (KBr, cm^{-1}): 3067, 3002 ($\nu_{(CH3)}$), 1601 - 1435 ($\upsilon_{C=C}$, $\upsilon_{C=N}$), 1250 ($\nu_{as\,(C\text{-}O\text{-}C)}$), 1023 ($\nu_{s\,(C\text{-}O\text{-}C)}$);

^{1}H-NMR (DMSO-d_6, δ/ppm): 8.86 (overlapped peaks, 6H), 8.25 (m, 4H), 7.83 (m, 2H), 7.12 (d, ^3J = 8.5 Hz, 2H), 3.87 (s, 3H).

Synthesis of C20

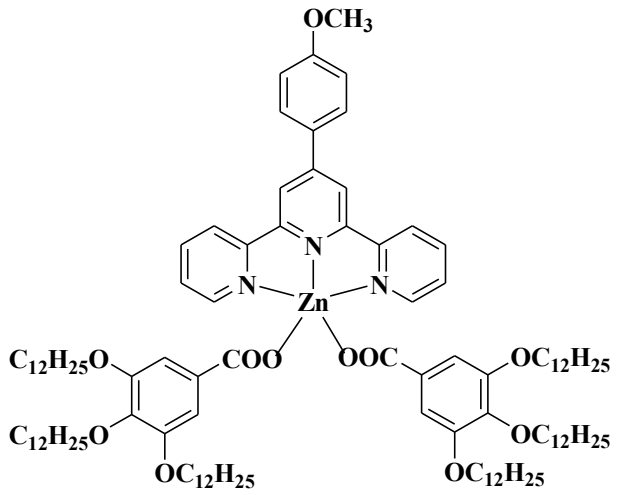

A solution of complex **C14** (0.329 g, 0.42 mmol) in 100 mL $CHCl_3$ was added drop wise to a solution of **C18** (0.100 g, 0.210 mmol) in 150 mL of $CHCl_3$. The reaction mixture was stirred at room temperature for 4h. After the removal of AgCl by filtration, the solution was concentrated under vacuum and acetone was added. The precipitate formed was filtrated out, and the pure product was obtained from the mother solution by recrystallization from $CHCl_3$/MeOH (0.265 g, 0.151, 72%).

FT-IR (KBr, cm^{-1}): 2922 ($\nu_{as,(-CH_2-)}$), 2851 ($\nu_{s,(-CH_2-)}$), 1611 ($\nu_{as,(COO^-)}$), 1562– 1436 ($\upsilon_{C=C}$, $\upsilon_{C=N}$) 1368 ($\nu_{s(COO^-)}$);

^{1}H-NMR ($CDCl_3$-d, δ/ppm): 9.00 (dt, J = 4.8, 1.5 Hz, 2H), 8.31 (s, 2H), 8.19 (d, J = 8.0 Hz, 2H), 7.84 (td, J = 7.8, 1.7 Hz, 2H), .78 – 7.67 (m, 2H), 7.55 – 7.45 (m, 2H), 7.32 (s, 4H), 6.95 (d, J = 8.9 Hz, 2H), 3.93 (overlapped peaks, 15H), 1.75 (m, 12H), 1.42 – 1.26 (overlapped peaks, 108H), 0.89 (m, 18H).

Synthesis of C21

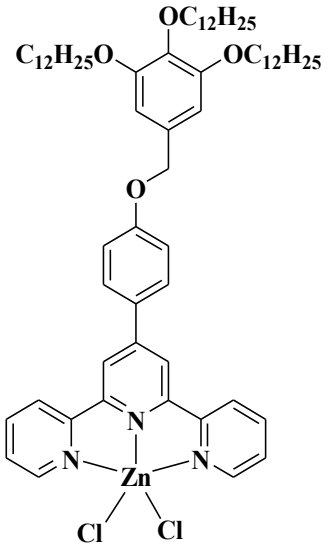

A solution of $ZnCl_2$ (0.083 g, 0.620 mmol) in 30 mL of MeOH was added dropwise to a solution of **L11** (0.500 g, 0.516 mmol) in 30 mL $CHCl_3$. The reaction mixture was stirred for 1.5 h at r. t. Then, the pale pink solution was filtered. The mother liquor was taken to dryness. The pure compound was obtained after recrystallization from $CHCl_3$/MeOH, the pale pink precipitate was filtered and dried under vacuum to yield complex **C19** (0.400 g, 0.3621 mmol, 70 %).

FT-IR (KBr, cm^{-1}): 2926 ($\nu_{as,(-CH2-)}$), 2851 ($\nu_{s,(-CH2-)}$), 1608 - 1442 ($\upsilon_{C=C}$, $\upsilon_{C=N}$), 1250 (ν_{as} (C-O-C)), 1068 (ν_s (C-O-C));

^{1}H-NMR ($CDCl_3$-d, δ/ppm): δ 9.01 (dd, *J* = 5.0, 1.6 Hz, 2H), 8.09 – 7.97 (m, 4H), 7.71 (td, *J* = 7.5, 6.9, 1.9 Hz, 4H), 7.45 (dd, *J* = 7.6, 5.0 Hz, 2H), 6.91 (d, *J* = 8.7 Hz, 2H), 6.68 (s, 2H), 4.98 (s, 2H), 4.06 (t, *J* = 6.4 Hz, 4H), 4.00 (t, *J* = 6.5 Hz, 2H), 1.83 (dt, *J* = 21.7, 7.4 Hz, 6H), 1.29 (d, *J* = 5.1 Hz, 48H), 0.89 (t, *J* = 6.3 Hz, 9H).

Synthesis of C22

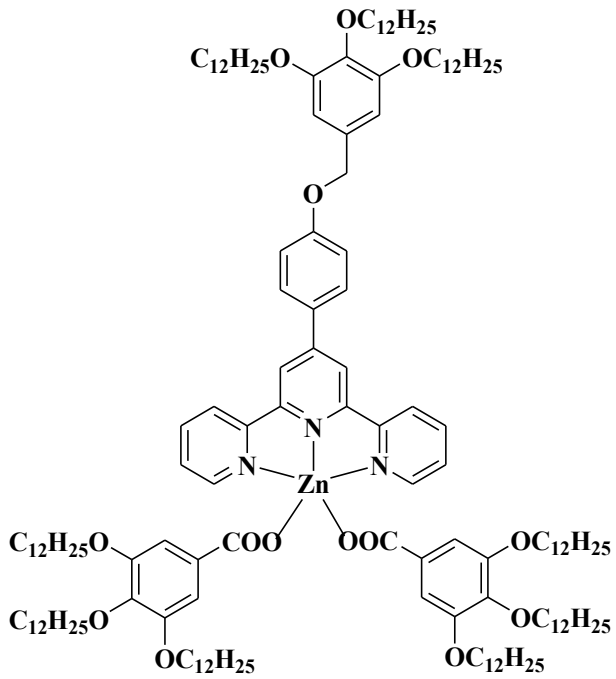

A solution of complex **C14** (0.187 g, 0.239 mmol) in 50 mL $CHCl_3$ was added drop wise to a solution of **C21** (0.120 g, 0.109 mmol) in 50 mL of $CHCl_3$. The reaction mixture was stirred at room temperature for 4h. After the removal of AgCl by filtration, the solution was concentrated under vacuum and acetone was added. The precipitate formed was filtrated out, and the pure product was obtained from the mother solution by recrystallization from $CHCl_3$/MeOH (0.205 g, 0.086, 79%).

FT-IR (KBr, cm^{-1}): 2923 ($\nu_{as,(-CH2-)}$), 2853 ($\nu_{s,(-CH2-)}$), 1598 - 1442 ($\upsilon_{C=C}$, $\upsilon_{C=N}$), 1570 ($\nu_{as(COO^-)}$, 1370 ($\nu_{s(COO^-)}$), 1250 (ν_{as} (C-O-C)), 1068 (ν_s (C-O-C));

^{1}H-NMR ($CDCl_3$-d, δ/ppm): 9.01 (dd, J = 5.3, 1.7 Hz, 2H), 8.33 (s, 2H), 8.24 (d, *J* = 8.0 Hz, 2H), 7.92 (td, J = 7.8, 1.7 Hz, 2H), 7.73 (d, J = 8.7 Hz, 2H), 7.50 (dd, J = 7.6, 5.1 Hz, 2H), 7.31 (s, 4H), 7.11 (d, J = 8.8 Hz, 2H), 6.68 (s, 2H), 5.03 (s, 2H), 3.93 (overlapped peaks, 18H), 1.77 (m, 18H), 1.42 – 1.26 (overlapped peaks, 144H), 0.89 (m, 27H).

Synthesis of Au@OA

200 mg of $HAuCl_4 \cdot 3H_2O$ were dissolved in 20 mL of oleylamine and 20 mL of tetralin. 1 mmol of TBAB dissolved in 2 mL of oleylamine and 2 mL of tetralin was then quickly injected into the stirring gold solution. The mixture was left stirring open to the atmosphere for one hour. The NPs were precipitated with isopropanol and centrifuged. The solid pellet of NPs was redispersed in hexanes. The NPs were washed twice more with isopropanol before finally redispersed in 20 mL of hexane. [4]

Synthesis of I6

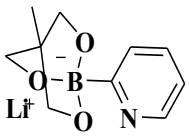

1g of 2-bromo-pyridine (0.0064 mol, 0.62 mL) were dissolved in 19 mL of dry THF, the mixture was degased and was kept under an argon atmosphere. The mixture was cooled to -78^0 C. 4 mL of n-BuLi (0.0064 mol, 1.6 M in hexane) were added dropwise (1ml/min). The reaction mixture was stirred for 45 min at -78^{0}C. 0.72 mL of $B(OMe)_3$ were added dropwise in one minute. The reaction mixture was stirred for an additional hour, and after that was warmed to room temperature, yielding an orange solution.

0.768g 1,1,1-tris(hydroxymethyl)-ethane (0.0064 mol) were added in one portion. The reaction mixture was refluxed for 30 min, cooled to room temperature and was poured in 90 mL of hexanes. The precipitate was filtered and dried (1.3 g, pale pink powder, reported white). The compound was used without further purification.

^{1}H-NMR (300 MHz, DMSO-d_6, δ/ppm): 8.25 (d, 1H); 7.5 (t, 1H); 7.33 (d, 1H); 7.05 (m, 1H); 3.57 (s, 6H); 0.49 (s, 3H);

Synthesis of I7

Compound **I7** was synthesized in a multistep reaction, using 2-amino-4-methylpiridine as starting material, as described in **Scheme 5-1**:

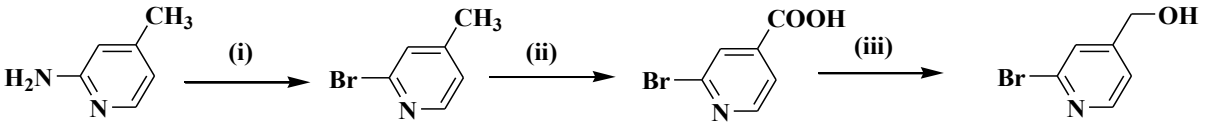

4-methylpyridin-2-amine | **2-bromo-4-methylpyridine** | **2-bromopyridine-4-carboxylic acid** | **(2-bromopyridin-4-yl)methanol**

(I7)

Scheme 5-1. Reaction pathway of compound **I7**. Reagents and conditions: **(**i) a: 48% HBr, Br_2, b: NaNO2, -20 °C, c: NaOH, -15°C; (ii) a: $K_2Cr_2O_7/H_2SO_4$, (iii) a: EtOH, H_2SO_4, b: $NaBH_4$, EtOH.

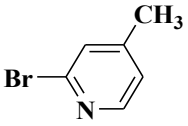

2-bromo-4-methylpyridine

In a three necked round bottom flask, equipped with an internal thermometer, 25 mL of hydrobromic acid, HBr 48% were added. Then, 5 g of 2-amino-4-methylpyrdine (46 mmol) were added at 20-30 °C. After the complete dissolution of the compound, the reaction mixture was cooled to -20 °C. 7 mL of bromine were slowly added to the mixture, during 30 minutes while maintaining the internal temperature at -20 °C. The resulting paste was stirred at this temperature for another 90 minutes. Sodium nitrate (8.5 g in 12.5 mL of H_2O) was added dropwise, after that the reaction mixture was allowed to warm to room temperature during one hour, and was stirred for additional 45 minutes. The mixture was then cooled to -20 °C and treated with sodium hydroxide (33.35 g in 50 mL of H_2O). During the addition of the sodium hydroxide solution the internal temperature was kept bellow -10 °C. The reaction mixture was then warmed to room temperature and extracted with ethyl acetate, the organic layers were dried on anhydrous Na_2SO_4, and the solvent was removed under vacuum to yield 2-bromo-4-methyl-pyridine (η= 77%).

^{1}H-NMR (300 MHz, $CDCl_3$-d, δ/ppm): 8.12 (d, 1H), 7.25 (s, 1H), 7.00 (d, 2H), 2.26 (s, 3H);

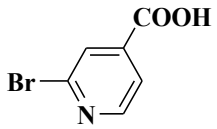

2-bromopyridine-4-carboxylic acid

2 g of 2-bromo-4-methyl-pyridine were slowly dissolved in 38 mL of concentrated H_2SO_4. The reaction mixture was warmed to 60ºC and 7.58 g of $K_2Cr_2O_7$ were added in portions while keeping the temperature bellow 70ºC. After the addition of $K_2Cr_2O_7$ the mixture was cooled to room temperature, and slowly poured over 300 mL (H_2O and ice), filtered and washed with water to yield 2-bromopyridine-4-carboxylic acid as a white powder (η= 70 %).
^{1}H-NMR (300 MHz, DMSO-d_6, δ/ppm): 8.53 ppm (d, 1H); 8.07 (s, 1H); 7.9 (d, 1H).

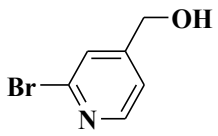

(2-bromopyridin-4-yl)methanol

(I7)

a: 1 g of 2-bromopyridine-4-carboxylic acid was suspended in 21 mL of EtOH and 1.25 mL of concentrated H_2SO_4. The progress of the reaction was followed by TLC (CH_2Cl_2: MeOH= 99:1). The reaction mixture was kept under reflux for 24 hours, cooled to room temperature and evaporated under vacuum. The residue was transferred into an extraction funnel charged with 50 mL of water, and the aqueos layer was extracted 4 times with CH_2Cl_2, dried over Na_2SO_4, filtered and the organic layer was evaporated under vacuum to yield the desired ester.
^{1}H-NMR (300 MHz, DMSO-d_6, δ/ppm): 8.59 ppm (d, 1H); 7.97 (s, 1H); 7.85 (d, 1H); 4.35 (q, 2H); 1.32 (t. 3H);

b: 1 g of the ethylic ester previously obtained was suspended in 35 mL of EtOH, then 1 g of $NaBH_4$ was slowly added. The progress of the reaction was followed by TLC (CH_2Cl_2: MeOH= 99:1). The reaction mixture was kept under reflux until the completion of the reaction, cooled to room temperature and the 35 mL of saturated NH_4Cl were slowly added under stirring. The ethanol was evaporated, and the compound was extracted with CH_2Cl_2, dried over Na_2SO_4 anhydrous, filtered and taken to dryness.
^{1}H-NMR (300 MHz, DMSO-d_6, δ/ppm): 8.3 ppm (d, 1H); 7.54 (s, 1H); 7.35 (d, 1H); 5.57 (t, 1H); 4.54 (d, 3H);

Synthesis of L12

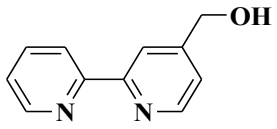

0.996 g of boronic compound I6 (0.00467 mol), 0.290 g of I7 and 0.054 g $Pd(PPh_3)_4$ were added in a 2 necked flask and were flushed with argon. 20 mL of DMF were added and the reaction mixture was refluxed under argon atmosphere for 21 hours. The mixture was then allowed to cool to room temperature and after that was transferred into a separator funnel charged with ethyl acetate (40 mL) and saturated aq. NH_4Cl solution (40 mL). The aqueous layer was extracted with EtOAc (2 x 20 mL). The combined organic layer was washed with saturated aq. NaCl solution (5 x 40 mL). The organic layer was dried over anhydrous $MgSO_4$, filtered and concentrated under reduced pressure to afford crude solid product. The final product was obtain in a very low yield (< 4%).

^{1}H-NMR (300 MHz, DMSO-d6): 8.29 (d, 1H) 7.57 (m, 2H), 7.35 (d, 1H), 7.23 (m, 1H), 7.15 (m, 2H), 5.55 (t, 1H), 4.52(d, 1H). The NMR spectra also showed the presence of impurities in the final product.

Synthesis of I8

Compound **I8** was synthesized in a two-step reaction, using pyridine 4-carboxylic acid as starting material, as described in **Scheme 5-2.**

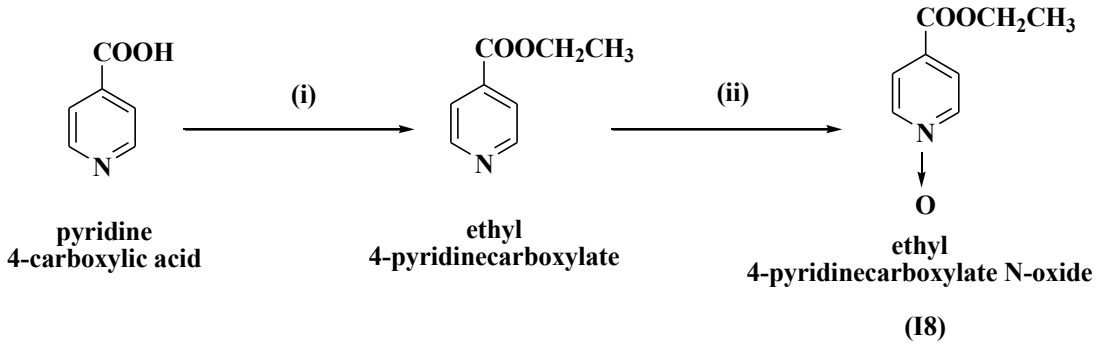

Scheme 5-2. Reaction pathway of compound **I8**. Conditions: **(**i) EtOH, H_2SO_4, ΔT, (ii) CH_3COOH, H_2O_2, ΔT.

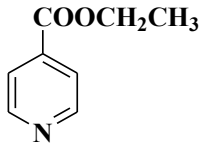

ethyl
4-pyridinecarboxylate

11 g of isonicotinic acid were dissolved in 200 mL of ethanol, and 13.75 mL of concentrated sulfuric acid. The reaction mixture was stirred under reflux, until the consumption of the starting material (followed by TLC, using CH_2Cl_2: MeOH= 99:1), approximately 12h. The solvent was evaporated under vacuum, the residue was taken with 30 mL of 1 M Na_2CO_3 solution, and the compound was extracted with diethyl ether (3x 60mL). The organic phase dried on anhydrous $MgSO_4$, filtered and evaporated under vacuum, to obtain ethyl 4-pyridinecarboxylate as a colourless oil (η=81%).

^{1}H-NMR (300 MHz, $CDCl_3$-d, δ/ppm), δ: 8.73 (d, 2H), 7.80 (d, 2H); 4.37 (q, 2H), 1.37 (t, 3H);

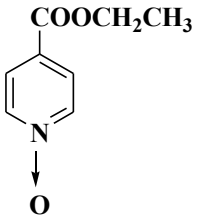

ethyl
4-pyridinecarboxylate N-oxide

I8

0.0135 of ethyl 4-pyridinecarboxylate were suspended in 15 mL of concentrated acetic acid. 1.67 mL (1.2 eq.) of hydrogen peroxide 30% were added dropwise. The reaction mixture was stirred at 70 ^{0}C, until the consumption of the substrate as judged by TLC. The acetic acid was removed under reduced pressure. The residue was slowly basified with a sodium bicarbonate solution, and extracted with CH_2Cl_2. The organic layer was dried on anhydrous $MgSO_4$, filtered and evaporated under vacuum, to obtain ethyl 4-pyridinecarboxylate N-oxide.

^{1}H-NMR (300 MHz, $CDCl_3$-d, δ/ppm), δ: 8.22 (d, 2H), 7.88 (d, 2H); 4.40 (q, 2H), 1.60 (t, 3H);

Synthesis of I9

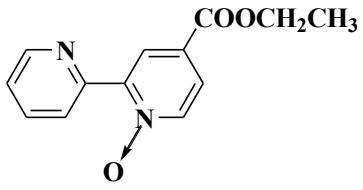

Compound **I8** (0.7 g, 4.19 mmol), $Pd(OAc)_2$ (0.023g, 0.105 mmol) and K_2CO_3 (0.579 g, 4.19 mmol) were added in a Schlenk tube, then degassed and charged with argon three times. Under an argon atmosphere 0.12 mmol P(*t*Bu)$_3$ were dissolved in toluene (4 ml) and was added over the solids. 2-bromopyridine (0.331 g, 2.09 mmol) was added via a Hamilton syringe and the mixture was stirred for 15 min at r.t. and 24 h at 120 °C. Then, the reaction mixture was directly purified by column chromatography (acetone/hexane, 0%-100%, 10% increments per 100ml with 200ml of 20%). Yield 5%.

^{1}H-NMR (300 MHz, DMSO-d6, δ/ppm): 8.76 (dd, 2H), 8.6 (d, 2H), 8.46 (d, 2H), 7.96 (t, 2H), 7.87 (dd, 2H), 7.52 (m, 2H), 4.35 (q, 2H), 1.33 (t, 3H).

Synthesis of L13

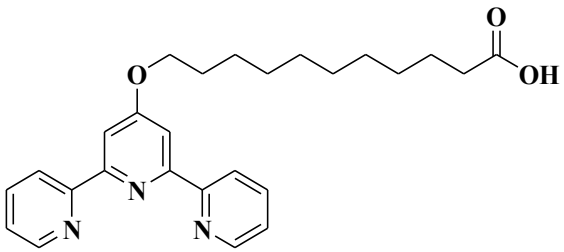

L8 was refluxed in EtOH with NaOH until the complete consumption of the reactant (2-3 hours). The reaction was followed on TLC (Al2O3: CH_2Cl_2). The reaction mixture was cooled to room temperature; water was then added and acidified with concentrated HCl. At pH=5 a white precipitate was formed, filtered off and washed well with water and ethanol.

^{1}H-NMR (300 MHz, DMSO-d6, δ/ppm): 8.71 (d, 2H), 8.61 (d, 2H), 8.09 – 7.92 (m, 4H), 7.59 – 7.41 (m, 2H), 4.22 (t, 2H), 2.18 (t, 2H), 1.77 (dd, 2H), 1.61 – 1.15 (m, 14H).

Synthesis of I10

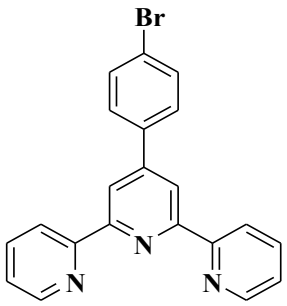

A solution of acetylpyridine (12.1 g, 99.08 mmol), KOH (8.5 g, 151.5 mmol) and 145 mL NH_4OH in 200 mL EtOH were added dropwise over a solution of 4-bromobenzaldehyde (10 g, 54.04 mmol) in 150 mL EtOH at 0ºC. The reaction mixture was refluxed for 24h, cooled to room temperature and stirred for an additional hour. The precipitate was filtered and washed with cold EtOH, yielding a white solid (8.2 g, 21.12 mmol, 39.1 %).

^{1}H-NMR (300 MHz, $CDCl_3$, δ/ppm): 8.67 (d, J = 7.9 Hz, 2H), 7.88 (td, J = 7.8, 1.6 Hz, 2H,), 7.78 (d, J =8.4 Hz, 2H), 7.64 (d, J = 8.5 Hz, 2H), 7.38 – 7.33 (m, 2H).

Synthesis of L14

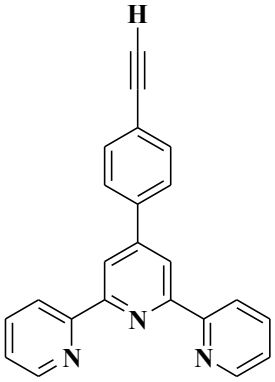

Compound **I10** (8.2 g, 21.12 mmol), $Pd(PPh_3)_4$ (2.4 g, 2.07 mmol) and CuI (1.61 g, 8.45 mmol) were placed in a 500 mL round bottom flask, which was degassed and flushed with argon (x3). Anhydrous THF (100 mL) and NEt_3 (200 mL) were then added, followed by TMSA (6.22 g,

8.77 mL, 63.36 mmol). The mixture was heated at 70ºC and stirred at this temperature for 12h The reaction mixture was cooled to room temperature, then 400 mL H_2O were added. The mixture was extracted with $CHCl_3$, dried over anhydrous Na_2SO_4 and the solvent was evaporated under vacuum. The raw product was suspended in 60 mL of chloroform and 240 mL of methanol, and then K_2CO_3 (8.79 g, 63.73 mmol) was added in one portion. The suspension was then stirred at room temperature for 3 h. After this, 400 mL of H_2O was added and extracted with $CHCl_3$, the combined organic layers were dried over anhydrous Na_2SO_4 and the solvent was evaporated under vacuum. The raw product was purified by column chromatography on SiO_2 ($CHCl_3$:MeOH = 100:1) to afford the desired compound as a white solid (2.85 g, 85.6 %).

^{1}H NMR (300 MHz, $CDCl_3$, δ- ppm): 8.81 – 8.58 (m, 6H), 7.97 – 7.74 (m, 4H), 7.62 (d, J = 8.2 Hz, 2H), 7.32 (dt, J = 17.9, 8.8 Hz, 2H), 3.19 (s, 1H).

Synthesis of I11

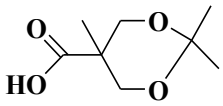

Bis-MPA (10 g, 0.075 mol), 2,2-dimethoxy-propane (13.75 mL, 11.55 g, 0.111 mol), pare-toluene-sulfonic acid (0.71 g, 0.00412 mol) were dissolved in 50 mL of dry acetone, resulting in a pale colourless solution. The reaction mixture was stirred at room temperature for 2h, and the catalyst was neutralized with 0.85 mL (EtOH: NH_3= 50-50). A milky white suspension was obtained. Then the solvent was evaporated under vacuum at r.t., yielding a white product. The product was dissolved in CH_2Cl_2 (300 mL), and washed 2 times with 30 mL of H_2O. The organic layer was dried on $MgSO_4$, filtered, and the solvent was evaporated under vacuum, yielding a white powder. (η=68.9 %)

^{1}H-NMR (300 MHz, $CDCl_3$, δ- ppm): 4.19 (d,2H), 3.69 (d, 2H), 1.44 (d, 6H), 1.22 (s, 3H).

Synthesis of I11

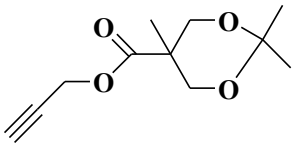

Propargyl alcohol (4.31 g, 77 mmol), compound **I11 (**51.7 mmol)**,** and DMAP were dissolved (27.2 mmol) in 50 mL CH_2Cl_2. Then, DCC (0.0616 mol) was dissolved in 15 mL CH_2Cl_2 and added dropwise to the reaction mixture. The reaction was followed by TLC (using a vanillin solution as a developer). After the reaction was completed, the solution was filtered, the filtrate was transferred into a separating funnel and washed with H_2O (2 x 50 mL). The organic phase was dried on anhydrous $MgSO_4$ and the solvent was evaporated. The compound was purified by column chromatography (SiO_2, using a gradient eluent petroleum ether: ethyl acetate of 10:1), yielding a colorless oil (η=61.5 %).

^{1}H-NMR (300 MHz, $CDCl_3$, δ- ppm): 4.74 (d, 2H), 4.21 (d, 2H), 3.66 (d, 2H), 2.47 (t, 1H), 1.41 (d, 6H), 1.22 (s, 3H).

Synthesis of G_A1

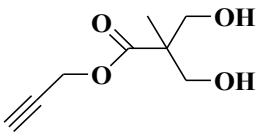

30 mmol mol of **I11** were dissolved in MeOH and 1.22 g of Dowex resin were added. Then the resulting suspension was stirred for 2h at 40ºC, filtered taken to dryness, resulting in a yellow oil. The oil was dissolved in CH_2Cl_2, and hexane was added, filtrated and the solvent was evaporated under vacuum, yielding compound **G1** as a white powder (η= 99.5 %).

^{1}H-NMR (300 MHz, $CDCl_3$): 4.78 ppm (d, 2H), 3.95 ppm (d, 2H), 3.75 ppm (d, 2H), 2.5 ppm (t, 1H), 1.11 ppm (s, 3H).

Synthesis of I13

In order to synthesize $\mathbf{G_A2}$, first 2,2,5-trimethyl-1,3-dioxane-5-carboxylic anhydride was synthesized starting from compound **I11**, as described in **Scheme 5-3**.

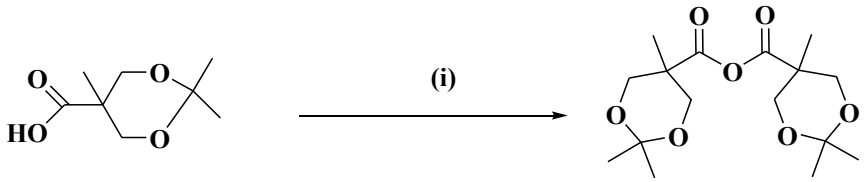

(I11)

2,2,5-Trimethyl-1,3-dioxane-5-carboxylic anhydride

Scheme 5-3. Reaction pathway of 2,2,5-trimethyl-1,3-dioxane-5-carboxylic anhydride. Conditions: **(**i) DCC, DCM, r.t, 2h.

2,2,5,-trimethyl-1,3-dioxane-5 carboxylic acid (13.8 g, 0.079 mol) was suspended in 70 mL dry CH_2Cl_2. Then, DCC (8.142g) was dissolved in 15 mL of dry CH_2Cl_2 and added dropwise to the suspension, resulting in a white suspension, which was stirred at room temperature for 24 h. The urea DCC by-product was filtered off and washed with a small amount of dry CH_2Cl_2. The solvent was evaporated and the resulting residue was taken with EtOAc. DCU was removed by filtering the resulting suspension and the solvent was evaporated under vacuum, thus obtaining compound 2,2,5-trimethyl-1,3-dioxane-5-carboxylic anhydride as colourless oil. (η=91%).

Synthesis of I14

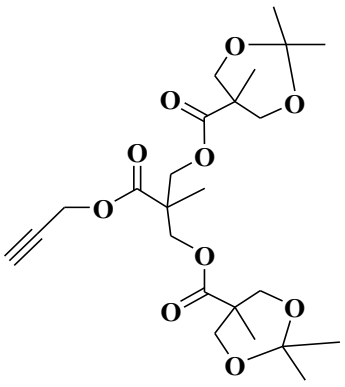

To a stirred solution of **G1** (14.52 mmol), DMAP (5.81 mmol) and pyridine (43.65 mmol) in CH_2Cl_2 (70 mL), 2,2,5-trimethyl-1,3-dioxane-5-carboxylic anhydride (34.85 mmol) was added.

The resulting mixture was stirred at r.t for 24 h, then quenched with 5 mL H_2O. An additional 175 mL of CH_2Cl_2 were added, washed with CH_3COOH 0.1M (2 x 100 mL), Na_2CO_3 1M (2 x 100 mL) and brine (50 mL). The organic layer was dried over Na_2SO4 and taken to dryness. The residue was purified on SiO_2, EtOAc:hexane = 0 – 50%) to obtain compound **I14** as a white powder (η= 88%).

Synthesis of G_A2

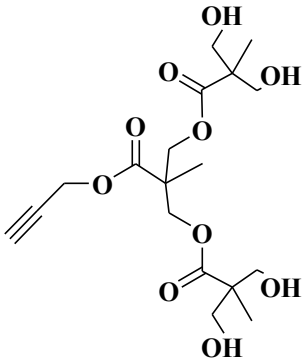

Compound **I14** (15.28 mmol) was dissolved in MeOH and 4.15 g of Dowex H^+ were added. The mixture was stirred at 40 °C for 2h, filtered and the solvent was evaporated under vacuum. Compound **G_A2** was obtained as a white powder (η= 97%).

Synthesis of I15

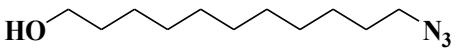

To a solution of 11-brom-1-undecanol (39.8 mmol) in DMF (50 mL) was added NaN_3 (79.6 mmol) and the resulting mixture was stirred at 70 °C for 12 h. The mixture was cooled to 23 °C, filtered and the filtrate extracted with hexane (5 x 100 mL). The hexanes fractions were combined and washed with H_2O (2 x 50 mL), dried over anhydrous Na_2SO_4 and concentrated under reduced pressure to afford 11-azidoundecan-1-ol (85 %) as a colourless oil.

^{1}H NMR (300 MHz, $CDCl_3$, δ- ppm): 3.60 (t, *J* = 6.6 Hz, 2H), 3.23 (t, *J* = 6.9 Hz, 2H), 1.85 (s, 1H), 1.62-1.49 (m, 4H), 1.26 (s, 14H).

Synthesis of I16

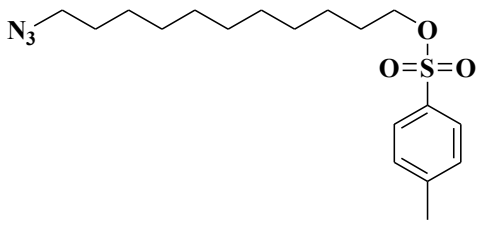

A mixture of 11-azido-1- undecanol (22.75 mmol) and p-toluene sulfonyl chloride (22.75 mmol) in dry CH_2Cl_2 (30 mL) was cooled to 0°C and then NEt_3 (34 mmol) was added dropwise (over a period of 30 min.). The resulting mixture was stirred under argon for 12 h. The mixture was diluted with CH_2Cl_2 (20 mL) and washed with 1N HCl (3 x 100 mL), dried over anhydrous $MgSO_4$ and concentrated under reduced pressure. The residue was purified by column chromatography (SiO_2, EtOAc:hexanes = 0 – 50%) to yield compound 3.17 (η=61.5 %) as a colourless oil.

^{1}H NMR (300 MHz, $CDCl_3$, δ- ppm): 7.79 (d, 2H), 7.35 (d, 2H), 4.02 (t, 2H), 3.26 (t, 2H), 2.41 (s, 3H), 1.60 (m, 4H), 1.23 (m, 14H).

Synthesis of Anc_1

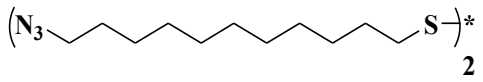

A mixture of **I17** in 30 mL EtOH, 20.6 mmol of thiourea were added and the mixture was stirred at 80°C for 20h, cooled to room temperature, basified with 20 mL NaOH 2M and stirred for 30 min. The mixture was then acidified with 2N H_2SO_4 (23 mL), concentrated under reduced pressure and extracted with CH_2Cl_2 (3 x 75mL). The organic layer was dried over anhydrous Na_2SO_4, filtered and concentrated under reduced presure. The residue was mixed with MeOH (15 mL) and treated with solution of iodine (1M solution in MeOH) until colour of suspension turned yellow. Na_2SO_3 was then added to remove the excess of iodine. After that the mixture was concentrated under vacuum, the residue was extracted with CH_2Cl2 (2 x 50 mL), concentrated and purified by column chromatography (SiO2, $CHCl_3$: hexane = 0 – 50%) to afford Anc_1 as a colorless liquid.

^{1}H NMR (300 MHz, $CDCl_3$, δ- ppm): 3.26 ppm (t, 4H), 2.68 ppm (t, 4H), 1.63 ppm (m, 8H), 1.32 ppm (m, 28H).

Synthesis of I20

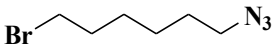

To a solution of 1,6-dibromohexane (10 g, 40.99 mmol) in DMF at r.t, NaN_3 (1.07 g, 16.40 mmol) was added. The mixture was stirred overnight. H_2O (50 mL) was added into the solution then extracted with Et_2O (2 x 90 mL). The organic layer was dried over anhydrous Na_2SO_4 and taken to dryness. The pure product was obtained after purification on column chromatography (SiO_2: gradient elution: hexane, then hexane: Et_2O = 95:5) yielding a colorless oil (2.39g, 11.6 mmol, 71%).

^{1}H NMR (300 MHz, $CDCl_3$, δ- ppm): 3.33 (t, 2H), 3.26 (t, *J* = 6.8 Hz, 2H), 1.84 (m, 2H), 1.60 (m, 2H), 1.42 (m, 4H).

Synthesis of G_B1

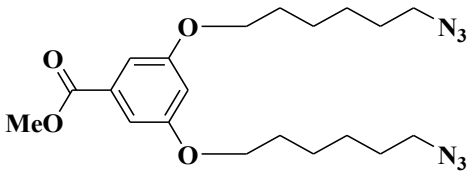

Methyl 3,5-dihydroxybenzoate (1.29 g, 7.65 mmol), **I15** (3.88 g, 18.83 mmol), anhydrous K_2CO_3 (3.26 g, 23.62 mmol), KI (0.132 g, 0.8 mmol) were suspended in 20 mL dry DMF, and stirred at 80 °C for 24 h, then diluted with 150 mL of EtOAc. The organic phase was washed with H_2O (3×100 mL), saturated NH_4Cl (100 mL), dried over anhydrous Na_2SO_4 and concentrated under vacuum. The raw product was purified by column chromatography (SiO_2, hexane: /EtOAc = 80:20) yielding the desired product as a colorless oil (2.64 g, 6.32 mmol, 82.6 %).

^{1}H NMR (300 MHz, $CDCl_3$, δ- ppm): 7.15 (d, 2H), 6.62 (t, 1H), 3.96 (t, 4H), 3.90 (s, 3H), 3.28 (t, 4H), 1.84 (m, 4H), 1.63 (m, 4H), 1.47 (m, 8H).

Synthesis of I21

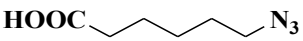

6-bromohexanoic acid (5 g, 25.63 mmol) and NaN_3 (2 g, 30.76 mmol) were dissolved in 50 mL DMF and stirred at 80ºC overnight. The mixture was cooled to room temperature, diluted with 100 mL H_2O and extracted with Et_2O (3 x 100mL). The combined organic layers were washed with H_2O (3 x 100mL) and brine (100mL), dried over anhydrous Na_2SO_4 and concentrated under reduced pressure yielding colourless oil (3.3 g, 20.99 mmol, 82 %).

^{1}H NMR (300 MHz, $CDCl_3$, δ- ppm): 10.86 (bs, 1H), 3.14 (td, 2H), 2.23 (td, 2H), 1.41 (m, 10H).

Synthesis of I22

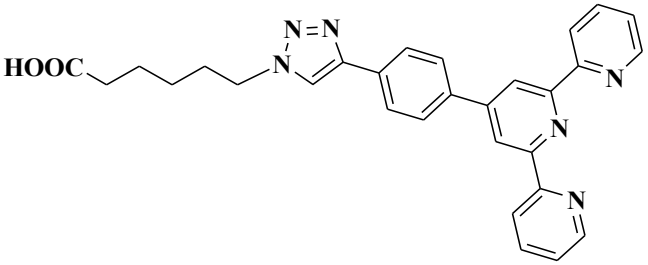

I16, 6-azidohexanoic acid (236 mg, 1.5 mmol) and 4'-(4-ethynylphenyl)-2,2':6',2''-terpyridine (500 mg, 1.5 mmol) were dissolved in 30 mL of H_2O/THF (1:1). A 1M solution of L-sodium ascorbate (505 mg, 2.55 mmol) in H_2O was added to the reaction mixture, followed by the addition of $CuSO_4$ x $5H_2O$ (247 mg, 0.99 mmol). The reaction mixture was stirred at 70ºC for 24 h.

Synthesis of I25

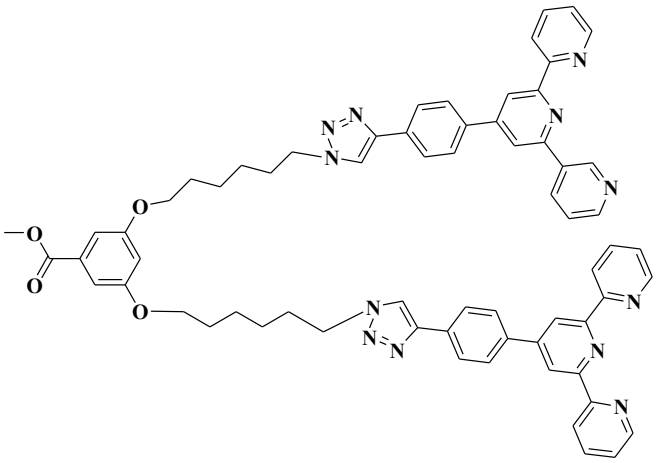

Compound **G_B1** (313 mg, 0.75 mmol) and **L14** (500 mg, 1.5 mmol) were dissolved in 30 mL of H_2O/THF (1:1). A 1M solution of L-sodium ascorbate (264 mg, 1.33 mmol) in H_2O was added to the reaction mixture, followed by the addition of $CuSO_4$ x $5H_2O$ (123 mg, 0.49 mmol). The reaction mixture was stirred at 70ºC for 24 h. The solvent was removed under vacuum, saturated NH_4Cl was added and the mixture was extracted with DCM. The raw product was purified by column chromatography (Al_2O_3, hexane:EtOAc = 30:10, then $CHCl_3$, $CHCl_3$:MeOH= 10:0.2). The product was obtained as a transparent solid (350 mg, 0.327 mmol, 44 %).

Synthesis of G_C0_I4

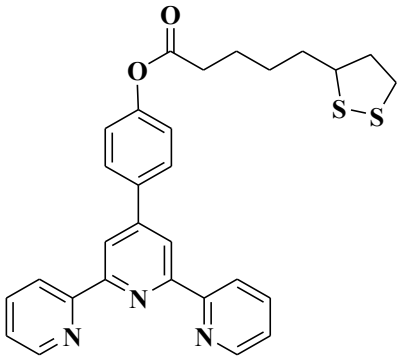

I4 (1.00 g, 3.072 mmol), **Anc_2** (0.528 g, 2.56 mmol) and DMAP (0.125 g, 1.02 mmol) were suspended in 44 mL THF/DMF mixture (10:1) and stirred under argon for 30 min. Then, DCC (0.634 g, 3.072 mmol) dissolved in 10 mL THF was added dropwise. The reaction mixture was

stirred for 7 days at r.t., then it was filtered to remove the DCU formed, washed with cold EtOAc, dried over Na_2SO_4 anhydrous, filtered and taken to dryness. The residue was then taken with EtOAc and kept in the fridge for 3 hours. Some traces of the DCU were formed, which were filtered out and the mother liquor was taken to dryness. This procedure was repeated 3 times. The pure compound was obtained by recrystallization from EtOAc/EtOH, resulting in a pale-yellow precipitate (0.890 g, 1.732 mmol, 67.6 %)

^{1}H-NMR: (300 MHz, $CDCl_3$, δ/ppm): 8.86 – 8.59 (m, 6H), 8.21 – 7.71 (m, 4H), 7.36 (dt, J = 21.7, 11.0 Hz, 2H), 7.24 (overlapped with $CDCl_3$ signal, 2H), 3.71 – 3.50 (m, 1H), 3.33 – 3.05 (m, 2H), 2.72 – 2.55 (m, 2H), 2.51 (td, J = 12.4, 6.4 Hz, 1H), 2.08 - 1.48 (m, 7H).

Synthesis of I27

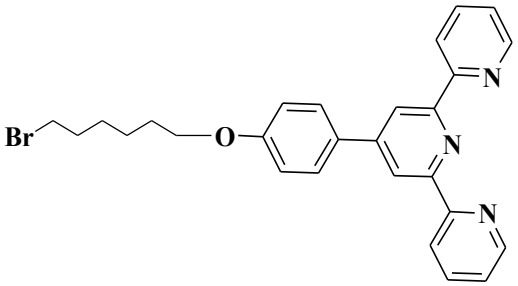

I4 (1.65 g, 5.086 mmol), 1,6-dibromohexane (12.36 g, 50.68 mmol) and K_2CO_3 (4.18 g, 0.0304 mmol) were suspended in 50 mL of DMF. The reaction mixture was stirred at 80°C, under argon, for 24 h. The reaction mixture was then cooled to room temperature, filtered over celite, then 100 mL H_2O were added and the aqueous phase was extracted with DCM (3 x 100mL). The combined organic layers were washed with H_2O (2 x 100 mL), NaCl sat. (100 mL), NH_4Cl sat. (100 mL) dried over Na_2SO_4 anhydrous. The product was recrystallized from Et_2O, resulting in a white precipitate (740 mg, 1.515 mmol, 30 %).

^{1}H-NMR: (300 MHz, $CDCl_3$, δ/ppm): 8.92 – 8.54 (m, 6H), 8.04 – 7.78 (m, 4H), 7.35 (dt, *J* = 22.3, 11.2 Hz, 2H), 7.03 (d, *J* = 8.7 Hz, 2H), 4.15 – 3.91 (m, 2H), 3.44 (dt, *J* = 9.2, 6.8 Hz, 2H), 1.89 (dt, *J* = 23.0, 6.9 Hz, 4H), 1.79 – 1.39 (m, 4H).

Synthesis of I28

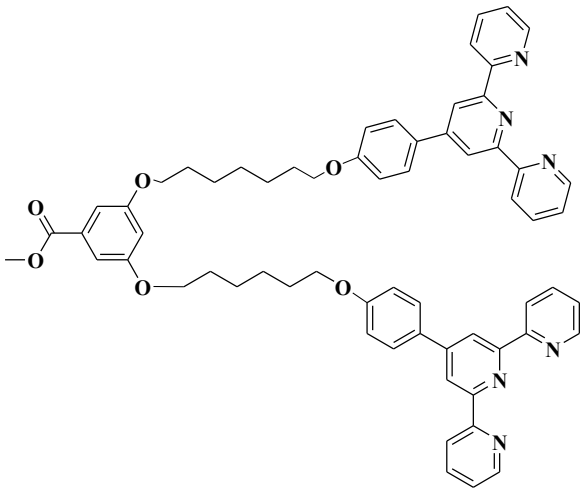

I27 (0.72 g, 1.560 mmol), 3,5-dihydroxy methyl benzoate (0.118 g, 0.709 mmol) and K_2CO_3 (1.17 g, 8.51 mmol) were suspended in 50 mL of DMF. The reaction mixture was stirred at 80ºC, under argon, for 24 h. The reaction mixture was then cooled to room temperature, filtered over celite, then 100 mL H_2O were added and the aqueous phase was extracted with DCM (3 x 100mL). The combined organic layers were washed with H_2O (2 x 100 mL), NaCl sat. (100 mL), NH_4Cl sat. (100 mL) dried over Na_2SO_4 anhydrous. The product was recrystallized from Et_2O, resulting in a white precipitate (740 mg, 1.515 mmol, 30 %).

^{1}H-NMR: (300 MHz, $CDCl_3$, δ/ppm): 8.88 – 8.59 (m, 12H), 7.89 (dd, J = 7.2, 5.0 Hz, 8H), 7.57 – 7.32 (m, 4H), 7.19 (s, 2H), 7.03 (d, *J* = 8.5 Hz, 4H), 6.67 (s, 1H), 4.24 – 3.81 (overlapped peaks, 11H), 1.73 (m, 9.5 Hz, 16H).

Synthesis of G_C0_I4_Zn

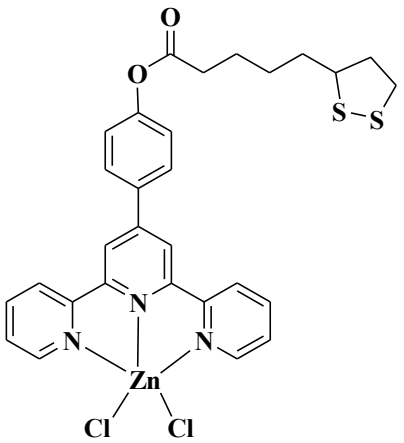

A solution of $ZnCl_2$ (0.145 g, 0.106 mmol) in 20 mL of MeOH was added dropwise to a solution of **L14** (0.300 g, 0.0884 mmol) in 20 mL $CHCl_3$. The reaction mixture was stirred for 1.5 h at r. t. A yellow precipitate was formed, which was filtered out and washed with MeOH. The precipitate was dried under vacuum to yield complex **C19** (0.379 g, 0.796 mmol, 90 %).
FT-IR (KBr, cm^{-1}): 2933($\nu_{as,(-CH2-)}$), 2866($\nu_{s,(-CH2-)}$), 1607- 1426 ($\upsilon_{C=C}$, $\upsilon_{C=N}$).

Ligand exchange between Au@OA and metallodendritic branches

The ligand exchange was realized according to a literature procedure. 5 mg oleylamine-capped Au@OA in hexanes at 5 mg/mL was added to a solution of 10 mL of DMF in which 26 mg of the replacement ligand **G0_I4_Zn** were dissolved. The reaction was stirred at room temperature. During this time a brown precipitate was formed which was filtered and washed well with DMF to remove the unreacted ligand, then with acetone. The precipitate was dried under vacuum.
FT-IR (KBr, cm^{-1}): 2933($\nu_{as,(-CH2-)}$), 2866($\nu_{s,(-CH2-)}$), 1590 - 1436 ($\upsilon_{C=C}$, $\upsilon_{C=N}$).

EDAX ZAF Quantification (Standardless):

Element	Wt %	At %	K-Ratio	Z	A	F
C K	47.72	71.13	0.1477	1.0802	0.2864	1.0001
N K	8.82	11.28	0.0096	1.0694	0.1018	1.0001
O K	10.23	11.44	0.0129	1.0595	0.1192	1.0000
Na K	3.82	2.98	0.0082	0.9883	0.2176	1.0000
Au M	28.18	2.56	0.3744	0.6924	1.9185	1.0000
Cl K	1.22	0.62	0.0045	0.9558	0.3814	1.0000
Total	100.00	100.00				

Chapter 6. Conclusions

The original contribution presents the results regarding the synthesis and characterization of TMCs based on oligopyridine ligands (*phen, bpy, bq and tpy*) having Zn(II) and Cu(I) as metal centers, which had the following outcomes:

1. **Seven N-donor ligands** were obtained, belonging to the oligopyridines class, out of which **one ligand** is new, and the other **six** were synthesized according to published procedures.
2. **Twenty one Zn(II)** and **Cu(I)** metal complexes were prepared using N-donor ligands as chelating unit, out of which **fourteen** of them are new. For these complexes the following properties were targeted: luminescence, antioxidant activity and mesomorphism.

- The new complexes **C3**, **C4** and **C5 Zn(II) c**omplexes and their corresponding ligands were tested for their antioxidant activity. Complexes **C3** and **C4** with the general formula **(N^N)ZnQCl** were found to have antioxidant activity comparable to that of the quercetin ligand, whereas complex **C5**, with the formula bqTEGZnCl_2, and its corresponding ligand **L4** did not possess this property. The high sensitivity to oxygen was related to antioxidant potency due to a direct trapping of reactive oxygen species (ROS) mechanism, thus protecting the cells against oxidative stress.
- **C6** – **C9** Cu(I) complexes with *phen* as ligand, with the formula **[(*phen*)$_2$Cu(I)]$^+$Y$^-$,** where **Y$^-$** = ClO_4^-, I^-, SCN^- and BF_4^- were evaluated for their stability. Based on ^{1}H-NMR analysis in concentrated solution and UV-Vis absorption spectroscopy in the solid state, complexes **C6** and **C9**, having non coordinating counterions ClO_4^- and BF_4^- were found to be more stable.
- Due to the higher stability of complexes **C6** and **C9**, we have chosen ClO_4^- and BF_4^- to further synthesize **C10** – **C13** Cu(I) metallomesogens with biquinoline ligands. The presence of long alkyl chains as substituents on the *bq* ligand, induced liquid crystalline behaviour on the resulting Cu(I) complexes, the type and symmetry depending on the number of the alkyl chains grafted. The dicatenar ligand **L5** induced lamello-columnar mesophases, whereas the hexacatenar **L6** ligand induced columnar hexagonal mesophases in the final complexes. Complex **C10** was included in a carbon nanofiber paste electrode and used as a sensor for glucose detection in alkaline medium.
- The **four new Zn(II) complexes C16**, **C18**, **C20** and **C22,** with the general formula **[Zn(Ln)(Gal)$_2$]**, where Ln – *tpy* derivatives, were investigated for their luminescent and mesomorphic properties. A systematic characterization of the mesophases through POM observations, DSC and SWAXS analyses revealed the temperature range of the mesophase existence and respectively the nature of the mesophases: SmA in case of **C16**, and Col_{hex} mesophase for **C18**, **C22** and a 3D-like hexagonal M_{hex} mesophase for **C20**. All of the

- complexes were found to be luminescent in solution and in the condensed states. Complex **C16** was included in a carbon nanofiber paste electrode and is currently being tested by our group as sensor for the electrochemical detection of glucose, ascorbic acid and uric acid.

3. In order to sustain our concept regarding the obtaining supramolecular architectured gold nanoparticles as carriers for a potential active coordination compound, further we have obtained AuNPs functionalized with dendritic shells that contain a *tpy* derivative, **I4**, coordinated to Zn(II) metal centres, giving **Au@GC0_I4_Zn.** The results of this work present the following outcomes:

- Au@OA capped with oleylamine with an average diameter of 6.6 nm were synthesized.
- To ensure the ligand exchange between the **Au NPs** and the dendritic units, two different anchoring units were taken into consideration: **Anc_1** and **Anc_2**.
- Various dendritic branches were obtained using 3-hydroxy-2-(hydroxymethyl)-2-methylpropanoic acid (**G_A1** and **G_A2**) or 3,5-dihydroxy methyl benzoate (**G_B1** and **G_C1**).
- Several strategies were applied to functionalize the dendritic branches with different *tpy* units, through cycloaddition reactions, esterification and/ or etherification reactions (**G_A0_L13**, **G_A1_L13, G_B0_L14, G_B1_L14, G_C0_I4 and G_C1_I4**).
- due to the higher yields and the ease of functionalization the dendritic branches with **I4** tpy derivative was further used to realize the targeted Au NPs assembly, **Au@G_C0_I4_Zn**.
- Further steps are still needed to prepare **G_C1_I4.**

Measurements of very low levels of biomolecules, including proteins and nucleic acids, remain a critical challenge in many clinical diagnostic applications due to insufficient sensitivity. Liquid crystals are known to be used as sensors for biological species.[392]

By combining the luminescent properties of TMCs, with the conformational flexibility and the nano-scale dimensions of the dendritic branches and the surface plasmon resonance of the Au NPs the targeted hybrid nanostructures are promising candidates as theranostic agents. Therefore, by controlling the delivery (Au NPs) of the active substance (TMCs based on *tpy*) a minimally invasive system with both diagnosis and therapeutic applications may be obtained. Moreover, the dosage of the active compound can be controlled through dendritic growth and therefore by the number of the *tpy* active sites. Considering the active role of platinum(II) complexes in cancer therapy, the future step in our research will refer to anchor the active species on Au NPs carriers *via* dendritic moiety in a way well proved by the works in this thesis. The advantages of this system include the avoid/reduced side effects also by controlling the concentration of active species through the degree of dendritic moiety. Preliminary studies have

been done and they refer to the platinum(II) complexes, obtaining of dendritic bridges with more branches and anchoring them on Au NPs.

References

REFERENCES

[1] B. J. Pages, D. L. Ang, E. P. Wright, J. R. Aldrich-Wright, *Dalton Trans.* **2015**,44, 3505–3526.
[2] K. J. Franz, N. Metzler-Nolte, *Chem. Rev.* **2019**, 119(2), 727–729.
[3] F. P. Dwyer, E. C. Gyarfas, W. P. Rogers, J. H. Koch, *Nature* **1952**, 170, 190–191.
[4] F. P. Dwyer, E. Mayhew, E. M. F. Roe, A. Shulman, *Br. J. Cancer* **1965**, 19, 195–199.
[5] F. P. Dwyer, I. K. Reid, A. Shulman, G. M. Laycock, S. Dixson, *Aust. J. Exp. Biol. Med. Sci.* **1969**, 47, 203–218.
[6] B. Rosenberg, L. Vancamp, J. E. Trosko, V. H. Mansour, *Nature* **1969**, 222, 385–386.
[7] B. Rosenberg, L. Van Camp, T. Krigas, *Nature* **1965**, 205(4972), 698–699.
[8] B. Rosenberg, L. Van Camp, E. B. Grimley, A. J. Thomson, *J. Biol. Chem.* **1967**, 242(6), 1347–1352.
[9] T. C. Johnstone, G. Y. Park, S. J. Lippard, *Anticancer Res.* **2014**, 34, 471–476.
[10] S. Bellemin-Laponnaz, *Eur. J. Inorg. Chem. (Special Issue)* **2020**, 1, 10–20.
[11] M. Frezza, S. Hindo, D. Chen, A. Davenport, S. Schmitt, D. Tomco, Q. Ping Dou, *Curr. Pharm. Des.* **2010**, 16(16), 1813–1825.
[12] I. Kostova, *Curr Med Chem.* **2006**, 13(9), 1085–1107.
[13] A. Bindoli, M. Pia, G. Scutari, C. Gabbiani, A. Casini, L. Messori, *Coord. Chem. Rev.* **2009**, 253, 1692–1707.
[14] V. Milacic, D. Fregona, Q.P. Dou, *Histo Histopathol.* **2008**, 23(1), 101–108.
[15] U. Kalinowska-Lis, A. Felczak, L. Checinska, I. Szabłowska-Gadomska, E. Patyna, M. Małecki, K. Lisowska, J. Ochocki, *Molecules* **2016**, 21(2), 87.
[16] K. R. Harrap, Cancer *Treat. Rev.* **1985**, 12, 21–33.
[17] A. Küng, D. B. Strickmann, M. Galanski, B. K. Keppler, *J. Inorg. Chem.* **2001**, 86, 691–698.
[18] S. Dilruba, G. V. Kalayda, *Cancer Chemother. Pharmacol.* **2016**, 77(6), 1103–1124.
[19] A. Bhargava, U. N. Vaishampayan, *Expert Opin. Invest. Drugs* **2009**, 18, 1787–1797.
[20] M. Bouché, G. Dahm, M. Wantz, S. Fournel, T. Achard, S. Bellemin-Laponnaz, *Dalton Trans.* **2016**, 45, 11362–11368.
[21] M. Bouché, A. Bonnefont, T. Achard, S. Bellemin-Laponnaz, *Dalton Trans.* **2018**, 47, 11491–11502.
[22] L. Bai, C. Gao, Q. Liu, C. Yu, Z. Zhang, L. Cai, B. Yang, Y. Qian, J. Yang, X. Lia, *Eur. J. Med. Chem.* **2017**, 140, 349–382.
[23] B. J. Pages, F. Li, P. Wormell, D. L. Ang, J. K. Clegg, C. J. Kepert, L. K. Spare, S. Danchaiwijit, J. R. Aldrich-Wright, *Dalton Trans.* **2014**, 43, 15566–15575.
[24] K. D. Mjos, C. Orvig, *Chem. Rev.* **2014**, 114, 8, 4540–4563.
[25] S. Dasari, P. B. Tchounwou, *Eur. J. Pharmacol*. **2014**, 364–378.
[26] L. Oliveira, J. M. Caquito Jr, M. S. Rocha, *Biophys. Chem.* **2018**, 241, 8–14.
[27] B. K. Keppler, M. Hartmann, *Met.-Based Drugs* **1994**, 1, 145–150.
[28] S. J. Lippard, P. J. Bond, K. C. Wu, W. R. Bauer, *Science* **1976**, 194, 726–728.
[29] S. Dhar, M. Nethaji, A. R. Chakravarty, *Inorg. Chem.* **2006**, 45, 11043–11050.
[30] A. Robertazzi, A. V. Vargiu, A. Magistrato, P. Ruggerone, P. Carloni, P. D. Hoog, J. Reedijk, *J. Phys. Chem. B* **2009**, 113, 10881–10890.
[31] K. W. Jeanette, S. J. Lippard, G. A. Vasiliades, W. R. Bauer, Proc. Natl. Acad. Sci. U. S. A., 1974, 71, 3839.
[32] V. W. R. Moraes, A. C. F. Caires, E. J. Paredes-Gamero, T. Rodrigues, *Cell Death Dis.* **2013**, 4, e658.
[33] E. Gao, L. Liu, M. Zhu, Y. Huang, F. Guan, X. Gao, M. Zhang, L. Wang, W. Zhang, Y. Sun, *Inorg. Chem.* **2011**, 50, 4732–4741;
[34] C. K. Mirabelli, R. K. Johnson, C. M. Sung, L. Faucette, K. Muirhead, S. T. Crooke, *Cancer Res.* **1985**, 45, 32–39.
[35] D. Lahiri, R. Majumdar, D. Mallick, T. K. Goswami, R. R. Dighe, A. R. Chakravarty, *J. Inorg. Biochem.* **2011**, 105, 1086–1094.
[36] E. C. Constable, C. E. Housecroft, *Coord. Chem. Rev.* 2017, 350, 84–104.
[37] A. Bencini, V. Lippolis, *Coord. Chem. Rev.* **2010**, 254, 2096–2180.
[38] H. Abrahamse, M. R. Hamblin, *Biochem J.* **2016**, 473(4), 347–364.
[39] T. Gianferrara, I. Bratsos, E. Alessio, *Dalton Trans.* **2009**, 7588 –7598.
[40] J. Lau, K.-S. Lin, F. Bénard, *Theranostics.* **2017**, 7(17), 4322–4339.
[41] J. Alzeer, B. R. Vummidi, P. J. Roth, N. W. Luedtke, *Angew. Chem. Int. Ed.* **2009**, 121, 9526-9529.

[42] Q. Zhao, C. Huang, F. Li, *Chem. Soc. Rev.* **2011**, 40, 2508–2524.
[43] K. K.-W. Lo, A. W.-T. Choi, W. H.-T. Law, *Dalton Trans.* **2012**, 41, 6021–6047.
[44] A. Vlcek, Jr., *Coord. Chem. Rev.* **1998**, 177, 219–256.
[45] S. Ranjan, S.-Y. Lin, K.-C. Hwang, Y. Chi, W.-L. Ching, C.-S. Liu, Y.-T. Tao, C.-H. Chien, S.-M. Peng, G.-H. Lee, *Inorg. Chem.* **2003**, 42, 4, 1248–1255.
[46] P. T. Chou, Y. Chi, *Chem. Eur. J.* **2007**, 13, 380–395.
[47] T. Sano, Y. Nishio, Y. Hamada, H. Takahashi, T. Usukia, K. Shibataa, *J. Mater. Chem.* **2000**, 10, 157–161.
[48] V. W. W. Yam, W. K. Lee, T. F. Lai, *J. Chem. Soc., Chem. Commun.* **1993**, 1571–1573.
[49] V. W. W. Yam, K. K. W. Lo, K. K. Cheung, *Inorg. Chem.* **1996**, 35, 3459–3462.
[50] A. Vogler, H. Kunkely, *Comments Inorg. Chem.,* **1990**, 9, 201–220.
[51] V. W.-W. Yam, K. M.-C. Wong, N. Zhu, *J. Am. Chem. Soc.* **2002**, 124, 6506–6507.
[52] J. Shum, P. K.-K. Leung, K. K.-W. Lo, *Inorg. Chem.* **2019**, 58(4), 2231–2247.
[53] V. Fernández-Moreira, F.L. Thorp-Greenwood, M.P. Coogan, *Chem. Commun.* **2010**, 46, 186–202.
[54] S.-K. Leung, H.-W. Liu, K. K.-W. Lo*, Chem. Commun.* **2011**, 47, 10548–10550.
[55] E. Baggaley, J. A. Weinstein, J. A. Williams, *Coord. Chem. Rev.* **2012**, 256, 1762–1785.
[56] F. L. Thorp-Greenwood, R.G. Balasingham, M. Coogan, *J. Organomet. Chem.* **2012**, 714, 12–21.
[57] E. Cavero, S. Uriel, P. Romero, J. L. Serrano, R. Gimenez*, J. Am. Chem. Soc.* **2007**,129, 11608–11618.
[58] F. Neve, *Adv. Mater.* **1996**, 8, 277–289.
[59] B. Donnio, D. W. Bruce, "Metallomesogens" in Liquid Crystals II, edit. by D. M. P. Mingos, Springer, Berlin, **1999**.
[60] J. L. Serrano, "Metallomesogens: Synthesis, Properties, and Applications", edit. by J. L. Serrano, VCH, Weinheim, **1996**, 1–20.
[61] A. Crispini, M. Ghedini, D. Pucci, *Beilstein J. Org. Chem.* **2009**, 5(54), doi:10.3762/bjoc.5.54.
[62] J. M. Lehn, *Supramolecular Chemistry : Concepts and Perspectives*, VCH, Weiheim, 1995 ; E.C. Constable, Metals and Ligand Reactivity : An Introduction to Organic Chemistry of Metal Complexes, VCH, Weinheim, **1995**.
[63] C. Tschierske, *Angew. Chem. Int. Ed.* **2000**, 39, 2454-2458.
[64] B. Donnio, *Curr. Op. Coll. Interface Sci.* **2002**, 7, 371-394.
[65] D. Pucci, G. Barberio, A. Crispini, M. Ghedini, O. Francescangeli, *Mol. Cryst. Liq. Cryst.* **2003**, 395, 325–335.
[66] D. Pucci, G. Barberio, A. Crispini, O. Francescangeli, M. Ghedini, M. La Deda, *Eur. J. Inorg. Chem.* **2003**, 2003, 3649–3661.
[67] S.-Y. Chou, C.-J. Chen, S.-L. Tsai, H.-S. Sheu, G.-H. Lee and C. K. Lai, *Tetrahedron* **2009**, 65, 113.
[68] D. Pucci, G. Barberio, A. Bellusci, A. Crispini, M. Ghedini, E. I. Szerb, *Mol. Cryst. Liq. Cryst.* **2005**, 441, 251–260.
[69] D. W. Bruce, *Acc. Chem. Res.* **2000**, 33, 831–840.
[70] C. E. Conn, V. Panchagnula, A. Weerawardena, L. J. Waddington, D. F. Kennedy, C. J. Drummond, *Langmuir* **2010**, 26(9), 6240-6249.
[71] D. Septiadi, A. Aliprandi, M. Mauro, L. De Cola, *RSC Adv.* **2014**, 4, 25709-25718.
[72] A. Colombo, F. Fiorini, D. Septiadi, C. Dragonetti, F. Nisic, A. Valore, D. Roberto, M. Mauro, L. De Cola, *Dalton Trans.* **2015**,44, 8478-8487.
[73] M. Çamur, M. Durmus, M. Bulut, *Polyhedron* **2012**, 41, 92–103.
[74] M. Sandroni, M. Kayanuma, M. Rebarz, H. Akdas-Kilig, Y. Pellegrin, E. Blart, H. Le Bozec, C. Daniel, F. Odobel, *Dalton Trans.* **2013**, 42, 14628–14638.
[75] M. Mauro, A. Aliprandi, D. Septiadi, N. Seda Kehr, L. De Cola, *Chem. Soc. Rev.* **2014**, 43, 4144-4166.
[76] N. Armaroli, G. Accorsi, F. Cardinali, A. Listorti, *Top. Curr. Chem.* **2007***,* 280, 69–115.
[77] S. Xu, S. Gozem, A. I. Krylov, C. R. Christopherc, J. M. Weber, *Phys. Chem. Chem. Phys.* **2015**, 17, 31938-31946.
[78] G. Mani, V. Subramaniyan, "Homoleptic and heteroleptic copper(I) complexes bearing diimine-diphosphine ligands" in Copper(I) Chemistry of Phosphines, Functionalized Phosphines and Phosphorus Heterocycles, 1st ed., edit. by M. Balakrishna, Elsevier, **2019**, 237–258.

[79] R. R. Conry, K. D. Karlin " Encyclopedia of Inorganic Chemistry" in Copper: Inorganic & Coordination Chemistry, 1st ed., edit. by R. B. King, R. H. Crabtree, C. M. Lukehart, D. A. Atwood, R. A. Scott, **2006**, John Wiley & Sons, Ltd, 1-19.
[80] L. X. Chen, G. B. Shaw, I. Novozhilova, T. Liu, G. Jennings, K. Attenkofer, G. J. Meyer, P. Coppens, *J. Am. Chem. Soc.* **2003,** 125, 7022-7034.
[81] M. T. Buckner, T. G. Matthews, F. E. Lytle, D. R. McMillin, *J. Am. Chem. Soc.* **1979**, 101, 5846–5848.
[82] S. M. Kuang, D. G. Cuttell, D. R. McMillin, P. E. Fanwick, R. A. Walton, *Inorg. Chem.* **2002**, 41, 3313–3322.
[83] A. Kaeser, M. Mohankumar, J. Mohanraj, F. Monti, M. Holler, J. Cid, O. Moudam, I. Nierengarten, L. Karmazin-Brelot, C. Duhayon, B. Delavaux-Nicot, N. Armaroli, J. Nierengarten, *Inorg. Chem.* **2013**, 52, 12140–12151.
[84] M. Alkan-Zambada, X. Hu, *Organometallics* **2018**, 37 (21), 3928-3935.
[85] M. Porchia, F. Tisato, M. Zancato, V. Gandin, C. Marzano, *Arab. J. Chem.* **2020**, 13(1), 998-1010.
[86] N. Alvarez, M. G. Kramer, J. Ellena, A. Costa-Filho, M. H Torre, G. Facchin, *Cancer Rep. Rev.* **2018**, 2(4).
[87] L. D. Williams, J. Thivierge, I. H. Goldberg, *Nucleic Acids Res.* **1988**, 16, 11607-11615.
[88] J. M. Veal, R. L Rill, *Biochemistry* **1989**, 28, 3243-3250
[89] D. S. Sigman, R. Landgraf, D. M. Perrin, L. Pearson, *Met. Ions Biol. Syst*. **1996**, 33, 485-513.
[90] J. M. Veal, R. L. Rill, *Biochemistry* **1991**, 30, 1132–1140.
[91] S. Basak, V. Nagaraja, *Nucleic Acids Res* **2001**, 29, e105–e105.
[92] D. S. Sigman, *Acc. Chem. Res.* **1986**, 19, 180-186.
[93] A. Mohindru, J. M. Fisher, M. Rabinovitz, *Biochem. Pharmacal.,* **1983***, 32,* 3627-3632.
[94] A. Mazumder, M. Gupta, D. M. Perrin, D. S. Sigman, M. Rabinovitz, Y. Pommier, *AIDS Res. Hum. Retrovirus* **1995**, 11 , 115-125.
[95] B. F. Ali, K. Al-Sou'od, N. Al-Ja'ar, A. Nassar, M. H. Zaghal, Z. Judeh, R. Al-Far, M. Al-Refai, M. Ibrahim, K. Mansi, K. H. Al-Obaidi, *J. Coord. Chem.* **2006**, 59, 229-241.
[96] R. Starosta, A. Bykowska, A. Kyzioł, M. Płotek, M. Florek, J. Król, M. Jeżowska-Bojczuk, *Chem. Biol. Drug. Des.* **2013**, 82, 579–586.
[97] R. Starosta, M. Florek, J. Król, M. Puchalska, A. Kochel, *New J. Chem.* **2010**, 34, 1441–1449.
[98] M. Plotek, K. Dudek, A. Kyziol, *Chemik* **2013**, 67(12), 1181–1190.
[99] U. K. Komarnicka, R. Starosta, A. Kyzioł, M. Jeżowska-Bojczuk, *Dalton Trans.* **2015**, 44, 12688–12699.
[100] V. Gandin, A. Trenti, M. Porchia, F. Tisato, M. Giorgetti, I. Zanusso, L. Trevisi, C. Marzano, *Metallomics* **2015**, 7, 1497–1507.
[101] D. Varna, A. G. Hatzidimitriou, E. Velali, A. A. Pantazaki, A. Aslanidis, *Polyhedron* **2015**, 88, 40–47.
[102] B. Maity, M. Roy, B. Banik, R. Majumdar, R. R. Dighe, A. R. Chakravarty, *Organometallics* **2010**, 29, 3632–3641.
[103] S. S. Bhat, V. K. Revankar, V. Kumbar, K. Bhat, V. A. Kawade, *Acta Crystallogr. C* **2018**, 74, 146–151.
[104] A. Kellett, O. Howe, M. O'Connor, M. McCann, B. S. Creaven, S. McClean, A. Foltyn-Arfa Kia, A. Casey, M. Devereux, *Free Radic. Biol. Med.* **2012**, 53, 564–576.
[105] J. D. Ranford, P. J. Sadler, D. A. Tocher, *J. Chem. Soc., Dalton Trans.,* **1993**, 3393–3399.
[106] M. A. Zoroddu, S. Zanetti, R. Pogni, R. Basosi, *J. Inorg. Biochem.* **1996**, 63, 291-300.
[107] D. K. Saha, U. Sandbhor, K. Shirisha, S. Padhye, D. Deobagkar, C. E. Anson, A. K. Powell, *Bioorg. Med. Chem. Lett.* **2004**, 14, 3027–3032.
[108] S. Kashanian, M. M. Khodaei, H. Roshanfekr, N. Shahabadi, A. Rezvani, G. Mansouri, *DNA and cell biol.* **2011**, 30(5), 287–296.
[109] M. Devereux, D. O'Shea, M. O'Connor, H. Grehan, G. Connor, M. McCann, G. Rosair, F. Lyng, A. Kellett, M. Walsh, D. Egan, B. Thati, *Polyhedron* **2007**, 26, 4073–4084.
[110] M. W. Blaskie, D. R. McMillin*, Inorg. Chem.* **1980**, 19, 3519–3522.
[111] C. O Dietrich-Buchecker, P.A Marnot, J. P Sauvage,J. R Kirchhoff, D. R. McMillin*, Chem. Soc., Chem. Commun.* **1983**, 513–515.
[112] M. K. Eggleston, D. R. McMillin, K. S. Koenig, A. J. Pallenberg, *Inorg. Chem.* **1997**, 36, 172–176.
[113] M. T. Miller, P. K. Gantzel, T. B. Karpishin, *Inorg. Chem.* **1999**, 38, 3414–3422.
[114] S. Sakaki, T. Kuroki, T. Hamada*, J. Chem. Soc., Dalton Trans.* **2002**, 6, 840–842.
[115] M. Pirtsch, S. Paria, T. Matsuno, H. Isobe, O. Reiser, *Chem. Eur. J.* **2012**, 18, 7336–7340.
[116] L. N. Ashbrook, C. M. Elliott*, J. Phys. Chem. C* **2013**, 117, 3853−3864.

[117] M. Iliş, V. Cîrcu, *J. Chem.* **2018**, 2018, Article ID 7943763, 10 pages.
[118] A. El-Ghayoury, L. Douce, A. Skoulios, R. Ziessel, *Angew. Chem., Int. Ed. Engl.* **1998**, 37, 2205−2208.
[119] R. Ziessel, L. Douce, A. El-Ghayoury, A. Harriman, A. Skoulios, *Angew. Chem., Int. Ed.* **2000**, 39, 1489−1493.
[120] R. Ziessel, G. Pickaert, F. Camerel, B. Donnio, D. Guillon, M. Cesario, T. Prangeé, *J. Am. Chem. Soc.* **2004**, 126, 39, 12403-12413.
[121] E. D. Baranoff, J. Voignier, T. Yasuda, V. Heitz, J.-P. Sauvage, T. Kato, *Angew. Chem., Int. Ed.* **2007**, 46, 4680−4683.
[122] C. R. Hammond," The elements" in Handbook of Chemistry and Physics, 87th ed., edit. by D. R. Lide, CRC Press, Taylor & Francis Group., Boca Raton, Florida, **2006**, 4-1 – 4-42
[123] J. Tang, H.-Y. Yin, J.-L. Zhang, "Luminescent Zinc Complexes as Bioprobes for Imaging Molecular Events in Live Cells" in Inorganic and Organometallic Transition Metal Complexes with Biological Molecules and Living Cells, edit. by K. K.-W. Lo, Academic Press, **2017**, 1–53.
[124] A. Krężel, W. Maret, *Arch. Biochem. Biophys.* **2016**, 611, 3–19.
[125] M. Weil, *Crystals* **2017**, 7(11), 340.
[126] E. C. Constable," The Coordination Chemistry of 2,2′:6′,2″-Terpyridine and Higher Oligopyridines" in Advances in Inorganic Chemistry, edit. by H. J. Emeléus, vol. 30, Elsevier, **1986**, 69–121.
[127] X. Bi, Y. Pang, *J. Phys. Chem. B* **2016**, 120, 3311–3317.
[128] J. Li, R. Liu, J. Jiang, X. Liang, L. Huang, G. Huang, H. Chen, L. Pan, Z. Ma, *Molecules* **2019**, 24, 4519.
[129] D. Zare, A. Prescimone, E. C. Constable, C. E. Housecroft, *Crystals* **2018**, 8, 461.
[130] N. Roohani, R. Hurrell, R. Kelishadi, R. Schulin, *J. Res. Med. Sci.* **2013**, 18, 144–157.
[131] A. Tarushi, J. Kljun, I. Turel, A. A. Pantazaki, G. Psomas, D. P. Kessissoglou, *New J. Chem.* **2013**, 37, 342–355.
[132] Y. Yoshikawa, H. Yasui, *Curr. Top. Med. Chem.* **2012**, 12, 210–218.
[133] D. Pucci, A. Crispini, B. Sanz Mendiguchía, S. Pirillo, M. Ghedini, S. Morelli, L. D. Bartolo, *Dalton Trans.* **2013**, 42, 9679–9687.
[134] B. Sanz Mendiguchia, I. Aiello, A. Crispini, *Dalton Trans.* **2015**, 44, 9321–9334.
[135] G. K. Walkup, S. C. Burdette; S. J. Lippard, R. Y. Tsien, *J. Am. Chem. Soc.* **2000**, 122(23), 5644–5645.
[136] F. Chioma, A. C. Ekennia, A. A. Osowole, S. N. Okafor, C. U. Ibeji, D. C. Onwudiwe, O. T. Ujam, *Open Chem.* **2018**, 16, 184–200.
[137] M. Darawsheh, H. Abu Ali, A. L. Abuhijleh, E. Rappocciolo, M. Akkawi, S. Jaber, S. Maloul, Y. Hussein, *Eur. J. Med. Chem.* **2014**, 82, 152–163.
[138] Y. Zhu, X. Xiong, Z. Suo, P. Tang, Q. Sun, X. Ding, H. Li, *Inorg. Chem. Commun.* **2019**, 103, 6–11.
[139] T. K. Rundstadler, A. Eskandari, S. M. Norman, K. Suntharalingam, *Molecules* **2018**, 23, 2253.
[140] H. K. Sandhar, B. Kumar, S. Prasher, P. Tiwari, M. Salhan, P. Sharm, *Internationale Pharmaceutica Sciencia* **2011**, 1(1), 25-41.
[141] Y. Song, J. Kang, J. Zhou, Z. Wang, X. Lu, L. Wang, J. Gao, *Spectrochim. Acta Part A* **2000**, 56, 2491–2497.
[142] Y. Li, Z.-Y. Yang, M.-F. Wang, *J. Fluoresc.* **2010**, 20, 891–905.
[143] Y. Li, Z.-Y. Yang, T.-R. Li, *Chem. Pharm. Bull.* **2008**, 56, 1528–1534.
[144] Y. Li, Z.-Y. Yang, T.-R. Li, *Transit. Metal. Chem*. **2006**, 31, 470–474.
[145] R. F. V. de Souza, W. F. De Giovani, *Redox Report.* **2004**, 9, 97–104.
[146] V. Uivarosi, M. Badea, R. Olar, C. Draghici, S. F. Barbuceanu, *Molecules* **2013**, 18, 7631
[147] M. Yamane, Y. Adachi, Y. Yoshikawa, H. Sakurai, *Chem. Lett.* **2005**, 34, 1694–1695.
[148] Y. Naito, Y. Yoshikawa, K. Yoshizawa, A. Takenouchi, H. Yasui, *In Vivo* **2017**, 31, 1145–1151.
[149] M. I. Khalil, A. M. AL-Zahem, M. M. Qunaibit, *Med. Chem. Res.* **2014**, 23, 1683-1689.
[150] H. Venkatachalam, B. S. Jayashree, S. Nigam, *Indian J. Pharm. Sci.* **2017**, 79, 838–844.
[151] P. F. Liguori, A. Valentini, M. Palma, A. Bellusci, S. Bernardini, M. Ghedini, M. L. Panno, C. Pettinari, F. Marchetti, A. Crispini, D. Pucci, *Dalton Trans.* **2010**, 39, 4205–4212.
[152] Q. Wang, M. Huang, Y. Huang, J.-S. Zhang, G.-F. Zhou, R.-Q. Zeng, X.-B. Yang, *Med. Chem. Res.* **2014**, 23, 2659–2666.
[153] S. Vimalraj, S. Rajalakshmi, S. Saravanan, D. Raj Preeth, R. L.A Vasanthi, M. Shairam, S. Chatterjee, *Colloids Surf. B Biointerfaces* **2018**, 167, 134–143.
[154] Z. Naseri, A. Nemati Kharat, A. Banavand, A. Bakhoda, S. Foroutannejad, *Polyhedron* **2012**, 33 (1), 396-403.

[155] S. Wang, W. Chu, Y. Wang, S. Liu, J. Zhang, S. Li, H. Wie, G. Zhou, X. Qin, *Appl. Organomet. Chem.* **2013**, 27, 373–379.
[156] K. Malarz, D. Zych, M. Kuczak, R. Musiol, A. Mrozek-Wilczkiewicz, *Eur. J. Med. Chem.* **2020**, 189, 112039.
[157] E. D. Baranoff, J.-P. Collin, L. Flamigni, J.-P. Sauvage, *Chem. Soc. Rev.* **2004**, 33(3), 147–155.
[158] Z. Ma, W. Lu, B. Liang, A. J. L. Pombeiro, *New J. Chem.* **2013**, 37, 1529–1537.
[159] W.-J. Wu, H.-X. Huang, M. Chen, D.-J. Qian, *Chin. Chem. Lett.* **2015**, 26, 343–347.
[160] T. Tsukamoto, R. Aoki, R. Sakamoto, R. Toyoda, M. Shimada, Y. Hattori, M. Asaoka, Y. Kitagawa, E. Nishibori, M. Nakano, H. Nishihara, *Chem. Commun.* **2017**, 53, 3657–3660.
[161] Y. Zhang, Y. Yang, S. Zhou, Z. Ma, Inorg. *Nano-Met. Chem.* **2017**, 47, 876–880.
[162] Y. Ma, P. She, K. Y. Zhang, H. Yang, Y. Qin, Z. Xu, S. Liu, Q. Zhao, W. Huang, *Nat. Commun.* **2018**, 9, 3.
[163] T. Tsukamoto, K. Takada, R. Sakamoto, R. Matsuoka, R. Toyoda, H. Maeda, T. Yagi, M. Nishikawa, N. Shinjo, S. Amano, T. Iokawa, N. Ishibashi, T. Oi, K. Kanayama, R. Kinugawa, Y. Koda, T. Komura, S. Nakajima, R. Fukuyama, N. Fuse, M. Mizui, M. Miyasaki, Y. Yamashita, K. Yamada, W. Zhang, R. Han, W. Liu, T. Tsubomura, H. Nishihara, *J. Am. Chem. Soc.* **2017**, 139, 5359–5366.
[164] Z. Zhang, M. Zhang, X. Li, K. Li, X. Lü, Y. Wang, X. Zhu, *ACS Sustainable Chem. Eng*. **2018**, 6, 11614–11623.
[165] P. D. Vellis, J. A. Mikroyannidis, C.-N. Lo, C.-S. Hsu*, J. Polym. Sci. A Polym. Chem.* **2008**, 46, 7702–7712.
[166] E. Selimović, T. Soldatović*, Prog. React. Kinet. Mec.* **2019**, 44, 105–113.
[167] S. M. Brombosz, A. J. Zucchero, R. L. Phillips, D. Vazquez, A. Wilson, U. H. F. Bunz, *Org. Lett.* **2007**, 9, 4519–4522.
[168] P. Zhou, L. Huang, Y. Zhang, X. Xue, Y. Zhou, Z. Ma, *J. Photochem. Photobiol. A 2018,* 358, 17–25.
[169] V. M. Manikandamathavan, T. Weyhermüller, R. P. Parameswari, M. Sathishkumar, V. Subramanian, B. U. Nair, *Dalton Trans.* **2014**, 43, 13018- 13031.
[170] Z. Hai, Y. Bao, Q. Miao, X. Yi, G. Liang, *Anal. Chem.* **2015**, 87, 2678–2684.
[171] W.-W. Fu, D. Peng, Y.-Q. Li, J.-R. Shen, S.-H. Li, *Z. Naturforsch. B* **2017**, 72, 687–695.
[172] L. Huang, R. Liu, J. Li, X. Liang, Q. Lan, X. Shi, L. Pan, H. Chen, Z. Ma, *J. Inorg. Biochem.* **2019**, 201, 110790.
[173] W. Chu, Y. Wang, S. Liu, X. Yang, S. Wang, S. Li, G. Zhou, X. Qin, C. Zhou, J. Zhang, *Bioorg. Med. Chem. Lett.* **2013**, 23, 5187–5191.
[174] Z. Ma, Y. Q. Cao, Q. S. Li, M. F. C. G. Silva, J. J. R. F. Silva, A. J. L. Pombeiro, *J. Inorg. Biochem.* **2010**, 104, 704-711.
[175] J. Jiang, J. Li, C. Liu, R. Liu, X. Liang, Y. Zhou, L. Pan, H. Chen, Z. Ma, *J. Biol. Inorg. Chem.* **2020**, 25, 311–324.
[176] A. Barbieri, G. Accorsi, N. Armaroli, *Chem. Commun.* **2008**, 2185–2193.
[177] S. Das, A. Jana, V. Ramanathan, T. Chakraborty, S. Ghosh, P. K. Das and P. K. Bharadwaj, *J. Organomet. Chem.* **2006**, 691, 2512–2516.
[178] V. Aubert, V. Guerchais, E. Ishow, K. Hoang-Thi, I. Ledoux, K. Nakatani, H. Le Bozec, *Angew. Chem.* **2008**, 120, 587–590.
[179] D. Roberto, F. Tessore, R. Ugo, S. Bruni, A. Manfredi, S. Quici, *Chem. Commun*. **2002**, 846–847.
[180] F. Tessore, D. Roberto, R. Ugo, M. Pizzotti, S. Quici, M. Cavazzini, S. Bruni, F. De Angelis, *Inorg. Chem.* **2005**, 44, 8967–8978.
[181] V. W.-W. Yam, K. K.-W. Lo, *Chem. Soc. Rev.* **1999**, 28, 323–334.
[182] A. Ojida, T. Sakamoto, M. Inoue, S. Fujishima, G. Lippens, I. Hamachi, *J. Am. Chem. Soc.* **2009**, 131, 6543–6548.
[183] A. Ojida, Y. Mito-Oka, M. Inoue, I. Hamachi, *J. Am. Chem. Soc.* **2002**, 124, 6256–6258.
[184] Y. Kurishita, T. Kohira, A. Ojida, I. Hamachi, *J. Am. Chem. Soc.* **2012**, 134, 18779–18789.
[185] D. Oltmanns, S. Zitzmann-Kolbe, A. Mueller, U. Bauder-Wuest, M. Schaefer, M. Eder, U. Haberkorn, M. Eisenhut, *Bioconjugate Chem.* **2011**, 22, 2611–2624.
[186] B. A. Smith, S. T. Gammon, S. Xiao, W. Wang, S. Chapman, R. McDermott, M. A. Suckow, J. R. Johnson, D. Piwnica-Worms, G. W. Gokel, B. D. Smith, W. M. Leevy, *Mol. Pharm.* **2011**, 8, 583–590.
[187] D. Li, Q. Zhang, P. Wang, J. Wu, Y. Kan, Y. Tian, H. Zhou, J. Yang, X. Tao, M. Jiang, *Dalton Trans.* **2011**, 40, 8170 - 8178.
[188] X. Tian, S. Hussain, C. de Pace, L. Ruiz-Pérez, G. Battaglia, *Chem. Asian J.* **2019**, 14, 509–526.

[189] A. Gil, M. Melle-Franco, V. Branchadell, M. J. Calhorda, *J. Chem. Theory Comput.* **2015**, 11, 2714–2728.
[190] M. Cusumano, A. Giannetto, *J. Inorg. Biochem.* **1997**, 65, 137– 144.
[191] D. Pucci, T. Bellini, A. Crispini, I. D'Agnano, P. F. Liguori, P. Garcia-Orduña, S. Pirillo, A. Valentini, G. Zanchetta, *Med. Chem. Commun.* **2012**, 3(4), 462-468.
[192] L. Ricciardi, D. Pucci, S. Pirillo, M. La Deda, *J. Lumin.* **2014**, 151, 138–142.
[193] C. Kong, M. Peng, H. Shen, Y. Wang, Q. Zhang, H. Wang, J. Zhang, H. Zhou, J. Yang, J. Wu, Y. Tian, *Dyes Pigm.* **2015**, 120, 328–334.
[194] L. J. Liang, X. J. Zhao, C. Z. Huang, *Analyst* **2012**, 137, 953–958.
[195] M. Kong, Y. Liu, H. Wang, J. Luo, D. Li, S. Zhang, S. Li, J. Wu and Y. Tian, *Spectrochim. Acta A* **2015**, 135, 521–528.
[196] P. Das, A. Ghosh, M. K. Kesharwani, V. Ramu, B. Ganguly, A. Das, *Eur. J. Inorg. Chem.* **2011**, 3050–3058.
[197] Y. Tang, M. Kong, X. Tian, J. Wang, Q. Xie, A. Wang, Q. Zhang, H. Zhou, J. Wu, Y. Tian, *J. Mater. Chem. B* **2017**, 5, 6348–6355.
[198] X. Liang, J. Jiang, X. Xue, L. Huang, X. Ding, D. Nong, H. Chen, L. Pan, Z. Ma, *Dalton Trans.* **2019**, 48, 10488–10504.
[199] Y. Pan, Y. Yan, Y. Li, X.-W. Gao, D. Chao, *New J. Chem.* **2019**, 43, 15120–15125.
[200] A. Winter, C. Friebe, M. Chiper, M. D. Hager, U. S. Schubert, *J. Polym. Sci. A Polym. Chem.* 2009, **47**, 4083–4098.
[201] Q. Zhang, X. Tian, Z. Hu, C. Brommesson, J. Wu, H. Zhou, S. Li, J. Yang, Z. Sun, Y. Tian, K. Uvdal, *J. Mater. Chem. B* **2015**, 3, 7213-7221.
[202] S. Righetto, S. Rondena, D. Locatelli, D. Roberto, F. Tessore, R. Ugo, S. Quici, S. Roma, D. Korystov, V. I. Srdanov, *J. Mater. Chem.* **2006**, 16, 1439.
[203] P. Shi, Q. Jiang, X. Zhao, Q. Zhang, Y. Tian, *Dalton Trans*. **2015**, 44, 8041–8048.
[204] Z. Feng, D. Li, M. Zhang, T. Shao, Y. Shen, X. Tian, Q. Zhang, S. Li, J. Wu, Y. Tian, *Chem. Sci.* **2019**, 10, 7228–7232.
[205] C. Cuerva, P. Ovejero, J. A. Campo, M. Cano, *New J. Chem.* **2014**, 38, 511–517.
[206] G. Barberio, A. Bellusci, A. Crispini, M. Ghedini, A. Golemme, P. Prus, D. Pucci, *Eur. J. Inorg. Chem.* **2005**, 181–188.
[207] D. Pucci, A. Crispini, M. Ghedini, M. La Deda, P.F. Liguori, C. Pettinari, E.I. Szerb, *RSC Adv.* **2012**, 2, 9071–9078.
[208] N. S. Saleesh Kumar, M. Z. Shafikov, A. C. Whitwood, B. Donnio, P. B. Karadakov, V. N. Kozhevnikov, D. W. Bruce, *Chem. Eur. J.* **2016**, 22(24), 8215–8233.
[209] S. Medici, M. Peana, V. M. Nurchi, J. I. Lachowicz, G. Crisponi, M. A, Zoroddu, *Coord. Chem. Rev.* **2015**, 284, 329–350.
[210] M. Azharuddin, G. H. Zhu, D. Das, E. Ozgur, L. Uzun, A. P. F. Turner, H. K. Patra, *Chem. Commun.* **2019**, 55, 6964–6996.
[211] C. I. Yeo, K. K. Ooi, E. R. T. Tiekink, *Molecules* **2018**, 23, 1410.
[212] S. P. Fricker, *Gold Bull.* **1996**, 29(2), 53-60.
[213] M. F. Hornos Carneiro, F. Barbosa, Jr, *J. Toxicol. Environ. Health. B Crit. Rev.* **2016**, 19 (3-4), 129–148.
[214] N. Elahi, M. Kamali, M. H. Baghersad, *Talanta* **2018**, 184, 537–556.
[215] R. Sardar, J. S. Shumaker-Parry, *J. Am. Chem. Soc.* **2011**, 133(21), 8179–8190.
[216] K. Saha, S. S. Agasti, C. Kim, X. Li, V. M. Rotello, *Chem. Rev.* **2012**, 112(5), 2739–2779.
[217] K. Alaqad, T. A. Saleh, *J. Environ. Anal. Toxicol*. **2016**, 6, 4, DOI:10.4172/2161-0525.1000384.
[218] B. S. Kim, Y.-T. Chen, P. Srinoi, M. D. Marquez, T. R. Lee, *IJMS* **2019**, 20, 3422.
[219] O. B. Knights, S. Ye, N. Ingram, S. Freear, J. R. McLaughlan, *Nanoscale Adv.* **2019**, 1, 1472–1481.
[220] C. Noguez, I. L. Garzón, *Chem. Soc. Rev*. **2009**, 38, 757–771.
[221] W. Niu, Y. A. A. Chua, W. Zhang, H. Huang, X. Lu, *J. Am. Chem. Soc.* **2015**, 137, 10460–10463.
[222] W. Cai, T. Gao, H. Hong, J. Sun, *Nanotechnol. Sci. Appl.* **2008**, 1, 17–32.
[223] J. Turkevich, P. C. Stevenson, J. Hillier, *Discuss. Faraday Soc.* **1951**, 11, 55−75.
[224] M. Brust, M. Walker, D. Bethell, D. J. Schiffrin, R. Whyman, *Chem. Commun.* **1994**, 801−802.
[225] A. J. Mieszawska, W. J. Mulder, Z. A Fayad, D. P. Cormode, *Mol Pharm.* **2013**, 10(3), 831–847.
[226] Z. Yang, Z. Li, X. Lu, F. He, X. Zhu, Y. Ma, R. He, F. Gao, W. Ni, Y. Yi, *Nano-Micro Lett.* **2017**, 9, 6.
[227]A. M. Craciun, M. Focsan, K. Magyari, A. Vulpoi, Z. Pap, *Materials* **2017**, 10(7), 836.

[228] K. A. Kang, J. Wang, J. B. Jasinski, S. Achilefu, *J. Nanobiotechnology* **2011**, 9, 16.
[229] S. Eustis, M. A. El-Sayed, *Chem. Soc. Rev.* **2006**, 35, 209–217.
[230] C. Rizal, V. Belotelov, D. Ignatyeva, A. K. Zvezdin, S. Pisana, *Condensed Matter.* **2019**, 4, 50.
[231] J. Olson, S. Dominguez-Medina, A. Hoggard, L.-Y. Wang, W.-S. Chang, S. Link, *Chem. Soc. Rev.* **2015**, 44, 40–57.
[232] M. A. K. Abdelhalim, M. M. Mady, *J. Nanomedic. Nanotechnol*. **2012**, 3(3), 1000133.
[233] Y. C. Yeh, B. Creran, V. M. Rotello, *Nanoscale* **2012**, 4(6), 1871–1880.
[234] A. A. Bogdanov Jr., S. Gupta, N. Koshkina, S. J. Corr, S. Zhang, S. A. Curley, G. Han, *Bioconjug. Chem.* **2015**, 26(1), 39–50.
[235] H. Deng, Y. Zhong, M. Du, Q. Liu, Z. Fan, F. Dai, X. Zhang, *Theranostics* **2014**, 4(9), 904–918.
[236] X. Wu, Y. Gao, C. -M. Dong, *RSC Adv.* **2015**, 5, 13787–13796.
[237] Z. Zhang, L. Wang, J. Wang, X. Jiang, X. Li, Z. Hu, Y. Ji, X. Wu, C. Chen, *Adv. Mater.* **2012**, 24, 1418–1423.
[238] S. Akhter, M. Z. Ahmad, F. J. Ahmad, G. Storm, R. J. Kok, *Expert Opin. Drug Deliv.* **2012**, 9, 1225–1243.
[239] Z. Skeete, H. Cheng, E. Crew, L. Lin, W. Zhao, P. Joseph, S. Shan, H. Cronk, J. Luo, Y. Li, Q. Zhang, C. -J. Zhong, *ACS Appl. Mater. Interfaces* **2014**, 6, 21752–21768.
[240] M. Chen, S. Tang, Z. Guo, X. Wang, S. Mo, X. Huang, G. Liu, N. Zheng, *Adv. Mater.* **2014**, 26(48), 8210–8216.
[241] H. Daraee, A. Eatemadi, E. Abbasi, S. F. Aval, M. Kouhi, A. Akbarzadeh, *Artif. Cells Nanomed. Biotechnol.* **2016**, 44, 410–422.
[242] N. Elahi, M. Kamali, M. H. Baghersad, *Talanta* **2018**, 184, 537–556.
[243] T. B. Norsten, B. L. Frankamp, V. M. Rotello, *Nano Lett.* 2002, 2(12), 1345–348.
[244] M. Montalti, L. Prodi, N. Zaccheroni, M. Beltrame, T. Morottib, S. Quicib, *New J. Chem.* **2007**, 31, 102–108.
[245] H. Fang, C. Du, S. Qu, Y. Li, Y. Song, H. Li, H. Liu, D. Zhu, *Chem. Phys. Lett.*, 2002, **364**, 290–296.
[246] Y. Nishimori, K. Kanaizuka, M. Murata, H. Nishihara, *Chem. Asian J.* **2007**, 2, 367– 376.
[247] D. Hobara, S. Kondo, M.-S. Choi, Y. Ishioka, S. Hirata, M. Murata, K. Azuma, J. Kasahara, *Phys. Stat. Sol. (a)* **2007**, 204(6), 1706–1711.
[248] M. Alvaro, C. Aprile, B. Ferrer, F. Sastre, H. Garcia, *Dalton Trans.* **2009**, 7437–7444.
[249] X. Wang, X. Wang, Z. Guo, *Acc Chem Res.* **2015**, 48(9), 2622–2631.
[250] S. Bhattacharyya, M. Gonzalez, J. D. Robertson, R. Bhattacharyaa, P. Mukherjee, *Chem. Commun.* **2011**, 47, 8530−8532.
[251] N. Masilela, E. Antunes, T. Nyokong, *J. Porphyr. Phthalocyanines* **2013**, Vol. 17(06n07), 417−430.
[252] E. Dube, D. O. Oluwole, N. Nwaji, T. Nyokong, *Spectrochim. Acta A* **2018**, 203, 85−95.
[253] W. Sun, N. Wu, W. Wang, L. Kong, J. Wu, S. Li, Y. Tian, *Dyes Pigm.* **2016**, 133, 86–92.
[254] D. Astruc, E. Boisselier, C. Ornelas, *Chem. Rev.* **2010**, 110, 1857–1959.
[255] R. Kreiter, A. W. Kleij, R. J. M. Klein Gebbink, G. van Koten, *Top. Curr. Chem.* **2001**, 217, 164–197.
[256] G. M. Dykes, *J. Chem. Technol. Biotechnol.* **2001**, 76(9), 903-918.
[257] F. Vogtle, S. Gestermann, R. Hesse, H. Schwierz, B. Windisch, *Prog. Polym. Sci.* **2000**, 25, 987–1041.
[258] F. J. Stoddart, T. Welton, *Polyhedron* **1999**, 18, 3575–3591.
[259] E. W. Buhleier, W. Wehner, F. Vogtle, *Synthesis* **1978**, 155–158.
[260] M. Sowinska, Z. Urbanczyk-Lipkowska, *New J. Chem.* **2014**, 38, 2168–2203.
[261] C. Hawker, J. M. J. Fréchet, *J. Chem. Soc., Chem. Commun.* **1990**, 1010–1013.
[262] B. Donnio, *Inorg. Chim. Acta* **2014**, 409, 53–67.
[263] G. R. Newkome, F. Cardullo, E. C. Constable, C. N. Moorefield, A. M. W. C. Thompson, *Chem. Commun.* **1993**, 925–927.
[264] V. Marvaud, D. Astruc, *Chem. Commun.* **1997**, 773–774.
[265] H. F. Chow, I. Y. K. Chan, P. S. Fung, T. K. K. Mong, M. F. Nongrum, *Tetrahedron* **2001**, 57, 1565–1572.
[266] U.S. Schubert, H. Hofmeier, G. R. Newkome Modern Terpyridine Chemistry, **2006**, WILEY-VCH Verlag GmbH & Co. KGaA, Weinheim
[267] V. Balzani, A. Credi, M. Ventura, *Chem. Sus. Chem.* **2008**, 1, 26–58.
[268] R. Frański., M. Kowalska, J. Czerniel, M. Zalas, B. Gierczyk, M. Cegłowski, G. Schroeder, *Cent. Eur. J. Chem.*, 11(12), **2013,** 2066-2075.
[269] B. Mishra, A. Barik, K. I. Priyadarsini, H. Mohan, J Chem Sci, 2005, 117, 641–647.

[270] R. Ravichandran, M. Rajendran, D. Devapiriam, *Food Chem.* **2014**, 146, 472–478.
[271] A. Raza, X. Xu, L. Xia, C. Xia, J. Tang, Z. Ouyang, *J. Fluoresc.* **2016**, 26, 2023–2031.
[272] M. R. de Oliveira, S. M. Nabavi, N. Braidy, W. N. Setzer, T. Ahmed S. F. Nabavi, *Biotechnol. Adv.* **2016**, 34, 532–549.
[273] N. K. Shah, N. M. Shah, M. Patel, R. Patel, *J. Serb. Chem. Soc.* **2012**, 77, 279–286.
[274] M. A. Jakupec, M. Galanski, V. B. Arion, C. G. Hartinger, B. K. Keppler, *Dalton Trans.* **2007**, 183–194.
[275] E. Wachter, D. K. Heidary, B. S. Howerton, S. Parkin, E. C. Glazer, *Chem. Commun.*, 2012, 48, 9649.
[276] C.-N. Ko, G. Li, C.-H. Leung, D.-L. Ma, *Coord. Chem. Rev.* **2019**, 381, 79–103.
[277] R. Frański., M. Kowalska, J. Czerniel, M. Zalas, B. Gierczyk, M. Cegłowski, G. Schroeder, *Cent. Eur. J. Chem.*, 11(12), **2013,** 2066-2075.
[278] B. Mishra, A. Barik, K. I. Priyadarsini, H. Mohan, J Chem Sci, 2005, 117, 641–647.
[279] R. Ravichandran, M. Rajendran, D. Devapiriam, *Food Chem.* **2014**, 146, 472–478.
[280] A. Raza, X. Xu, L. Xia, C. Xia, J. Tang, Z. Ouyang, *J. Fluoresc.* **2016**, 26, 2023–2031.
[281] M. R. de Oliveira, S. M. Nabavi, N. Braidy, W. N. Setzer, T. Ahmed S. F. Nabavi, *Biotechnol. Adv.* **2016**, 34, 532–549.
[282] N. K. Shah, N. M. Shah, M. Patel, R. Patel, *J. Serb. Chem. Soc.* **2012**, 77, 279–286.
[283] M. A. Jakupec, M. Galanski, V. B. Arion, C. G. Hartinger, B. K. Keppler, *Dalton Trans.* **2007**, 183–194.
[284] E. Wachter, D. K. Heidary, B. S. Howerton, S. Parkin, E. C. Glazer, *Chem. Commun.*, 2012, 48, 9649.
[285] C.-N. Ko, G. Li, C.-H. Leung, D.-L. Ma, *Coord. Chem. Rev.* **2019**, 381, 79–103.
[286] D. Pucci, A. Crispini, M. Ghedini, E. I. Szerb, M. La Deda, *Dalton Trans.* **2011**, 40, 4614–4622.
[287] E. I. Szerb, D. Pucci, A. Crispini, M. L. Deda, *Mol. Cryst. Liq. Cryst.* **2013**, 573, 34–45.
[288] A. A. Andelescu, C. Cretu, L. Cseh, S. Marinescu, E. I. Szerb, O. Costisor, *Scien. Tech. Bull-Chem. Food Sci. Eng.* **2017***,* 14 (XV), 9–16.
[289] A. E. Ozel, S. Kecel, S. Akyuz, *Vib. Spectrosc.* **2008**, 48, 238–245.
[290] J. Stygar, G. Żukowska, W. Wieczorek, *Solid State Ion.* **2005**, 176, 2645–2652.
[291] N. Roeges, *A guide to the complete interpretation of Infrared Spectra of Organic Structures*, Wiley, **1994**, 1 – 340.
[292] J. A. G. Drake, D. W. Jones, *Org. Magn. Reson*., **1982**, 18, 42–44.
[293] T. Kelava**,** I. Ćavar**,** F. Čulo, *Period. Biol.* **2011**, 113 (3), 311–320.
[294] S. Fiorucci, J. Golebiowski, D. Cabrol-Bass, S. Antonczak, *J. Agric. Food Chem.* **2007**, 55, 903–911.
[295] A. E. Ozel, S. Kecel, S. Akyuz, *J. Mol. Struct*. **2007**, 834–836, 548–554.
[296] A. A. Schilt, R. C. Taylor, *J. Inorg. Nucl. Chem.* **1959**, 9, 211-221.
[297] A. Pekal, M. Biesaga, K. Pyrzynska, *Biometals* **2011**, 24, 41–49.
[298] S. Birjees Bukhari, S. Memon, M. Mahroof-Tahir, M. I. Bhanger, *Spectrochim. Acta A* 2009, 71, 1901–1906.
[299] A. Primikyri, G. Mazzone, C. Lekka, A. G. Tzakos, N. Russo, I. P. Gerothanassis, *J. Phys. Chem. B* **2015**, 119, 83-95.
[300] G. Accorsi, A. Listorti, K. Yoosaf, N. Armaroli, *Chem. Soc. Rev.* **2009**, 38, 1690–1700.
[301] J. Zhou, L. Wang, J. Wang, N. Tang, *Trans. Met. Chem.* **2001**, 26, 57-63.
[302] I. G. Zenkevich, A. Y. Eshchenko, S. V. Makarova, A. G. Vitenberg, Y. G. Dobryakov, V. A. Utsal, *Molecules* **2007**, 12, 654-672.
[303] W. Wang, C. Sun, L. Mao, P. Ma, F. Liu, J. Yang, Y. Gao, *Trends Food Sci. Technol.* **2016**, 56, 21–38.
[304] A. Zhou, O. A. Sadik, *J. Agric. Food Chem.* **2008**, 56, 12081–12091.
[305] A. A. Andelescu, C. Cretu, V. Sasca, S. Marinescu, L. Cseh, O. Costisor, E. I. Szerb*, Polyhedron* **2018**, 147, 120–125.
[306] W. Brand-Williams, M. E. Cuvelier, C. Berset, *Lebensm.-Wiss. u.-Technol.* **1995**, 28, 25–30.
[307] J. P. Cornard, J. C. Merlin, *J. Mol. Struct.* **2003**, 651–653, 381–387.
[308] S. V. Jovanovic, S. Steenken, M. Tosic, B. Marjanovic, M. G. Simic, *J. Am. Chem. Soc.* **1994**, 116, 4846–4851.
[309] L. Pazderski, J. Toušek, J. Sitkowski, L. Kozerski and E. Szłyk, Magn. Reson. Chem., 2007, 45, 1059–1071.
[310] S. Z. Vatsadze, A. V. Dolganov, A.V. Yakimanskii, M. Ya Goikhman, I. V. Podeshvo, K. A. Lyssenko, A. L. Maksimov, T. V. Magdesieva, *Russ. Chem. Bull., Int. Ed.* **2010**, 59(4), 724–732.
[311] W. J. Geary, *Coord. Chem. Rev.* **1971**, 7, 81–122.
[312] Y. Muranishi, Y. Wang, M. Odoko, N. Okabe, Acta *Cryst. C* **2005**, 61(6), m307–m310.

[313] S. Nigam, S. Rutan, Applied Spectroscopy, Applied Spectroscopy, 55(11), 362A–370A.
[314] M. H. Alu'datt, T. Rababah, M. N. Alhamad, S. Gammoh, H. A. Alkhaldy, M. A. Al-Mahasneh, C. C. Tranchant, S. Kubow, N. Masadeh, in Fermented Beverages, Elsevier, 2019, pp. 369–400.
[315] N. Armaroli, G. Accorsi, M. Holler, O. Moudam, J.-F. Nierengarten, Z. Zhou, R. T. Wegh, R. Welter, *Adv. Mater.* **2006**, 18, 1313–1316.
[316] H. Xu, R. Chen, Q. Sun, W. Lai, Q. Su, W. Huang, X. Liu, *Chem. Soc. Rev.* **2014**, 43, 3259–3302.
[317] A. C. Tsipis, *RSC Adv*. **2014**, 4, 32504–32529.
[318] D. Krajčiova, M. Melnik, E. Havranek, A. Forgacsova, P. Mikuš, *J. Coord. Chem.* **2014**, 67, 1493–1519.
[319] C. Santini, M. Pellei, V. Gandin, M. Porchia, F. Tisato, C. Marzano, *Chem. Rev.* **2014**,114, 815–862.
[320] D. V. Scaltrito, D. W. Thompson, J. A. O'Callaghan, G. J. Meyer, *Coord. Chem. Rev.* **2000**, 208, 243–266.
[321] M. T. Miller, P. K. Gantzel, T. B. Karpishin, *Angew. Chem. Int. Ed.* **1998**, 37, 1556–1558.
[322] C. T. Cunningham, K. L. H. Cunningham, J. F. Michalec, D. R. McMillin, *Inorg. Chem.* **1999**, 38, 4388–4392.
[323] Y. Pellegrin, M. Sandroni, E. Blart, A. Planchat, M. Evain, N. C. Bera, M. Kayanuma, M. Sliwa, M. Rebarz, O. Poizat, C. Daniel, F. Odobel, *Inorg. Chem.* **2011**, 50, 11309–11322.
[324] N. A. Gothard, M. W. Mara, J. Huang, J. M. Szarko, B. Rolczynski, *J. Phys. Chem. A* **2012**, 116, 1984−1992.
[325] M. W. Mara, D. N. Bowman, O. Buyukcakir, M. L. Shelby, K. Haldrup, J. Huang, M. R. Harpham, A. B. Stickrath, X. Zhang, J. F. Stoddart, A. Coskun, E. Jakubikova, L. X. Chen, *J. Am. Chem. Soc.* **2015**, 137, 9670−9684.
[326] P. C. Healy, *J. Chem. Soc. Dalton Trans.* **1985**, 2541–2545.
[327] A. Crispini, C. Cretu, D. Aparaschivei, A. A. Andelescu, V. Sasca, V. Badea, I. Aiello, E. I. Szerb, O. Costisor, *Inorg. Chim. Acta* **2018**, 470, 342–351.
[328] K. Nakamoto, Infrared spectra of inorganic and coordination compounds, John Wiley & Sons New York 1963, 112, 173.
[329]M. M. Campos-Vallette, R. E. Clavijo, F. Mendizabal, W. Zamudio, R. Baraona, G. Diaz, *Vib. Spectrosc.* **1996**, 12, 37–44.
[330] L. Barrientos, C. Araneda, B. Loeb, I. G. Crivelli, *Polyhedron* **2008**, 27, 1287–1295.
[331] R. Clarke, K. Latham, C. Rix, J. White, Acta Cryst. C 2003, 59, m7–m9.
[332] A. K. Ichinaga, J. R. Kirchhoff, D. R. McMillin, C. O. Dietrich-Buchecker, P. A. Marnot, J.-P. Sauvage, *Inorg. Chem.* **1987**, 26, 4290–4292.
[333] R. M. Everly, D. R. McMillin, *J. Phys. Chem.* **1991**, 95, 9071–9075.
[334] M. Magni, A. Colombo, C. Dragonetti, P. Mussini, *Electrochimica Acta* **2014**, 141,324–330.
[335] K. Shinozaki, Y. Kaizu, Bull. *Chem. Soc. Jpn.* **1994**, 67, 2435–2439.
[336] A. K. I. Gushurst, D. R. McMillin, C. O. Dietrich- Buchecker, J.-P. Sauvage, *Inorg. Chem.* **1989**, 28, 4070–4072.
[337] H. -C. Liang, K. D. Karlin, R. Dyson, S. Kaderli, B. Jung, A. D. Zuberbühler, *Inorg. Chem*. **2000**, 39(26), 5884–5994.
[338] D. L. Lewis, E. D. Estes and D. J. Hodgson, Journal of Crystal and Molecular Structure, 1975, 5, 67–74.
[339] H. Bonadeo and E. Silberman, Journal of Molecular Spectroscopy, 1969, 32, 214–221.
[340] N. Armaroli, *Chem. Soc. Rev.* **2001**, 30, 113.
[341] M. T. Miller, P. K. Gantzel, T. B. Karpishin, *Inorg. Chem.* **1998**, 37, 2285–2290.
[342] K. Goossens, K. Lava, C. W. Bielawski, K. Binnemans, *Chem. Rev.* **2016**, 116(8), 4643-4807.
[343] A. Crispini, D. Pucci, M. Ghedini (2013) Metallomesogens and Lamello-Columnar Phases. In: Reedijk, J. (Ed.) Elsevier Reference Module in Chemistry, Molecular Sciences and Chemical Engineering. Waltham, MA: Elsevier.
[344] N. Godbert, A. Crispini, M. Ghedini, M. Carini, F. Chiaravalloti, A. Ferrise, J. Appl. Crystallogr. 2014, 47, 668.
[345] C. Cretu, A. A. Andelescu, A. Candreva, A. Crispini, E. I. Szerb and M. L. Deda, J. Mater. Chem. C, 2018, 6, 10073–10082.
[346] S. Motoc, C. Cretu, O. Costisor, A. Baciu, F. Manea, E. I. Szerb, *Sensors* **2019**, 19, 5353.
[347] U. S. Schubert, S. Schmatloch, A. Precup, *Des. Monomers Polym.* **2002**, 5, 211.
[348] F. Chen, Y. -K. Tian, Y. Chen, *Chem. Asian J.* **2018**, 13, 3169 – 3172.
[349] B. G. G. Lohmeijer, U. S. Schubert, *J. Polym. Sci. A* **2003**, 41, 1413–1427.
[350] U. S. Schubert, S. Schmatloch, A. Precup, *Des. Monomers Polym.* **2002**, 5, 211–221.

[351] F. Kröhnke, *Synthesis* **1976**, 1–24.
[352] V. Percec, M. Peterca, Y. Tsuda, B. M. Rosen, S. Uchida, M. R. Imam, G. Ungar, P. A. Heiney, *Chem. Eur. J.* **2009**, 15(36), 8994–9004.
[353] S. Narimany, S. Ghammamy, *Global J. Pharmacol.* **2013**, 7(2), 187–191.
[354] A. Andelescu, B. Heinrich, M. A. Spirache, E. Voirin, M. La Deda, G. Di Maio, E. I. Szerb, B. Donnio and O. Costisor, Chem. Eur. J., 2020, 26, 4850–4860.
[355] K. Burger, F. E. Wagner, A. Vértes, É Bencze, J. Mink, I. Labádi, Zs Nemes-Vetéssy, *J. Phys. Chem. Solids* **2001**, 62(11), 2059–2068.
[356] N. V. Venkataraman, S. Bhagyalakshmi, S. Vasudevan, Ram Seshadri, Phys. Chem. Chem. Phys., 2002, 4, 4533–4538.
[357] G. B. Deacon, R. J. Phillips, *Coord. Chem. Rev.* **1980**, 33, 227–250.
[358] W. Goodall, J. A. G. Williams, *Chem. Commun*. **2001**, 2514–2515
[359] K. F. Bowes, I. P. Clark, J. M. Cole, M. Gourlay, A.M.E. Griffin, M.F. Mahon, L. Ooi, A. W. Parker, P. R. Raithby, H. A. Sparkes, M. Towrie *CCDC 263509: Experimental Crystal Structure Determination,* **2005**, DOI: 10.5517/cc8v69l
[360] F. Morale, R. W. Date, D. Guillon, D. W. Bruce, R. L. Finn, C. Wilson, A. J. Blake, Martin Schröder, B. Donnio, *Chem. Eur. J.* **2003**, 9, 2484–2501.
[361] X. Chen, Q. Zhou, Y. Cheng, Y. Geng, D. Ma, Z. Xie, L. Wang, *J. Lumin*. **2007**, 126, 81–90.
[362] D. Myśliwiec, B. Donnio, P. J. Chmielewski, B. Heinrich, M. Stępień, *J. Am. Chem. Soc*., **2012**, *134*, 4822–4833.
[363] D. E. C. Corbridge, E. G. Cox, *J. Chem. Soc.* **1956**, 594–603.
[364] L. A. Dykman, N.G. Khlebtsov, *Acta Naturae.* **2011**, 3(2), 34–55.
[365] N. G. Khlebtsov, *Quantum Electron.* **2008**, 38, 504–529.
[366] S. Peng, Y. Lee, C. Wang, H. Yin, S. Dai, S. Sun, Nano. Res. **2008**, 1, 229–234.
[367] R. M Silverstein, G. C. Bassler, T. C. Morrill, *Spectrometric Identification of Organic Compounds.* 4th ed. New York: John Wiley and Sons, **1981.**
[368] M. Selvaganapathy, N. Raman, *J. Chem. Biol. Ther.* **2016**, 1(2), 108.
[369] U. S. Schubert, C. Eschbaumer, *Angew. Chem. Int. Ed. Engl*. **2002**, 41, 2892–2926.
[370] A. A. Soliman, M. A. Amin, A. A. El-Sherif, C. Sahin, C.Varlikli, Arab. J. Chem. 2017, 10(3), 389–397.
[371] F. Blau, *Ber. Dtsch. Chem. Ges.* **1888**, 21, 1077 –1078.
[372] C. Kaes, A. Katz, M.W. Hosseini, *Chem. Rev*. **2000,** *100,* 3553–3590.
[373] U. S. Schubert, C. Eschbaumer, M.Heller, *Org. Lett.* **2000**, 2 (21), 3373–3376.
[374] A. Wild, A. Winter, F. Schlütter, U. S. Schubert, *Chem. Soc. Rev.* **2011**, 40, 1459–1511.
[375] G. T. Morgan, F. H. Burstall, *J. Chem. Soc. Abstr.* **1932**, 20.
[376] E. C. Constable, M. D. Ward, *J. Chem. Soc., Dalton Trans.* **1990**, 1405–1409.
[377] E. C. Constable, *Chem. Soc. Rev.* **2007**, 36, 246–263.
[378] C. Wei, Y. He, X. Shi, Z. Song, *Coord. Chem. Rev.* **2019**, 385, 1–19.
[379] A. Wild, A. Winter, F. Schlütter, U. S. Schubert, *Chem. Soc. Rev.* **2011**, 40, 1459–1511.
[380] I. Eryazici, C. N. Moorefield, G. R. Newkome, *Chem. Rev.* **2008**, 108, 1834–1895.
[381] S. Duric, C. C. Tzschucke, *Org. Lett.* **2011**, 13, 2310–2313.
[382] D. Zych, A. Słodek, M. Matussek, M. Filapek, G. Szafraniec-Gorol, S. Maślanka, S. Krompiec, S. Kotowicz, E. Schab-Balcerzak, K. Smolarek, S. Maćkowski, M. Olejnik, W. Danikiewicz, *Dyes Pigm.* **2017**, 146, 331–343.
[383] Z. Zhang, H. Wang, J. Shi, Y. Xu, L. Wang, S. Shihadeh, F.-J. Zhao, X.-Q. Hao, P. Wang, C. Liu, M. Wang, X. Li, *Macromol. Rapid Commun.* **2018**, 39(22), 1800404.
[384] D. Jishkariani, B. T. Diroll, M. Cargnello, D. R. Klein, L. A. Hough, C. B. Murray, B. Donnio, *J. Am. Chem. Soc.* **2015**, 137, 10728–10734.
[385] W. Xue, J. Wang, M. Wen, G. Chen, W. Zhang, *Macromol. Rapid Commun.* **2017**, 38, 1600733.
[386] R. J. Ouellette, J. D. Rawn, in Organic Chemistry (Second Edition), eds. R. J. Ouellette, J. D. Rawn, Academic Press, **2018**, 625–663.
[387] C. Yang, J. P. Flynn, J. Niu, *Angew. Chem. Int. Ed*. **2018**, 57(49), 16194-16199.
[388] O. A. Oyetade, V. O. Nyamori, B. S. Martincigh, S. B. Jonnalagadda, *RSC Adv.* **2016**, 6, 2731–2745.
[389] R. S. Nikolić, N. S. Krstić, G. M. Nikolić, G. M. Kocić, M. D. Cakić, D. H. Anđelković, *Polyhedron* **2014**, 80, 223–227.

[390] N. Ikuta, T. Endo, S. Hosomi, K. Setou, S. Tanaka, N. Ogawa, H. Yamamoto, T. Mizukami, S. Arai, M. Okuno, K. Takahashi, K. Terao, S. Matsugo, *Int. J. Mol. Sci.* **2015**, 16, 24614–24628.
[391] R. S. Nikolić, N. S. Krstić, G. M. Nikolić, G. M. Kocić, M. D. Cakić, D. H. Anđelković, *Polyhedron* **2014**, 80, 223–227.
[392] M. Mauro, A. Aliprandi, D. Septiadi, N. S. Kehr, L. De Cola, *Chem. Soc. Rev.* **2014**, 43, 4144–4166.